Multibeam Mapping of the Southern Reykjanes Ridge: Volcano Tectonic Structures Between 57°5' and 58°5'N

Renata de Miranda Franciscon Rocha

Faculty of Life and Environmental Sciences
University of Iceland
2017

Multibeam Mapping of the Southern Reykjanes Ridge: Volcano Tectonic Structures Between 57°5' and 58°5'N

Renata de Miranda Franciscon Rocha

60 ECTS thesis submitted in partial fulfillment of a
Magister Scientiarum degree in Geo-Information Science and Earth Observation for Environmental Modeling and Management

MS Committee
Ármann Höskuldsson
Rannveig Ólafsdóttir
Ingibjörg Jónsdóttir

Master's Examiner
Árni Vésteinsson at Landhelgisgæslan/Sjómælingar

Faculty of Life and Environmental Sciences
School of Engineering and Natural Sciences
University of Iceland
Reykjavik, 26 may 2017

Multibeam Mapping of the Southern Reykjanes Ridge: Volcano Tectonic Structures Between 57°5’ and 58°5’ N
Multibeam Mapping of the Southern Reykjanes Ridge
60 ECTS thesis submitted in partial fulfillment of a *Magister Scientiarum* degree in Geo-Information Science and Earth Observation for Environmental Modeling and Management

Faculty of Life and Environmental Sciences
School of Engineering and Natural Sciences
University of Iceland
Askja, Sturlugata 7
101, Reykjavik
Iceland

Telephone: 525 4000

Bibliographic information:
Renata de M. F. Rocha, 2017, *Multibeam Mapping of the Southern Reykjanes Ridge: Volcano Tectonic Structures Between 57°5' and 58°5'N*, Master’s thesis, Faculty of Life and Environmental Sciences, University of Iceland, pp. 156.

Printing: XX
Reykjavik, Iceland, 26/may/2017

Abstract

The Reykjanes Ridge, extending from Iceland to approximately 55°N, is the northernmost part of the Mid-Atlantic ridge. This region represents the tectonic boundary between the North American and Eurasian tectonic plates in combination with the Icelandic mantle hotspot, and therefore has very high volcanic activity. It is an anomalous mid-ocean ridge, with an axis-parallel morphology and the lack of transform faults, converging to its axis on approximately 58N. Such places are widely unexplored and might reserve important mineral resources. On this wok, we use new multibeam data to describe and analyze some of the main geological structures of an area in the Southernmost portion of the Reykjanes Ridge, between 57°5’ and 58°5’N. The axial volcanic ridges directions and the areas of the central volcanoes on the Reykjanes Ridge were mapped. In both East and West sides of the Mid-Atlantic Ridge, the normal faults were mapped and the geological orientation of the faulted planes analyzed. Data from the first multibeam bathymetric survey ever performed on the ridge were used for change detection analysis. Image differencing was performed, to detect changes on seafloor topography that might have happened within a time span of up to 23 years. The resulting images shows the intensity and value of change, where the negative values represent an increase in depth, and positive values represent a decrease in depth, or in other words, a decrease or increase in seafloor topographic elevation.

Útdráttur

Reykjaneshryggurinn nær frá Íslandi að Bight þverbrotabeltinu (um það bil 55° N). Hann er norðvesturhluti mið-Atlantshafs hryggjarins. Þetta svæði táknar flekamót milli Norður-Ameríku- og Evrasíuflekans. Þrátt fyrir að vera hæg gliðnunarflekamót ber Reykjaneshryggur einkenni hraðra gliðnunarflekamóta og má rekja það til möttulfráviks kennt við Ísland og oft nefnt „heitur reitur“. Einkenni „heitra reita“ er mjög mikil eldvirkni. Reykjaneshryggur er einkennilegur vegna þess að hann er skásettur á landreksstefnu. Gliðnunarflekamót eru að estu órannsökuð en talið er að þeim tengt sé að finna mikilvægar jarðefnaauðlindir. Í þessari vinnu notum við fjölgeislamæligögn til að lýsa og greina nokkrar af helstu jarðfræðilegum einkennum svæðisins á suðurhluta Reykjanesryggjar, milli 57°5‘ og 58°5’N. Öxulhryggir og svæði miðlægra eldfjalla á Reykjaneshrygg voru kortlögð. Beggja vegna sigdalsins, er markar flekamótin, var strik og halli jarðlaga kortlagður sem og hallastefna misgengja. Myndgreiningar voru gerðar til að greina breytingar á landslagi sem kunna að hafa átt sér stað síðustu 23 ár.

Dedication

I dedicate this thesis to all people who navigated or have yet to navigate over the vast and mysterious ocean, without even knowing what lies underneath their feet.

Preface

The first comprehensive map of the seafloor was carved by the hands of a woman who struggled to be acknowledged in a world where gender distinctions did matter. Today, at least in science, I fortunately do not share the same difficulties. Instead, I find on her inspiration to follow my dreams and the hope for equal rights and opportunities for all women in the world.

Decades after the seafloor was revealed, we found on it potential mineral resources to be explored. With modern societal pressures and current human lifestyles, especially in developed countries, it is very likely that these resources will be sought. In deep seas however, they coincide with the habitat of newly discovered species. These organisms are helping us understand the mechanisms of life, defying all previously known requirements for survival and flourishing in an environment that seems completely hostile to us.

Historically, humans cared little for the environment and were harmful in their endeavors. Now, we have become wiser, and I do believe that we are able to find solutions for our environmental problems, as long as we care for them. Seafloor exploration should be filled with this wisdom and care; we cannot destroy the last bit of untouched nature that still survives in our planet.

O primeiro mapeamento compreensível do fundo do mar foi esculpido pelas mãos de uma mulher, que lutou para ser aceita em um mundo onde distinções de gênero eram sim importantes. Nesta ocasião, ao menos na ciência, felizmente não compartilho as mesmas dificuldades. Em vez disso, encontro nela inspiração para seguir meus sonhos e anseio por direitos e oportunidades iguais para todas as mulheres do mundo.

Décadas após a revelação do fundo do mar, encontramos nele potenciais recursos minerais para explorar. Com as pressões da sociedade moderna e os atuais estilos de vida humano especialmente em países desenvolvidos, é muito provável que estes recursos sejam desejados. Em águas profundas, no entanto, eles coincidem com o habitat de espécies recém-descobertas. Estes organismos estão nos ajudando a entender os mecanismos da vida, desafiando todos os requerimentos para sobrevivência até então conhecidos, e florescendo em um ambiente que nos parece completamente hostil.

Historicamente, os humanos não têm se importado com o meio ambiente e têm sido prejudiciais em suas explorações. Hoje somos mais sábios, e eu creio que somos também capazes de encontrar soluções para nossos problemas ambientais, desde que nos importemos com eles. A exploração do fundo do mar deve ser recheada dessa sabedoria e consideração; não podemos destruir a última parte de natureza intocada que ainda sobrevive em nosso planeta.

Renata Rocha, Reykjavik, 05/17

Table of Contents

List of Equations

List of Figures

Abbreviations

3D: Three dimensional

AOI: Area of Interest

AVR: Axial Volcanic Ridge

DEM: Digital Elevation Model

GIS: Geo-Information System

HÍ: Háskoli Islands / University of Iceland

ITC: Faculty of Geo-Information Science and Earth Observation – University of Twente

MAR: Mid-Atlantic Ridge

MBES: Multibeam Echosounder

Ma: Million Years Ago

Km/Myr: Kilometers per Million years

NCEI: National Centers for Environmental Information (USA)

NOAA: National Oceanic and Atmospheric Administration (USA)

RR: Reykjanes Ridge

SBES: Single Beam Echosounder

SOEST: School of Ocean and Earth Science and Technology (Hawaii – USA)

USGS: United States Geological Survey (USA)

N: North

S: South

E: East

W: West

NE: Northeast

NW: Northwest

SE: Southeast

SW: Southwest

Acknowledgements

First and foremost, I would like to express my gratitude to my family, especially to my father who always believed in me and invested in my education throughout my life. I am also personally grateful to my boyfriend Martin and my good friend Melissa for giving me emotional support during this stressful moment of my life. I thank the universe for all of the friendships I made in both Iceland and the Netherlands, whom are now scattered through this small planet we inhabit.

I am extremely grateful to my supervisor Ármann Hoskuldsson for giving me the amazing opportunity of working with this wonderful study area. I also thank professor Inga and professor Rannveig for additional advice and support during the thesis execution. Furthermore, I thank the University of Iceland for the all the structure and support provided.

I acknowledge the faculty of Geo-Information science and earth observation from the University of Twente for having given me the theoretical basis for GIS analysis. I also acknowledge my two previous universities, FURG and Bangor for giving me background in oceanography and science. I specially thank professor Gilberto Griep for introducing me to geological oceanography and acoustic exploration.

At last, I acknowledge and thank the organizations that provided me data for my research. Specifically, to NOAA, SOEST, USGS and professor Roger Searle, who was very helpful and personally provided data from the Bridge project.

1 Introduction

The ocean represents the ultimate barrier for understanding how our planet was formed. The seafloor is still a mysterious province, comprising many hidden gems that have yet to be described. *Bathymetry* is the term used to refer to the study of submarine relief and bathymetric mapping is the initial point for seafloor exploration. It is basically equivalent to *topography* on land, but instead of information about elevation, bathymetry contains information about depth relative to sea level (Lawrence, 2009).

The data acquisition for bathymetry is, however, considerably more complex than for topography. Difficulties involved in acquiring marine geological data are primarily related to the presence of water, which considerably obstructs data acquisition. The early bathymetric measurements were performed by lowering a string with a weight into the water column and then measuring the length of the string that was used (Fig. 1.1). This method was very time consuming and not very accurate. Nevertheless, such measurements made it possible to recognize some of the most prominent features in the oceans (Dierssen & Theberge, 2014)

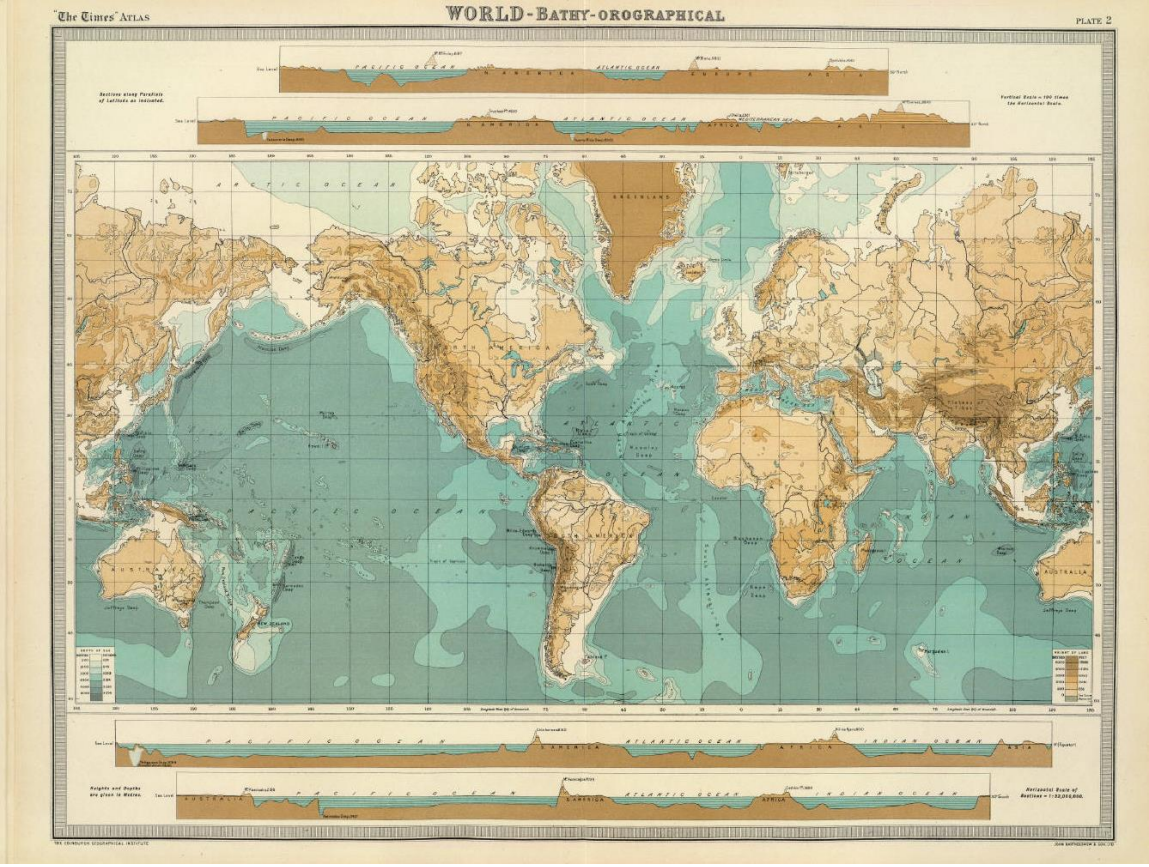

Figure 1.1 Map of the North Atlantic Ocean derived from the first bathymetric measurements made in the ocean, published in a World Atlas by The Times, London in 1922. Lighter blue represents lower depths. Topographic profiles across the oceans and continents on the top and bottom (Bartholomew, 1922).

In the early twenties, *acoustic* exploration was introduced, which, among other things, allowed more bathymetric measurements to be taken (Wille, 2005). The first map of the ocean floor derived from acoustic measurements (Fig. 1.2) was manually developed by the oceanography cartographer Marie Tharp and the geophysicist Bruce Heezen (North, 2010).

Even though the data quality was poor in early investigations, the maps produced by Tharp & Heezen were incredibly accurate, and revealed a range of mountains cutting through every ocean in Earth. These mountains were named mid-ocean ridges and these findings helped in the development of the *Plate Tectonics* theory (Heezen, Tharp & Ewing, 1959; Heezen, 1960; Hess, 1962, Heezen & Tharp, 1965).

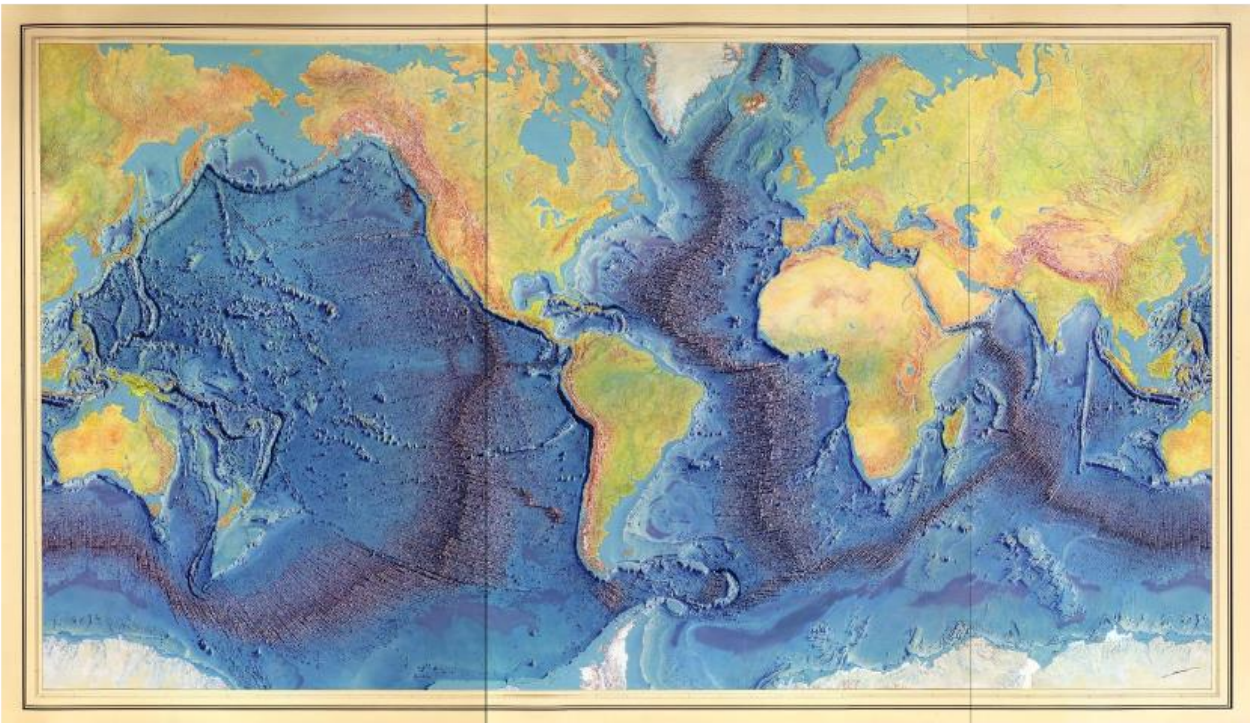

Figure 1.2 World bathymetry from early acoustic measurements (Heezen, Tharp & Ewing, 1959; Heezen, 1960; Hess, 1962; Heezen & Tharp, 1965).

Even though the advent of remote sensing has enabled large areas to be mapped with high accuracy, it is still not a simple task to acquire acoustic data in the ocean. Another methodology that can be applied for mapping the seafloor is *satellite altimetry* (e.g. Calmant, Berge-Nguyen, & Cazenave, 2002; Smith & Sandwell 1977). The presence of topographic features on the seafloor causes the ocean surface to bend following the relief underneath and such undulations can be detected by satellites (Fig. 1.3). The product resulting from satellite altimetry is, however, not as precise as the acoustics' and therefore, although satellite altimetry is efficient to provide a general topographic picture of the ocean floor, acoustic survey is still required for detailed mapping (Wille, 2005).

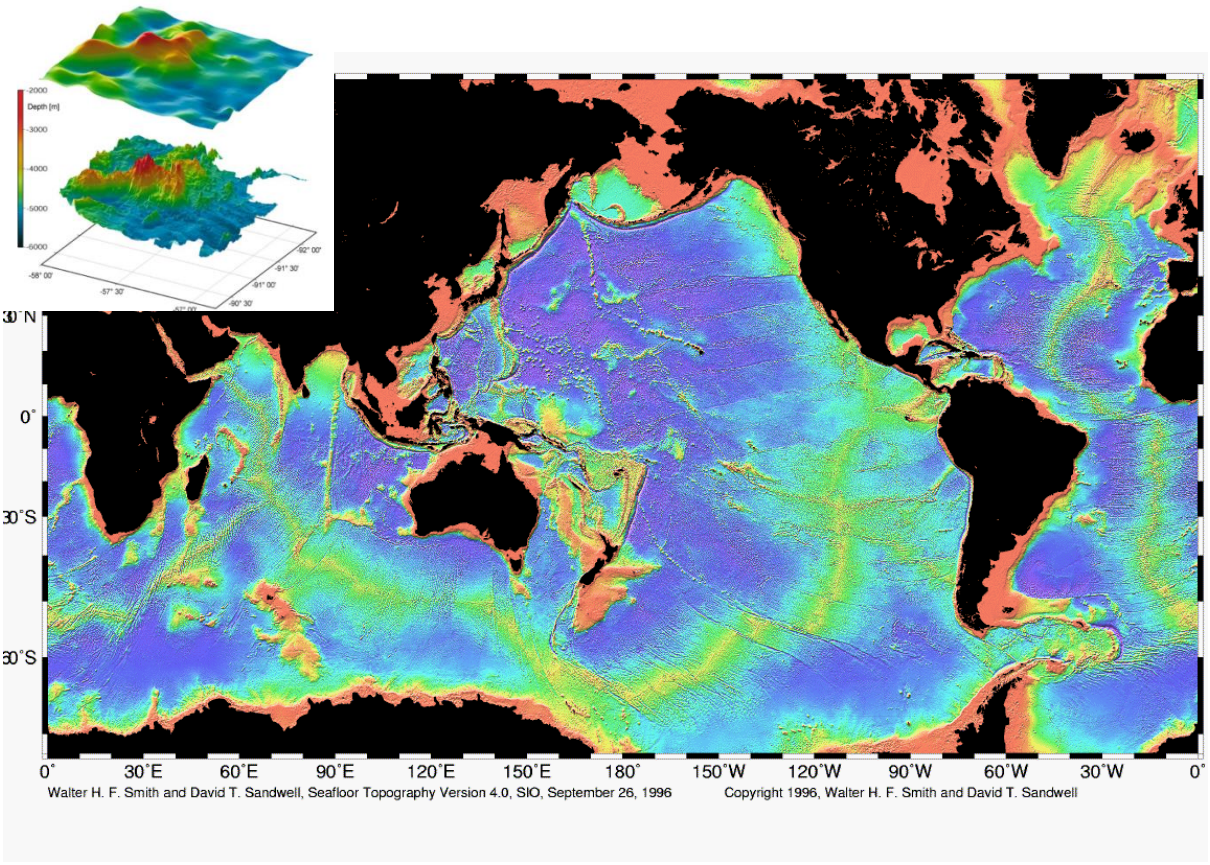

Figure 1.3 Seafloor Topography by satellite altimetry from Smith & Sandwell (1977). On the top left, comparison between satellite altimetry (top) and acoustic bathymetry data (bottom).

The work initiated by Tharp & Heezen and followed by many others allowed the identification of the main geological features in the ocean floor, the mid-ocean ridges. One of these features, the Reykjanes Ridge (RR) is the focus of this thesis. The RR is the part of the Mid-Atlantic Ridge (MAR) that connects to the South of Iceland. It presents high volcanic activity and it is considered to be an anomalous body (Keeton et al., 1996). For this reason, the RR has always caught the attention of scientists and therefore has been one of the most surveyed regions on the ocean floor (e.g. Hey et al., 2015; Höskuldsson, Hey, Kjartansson, & Guðmundsson, 2007; Keeton et al., 1996; Navin, Peirce, & Sinha, 1998).

In the past, however, storage and processing limitations on older computers prevented high resolution mapping. It wasn't until the last few years that technology allowed the improvement of data acquisition, storage and processing enabling therefore more sophisticated analysis to be carried out. The tools that are now available for data processing differs greatly than those available in the past, allowing the use of historic data in a way never done before, and generating scientific knowledge even with datasets that have already been explored (Wille, 2005).

To this date, four main bathymetric investigations were carried out in the RR: The Research Vessel (RV) M. Ewing mapped selected areas on the Southern, central and Northern regions (Parson, 1993); The BRIDGE bathymetry survey, incorporated 3 new cruises on board of the RV Charles Darwin to the previous dataset, to make the most complete description of the Ridge

until that date (Keeton et al., 1996); The R.V Knorr investigated in high resolution the Northernmost part of the region (Höskuldsson et al., 2007); finally, the RV Marcus Langseth, investigated the Southernmost region and the connection between the RR and The MAR, on the Bight Fracture Zone (Hey et al., 2015).

The early investigations described the general morphology of the Ridge (e.g.Keeton et al., 1996; Parson et al., 1993; Searle, Field & Owens, 1994). These surveys were limited to the area around the ridge axis and had poor resolution due to technological limitations. The later datasets detailed and expanded this description and were used in combination with other modern geophysical techniques (i.e. magnetics and gravity) to explain the evolutional history of the RR (e.g. Benediktsdóttir, Hey, Martinez, & Hoskuldsson, 2012; Martinez & Hey, 2017).

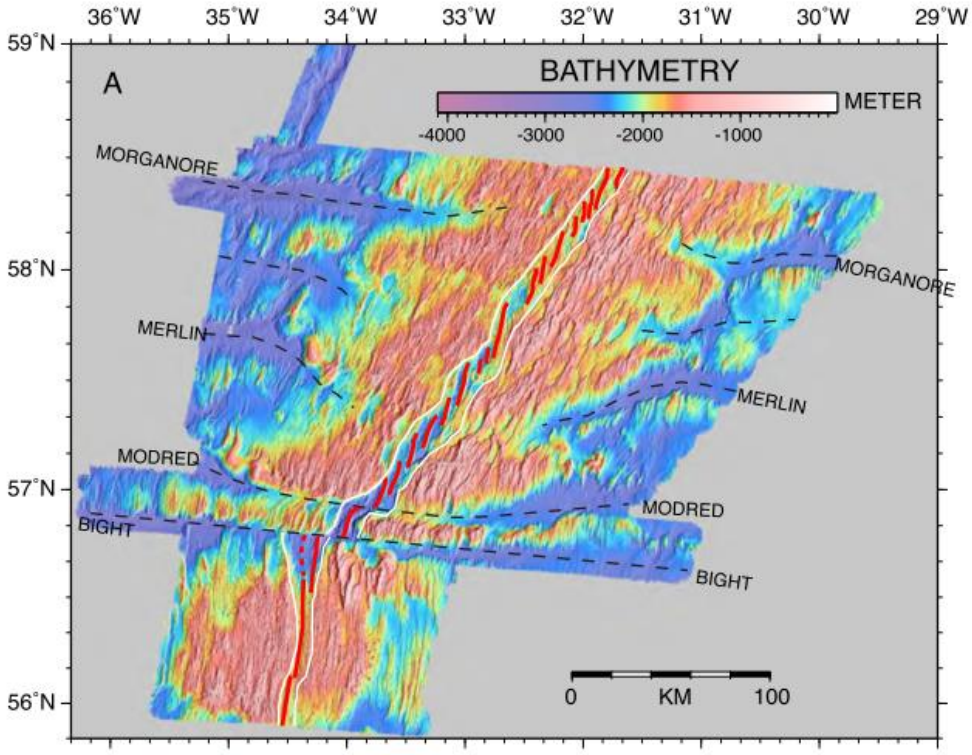

Figure 1.4 Bathymetry map from RV M. G. Lansgeth 2013. Red lines are direction of volcanic ridges. White lines are the tectonic boundaries. Black dashed lines are transfom boundaries. From Hey & Martinez (2017).

After the latest survey, Hey et al, (2015) reported that the southernmost portion of the ridge presents complicated morphology that can help explain its evolution history and later, Hey & Martinez (2017) suggested a new evolution model for the RR. In this work, a selected area on the southernmost portion of the ridge was investigated, making use of all the available acoustic bathymetry datasets. We analyze the previously cited surveys using modern GIS techniques to describe the main characteristics of seafloor spreading in this unique region of the globe.

1.1 Study Area

As mentioned before, the area targeted by this study area is located on the southernmost portion of the Reykjanes Ridge (Figure 1.6). It extends from 58°5’ to 57°5’ N and -35° to -30° W, covering a total area of 27,000km^2. This area is 100km long in the NS direction and 270km wide on the WE direction. Figure 1.5 shows the study area location in the globe and in relation to Iceland. The data from the RV M. Langseth, used in this work, were overlaid on imagery and bathymetry base maps.

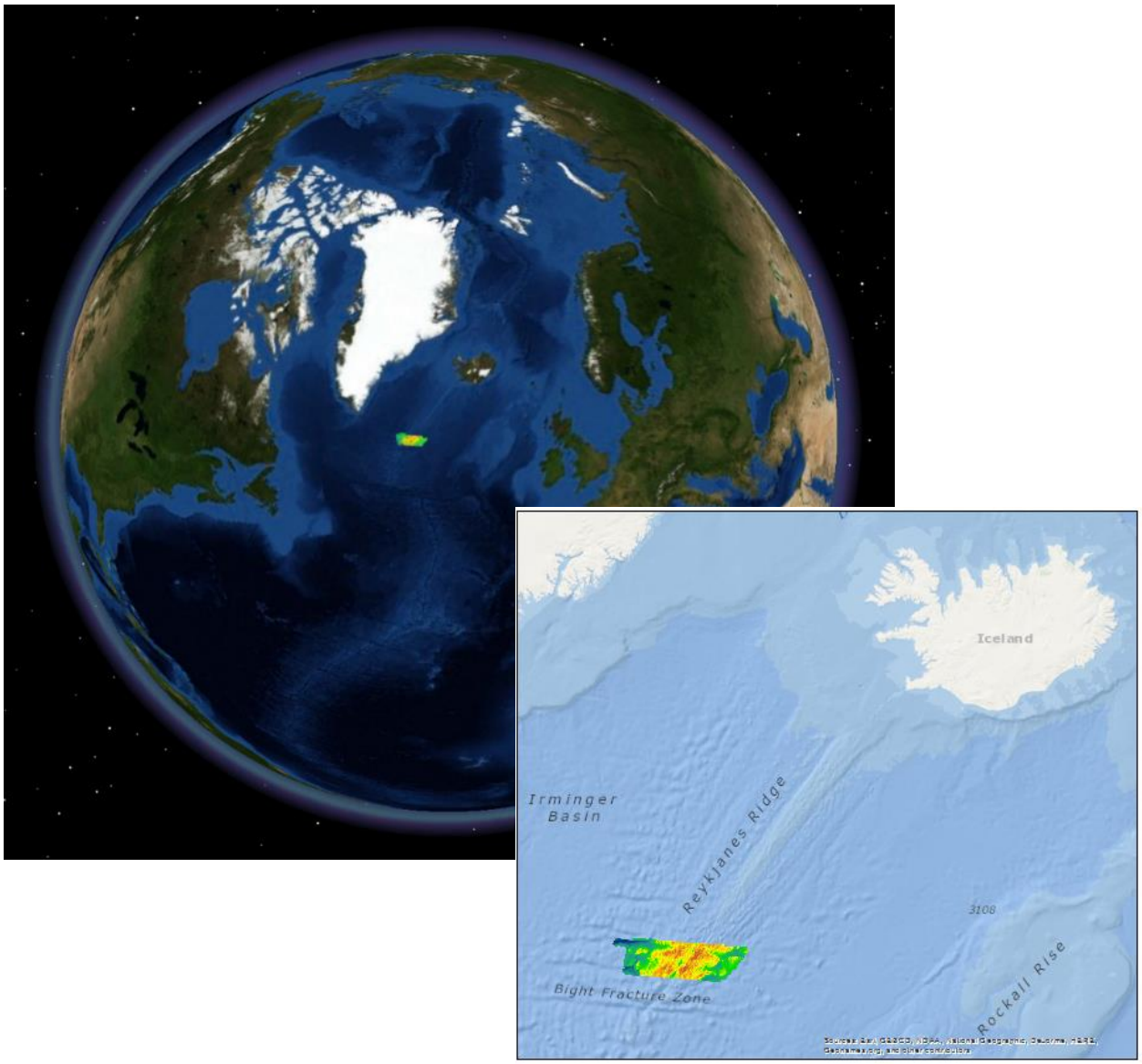

Figure 1.5 Study Area overlay of acoustic data from the RV MG Langseth (MGL1309) on Imagery basemap (above) and Bathymetry basemap by NOAA (right bottom corner).

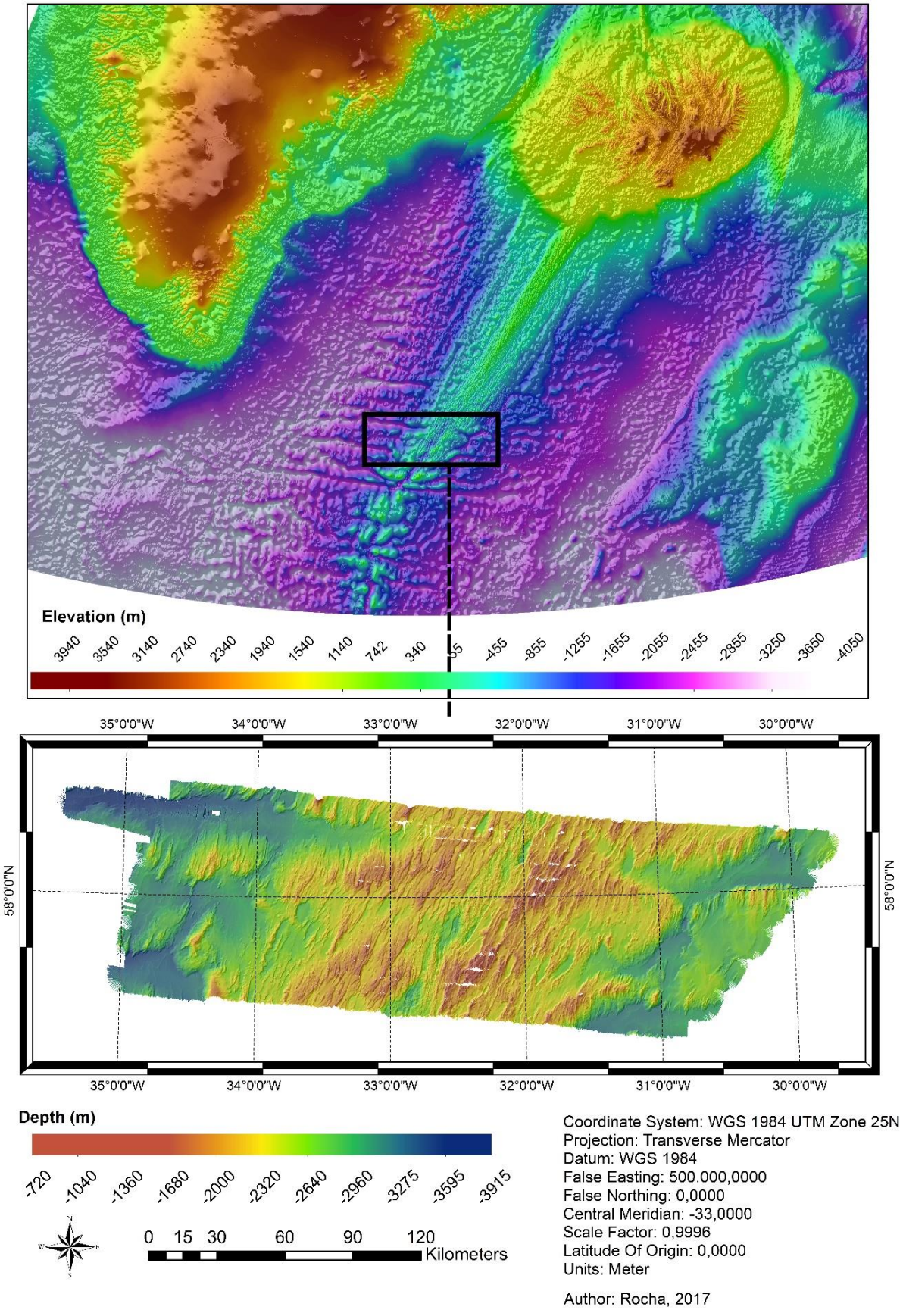

Figure 1.6 Digital Elevation Model of the North Atlantic highlighting the study area described in this study.

1.2 Research Aims

In 2013 the University of Hawaii, in partnership with the University of Iceland conducted a marine geologic survey along the RR axis on board of the RV M. Langseth. The main aim of this survey was to use up to date technology to explain the RR's geological history and try to solve an ongoing debate on the origin of its distinct landscape features (SOEST (University of Hawaii), 2013).

Other important expectation of this expedition was to generate detailed maps of the ridge's geological structures (SOEST (University of Hawaii), 2013). Therefore, this research aims to present the bathymetric analysis of a selected portion from the 2013 dataset. In addition to that, the present work also makes use of the historic data to check whether there has been a submarine volcanic eruption within the time span covered by available datasets.

1.2.1 General Objectives

- Bathymetric mapping
- Comparison with older datasets

1.2.2 Specific Objectives

- Describe the bathymetric features of the Reykjanes Ridge between 57°5' and 58°5' N
- Map the normal faults
- Identify and compare fault trends on different provinces
- Verify correlation between fault magnitude and distance to the tectonic boundary
- Verify correlation between the dip angle of the faulted blocks and distance to the tectonic boundary
- Identify if there were any detectable changes on seafloor topography that could be related to volcanic eruptions

2 Literature Review

This chapter offers the basic theoretical concepts that will be discussed on this thesis. These concepts include the physical structure of planet Earth and the plate tectonics theory, especially regarding ocean formation and evolution. The last two sections are dedicated to describing these concepts in relation to the study area; the Reykjanes Ridge and the Mid-Atlantic Ridge. This chapter will also present previous bathymetric research results in the study area.

2.1 Earth's Physical Structure

The chemical composition of our planet manifests itself as minerals on its surface, where the relatively low temperatures allow crystallization. It is however not like this throughout the interior of the planet. Earth's interior is composed by layers of different chemical compositions and physical properties. The main physical properties that affect the state of these layers are temperature and pressure (Anderson, 1989). Figure 2.1 shows the different interior layers of Earth and the corresponding seismic wave propagation record.

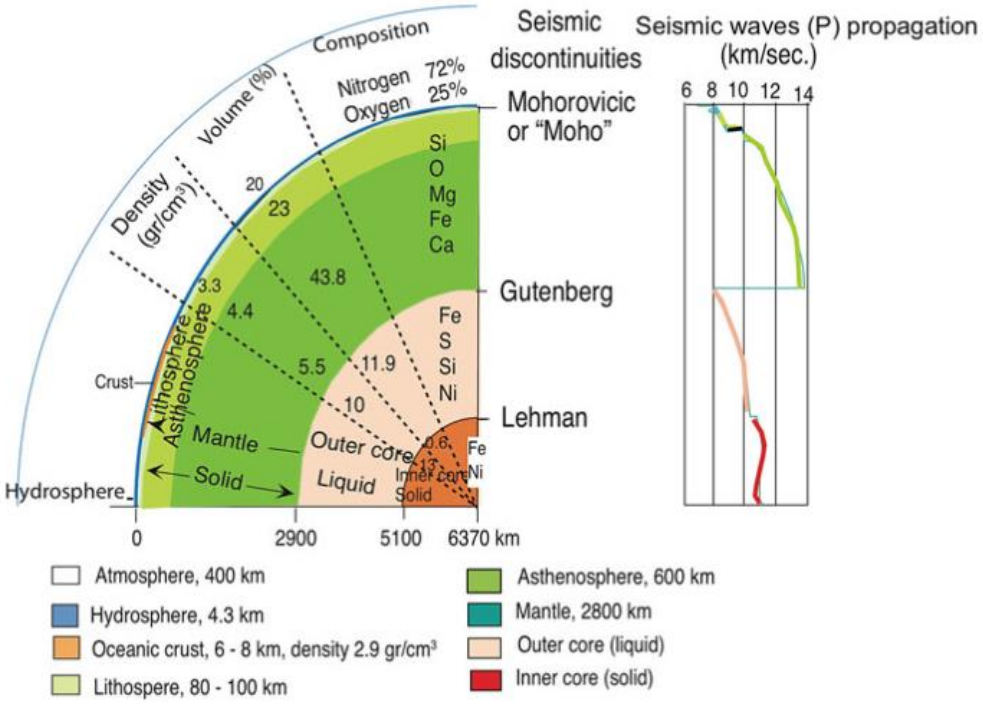

The temperature and pressure values are higher closer to Earth's center. Around this point, is the Earth's core, mostly composed of iron and nickel. In the interior of the core, the very high pressure causes the metals to solidify. In its outer portion, however, pressure and temperature values are in equilibrium, allowing the core to be in liquid state (Anderson, 1989).

Surrounding Earths' core and making up for most of the mass of the planet, is the mantle. The upper part of the mantle, also called asthenosphere, is composed by hot rock and has plastic properties. The lower mantle, or mesosphere, is a semi solid, plastic medium through which heat from Earth's interior circulates in convective currents and by conduction (Anderson, 2007; Jain, 2014).

Figure 2.1 Physical and chemical structure of Earth's interior with respective seismic record (Hekinian, 2014).

Finally, the outermost solid part of Earth, where we live and conduct all of our activities is called the lithosphere. The lithosphere is a thin layer composed of oceanic and continental crust. The continental crust is silica rich and in general thicker than the ocean crust, reaching up to 75km. On the other hand, the oceanic crust is low in silica and thus denser. It is of basaltic composition, reaching up to a maximum of 10km in thickness. The atmosphere and lithosphere complete the physical structure of the Earth, in a soup of loose molecules around the planet (Anderson, 2007; Jain, 2014).

The first theory that tried to explain the layout of Earth's crust was *The Continental Drift*, proposed by Alfred Wegener. This theory aimed to explain why the African and American continents seem to fit together. Later, the theory of continental drift evolved and today we believe that Earth's crust is composed by several individual *crustal plates* that move over and along the plastic portion of the mantle. As result of these dynamics, earthquakes and volcanic eruptions take place, releasing mantle material (magma) that solidifies on Earth's surface as rocks (Condie, 1976).

The causes of plate tectonics movements were later attributed to currents which produced mantle convection. In regions where the convection currents are convergent, subduction zones are formed. Continental ridges and oceanic trenches are located at such convergent boundaries. On the other hand, where the convection currents are at divergent, accretion zones are formed. Rift valleys and Mid-Ocean ridges are located on this last type of plate boundary (Condie, 1976; Hekinian, 2014; Jain, 2014).

Volcanic activity at divergent boundaries is caused by upwelling of mantle plumes. In the oceans these regions correspond to mid-ocean ridges, where new oceanic crust is formed by

volcanic eruptions on fissures and sporadic seamounts (Cann & Smith, 1994). The significance of this theory for understanding the evolution of ocean basins will be discussed in the next section of this chapter.

2.2 Ocean Tectonics

By exposing the existence of immense rift valleys in the ocean (mid-oceanic ridges), the bathymetric maps produced by Tharp & Heezen helped developing the plate tectonic theory (Heezen, Tharp & Ewing, 1959; Heezen, 1960; Hess, 1962, Heezen & Tharp, 1965). Another important contribution was made by the Canadian geophysicist J. Tuzo Wilson, who developed a theory to explain the evolution of the ocean basins (Wilson, 1954). This theory was then named after him and is today well known as the "Wilson cycle" (Condie, 1976; Hekinian, 2014).

According to Wilson's theory, old oceans basins are destroyed at convergent plate boundaries, where the oceanic crust is melted. The subducted crust is added to the mantle plume that circulates through Earth's interior. During this process, the volatiles released by this subducting crust, cause melting of the overlaying depleted mantle. This molten material is then released to the surface as volcanic eruptions on marginal continental ridges. The Pacific Ocean is an example of oceanic basin on this stage of evolution (Condie, 1976; Hekinian, 2014).

Contrary to this, oceanic basins are formed at divergent plate boundaries, where shallow convection in the upper mantle takes place. The decompressing of the plastic mantle generates a partial melt that reaches the surface on certain occasions, causing volcanic eruptions (Condie, 1976; Hekinian, 2014). The plate segregation gives origin to the mid-ocean ridges first portrayed by Heezen (1960), Hess (1962) and Vine & Mathews (1963). These acresction regions, therefore comprise the yougest portions of the litosphere (Muller, Roest, Royer, Gahagan, & Sclater, 1997). Figure 2.2 shows a map of the age of the ocean floor, plotted from magnetic data by (Müller, Sdrolias, Gaina, & Roest, 2008).

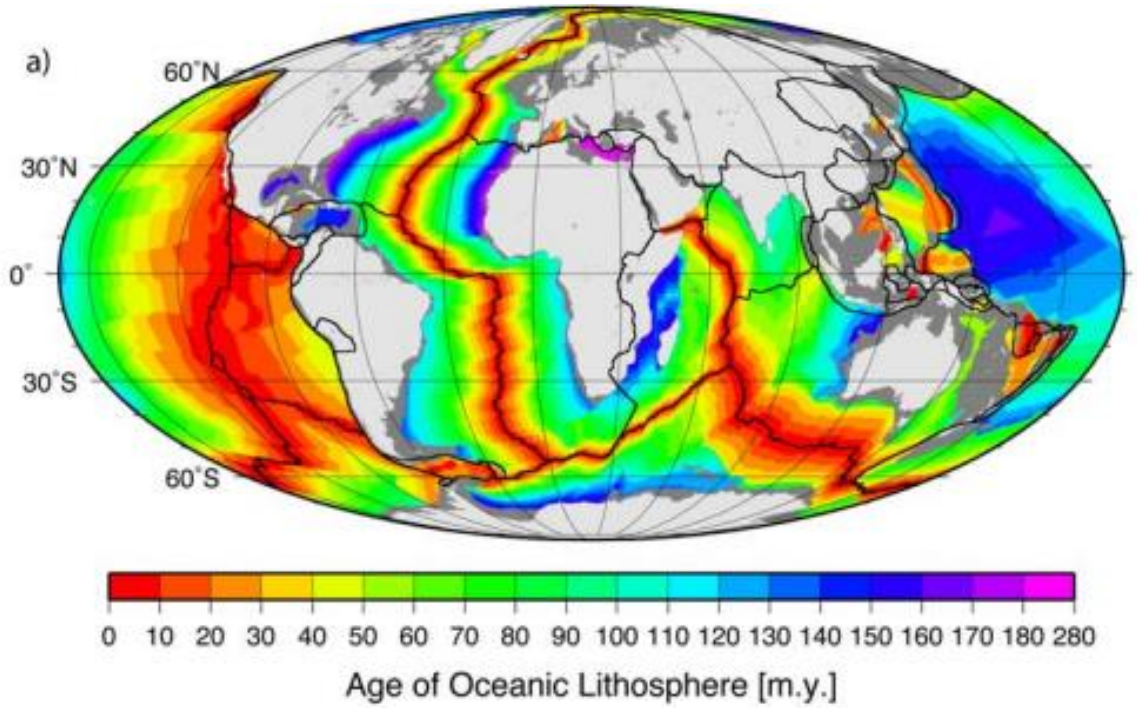

Figure 2.2 Age of the ocean floor derived from magnetic anomaly data (Müller et al., 2008).

Along with the theory of ocean basin's evolution, Wilson also introduced the existence of a third type of tectonic boundary (Wilson, 1965). On such boundaries, two tectonic plates move laterally in relation to each other, instead of converging or diverging. This type of boundary is called *transform*. Mid-ocean ridges are characterized by having a number of transform faults, perpendicular to its axis.

Another important contribution from Wilson was the theory of mantle hotspots. This theory was set forth to explain why there is volcanic activity in places off plate boundaries. According to Wilson, hot spots are areas of mantle convection not associated with plate boundaries. As the tectonic plates move, these spots remain in the same place (Condie, 1976; Hekinian, 2014). When located within oceanic plates, the volcanoes resulting from them form island chains. The youngest islands have active volcanoes, while at the older ones, volcanic activity has ceased. The Hawaiian archipelago is an example of this type of volcanism (Coffin & Whittaker, 2016; Hekinian, 2014). Figure 2.3 illustrates tectonism in the ocean and on continental margins.

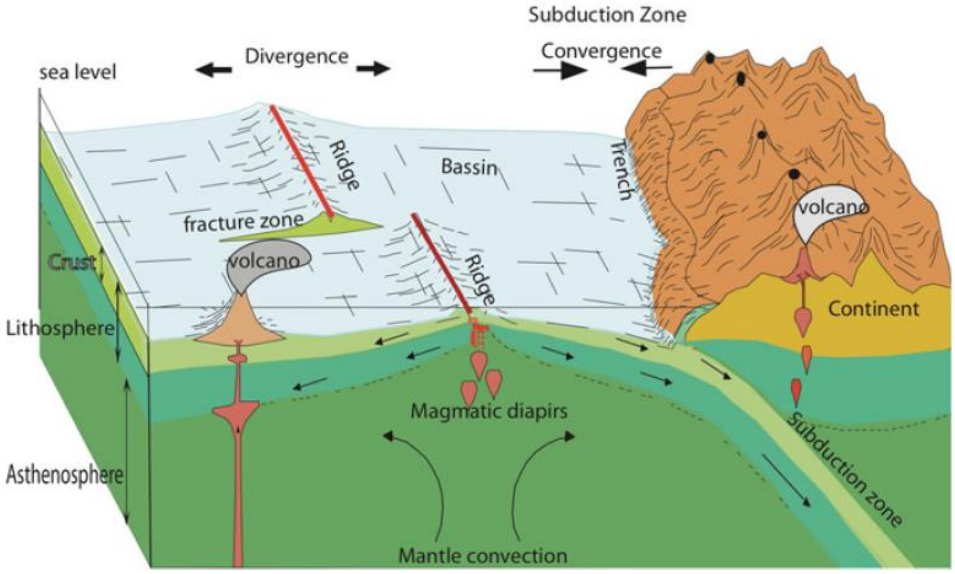

Figure 2.3 Schematic representation of seafloor being formed on divergent boundaries and destroyed on subduction zones. (Hekinian, 2014).

Iceland is located at a divergent plate boundary on top of the MAR. However, excess production of magma within the Icelandic region has been suggested to be associated with a mantle plume (e.g. Jones, 2003; Parnell-Turner et al., 2014). The Icelandic region is thus a combination of a divergent plate boundary and a mantle plume. The next sub-chapter will explain the typical structural morphology and evolution history of mid-ocean ridges. Further Characteristics of the MAR and the RR will be later empathized.

2.3 Mid-Ocean Ridge Evolution

Mid-ocean ridges are rifting systems that generate oceanic crust. They differ around the globe in their morphology but some features are common to all of them (Figure 2.4). The typical topography of mid-ocean ridges comprises a central depression located over the spreading center, making the plate boundary. This linear configuration is interrupted by a number of discontinuities that eventually evolve to create transform faults. These discontinuities also form normal faults and other fracturing features, that are more or less abundant depending on the type of spreading system (e.g. Macdonald, 2001; Macdonald & Atwater, 1978).

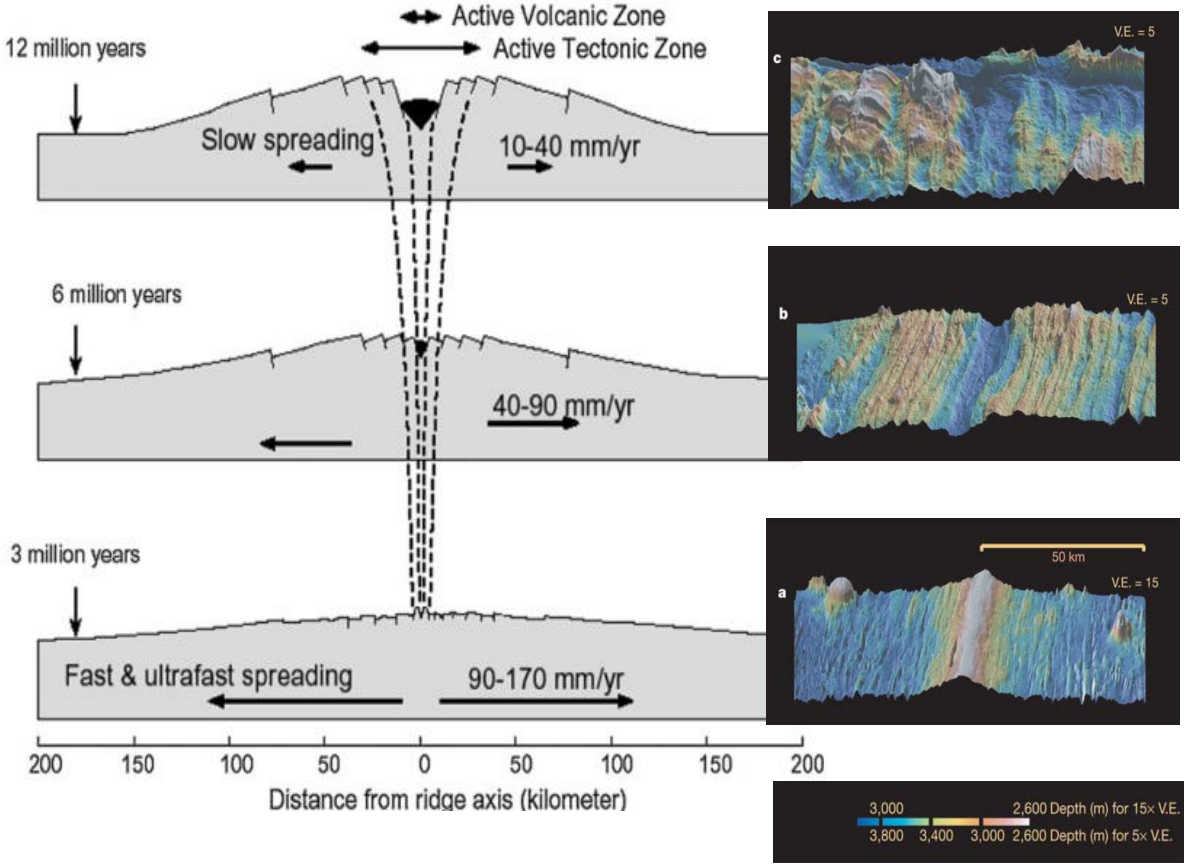

Figure 2.4 Topographic models and corresponding 3D bathymetry of different spreading centres: (a) Fast (b) Intermediate and (c) Slow. Dashed lines mark the area of volcanic activity. Modified from: (Buck et al., 2005 and Hekinian, 2014)

The first factor that causes mid-ocean ridges to differ in morphology is the speed at which the tectonic plates diverge away from each other. This speed is referred to as "the spreading rate" and can be calculated by dating the rocks forming the oceanic crust and correlating with magnetic record on the seafloor. (e.g. DeMets, Gordon, & Argus, 2010). According to the spreading rate, Mid-ocean ridges are classified as slow, intermediate or fast spreading centers.

The magma supply is the second most important factor affecting mid-ocean ridges morphology. Slow spreading centers are usually formed from a lower magma supply, while fast spreading centers result from higher magma supply (e.g. Langmuir & Forsyth, 2007; MacDonald & Atwater, 1978; Macdonald, 2001). Generally, the axis of slow spreading ridges is marked by a large central valley (graben) that can be up to 3km deep, while fast spreading ridges present an axial high with axial trough. However, with very high magma supply, an axial high can be formed even on slow spreading ridges, as it is the case for the Reykjanes Ridge (Macdonald, 2001).

The resulting mantle upwelling from the different types of reservoir causes discontinuities on the rifting system. These discontinuities give origin to spreading segments, forming undulations on the crust. These undulations are of higher amplitude on slow spreading ridges and of higher frequency on fast spreading ridges. Magma supply is abundant at segment centers and starved at segment ends. Segment ends are deeper parts of the seafloor presenting older crust and no volcanic activity (Macdonald, 2001).

The smaller discontinues are overlapping spreading centers and differ on slow and fast ridges. These features evolve to originate transform faults which are large linear features orthogonal to the tectonic boundary. Figure 2.5 is the model for discontinuity evolution proposed by (Macdonald & Atwater, 1978) and Figure 2.6 illustrates how magma supply and mantle upwelling could originate these discontinuities.

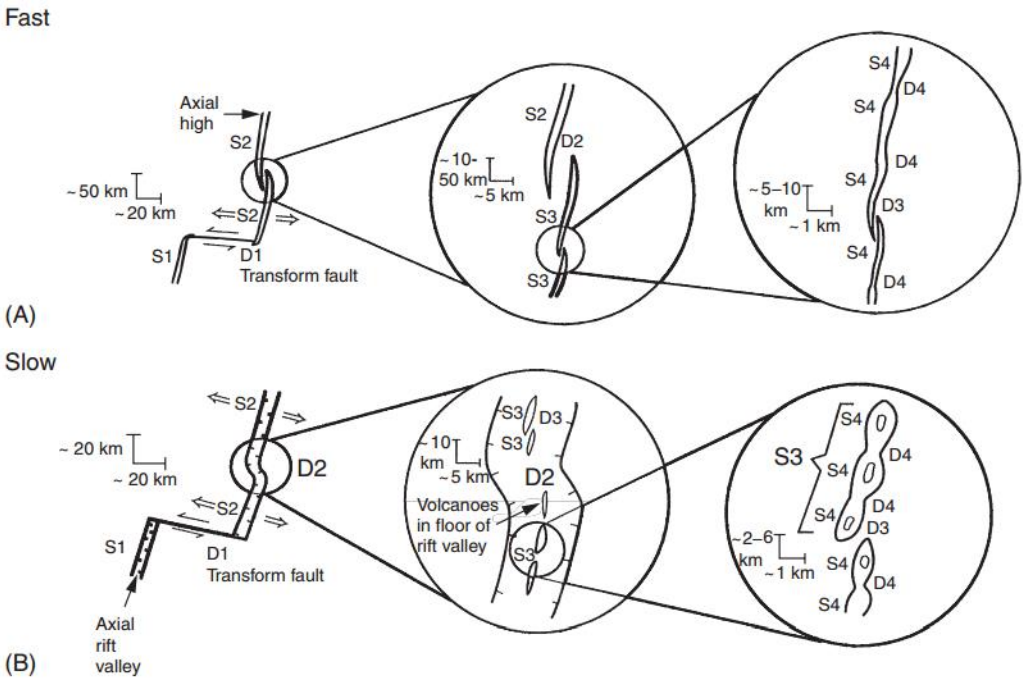

Figure 2.5 Model for discontinuities evolution for (a) fast and (b) slow spreading centres. D1, D2, D3, D4 are discontinuities of orders 1,2,3 and 4. S1,S2,S3 and S4 are segments of axial rift valley or orders 1,2,3 and 4. In both cases, the discontinuities evolve from order 4 to 1. The smaller discontinuities differ, but for both cases, D1 is a transform fault .(K. C. Macdonald, 2001)

At slow spreading ridges, the spreading segments in the central graben forms discontinuous axial volcanic ridges (AVRs). The summit of these ridges is located over the segment centers. At fast ridges, the axis is overlapped by an axial high with a very continuous axial trough that is only interrupted by volcanic eruptions or lack of magma supply. In this region, volcanic activity is intense and several active central volcanoes can be found. Crust is thicker over the AVRs, but thinner over the axial highs and axial troughs (Macdonald & Atwater, 1978).

As the plates are pulled apart by the Earth's interior forces, the ridges and mountains that were once formed over the axis are pulled to its sides. Fracturing then happens as a result of the crust cooling down, as it moves away from the tectonic boundary. There are several fault types that can be found on mid-ocean ridges. The most common one of them is the normal faulting (Behn, Lin, & Zuber, 2002; Cowie, 1998; McAllister, Cann, & Spencer, 1995).

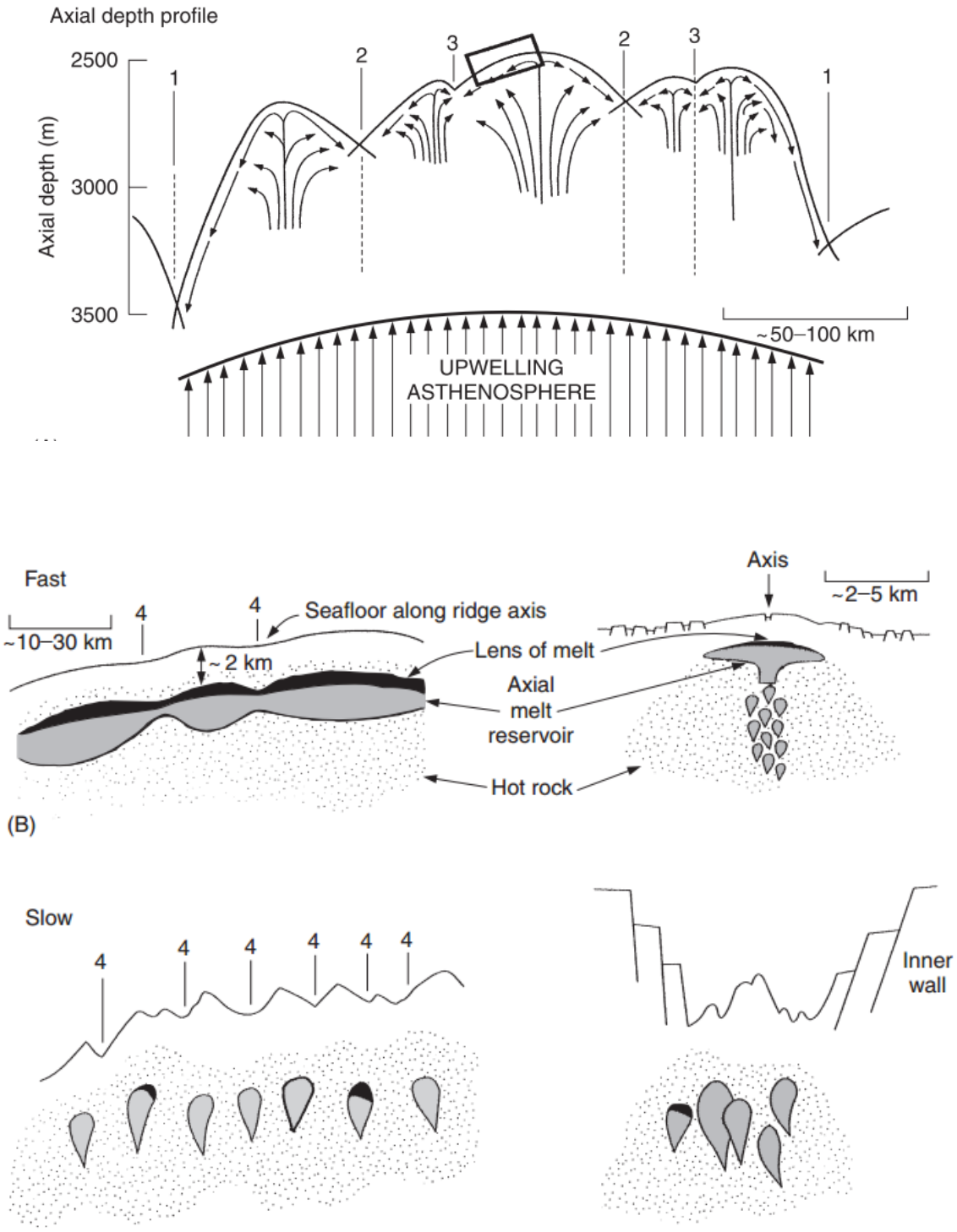

Figure 2.6 (A) Relation between mantle upwelling and the formation of discontinuities. The rectangle is a hypothetical zoomed-in cross section shown in (B): Differences in magma supply at fast and slow spreading centers. The images on the left are along axis cross-sections, while the ones on the right are across-axis. The numbers 1 to 4 are crustal discontinuities. From Macdonaldt et al., (2001)

Due to the larger volume of magma erupted, fast spreading centers are less affected by faulting and have more off-axis volcanism. On the other hand, for being cooler, slow spreading ridges suffer more fracturing and present less off-axis volcanism (Buck, Lavier, & Poliakov, 2005). Faulting is related not only to the magma supply, but also to lithospheric thickness. Fault spacing decrease with increasing lithospheric thickness. (Behn & Ito, 2008; Behn et al., 2002). Fault strikes tend to be perpendicular to the speading direction. For this reason, fault trends faithfully record changes in the direction of seafloor opening (Behn et al., 2002; Buck et al., 2005).

The evolution of a faulting system starts with a single normal fault that alternates between the right and the left side of the rift (Figure 2.7). As the rifting progresses and the plates spread away from each other, the faults can evolve in different ways, depending on the ridge spreading speed. The evolution of a faulting system starts with a single normal fault that alternates between the right and the left side of the rift (Macdonald, 2001; Macdonald & Atwater, 1978).

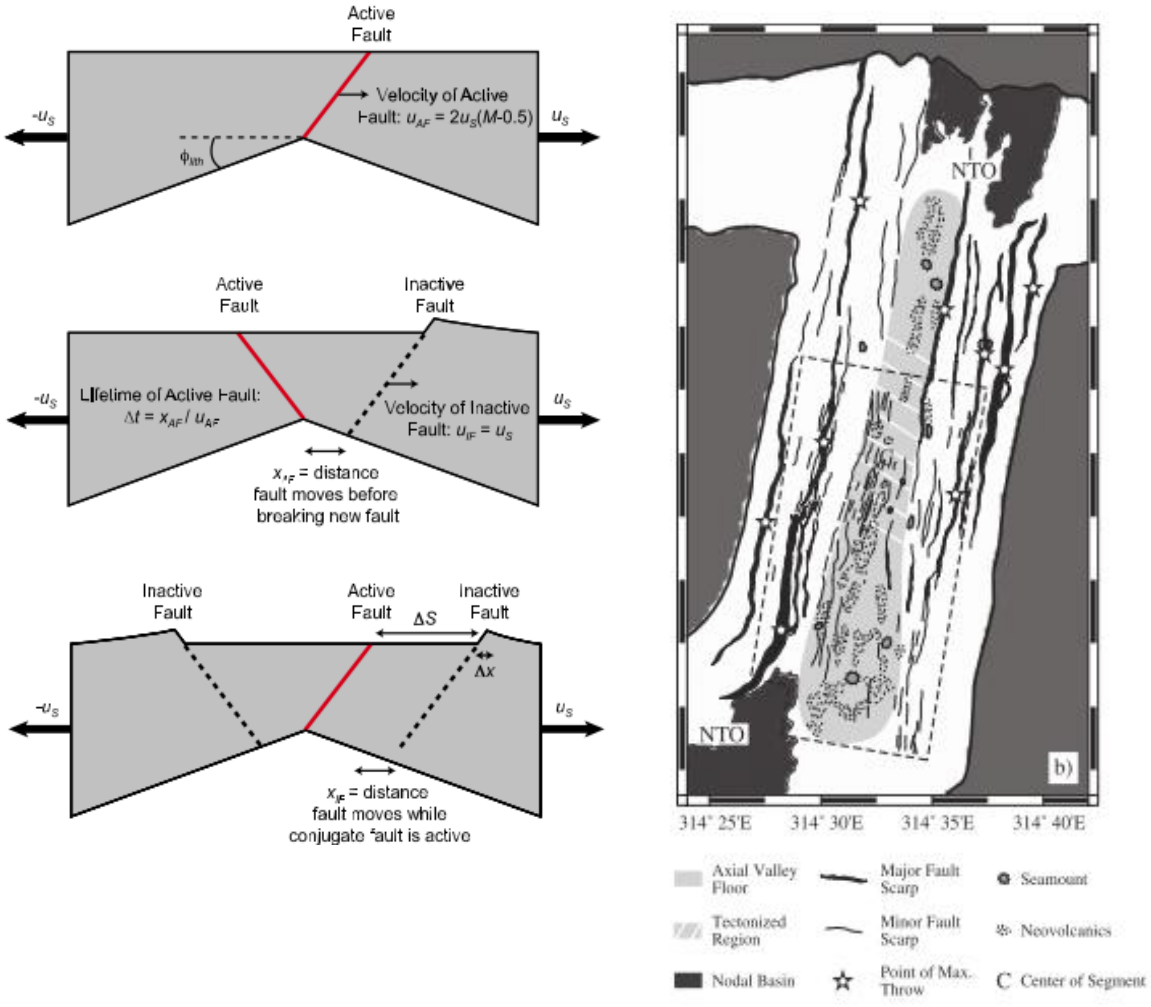

Figure 2.7 a) Evolution of normal faults, with active fault altering between the right and left side of the rift (left) and Mid-ocean ridge bathymetry with normal faults in evidence (right) (Behn & Ito, 2008).

As the rifting progresses and the plates spread away from each other, the faults can evolve in different ways, depending on the ridge spreading speed (Figure 2.9). At slow sprerading ridges, most normal faults face inwards. However, there is an increase in the number of faults facing outwards with the increase of spreading rate. At very fast spreading centers, inward and outward facing faults are almost equally abundant. (Macdonald, 2001; Macdonald & Atwater, 1978).

Another impotant process of seafloor formation, especially at slow spreading ridges result from long-lived normal faults, also known as detachment faults. These faults evolve to originate core complex massifs. These formations expose rocks from the upper mantle and lower crust to the surface (Figure 2.8), and normally show distinctive striations parallel to the spreading direction (e.g. Smith, Escartín, & Cann, 2012; Macleod et al., 2009).

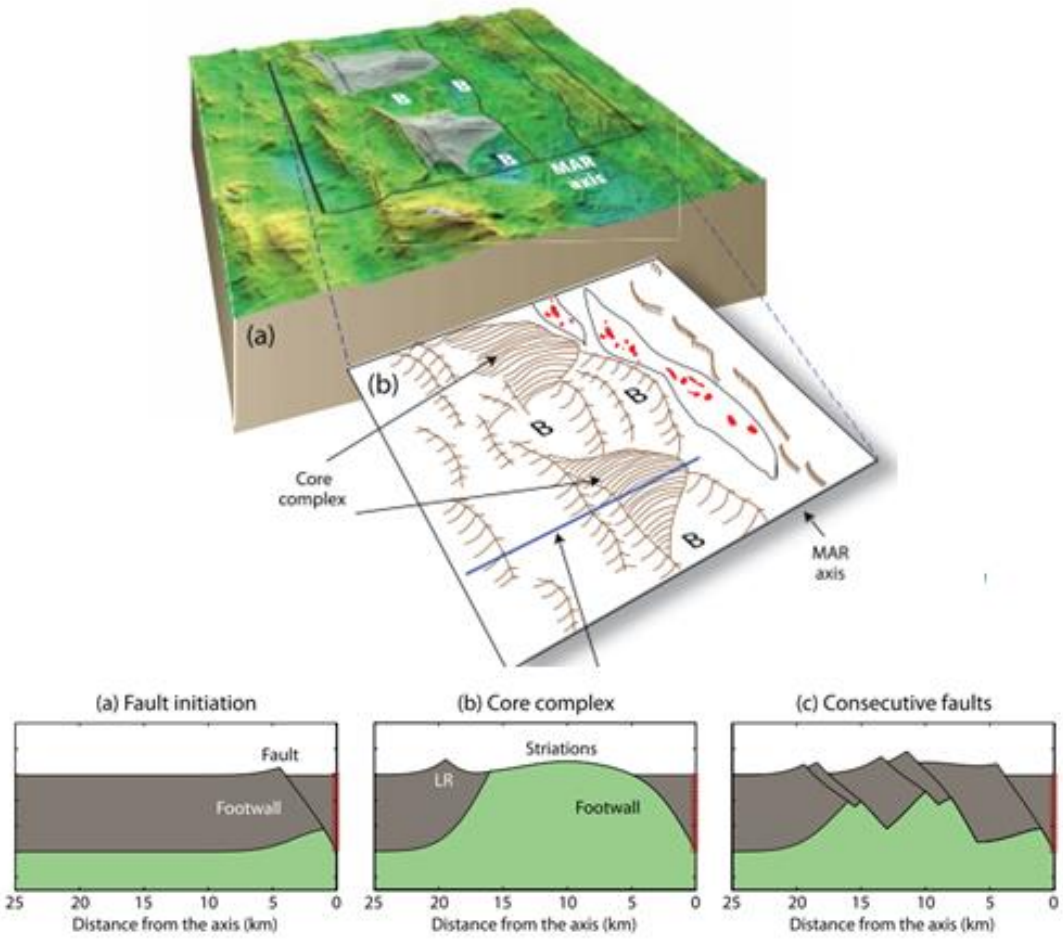

Figure 2.8 Core complex morphology (top) and evolution histories of normal faults (bottom) (b) represents the schematic representation of core complex formation. Modified from: (Smith et al., 2012).

After several km off axis, topography generated near the spreading center is preserved without many changes until subduction, with the exception of little sedimentation. This preserved landscape is what forms the Abyssal Hills (Macdonald & Atwater, 1978). Back tiltes fault blocks and half-grabens may be the dominant origin of abyssal hills; they happen when the magma supply is starved, normally at slow spreading centers. In places where the magma budget is abundant, the axial crust episodically thick enough to support volcanic construction. In these places, the abyssal hills might be formed of intact whole-volcano topography or split-volcanoes (Macdonald, 2001; Macdonald & Atwater, 1978).

Volcanic eruptions at fast spreading ridges happen on average every 5 to 100 years. At slow spreading ridges, the eruptions are much less frequent, happening every 5000 to 1000 years. In both fast and slow spreading ridges pillow and lobate lavas are the most common volcanic formation. Observations showed that volcanic eruptions and lava activity are accompanied by blooms of localized biological activity (Macdonald, 2001).

This biological activity happens around hydrothermal vents, thus the organisms that inhabit them are called *vent communities*. Hydrothermal vents are formed as a result of the interaction between water and magmatic or tectonic systems (German & Parson, 1998). These vents are towering features formed by precipitation of minerals and metals when in contact with high pressures over the seafloor (German et al., 1996.; Macdonald, 1998).

Macdonald (2001) shows that the number of vent communities is correlated with the distance to the discontinuity, since more vents appear to be present at segment centers and less at segment ends. Besides representing an incredible hotspot of life in an otherwise uninhabitable environment, hydrothermal vents have also raised interest of the mining industry, as mineral resources of economic interest are believed to be present at such sites (Dekov et al., 2010; German, Petersen, & Hannington, 2016).

At fast spreading ridges, the formation of hydrothermal systems is magma rich and dike controlled. On the other hand, at slow spreading ridges, hydrothermal systems are magma starved and controlled by penetration of seawater along faults near the ridge axis (Macdonald, 2001). Hydrothermal vents are expected to be present in most mid-ocean ridge segments. The location of these systems, however, remain largely unknown (Beaulieu, Baker, & German, 2015).

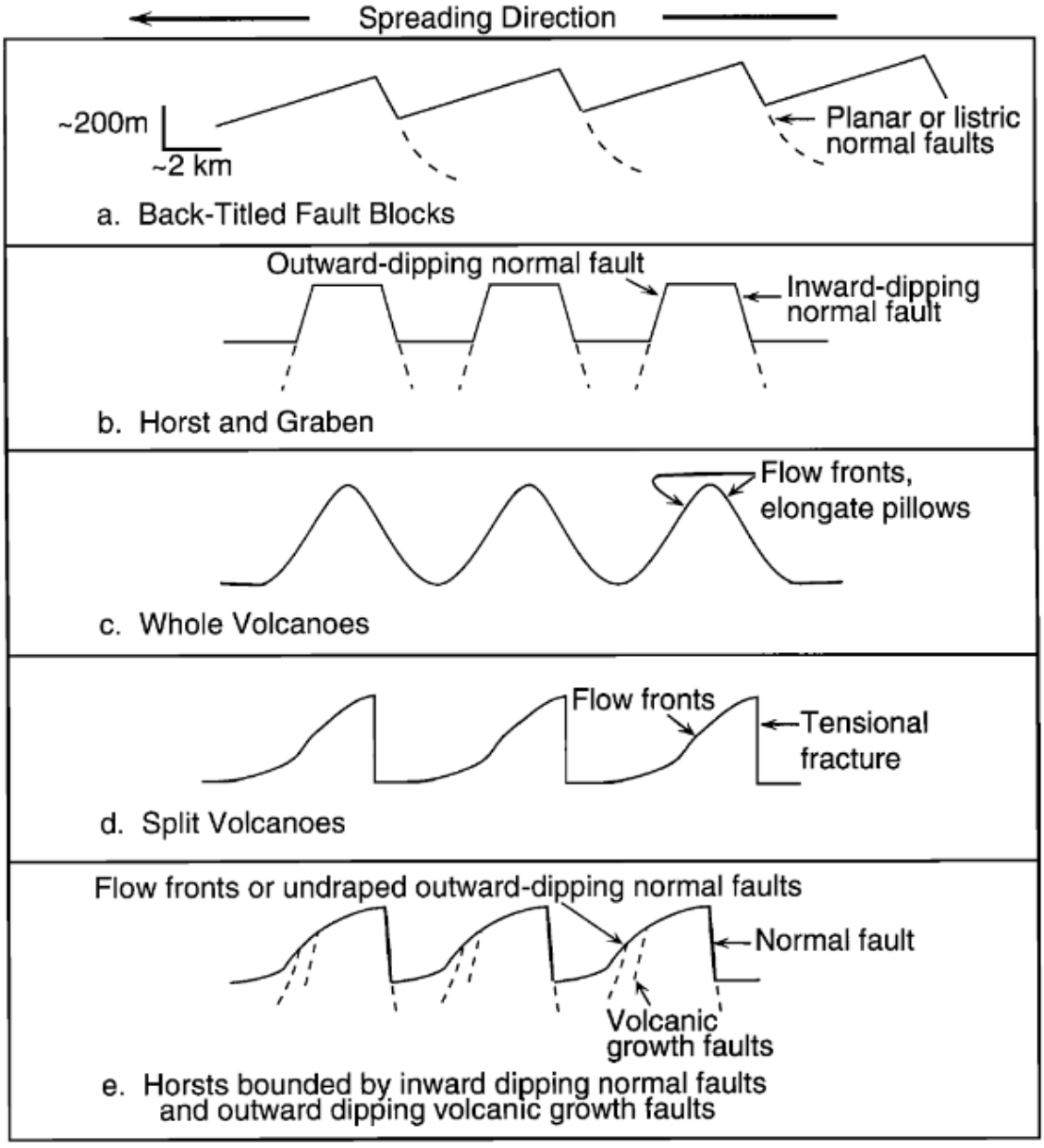

2.3.1 The Mid-Atlantic Ridge

Figure 2.9 Different histories of abyssal hills evolution and morphologies. At slow spreading ridges, the crust is too thick and easily destabilized, producing more faults (a, b). At very fast ridges, the crust is thin and volcanoes can be preserved with no faulting (c). With decreasing spreading rate, faulting happens giving origin to be split volcanes or horsts (d, e). (Macdonald, 2001).

The Mid-Atlantic Ridge (Figure 2.10) is one of the most well studied mid-ocean ridges in the world. It is a multidisciplinary area of interest, having raised attention of not only geologists, but also biologists, chemists and oceanographers. Many studies have been carried out along its axes throughout the years, in different latitudes and for the most varied purposes. (e.g. Appelgate & Shor, 1994; Goud & Karson, 1985; Lizarralde et. al.,2004;

Macdonald & Atwater, 1978; Murton & Rona, 2015; Niedzielski et al.,2013; Searle et al.,2010; German et al., 1994; Macleod et al., 2009; Miller, Read, & Dale, 2013; Parson et al., 1993; Carbotte, Welch, & Macdonald, 1991)

The Mid Atlantic Ridge (MAR) is the most common example of slow spreading center, with a total average spreading rate inferior to 3 cm/year. It extends from the Artic Sea to the Bouvet triple junction, covering a total of 14,000 km in length, with depths ranging to a maximum of 5,000 meters. It reaches the surface at several locations on volcanic islands such as Iceland, Azores, Jan Mayen, Ascension and Tristan da Cunha. The existence of these islands indicates the presence of mantle hotspots along the ridge system (Hekinian, 2014).

Due to its low magma supply, the MAR behaves as a relatively rigid structure. For the reasons previously described, this implies that the MAR presents an evident central graben and strong discontinuities, originating many transform faults (Hekinian, 2014; Wille, 2005). As a slow spreading system, the MAR also presents many detachment faults and hence core complex massifs along its extension (Condie, 1976).

Being a great bathymetric feature, the MAR influences ocean circulation. The abyssal hills acts not only to stir the circulation, but also as obstacles for the great ocean gyres (Gille, Metzger, & Tokmakian, 2004). Thermal fronts were proven to preferentially happen along the MAR's fault zones (Miller, Read, & Dale, 2013). Usually, thermal fronts are associated with high biological activity. The knowledge about the occurrence of such fronts is not only essential for marine conservation efforts, but also marine resources management (i.e. fishing, mining, energy).

The MAR's central graben is drastically interrupted in its northernmost region by the presence of the Icelandic hotspot. This massive mantle hotspot provides abundant magma supply, disturbing the typical slow spreading ridge morphology seen in other parts of the MAR. At this region, the RR is formed and at approximately 60°N, Iceland emerges to the sea surface, as the biggest hotspot influenced island in the world.

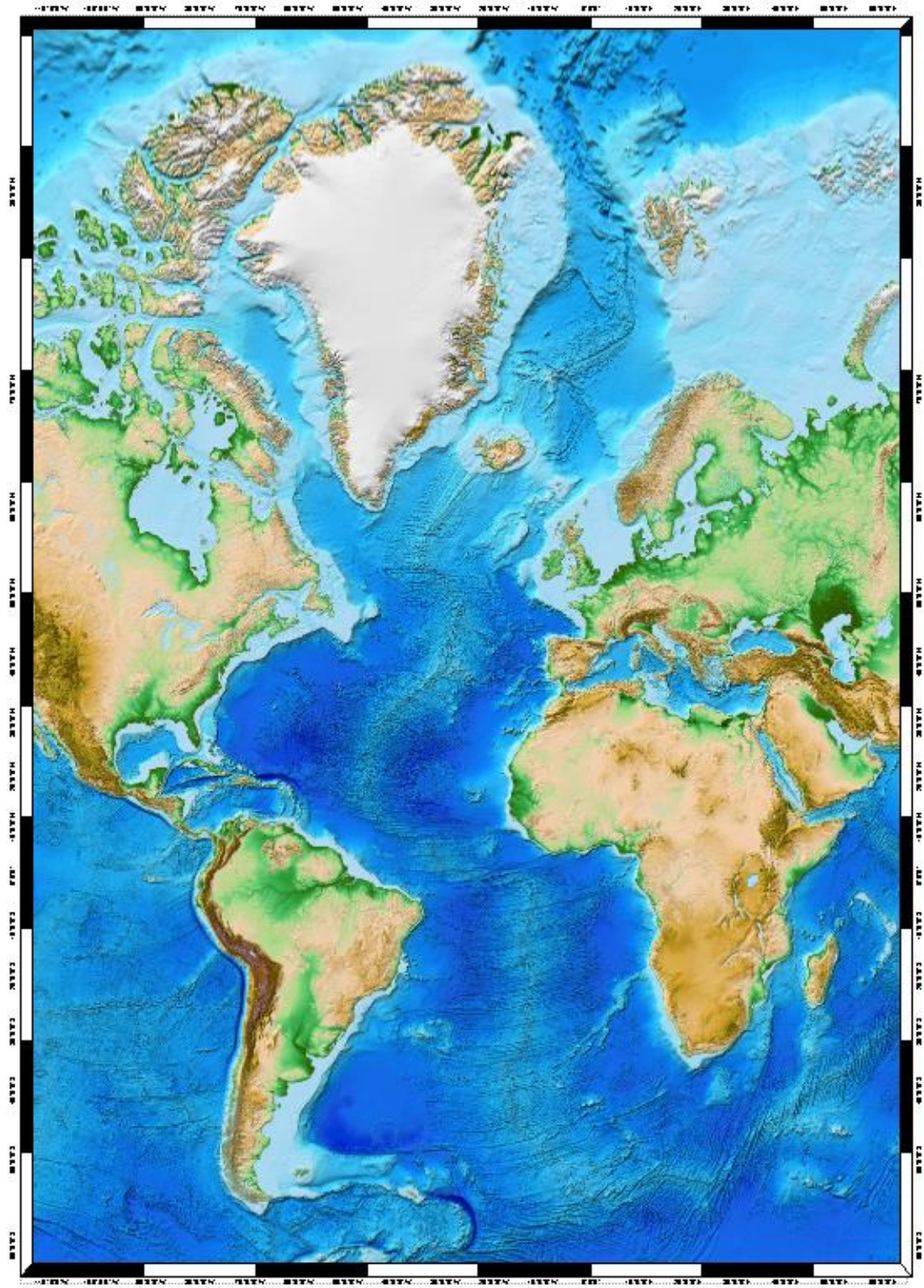

Figure 2.10 Digital Elevation model of combined satellite image and bathymetry from ETOPO – NOAA, National Centers for Environmental Information (NCEI).

2.3.2 The Reykjanes Ridge

The Reykjanes Ridge (Figure 2.11) is the longest oblique spreading ridge in the world, segregating the Eurasian and American tectonic plates South of Iceland. It extends for about 900km from approximately 58.3°N to Iceland, where it emerges to the sea surface at the Reykjanes Peninsula (64°N) (Keeton et al., 1996). Like the rest of the MAR, the RR is categorized as a slow spreading center, with an average spreading speed lower than 20 mm/year (DeMets et al., 2010).

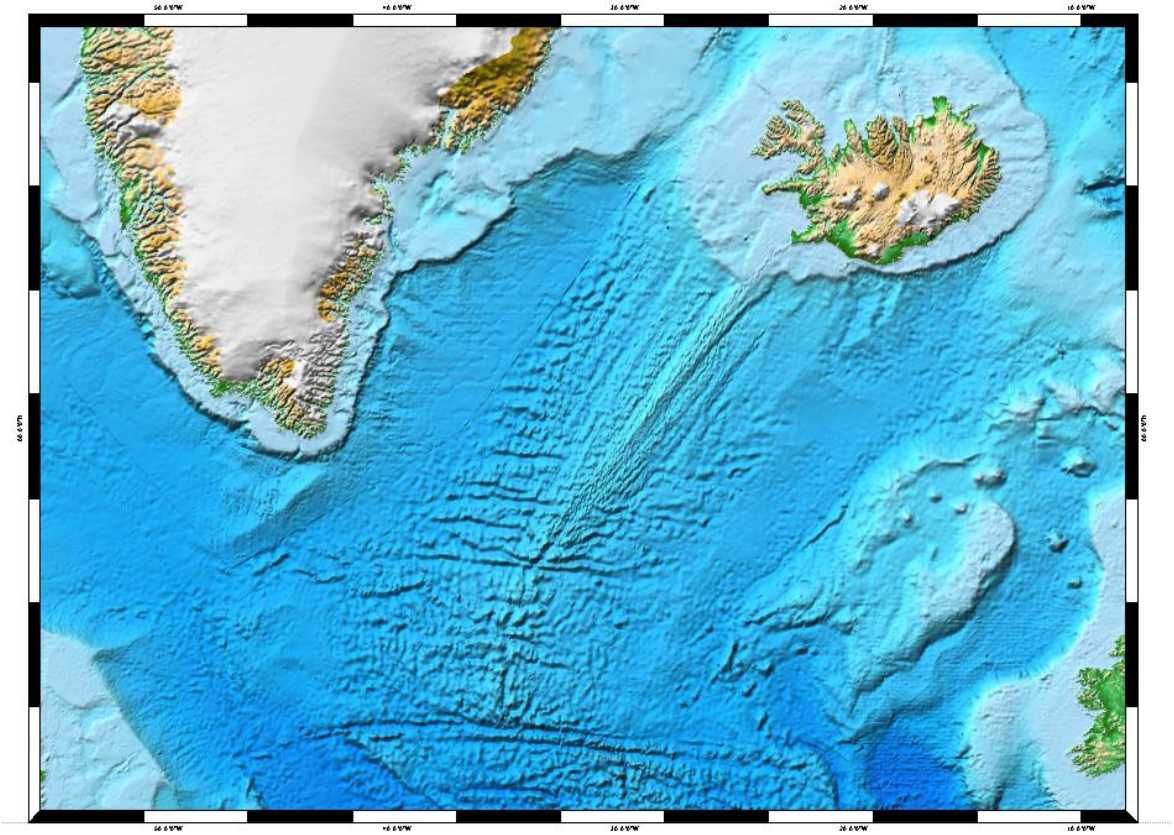

Figure 2.11 Reykjanes Ridge from ETOPO - NOAA, National Centres for Environmental Information (NCEI).

According to magnetic surveys, the evolution of the Reykjanes Ridge is resumed in 3 main phases: A first phase of oblique spreading forming a ridge without transform faults, a subsequent orthogonal spreading phase with the formation of transform faults, and a third phase of Southward propagation, resulting in the elimination of the transform faults, which is currently happening (White, 1997)

The seafloor at the RR is smoother then found elsewhere in the MAR and the zone of active volcanism is of 10 – 15 km wide around its axis. The Northern and Southern parts of the ridge differ in their axis morphology. In the North, the central portion of the ridge is marked by an axial high, which is more typical for fast spreading ridges. However, in the southern portion of the ridge, the center is marked by a prominent axial valley. The transition between the axial high and the central valley starts at 59.5°N (Laughton, Searle, & Roberts, 1979; Searle et al., 1998).

The ridge axis is 27° oblique, with en-echelon AVRs, which represent the youngest geological features found in the area. The AVRs evolve to get broken by faulting and covered by sediments as the rift propagates (Keeton et al., 1996a; Murton & Parson, 1993; Parson et al., 1993; Searle et al., 1998).

Circular seamounts are found in higher concentrations over the axis; however, a few can also be found off-axis. Normal faults are present in all its extension and orientated parallel, being therefore oblique to the AVRs (McAllister et al., 1995). Relative highs and lows tend to alternate between the sides, but at the southernmost region, the East is slightly higher. The highest AVRs occur South of 59° N and the amplitude of normal faults also increases towards the South (Searle et al., 1998).

The deepest axial deeps in the RR are found at 57º52N, 58º25N, 58º5N and 60º3N. They were associated with small positive magnetic anomalies and interpreted as segment boundaries of 2nd and 3rd orders. Contrasting with most slow spreading mid-ocean ridges, the RR lacks fracture zones, or active transform faults (1st order discontinuities) (Parson et al., 1993; Searle et al., 1998). In fact, the Southern limit of the RR is marked by the Bight Fracture zone, which is the last active transform fault found in the Northern MAR. The last transform fault being eliminated had evolved to a non-transform offset (NTO) and is located at the current re-organization tip at approximately 57° N (Hey et al., 2015).

Another distinction of the RR morphology is its "V-shape" appearance (Figure 2.12). This configuration is formed by a number of linear ridges, parallel to each other at an oblique angle to the tectonic boundary. They converge to the Ridge axis at the Bight Fracture zone, (Hey et al., 2015) and are commonly interpreted as diachrones (e.g. Hey et al., 2010; Jones et al., 2002; Searle et al.,1998) (Figure 2.12). Recent magnetic surveys confirm that the RR is currently propagating southwards, eliminating the previously established transform faults (Benediktsdóttir et al., 2012; Benediktsdóttir et al., 2016; Hey et al., 2010).

A number of theories were proposed to explain the anomalous morphology of the RR, largely based on two evolution models. The first and most discussed of them is referred to as the "thermal model". It states that the propagating V-shaped ridges result from crustal thickness variations caused by pulses of the Iceland mantle plume (e.g. Jones, 2003; Jones et al., 2002). The second is known as the "propagating rift model", and it states that the tectonic boundary of the RR is progressively shifting to the East, transferring lithosphere from the Eurasian to the American plate, and thus causing asymmetry (Benediktsdóttir et al., 2012; Hey et al., 2010).

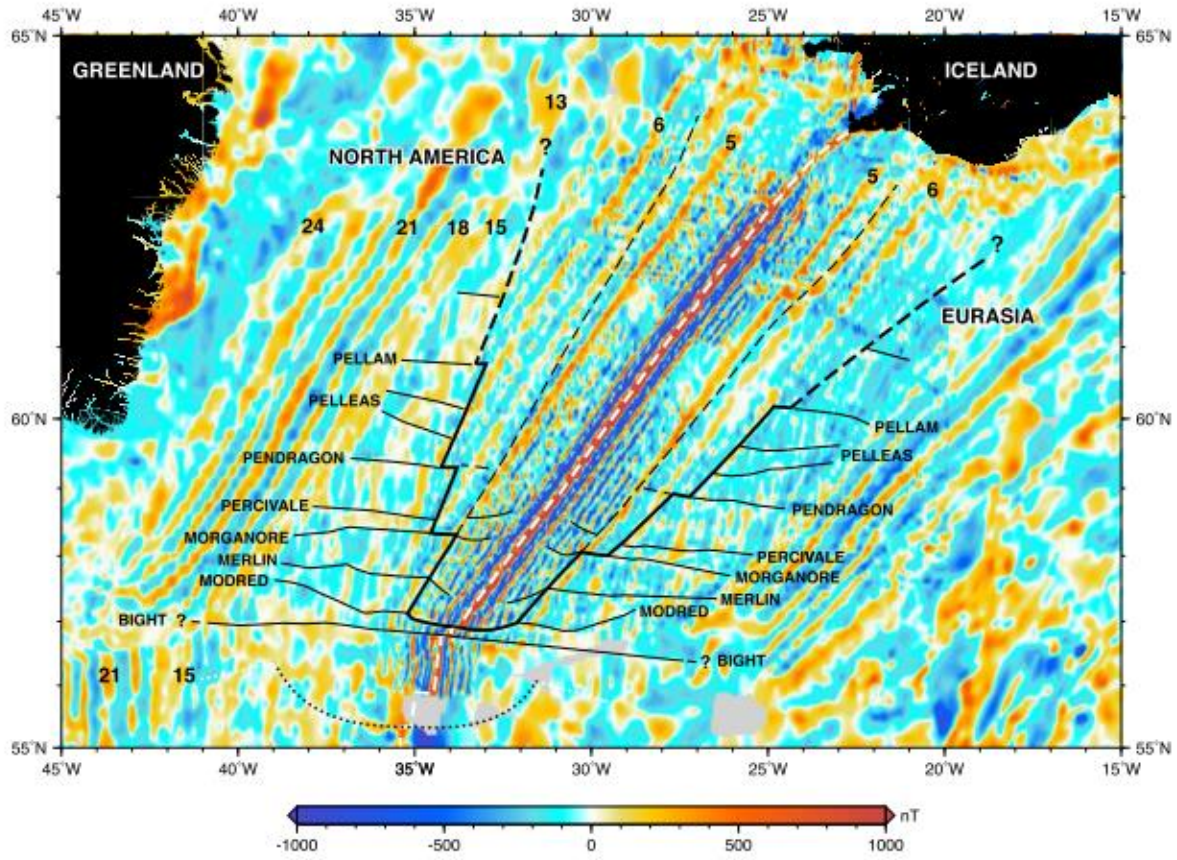

Figure 2.12 Magnetic anomaly map with interpretation from Hey 2015. Solid horizontal lines are transform faults with names of from (Vogt & Avery, 1974). Dashed black lines with numbers (5,6,13) are the V-shaped diachrones of spreading. Numbers 15,18,21 and 24 represent the first evolutionary phase of orthogonal spreading. The white dashed line represents the tectonic boundary.

However, with new multibeam data evidence (Figure 1.4), Hey et al., 2015 claimed that neither of the existing theories are enough to explain the plate boundary reorganization process that happens close to the BFZ. They propose an evolutionary history for the past 34Ma based on magnetic data and calculated that the transforms are eliminated at a rate of 110 km/Myr

In its most recent published work, Martinez & Hey, (2017) claims that the morphology of the RR reflects shallow buoyant mantle instabilities, like in any other slow spreading ridge. They explain the V-shaped ridge propagating South, as predicted by the kinematic model of Benediktsdóttir et al.,(2016), and eliminating the transform faults as a result of upwelling mantle flow coming from Iceland (Figure 2.13). According to the authors, these flows occur at shallow depths and therefore do not require a deep mantle source.

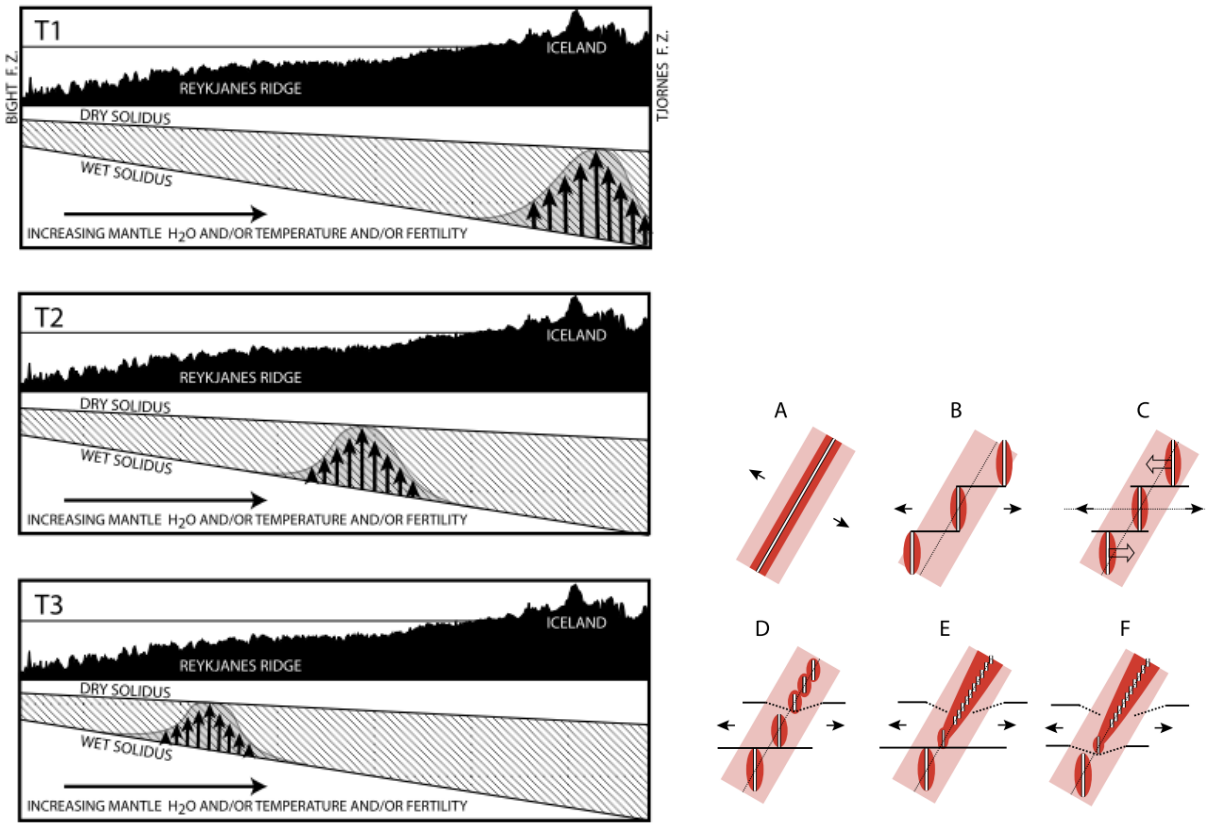

Figure 2.13 Left: Model of upwelling mantle plume from Iceland forming the RR. T1,T2 and T3 are different moments in time. Right: Evolution model of the RR (A) oblique spreading without transform faults, (B) change in spreading direction with segmentation of the ridge (C) transform boundaries established (D) propagation of the mantle plume southwards eliminating the transforms (E) V-shape established and (F) present V-shape configuration, propagating south and eliminating the Modred fault.

Little hydrothermal activity was reported at the RR, most of it being concentrated on its Northern region. This is mainly attributed to higher volcanic activity on the Northern part of the ridge, or lack of appropriate data (German et al., 1994; German & Parson, 1998; German et al., 1996).

3 Methodological Background

In this section, the principles of the methodology used in this work will be generally explained and referenced. The chapter is subdivided in "Acoustic Mapping" and "GIS analysis of multibeam data". The specific methodology applied and the operations performed by the author are later described in the next chapter of this thesis.

3.1 Acoustic Mapping

As mentioned before in the introductory chapter of this thesis, the most efficient remote sensing methodology used for seafloor mapping is based on acoustics. This sub-chapter describes the principles of sound propagation and sonar remote sensing in the oceans, as well as the characteristics and functionalities of the multibeam acquisition system.

3.1.1 Principles of Underwater Acoustics

Sound waves are mechanic waves, which characteristically travel through a medium without disturbing it. In principle, the pulse generated by an acoustic source (transmitter) travels through the water column until it reaches a target (or the seafloor) and is reflected back to the surface, where it is recorded by a receiver on board of the survey vessel (Medwin & Clay, 1998) (Figure 3.1). In reality, however, not all of the energy that is emitted comes back to the receiver, being partially lost in form of backscatter on the interface between water and seafloor, and as shear stress within the water column

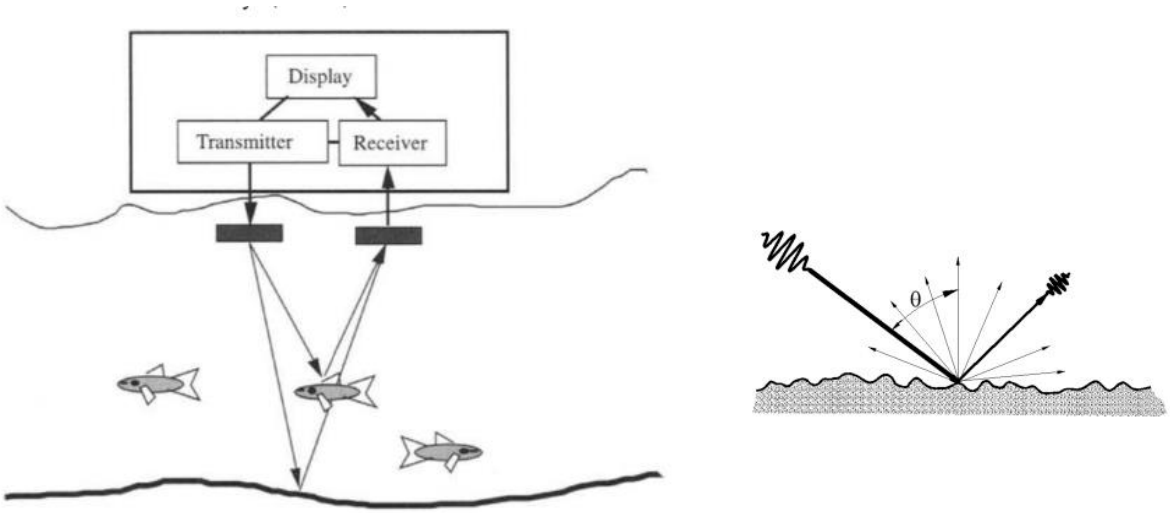

Figure 3.1 Simplified schematic representation of a single beam acoustic pulse travelling through the water column (left) (Medwin & Clay, 1998) and Illustration of backscattering produced by the water/seafloor interface (right) (Bjørnø, 2017).

The travel time of the returning acoustic pulse is computed by the receiver at the surface, and the depth of the reached target is derived from the relation between time and speed of the acoustic wave (equation I). The speed, on the other hand, depends on the properties of the medium at which the sound wave propagates. In the ocean, these properties correspond to pressure (depth), salinity and temperature (equation II) (Wille, 2005).

V*: Sound speed

T: Temperature

S: Salinity

D: Depth

T: Travel time

Equation I

$$V = \frac{2D}{t}$$

Equation II

$$V\ (T,S,D) = 1448.96 + 4.591T - 0.05304T^2 + 0.0002374T^3 + 1.34(S-35) + 0.0163D + 1.675 * 10^{-7}D^2 - 0.0125T(S-35) - 7.139 * 10^{-13}TD^3$$

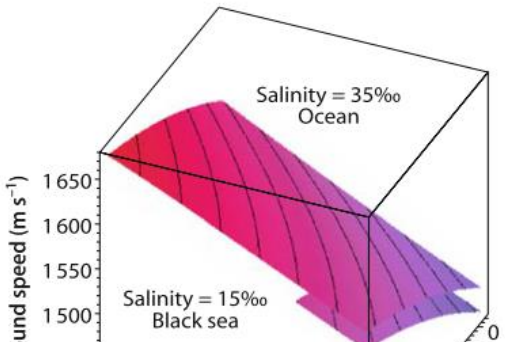

Figure 3.2 Relation between sound speed, salinity, depth and temperature. Modified from (Wille, 2005)

The receiver records the value for the first beam that reaches back to the surface, and computes this as the depth of a single point on the seafloor, in combination with a GPS measurement. However, the portion of seafloor ensonified by the acoustic beam actually corresponds to a circular area that is directly proportional to the travel distance, increasing as a function of depth. In greater depths the ensonified area is also larger, and since the recorded value is of the first arrival, it might not exactly correspond to the point right under the receiver, compromising the precision of the final product. Figure 3.1 illustrates the geometry of a single beam echosounder ensonified area and shows the error in depth recording (Odom, 2003).

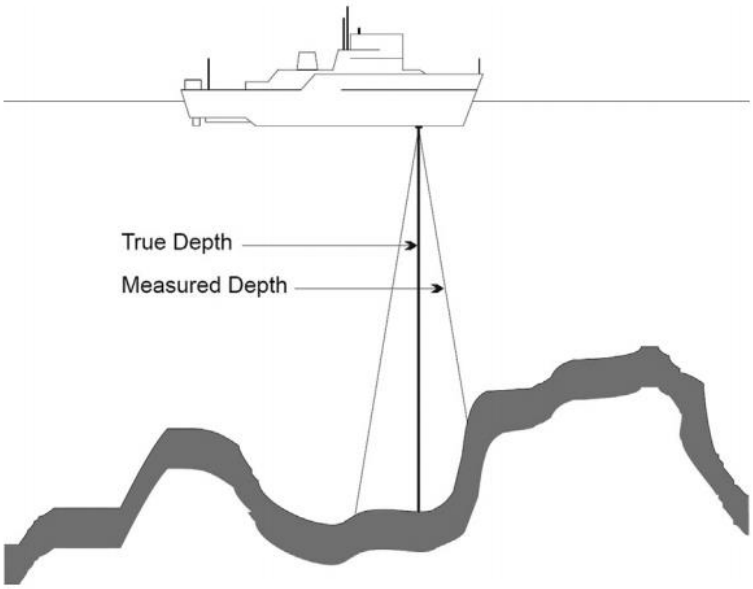

Figure3.3 Representation of a single beam emission and the imprecision in depth measurement caused by large ensonified area on complex seafloor (Bjørnø, 2017).

The resolution of the final image is dependent on the frequency of the acoustic pulse and the power of the transducer. A higher frequencies provide better resolution, however with the cost of reaching lower depths due to higher shear stress and scatter dissipation (Odom, 2003). This way, deep areas in the ocean can only be surveyed by relatively low frequency sources, resulting in relatively poor resolutions when compared to shallow water products (Richardson & Jackson, 2017).

3.1.2 Multibeam sonar

Single Beam Echosounders (SBES) are most commonly used for navigation and biological mapping, although having been used in the past for bathymetry. For seafloor mapping, the most efficient existent technology is the Multibeam Echosounder (MBES). The main reason why this method is considered satisfactory is that it allows surveying a large area in relatively little time, providing a 3D image of the seafloor as opposed to the 2D image resulting from the SBES (Bjørnø, 2017).

The MBES operates with an array of multiple beams alongside each other, mapping a strip of seafloor at once, instead of a single point of sight. Figure 3.4 shows the geometry of the MBES and how the sound beams are arranged in perspective with the seafloor. The individual beams reach the seafloor at different angles and therefore the MBES measurement has to account for this discrepancy. The depth measurement is then mainly based on the travel time and the angle values of each individual beam (Bjørnø, 2017).

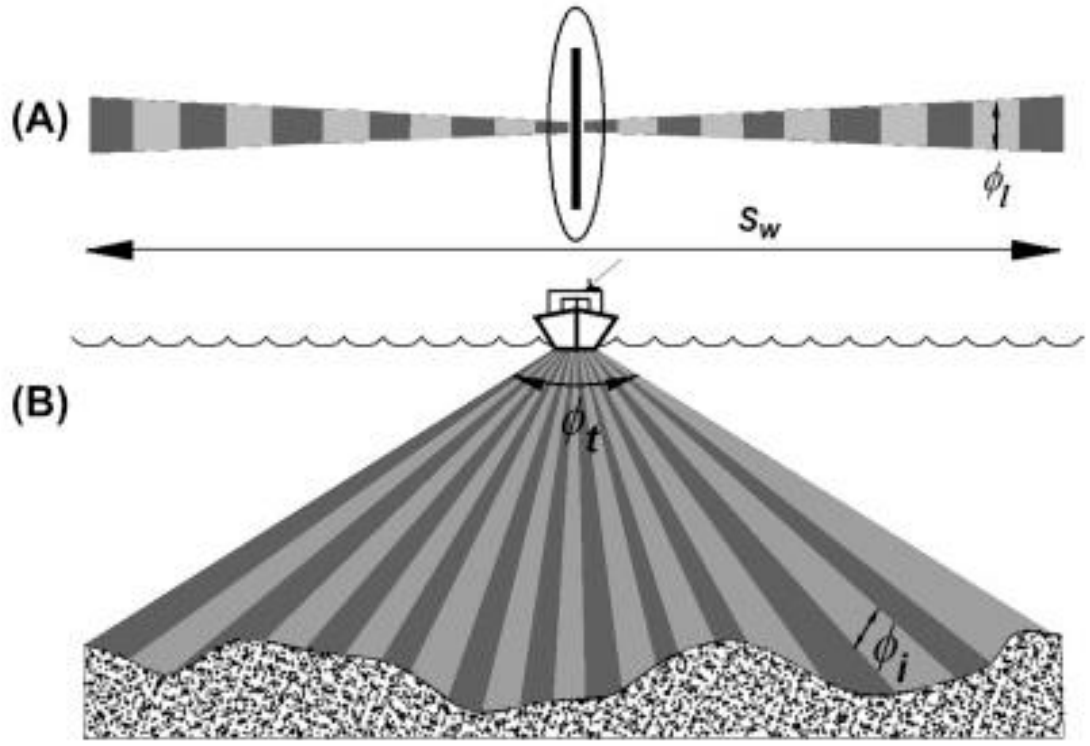

Figure 3.4 Multibeam Echosounder Geometry, where "Sw" is the total swath. (A) Beams seen from above with along-track transmitted beam width (ϕl) (B) Frontal view from the total fan aperture (ϕt) in across-track view and individual beam width (ϕi) (Bjørnø, 2017).

The length of the line (swath) ensonified by a MBES is directly proportional to the seafloor depth, and so is the spacing in between the individual beams. In other words, the greater the depth, the larger the total surveyed area, however lower the resolution, since the resulting measured points are greatly spaced from each other. The best existent multibeam systems operate with 800 beams and a maximum swath width of 7.5 times the depth with a 150 degrees total aperture angle. (Bjørnø, 2017)

Besides the depth, the total swath width is also dependent on the noise level and spectrum, sea state and water column conditions. For a number of reasons mentioned before, the beams that have larger individual width are most affected by noise and other environmental sources of imprecise measurements. Those beams are located on the swath extremities and therefore it can be expected that the side ends of the ensonified stripe will give the less reliable results (Bjørnø, 2017). The most common sources of noise and error in multibeam surveys will be discussed in the next section of this chapter.

3.1.3 Limitations in Multibeam Data Acquisition

When sensing the seafloor, bodies present in the water column might affect the quality of the data, causing noise. Common sources of noise on geo-acoustic data include the presence of fish shoals, large mammals, air bubbles, phytoplankton, the sea surface and even the research vessel itself. Bad weather conditions enhance the effect of such noises by causing the vessel to move vertically and rotate around its 3 axis.

These rotational movements are known as pitch, yaw and roll and are important causes of inaccuracies in the geographic positioning of the data and the vertical movement, called heave, might result in imprecise depth measurements. Beyond error in geographic positioning and noise enhancement, pitch roll and yaw also affect the maximum swath width of the MBES (Bjørnø, 2017). Figure 3.5 illustrates the pitch, yaw and roll and shows why they would be a source of error.

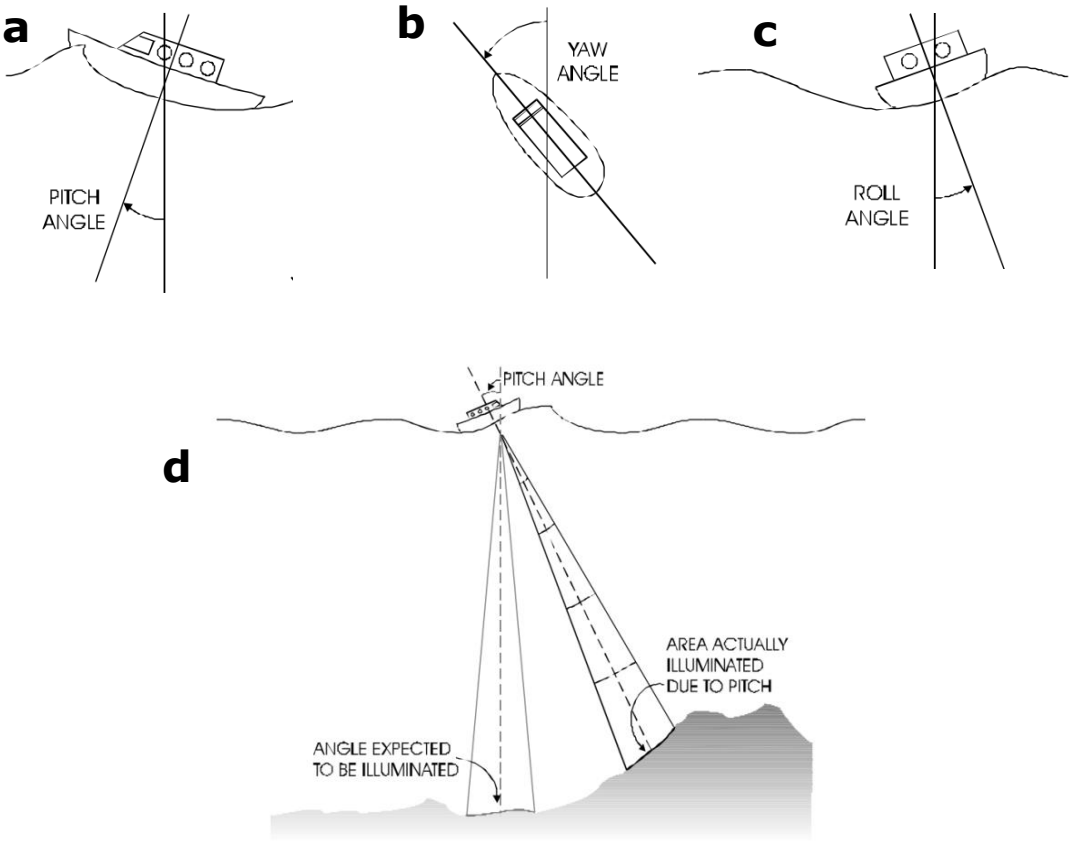

Figure 3.5 (a) pitch, yaw and roll (b) Illustration of error in measurement caused by pitch angle ("Multibeam Sonar Theory of Operation," n.d.)

Due to the MBES geometry, discussed in the previous section, in deep water the total coverage swath might reach tens of kilometers, and with a speed of sounds of 1500m/s, the beams on the edge might take several seconds to return to the receiver. Therefore, in order to minimize error and enhance the quality of the data, the vessel's maximum speed of cruise should be limited. The location where the MBES is mounted on the vessel is also essential to avoid and limit the influence of noise and error and, for the best results, the MBES survey lines should ideally overlap each other (Bjørnø, 2017).

All these factors make it very important to correct the MBES data both before and after acquisition, requiring several auxiliary measurements to be taken. Nevertheless, as long as all the parameters are correctly specified, these errors can generally be accounted for and corrected by algorithms in both acquisition and processing softwares. Any remaining outliers of depth values may be manually removed on post-processing (Buchanan, Gilbert, Wirgin, & Xu, 2004).

After all is taken into consideration and the corrections are made, a MBES image can be interpreted as a topographic image of the ocean floor. It is the methodology that more closely resembles to satellite altimetry, and with some imagination, the resulting image can look very much alike the ones taken of Earth's surface from space. Unfortunately, it is still a massive effort to perform a MBES survey and therefore only small portions of the ocean floor are to this date already mapped.

3.2 GIS analysis of Multibeam data

After acquisition, the MBES data are taken into a Geo-Information System (GIS), where it can be post-processed and analyzed as a digital elevation model (DEM). The basics of the GIS theory used for multibeam data analysis will be described in this section. All the images and operations shown as examples in this chapter were produced with ArcGIS® (ESRI, 2017) and all the GIS theories here explained, unless it stated otherwise, were based in the book: "The core of GIS science" published by The Faculty of Geo-Information Science & Earth Observation from the University of Twente (ITC, 2012).

A GIS is characteristically composed by two main types of data that are used in combination for analysis: "vector" and "raster". Vector layers are points, lines or polygons with defined boundaries, which store information in form of tables. Raster layers are images where information is stored in the form of pixels. In a raster image, each pixel has a single value, which for a MBES image, corresponds to depth. The resolution MBES resolution is reflected on the pixel size. Figure 3.6 shows the two types of data used to represent a DEM in a GIS and how they are combined for interpretation of geological features in the study area.

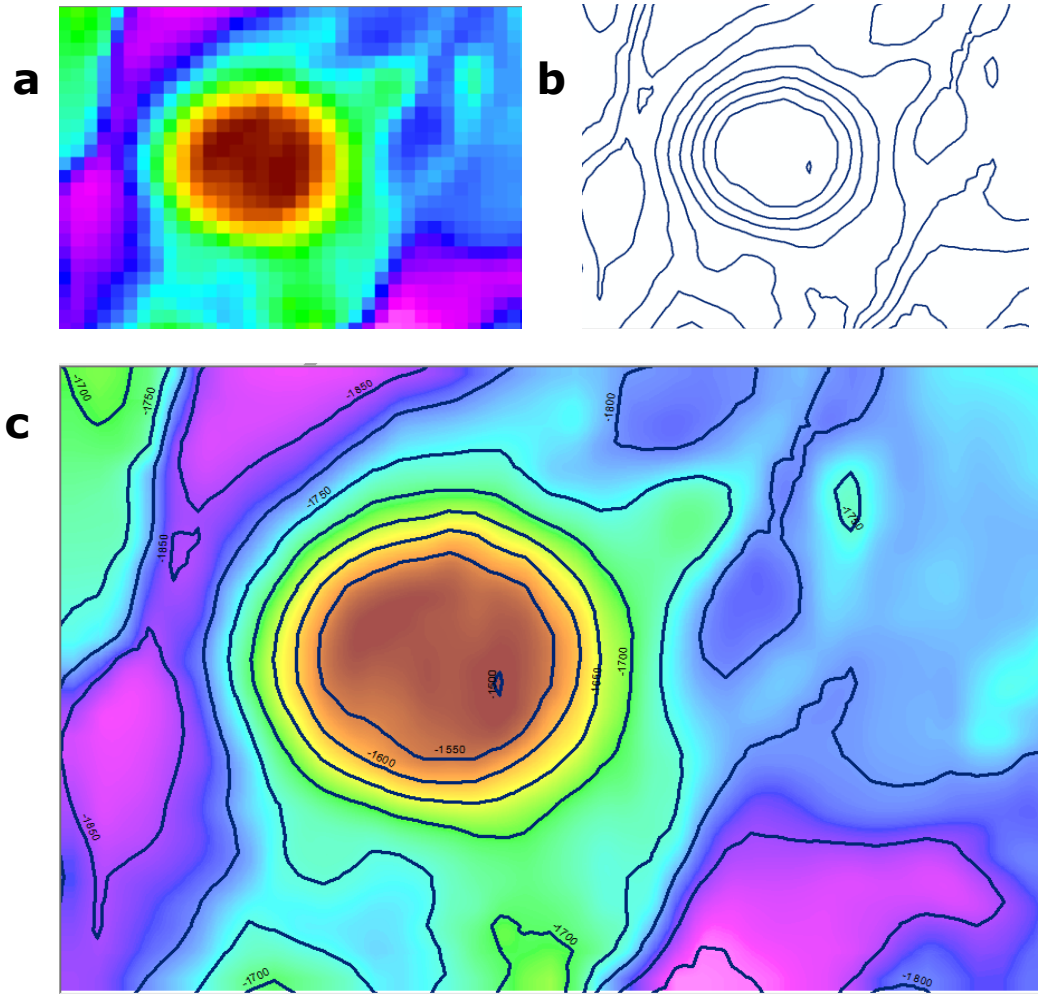

Figure 3.6 a) raster pixelated image of a seamount b) vector contour of the same seamount c) raster displayed with cubic convolution resample and overlaid with labelled contour lines representing isobaths.

3.2.1 Bathymetric Visual Analysis

From the raw MBES data a point layer is primary generated, which has to be transformed into a raster layer for modelling. The methodology used for transforming this vector layer of points into a continuous surface is called interpolation. This methodology is based on the theory of spatial auto-correlation, which is a fundamental principle based on Tobler's first law of geography. This law states that locations closer to each other are more likely to have the same values than locations that are further apart.

From the principle of spatial auto-correlation, interpolation uses mathematical expressions to calculate and assign values to the empty space in between punctual measurements, thus creating a continuous surface. Different interpolation algorithms are available and the most suitable algorithm depends on the nature of the dataset and the aim of the research (Arun, 2013; Chaplot et al., 2006; Šiljeg & Lozic, 2015; Zhang, Xu, & Xu, 2015). Naturally, MBES post-processing softwares use algorithms that are optimized for bathymetric survey.

The continuous surface resulting from a MBES dataset represents seafloor elevation, and therefore may also be called a digital elevation model (DEM). A DEM is a virtual representation of a three-dimensional plane, or in other words, a terrain. In a DEM, each pixel has a XY coordinate and an elevation value, or depth in bathymetry. These values might be used for simple visual identification of topographic features, such as seamounts, normal faults, ridges and dunes. It is also possible to derive structural information about the geology on the area, such as slope angle and direction variations.

Figure 3.7 is a DEM extracted from a small portion of the study area and will be used to illustrate the procedures described in this section.

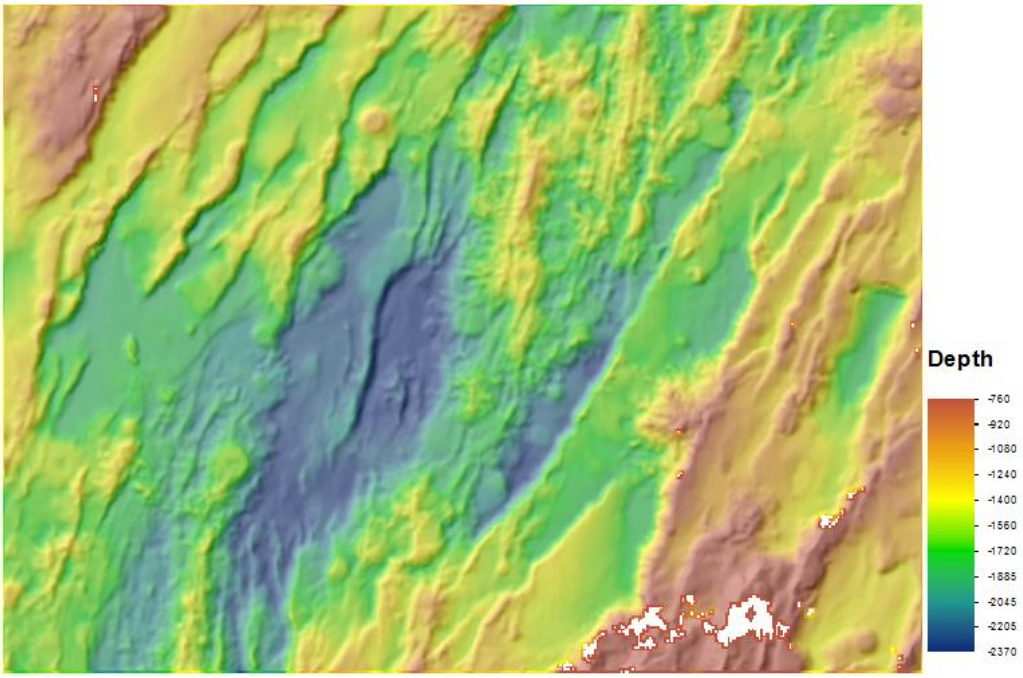

Figure 3.7 Example DEM from the central graben on the study area (depth in meters)

Combining different visualization techniques is very important when analyzing DEMs. The chosen color scheme is probably the most important display option and can be stretched or classified. The stretched option displays values along a continuous color ramp while the classified creates breaks on the values, assigning a same color to provinces of similar depth. Both options have its advantages and might be chosen according to the research purpose.

Another important display option is the data resampling, which is responsible for smoothing the display, avoiding the original pixilated images. Other common visualization aid is the shaded relief effect, which assigns values according to the variations in terrain giving the image a three-dimensional aspect. The shaded relief layer is used in combination with the original DEM to give it a more realistic topographic appearance. Figure 3.8 shows how simple visualization techniques enhance the visual understanding of a DEM.

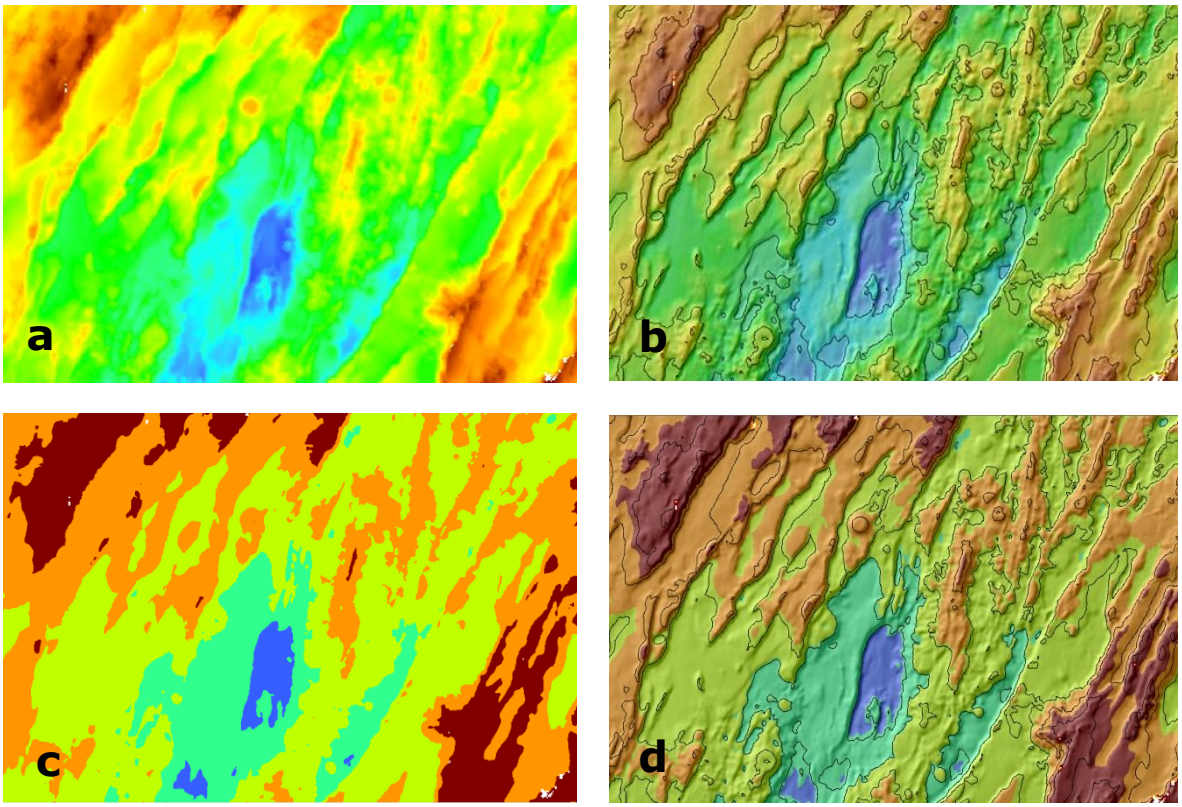

Figure 3.8 Different visualization techniques (a) stretched colour ramp with cubic convolution resample (b) streched colour ramp with cubic convolution resample overlaid with shaded relief and isobah contour (c) classified colouramp and (d) classified color ramp overlaid with shaded relief and isobath contours

The most sophisticated visualization technique is perhaps creating a three-dimensional model that can be used in combination with the other display methods for data interpretation. Visual inspection of 3D images can help validating results of map models. Figure 3.9 shows the 3D model of the same scene presented on Figure 3.8 and Figure 3.7, viewed under different perspective sights.

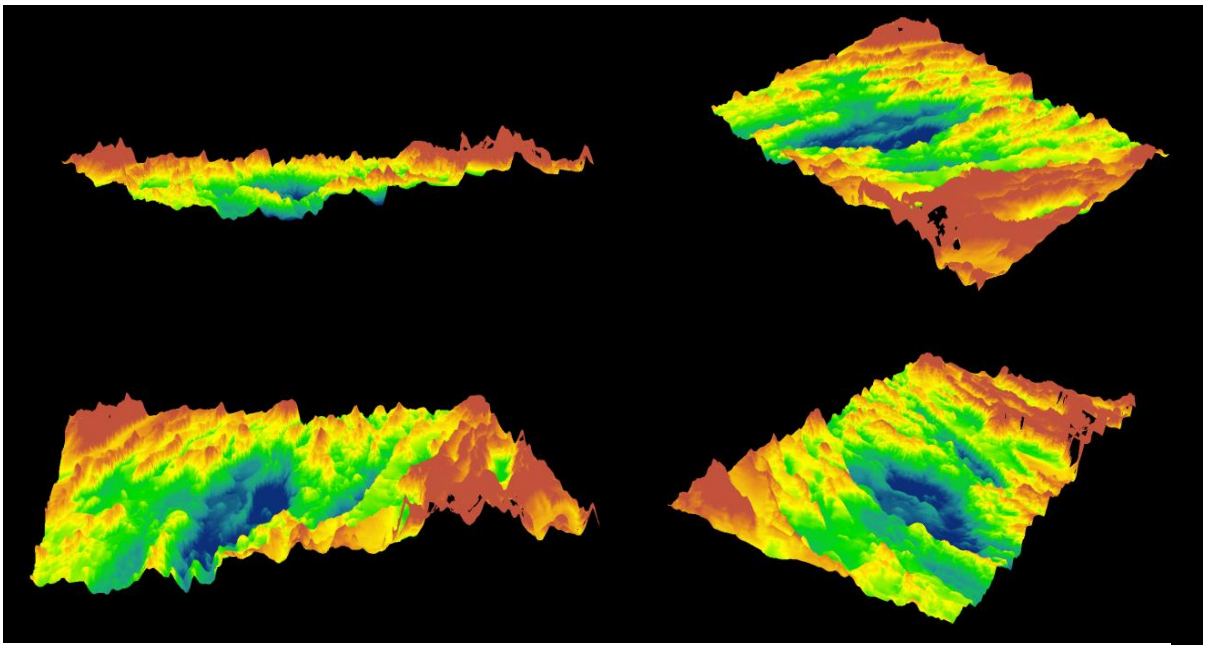

Figure 3.9 3D DEM rotated on different perspectives with vertical exaggeration of 5:1.

Three-dimensional modelling allows navigation through a scene, making it possible to visualize it at different perspective angles. 3D models apply vertical exaggeration, which is number that multiplies all the pixel values, stretching the image vertically. This number represents how bigger the vertical scale is compared to the horizontal. Vertical exaggeration helps data visualization, and even if is sometimes unrealistic, it can be very useful for identifying geological features.

Although most interpretative assumptions for DEMs can be generally based on visualization, more sophisticated analysis techniques are also enabled by modern GIS systems. The fundamentals of the analysis techniques applied in this work will be discussed in the next section of this chapter.

3.2.2 Bathymetric Structural Analysis

Bathymetric surveys have different purposes and as usual, the appropriate analysis methodology is chosen accordingly to the research aims. The most common tool on any kind of topographic analysis consists in creating a vector layer of contour lines. These lines connect areas of same value, and are referred to as *isobaths* in bathymetry. Isobaths are useful for observing how the bathymetry changes and where the terrain is more or less steep. Figure 3.10 shows a contour map of 100m interval over the example DEM.

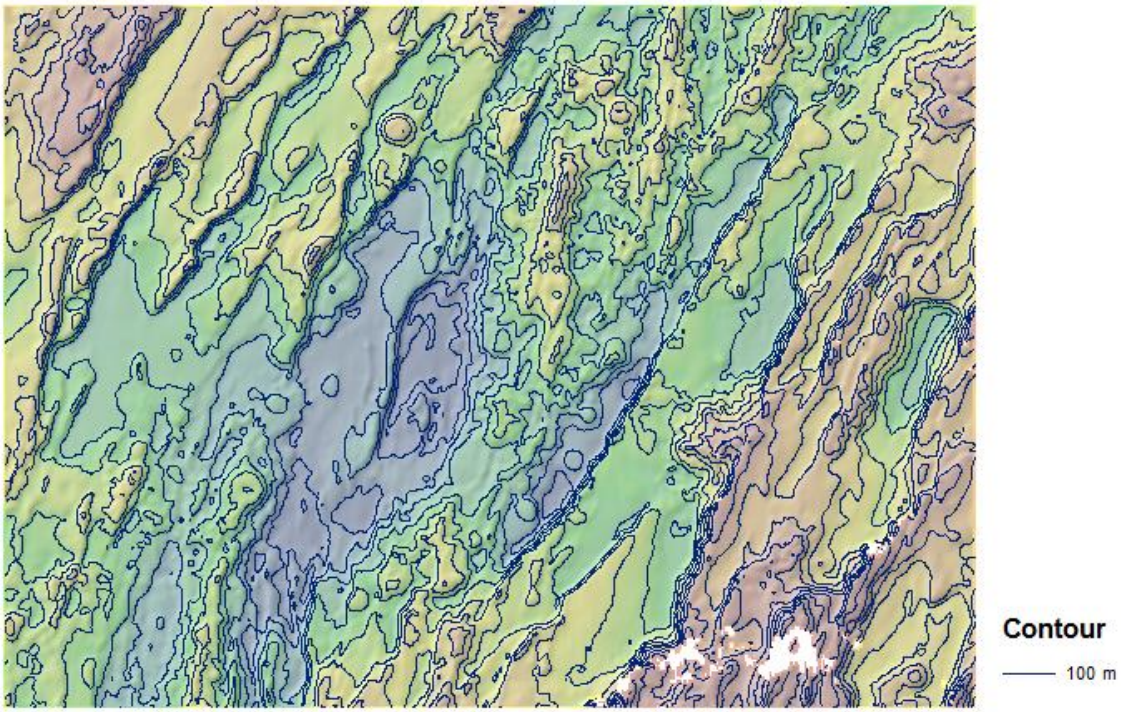

Figure 3.10 contour lines of 100 m interval over the example DEM.

For looking at the data in 2D perspective and deriving the height of individual structures, it is useful to create profile graphs that plot the depths in relation distance along a profile line. This profile might be purposefully selected over features of interest in the study area. The profile graph allows for a more detailed inspection of the bathymetric features, in a much finer scale than seen in the original DEM. Figure 3.11 shows an example of a profile graph over a seamount and a normal fault.

Besides the basics terrain analysis, modern GIS systems allow for calculations over the DEM. The results of such calculations generate another raster layer containing mathematical information, derived from the original dataset. These operations are useful for interpreting structural geology data, such as direction and orientation (dip/strike) of surfaces.

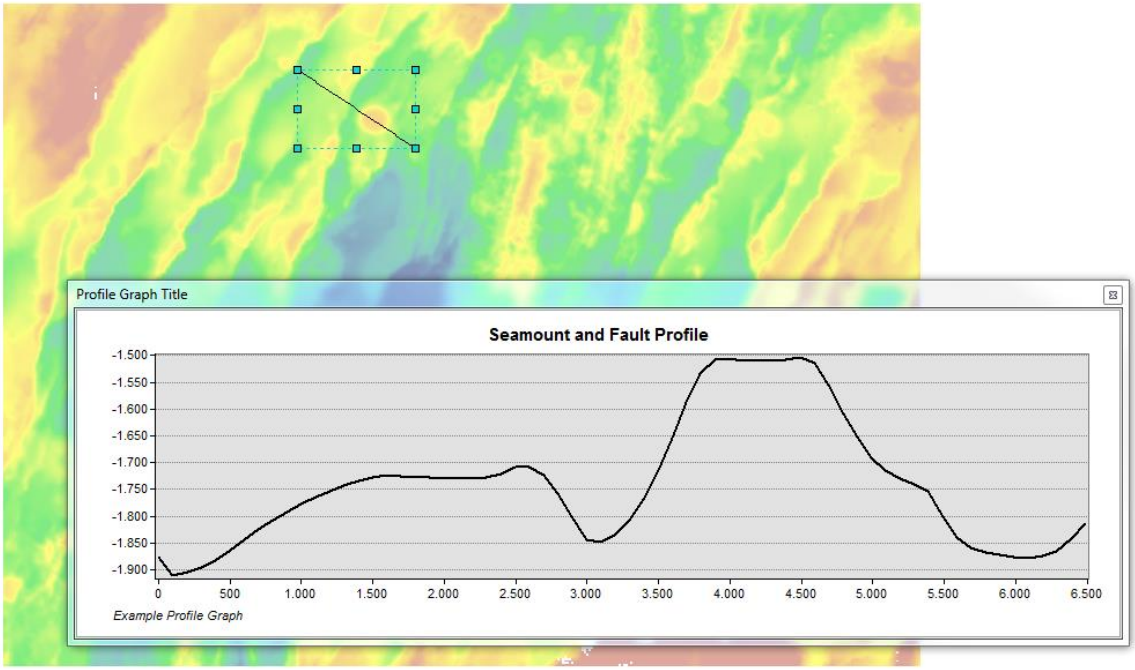

Figure 3.11 Topographic profile over a fault and a seamount on the study area. The profile is oriented from West to East. The vertical axis represents depth and the horizontal axis is the distance along the profile line.

For geological orientation interpretation, two raster operations from ArcGIS® are essential: Aspect and Slope. The slope calculation gives the rate of maximum change in z-value for each raster cell (Equation III). The aspect, on the other hand, identifies the maximum rate of change in value from each cell to its neighbors and indicates the slope direction (Equation IV). In structural geology terminology, Slope is correspondent to the dip angle and Aspect to the dip direction. Figure 3.12

Figure 3.13 show the visual representation of the algorithms used by the Slope and Aspect operations and the output rasters for the example DEM.

The Aspect map has values ranging from 0° to 360°, representing all the geographic directions. Flat surfaces are given a value of -1. The Slope map, on the other hand, has values ranging from 0° on flat surfaces to 90° on oblique. The bigger the value, the higher the dip angle and consequently, the steeper the slope at which the surface is tilted.

Equation III

$$Slope(degress) = ATAN\left(\sqrt{\left[\frac{dz}{dx}\right]^2 , -\left[\frac{dz}{dy}\right]^2}\right) * 57.29578$$

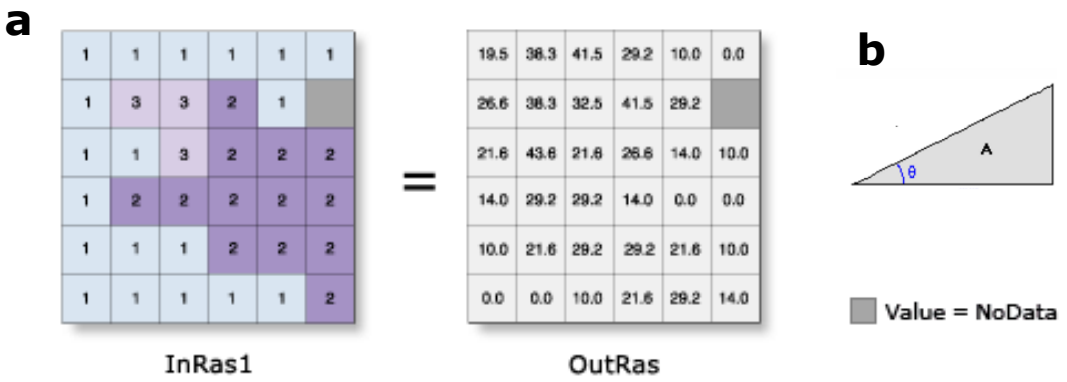

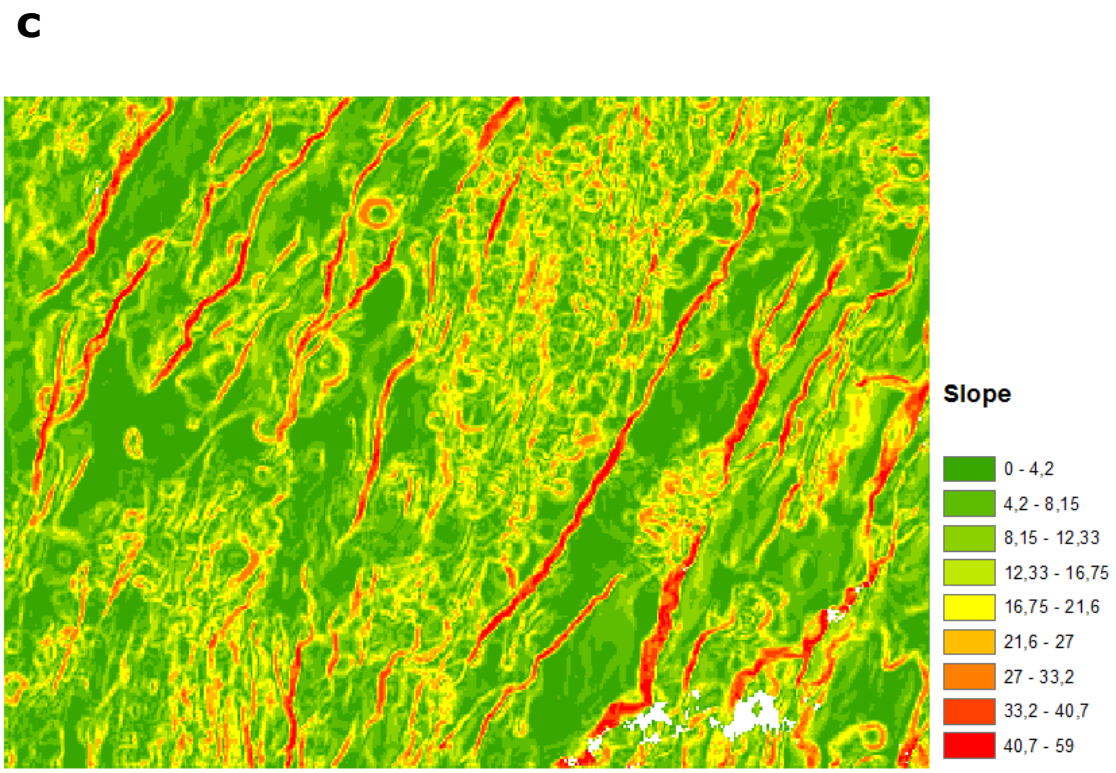

Figure 3.12 Illustration of slope algorithm in a raster layer (a) and what angle it represents (dip) (b). The output of slope is a raster layer classified into the angle values of dip, from the minimum to the maximum angle found in the dataset (c).

Equation IV

$$Aspect(degress) = 57.29578 * atan2\left(\left[\frac{dz}{dy}\right], -\left[\frac{dz}{dx}\right]\right)$$

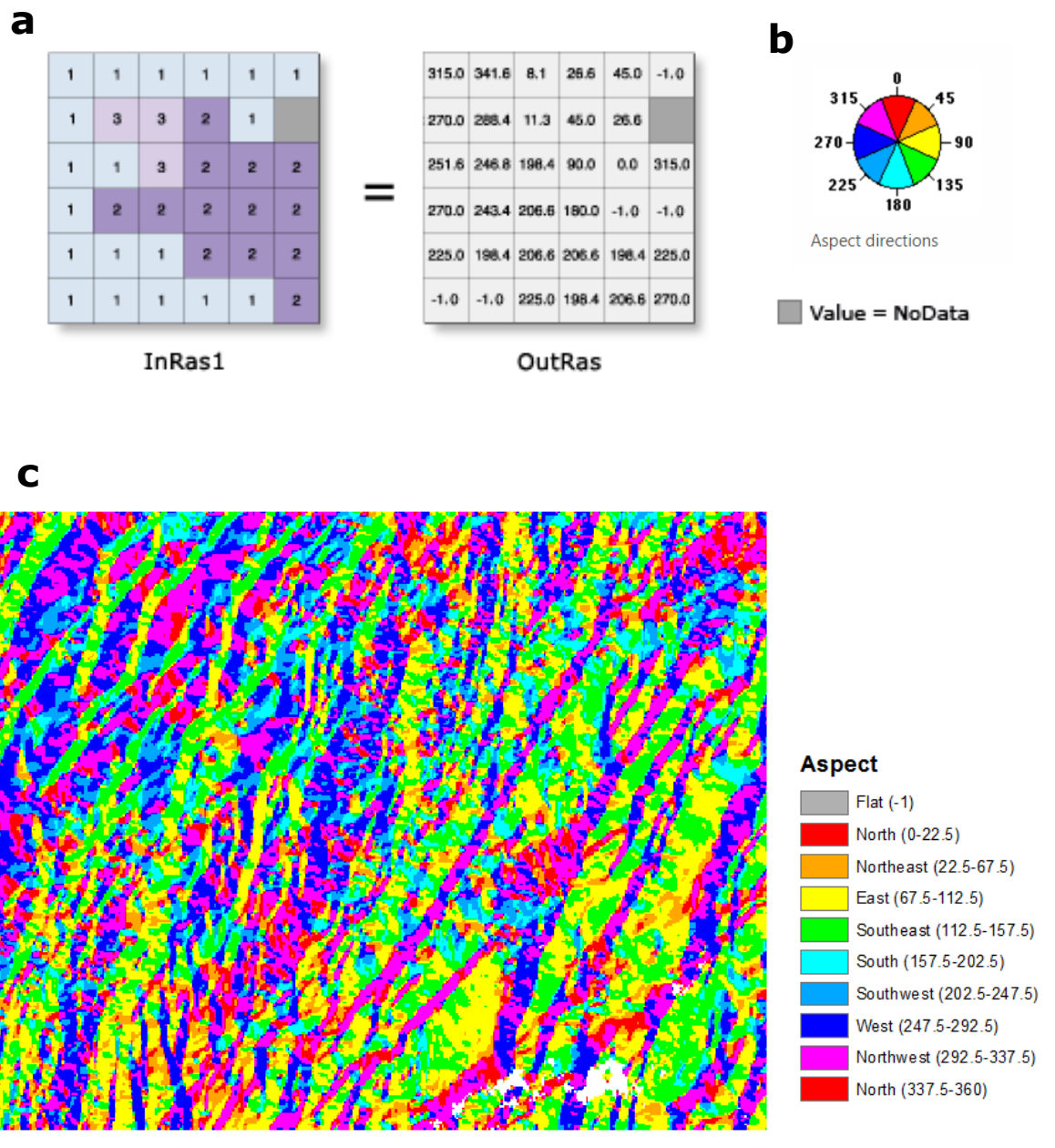

Figure 3.13 Illustration of Aspect algorithm in a raster layer (a) and what angle it represents (dip direction) (b). The output of aspect is a raster layer classified into the directions of the compass, indicating the geographical orientation of surfaces (c).

Beyond the visual analysis, one might wish to perform statistical analyses to check how topographic features spatially correlate to each other. Through the interaction between raster and vector, GIS makes enables extracting values from the map. These values are exported in tables, which can be statistically analyzed. A very common type of numeric analysis for structural geology data is the *rose diagram*. This diagram plots the sampled values in a circular format, representing geographic orientation, thus allowing interpretation of direction and magnitude of certain geological structures.

Several vector layers might be created to extract the information from the DEM. Lines are useful for calculations of length and direction, while polygons are useful for calculating area. Both of these layers can be manually digitized over the features of interest. Another way of deriving information from the raster to a table is by entering points over the raster image. Such points might be either randomly picked with the GIS software, or purposefully chosen with help of visualization techniques according to the purpose of the research. Figure 3.14 shows examples of digitized lines and polygons and randomly picked points with its corresponding attribute tables.

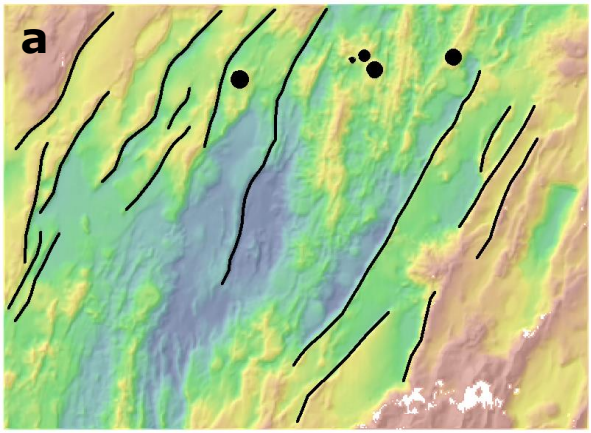

b

Table

Polygon_example

OBJECTID *	SHAPE *	SHAPE_Length	SHAPE_Area
1	Polygon	3991,805526	1265029,827908
7	Polygon	3651,44751	1052585,075329
8	Polygon	2716,654139	585461,556442
9	Polygon	1343,733588	138895,697544
12	Polygon	3731,39299	1104801,152689

1 (0 out of 5 Selected)

Polygon_example

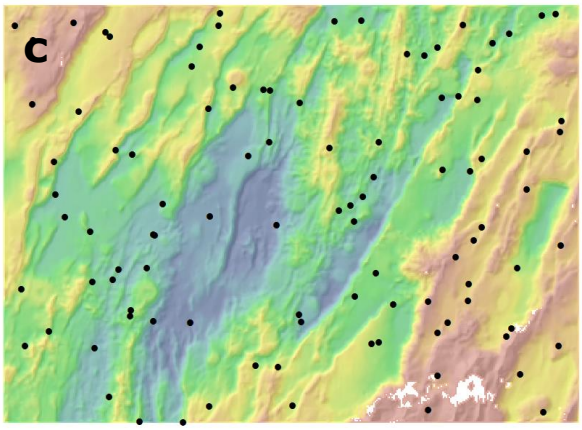

d

Table

Points on DEM

OID *	Shape *	Aspect	Slope
1	Point	117,56729	6,850262
2	Point	54,850613	4,797896
3	Point	285,07886	5,344099
4	Point	109,74697	3,095247
5	Point	288,96396	15,296507
6	Point	298,73444	12,013491

1 (0 out of 100 Selected)

Polygon_example | Points on DEM

Figure 3.14 (a) Lines and polygons over the example DEM. (b) table of polygons and area information. (c) Random points over the example DEM. (d) Table of information about the points with aspect and slope information derived

3.2.3 Change Detection Analysis

With the availability of datasets acquired in different times, it is possible to check for changes on topography. This section will describe the principles of change detection analysis for DEMs and how this methodology might be used for bathymetric comparison.

Change detection is the GIS methodology that aims to detect changes in the environment through comparison of datasets acquired at different moments in time. There are three kinds of geospatial changes to be distinguished: gradual changes, as in climatic changes or urbanization; periodic changes caused by cyclical phenomena, and sudden changes caused by unexpected punctual events, such as earthquakes, tsunamis and volcanic eruptions.

In remote sensing, it is becoming common the wish to perform this type of analysis in order to identify locations where changes happened over the years. Since satellite images can be acquired daily, sometimes within hours apart from each other, this methodology is very easily applied to aerial remote sensing. The same principle can be applied for the MBES DEM, given that there had been repeated surveys over the same area (e.g. Banul, 2014; Ganju et al., 2017; Garcia, Fearns, & McKinna, 2014; Zirek & Sunar, 2014).

Due to the rapid evolution of acquisition systems, it is often necessary to work with images of distinct sources and resolutions. For high quality change detection analysis, good data integration is essential when overlaying datasets. Therefore, when the images to be analyzed do not have the same resolution, it is important to resample the higher resolution image into the lower one.

There are several different methods for change detection analysis (Lu, Mausel, Brondínios, & Moran, 2003; Zirek & Sunar, 2014). The simplest and most efficient method that can be applied for the aims of this research is the "image differencing". This method consists in subtracting one layer from another, pixel by pixel (Equation V).

The resulting change map shows the difference between the two rasters for each pixel (figure 3.5). However, due differences in acquisition systems the resulting map always shows some degree of difference throughout the whole image. For this reason, it is necessary to classify the resulting values and set a threshold to exclude insignificant distinctions. The choice of such values is often arbitrary and has to be decided by the analyzer. The potential sites of change have to be visually inspected in both 2D and 3D maps in order to be evaluated.

Equation V

$$Difference\ in\ Topography = New\ data - Old\ data$$

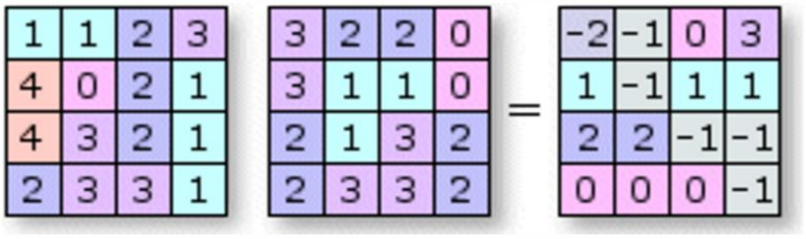

Figure 3.15 Image differencing illustration over a raster layer

Since the pixels of bathymetry represent depth values, the changes represent changes in depth, or in other words, changes on seafloor topography. Therefore, a negative change would represent a new topographic depression, while a positive change would represent an increase in elevation.

4 Methodology

To achieve the results presented in this work, the methodology consisted in four stages, as shown below in Figure 4.1. Each methodological step is detailed in the next sections of this chapter.

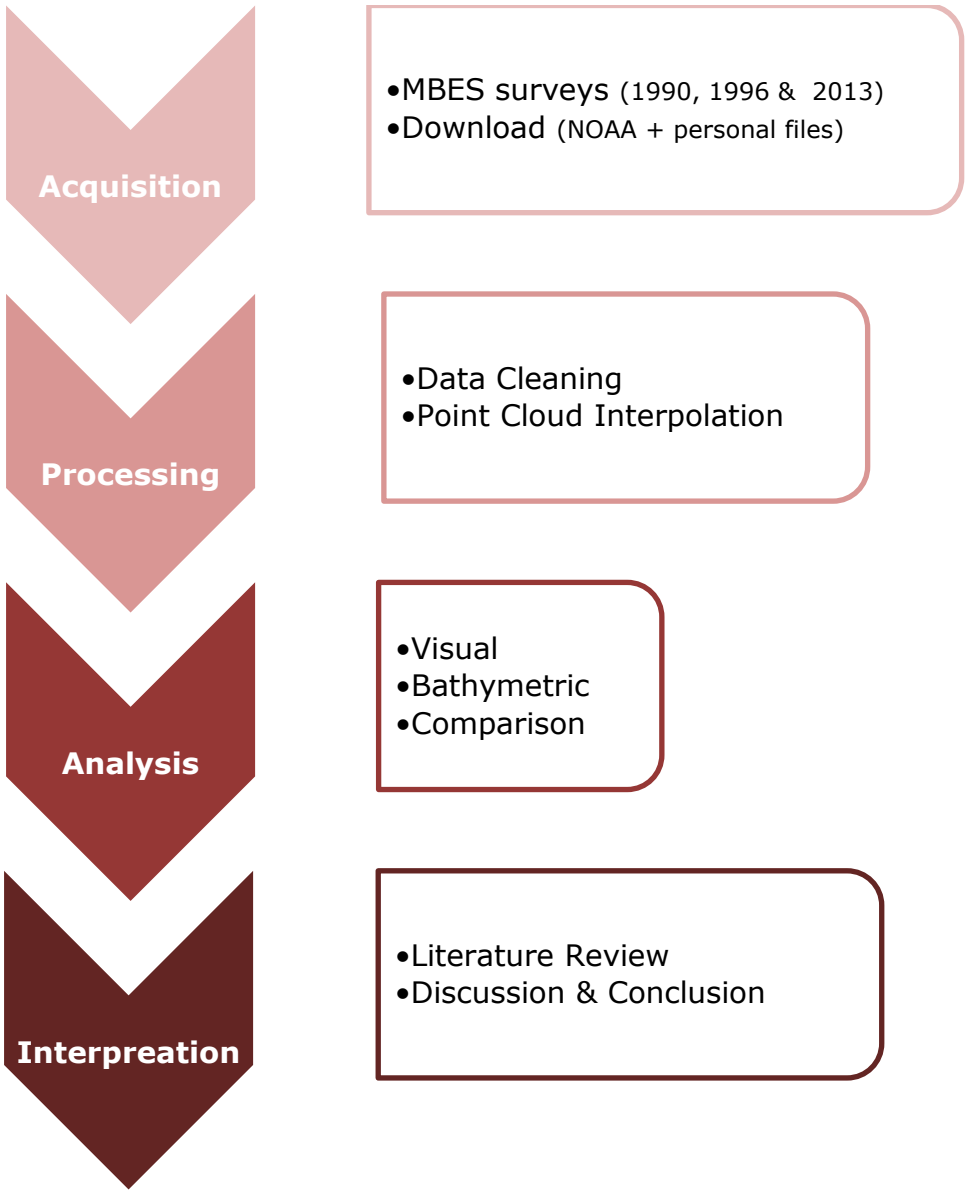

Figure 4.1 Flowchart diagram for the main research stages

4.1 Data

4.1.1 Acquisition

The MBES data used in this work were obtained from the official NCEI world bathymetry dataset (NOAA, 2004), from individual authors (Keeton et al., 1996b) and from the remote sensing laboratory at HÍ. The oldest survey dates from 1990 and the newest one is from 2013, proving a time spam of 23 years in total. Earthquakes locations within this time spam (1990 and 2013) were downloaded from the USGS website (USGS, n.d.).

The survey cruises have the following codes: EW9008 and EW9004 (RV M. Ewing); CD80 and CD87 (RV Charles Darwin) and MGL1309. The survey design for each cruise and further technical specifications for the used datasets can be observed in Appendix A. After acquisition, the data were processed and analyzed according the procedures described in the next sections.

4.1.2 Processing

- **MGL1309 (2013)**

This survey cruise was a joint initiative between the Universities of Iceland (HÍ) and Hawaii (SOEST), therefore this dataset was available at the HÍ remote sensing laboratory. Raw multibeam data were processed in Caris HIPS & SIPS®, as described by (Banul, 2014) and the Outliers were manually eliminated along the target profiles. After the data were satisfactorily cleaned, it was exported as a raster image of 50m resolution in UTM zone 25 N. With this image, all bathymetric mapping procedures described in section 4.2.1 were applied.

- **BRIDGE (1996)**

The Bridge project was a British funded effort to map portions of the Mid-Atlantic Ridge (Joe Cann, n.d.). In this project, a total of 4 cruises surveyed an area of the Reykjanes Ridge, they were: EW9004 and EW9008 on board of the American RV Maurice Ewing and CD81 and CD87 on board of the British RV Charles Darwin.

An already processed raster image from (Keeton et al., 1996) was personally provided by Prof. Roger Searle. All the processing procedures applied are described in the referred article. The provided raster image was masked with a polygon covering the study area, and all bathymetric mapping procedures described in section 4.2.1 were applied.

- **EW9004 & EW9008 (1990/1991)**

The American cruise on board of the RV M. Ewing was provided by NOAA in tabular format. In excel, the tables were edited and all the z values were converted to negative to represent depth. In ArcMap, the files were open through the "create feature class from XY table" command from ArcCatalog, generating a point cloud layer.

The design of the M. Ewing MBES survey consisted in a number of parallel lines, where the ship has navigated in a systematic way (Appendix B). A single table of data provided by NOAA was composed by several surveyed lines, originating very large files. These files were composed by millions of points, thus making the processing very intensive and time consuming. Therefore, the point cloud was split in several tables to be individually interpolated. The splitting was performed by selecting and exporting each surveyed line to a new feature class.

The multibeam survey lines from M. Ewing did not overlap each other, meaning that for generating a bathymetric surface with no data gaps, they would have to be interpolated in between. This would have caused the algorithm to create information over large areas where no actual data values were acquired, compromising the reliability of the change detection analysis. Due to this research aims; these large empty gaps were not interpolated.

The interpolation algorithm chosen was the "Topo to Raster" from the ArcMap Geostatistical Analyst. This algorithm is optimized for hydrographic surfaces, and therefore judged to be the more appropriate for the aims of this research. Other algorithms were also tried, but none proved to give a more satisfying result.

The individual interpolated images were added together using the "mosaic to new raster" tool from the Raster Dataset toolset in ArcMap. The number of bits was specified as 32-bit float and 1 band and the final resolution was of 120m in WGS84. With the obtained raster image, all bathymetric mapping procedures described in section 4.2.1 were applied.

4.2 Bathymetric Analysis

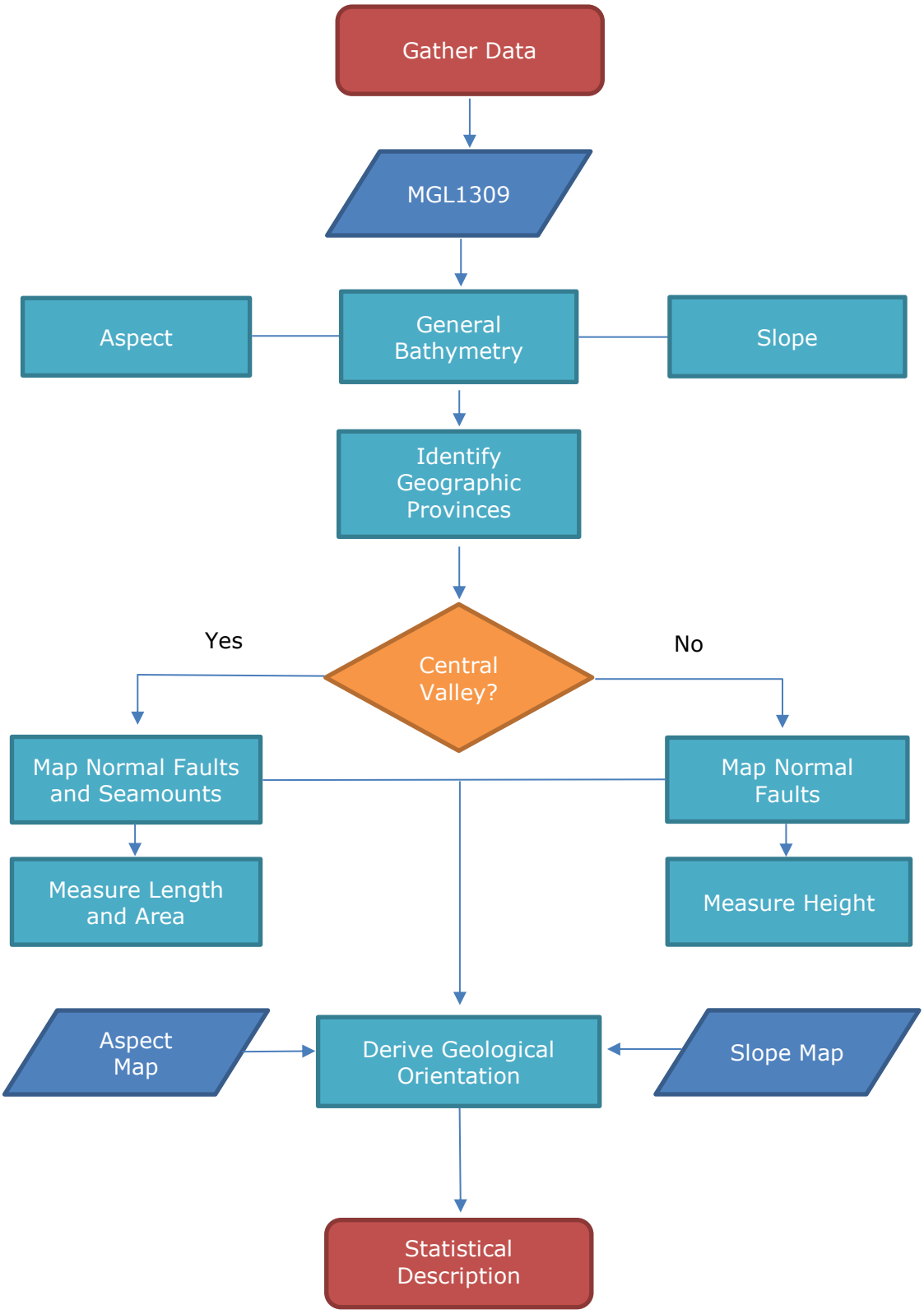

Figure 4.2 Flowchart of bathymetric analysis methodology

4.2.1 General Bathymetry

General bathymetric maps were generated for the MGL1309, M. Ewing and Bridge datasets for the whole study area, together with 10 smaller and more detailed bathymetric maps generated with the MGL1309 raster. All the DEMs were displayed on 3D with vertical exaggeration 10 on ArcScene.

For basic display and analysis of bathymetric data, a series of visual operations was performed. The first one was displaying the DEM raster with stretched color ramp and cubic convolution resampling method. Additionally, the DEM was classified and displayed in ten classes of depth values.

In both displays, a layer of shaded relief was draped with 50% transparency. This layer was created with the operation *hillshade*, from the analysis toolset in ArcMap, with azimuth angle of 135°.

Isobaths were generated by the operation *contour* from the 3D analyst toolset from ArcMap. The depth interval for the isobaths was chosen according to the range of values found in each bathymetric map.

The detailed maps are presented in combination with topographic profiles to exemplify the complexity of the study area and illustrate the differences in topography at distinct distances from the central valley. These maps follow one of the 12 profile lines analyzed, with distances ranging from 10 to 110km away from the central valley to both East and West sides.

Due to the spreading of the tectonic plates, the age of the seafloor increases with distance from the central valley. And as mentioned before, in the study area, the average spreading speed is of 20km/Myr (Carbotte et al., 1991). Based on this assumption, the Dip/Strike Map was plotted over the estimated seafloor ages in the study area.

Taking into consideration the geological structure of the study area, 3 provinces were identified for distinct analysis:

- ***Central Valley****: Active graben over the tectonic boundary*
- ***West:*** *Western Abyssal Hills and transform faults*
- ***East****: Eastern Abyssal Hills and transform faults*

.

4.2.2 Normal Faults

The normal faults appear in the study area as linear features, most frequently parallel to the tectonic boundary. To help performing the next analytical steps and to draw conclusions about the tectonics in the area, these faults had to be identified and digitized. The normal faults were visually identified with help of overlays in ArcMap. The first procedure was displaying the 50m isobaths. There is a sudden increase in depth where a normal fault is present. Therefore the contour lines appear significantly closer to each other, forming a very recognizable linear display on the map (

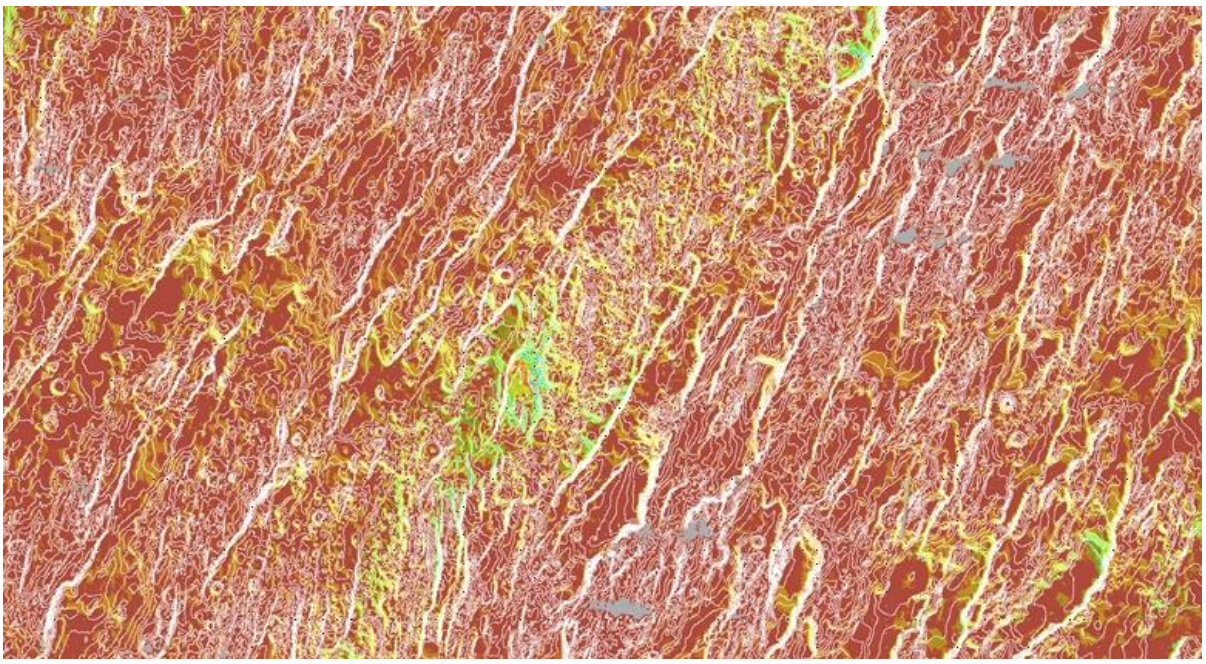

Figure 4.3 50m isobaths in white, illustrating the procedure used to identify major normal faults. Thicker white lines are several isobaths close to each other, coinciding with faults' locations.

Major faults were easily identified by the isobaths' spacing. The smaller ones, however, were less obvious. Therefore, the subsequent procedure was displaying the DEM with different illumination angles. As expected, the faults dip to opposite directions in the opposite sides of the rift. Therefore, to pick faults of different dipping angles, the illumination applied in the hillshade effect was altered from NW to SE (

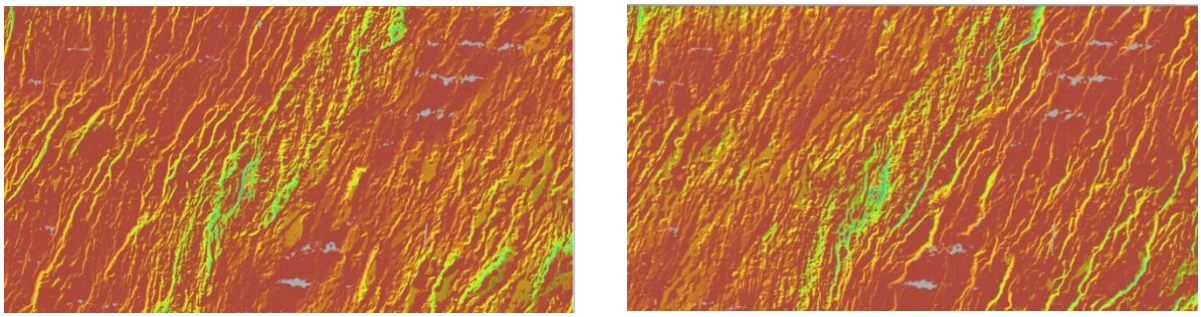

Figure 4.4 Illustration of the DEM with hillshade effect illuminated from opposite angles. Illumination from SE to identify faults in the West side of the rift valley (left) b) illumination from NW to identify faults in the East side of the rift (right)

This way, over 1200 fault lines were manually picked and digitized in the study area, creating a layer of polylines (Figure 4.5). Using this layer, a line density map was generated to represent the density of normal faults in the different provinces. This density analysis was performed with the function "line density" from the ArcMap's Spatial Analyst.

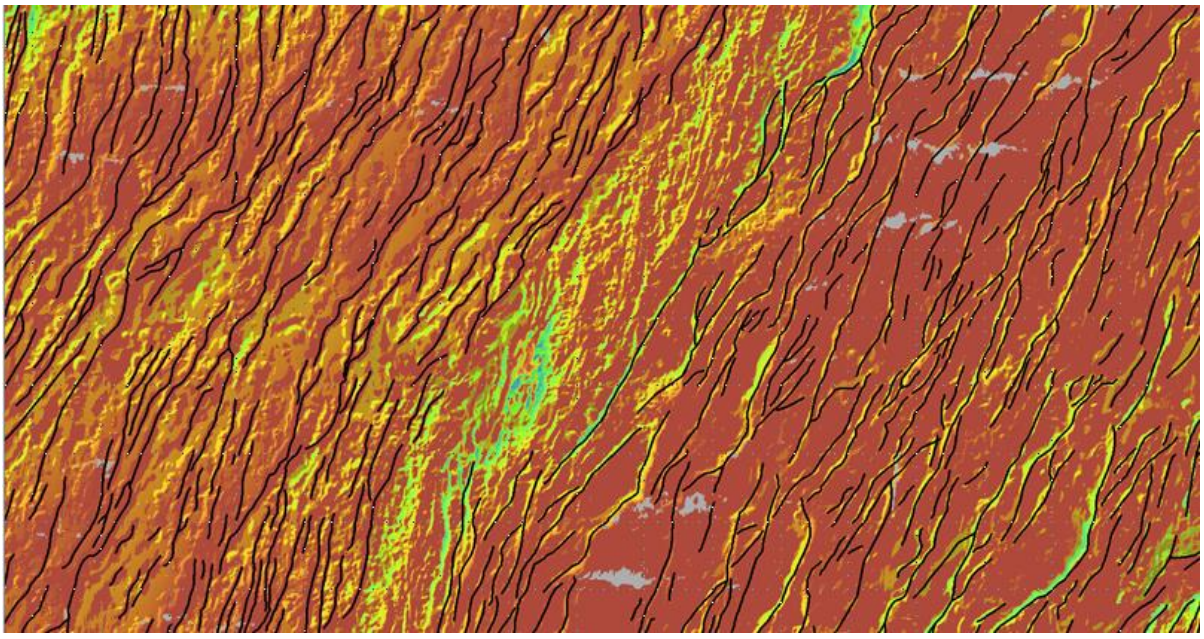

Figure 4.5 Sample of digitized fault lines in the study area with NW illumination. This figure shows only the normal faults in the West and East provinces.

To quantitatively analyze fault trends, the polylines were split at its vertices, generating straight lines. This procedure resulted in over 10,000 lineaments. In the attribute table of this layer, 4 fields were added (X1, X2, Y1, Y2) to compute XY coordinates for the start and end points of every single lineament. This was achieved with the "calculate geometry" function of the field calculator from the attribute table in ArcMap.

This layer of lineaments was exported as a CAD and later imported to Rockworks16. On Rockworks, the polylines' middle points and geometries were calculated. To represent fault trends, rose diagrams were plotted using a calculation methodology based on the lineaments' length. Three rose diagrams were created at this stage; one for each province (East, West, Central Valley).

In order to verify if there was a relation between faults amplitude and distance to the central valley, 220 topographic profiles of 10km length were analyzed using the 3D analyst from ArcMap. The topographic profiles were systematically picked within buffer zones of 10km distance increment from the central valley, always oriented from NW to SW. The profiles were also picked on a 10km distance apart from each other in the N/S direction. This orientation was purposefully chosen to cross most of the normal faults perpendicularly. In order to maintain a systematic sampling scheme, each profile follows a single straight line throughout the study area (Appendix F).

The profiles were individually analyzed and the normal faults were identified by its nearly vertical display. This way, heights of individual faults were determined by the difference between the top and bottom of the fault plane. Only inward facing faults that were of 50m height or higher were picked. The number of faults per profile was computed in order to back up the interpretation of the line density map generated by the previous analytical step.

To summarize the datasets, descriptive statistics of central tendency (mean, median and mode) and maximum and minimum values were computed (Appendix C). These values are shown for both of the analyzed variables (number of faults per profile and fault height). With the resulting values, a series of bar plots were generated, representing the characteristics of the faults on distances ranging from 10km to 110km away from the central valley.

In order to mathematically reply to the question of the objectives and determine whether or not there was a relation between "number and magnitude of faults" and "distance to the tectonic boundary", a basic regression calculation was applied using the descriptive statistics values. The correlation coefficient between "number of faults per profile" and "distance to the tectonic boundary"; and the correlation between "fault height" and "distance to the tectonic boundary" were calculated separately. All statistics calculations were performed in Excel.

4.2.3 Central Valley

The central valley is the main active graben over the tectonic boundary. Since this province is of lower depth than the immediate surroundings, its outer limits could be easily identified when classifying depth values in 3. This first identification was later adjusted with help of the other maps generated in this work.

The outer limits of the central valley were marked with a digitized polygon. This polygon was used to mask the DEM, creating a sub-DEM only for this province. This sub-DEM was displayed separately for detailed visual inspection over this area. The volcanic seamounts were digitized as circular polygons and their areas were derived from its attribute table. Basic descriptive statistics were performed with this dataset (Appendix D).

4.2.4 Geological Orientation

As mentioned before, in ArcGIS, dip angle is given by the function Slope, while dip direction is given by the function Aspect, both part of the Geo-Statistical Analyst. As a result of these tools, two new raster layers were generated: Slope and Aspect.

A third map containing points for which the aspect and slope were derived was created, in order to show these values in specific locations. For this purpose, 277 points were manually selected above the landmasses adjacent to the mapped normal faults (faulted blocks). Most of these points were picked over the analyzed topographic profiles.

Information about the aspect and slope was extracted from the raster images to the selected points using the tool "Extract Multi-values to points". The strike was calculated by the field calculator in the table of contents of this point layer. This calculation was performed by subtracting 90 from the aspect value, since strike is perpendicular to dip direction. The points were converted to dip/strike notation, rotated on the strike angle and labeled with the dip angle value (slope).

To indicate the dominant dip/strike on the different distances from the central valley, rose diagrams were created. For this purpose, 1000 points were randomly selected in each of the 10 km wide buffer zones (Figure 4.6). The buffer zones were created around the central valley polygon using the "multi-ring buffer" tool from ArcMap.

As opposed to the dip and strike map, the points used for plotting the rose diagram were randomly selected, and therefore cover the whole range of features present in the study area. The points were selected in both East and West provinces, totalizing 22,000 sampled points throughout the study area. This way, a total of 66 rose diagrams (Appendix G) were generated representing dip angle, strike and dip direction, using the open source software GeoRose.

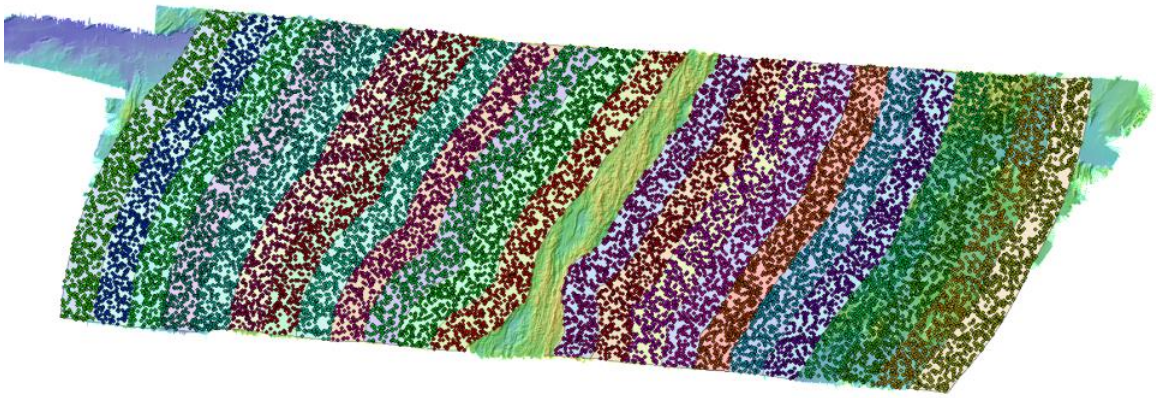

Figure 4.6 Randomly selected points over the 10 km buffers around the central valley

4.3 Change Detection Analysis

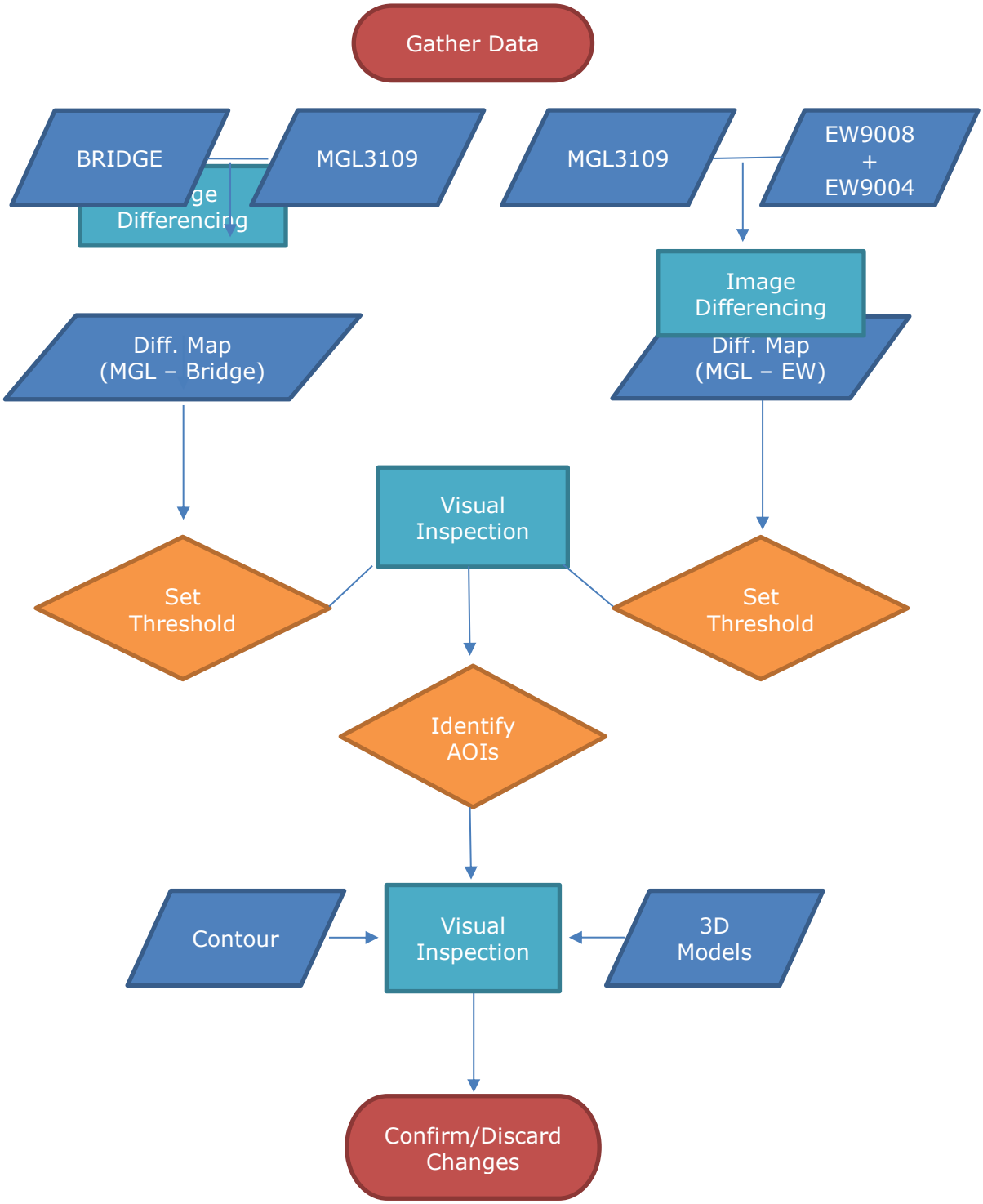

Figure 4.7 Flowchart of the change detection analysis methodology.

In this work, the change detection analysis was aimed to detect changes on seafloor

topography caused by large volcanic eruptions. For this reason, although ideal, a very extensive time series is unnecessary. Furthermore, the availability of bathymetric data to perform this analysis in the study area is very limited and therefore only 2 moments in time are compared: 1990 and 2013.

Since the older data had lower resolution, the first step taken for integrating the datasets was resampling the raster image from MGL1309 (resolution of 50m) to the same resolution as the older images (resolution of 120m).

The change detection technique chosen for this research was the map algebra of "image differencing", combined with visual inspection. The oldest dataset was subtracted from newer one using the raster calculator from the Raster Analysis toolset in ArcMap. This operation was performed twice: once subtracting the Bridge raster from the MGL1309 raster and once subtracting the EW9004+EW9008 raster from the MGL1309 raster, generating two difference maps.

As required by the methodology, a threshold value had to be selected, above and below which the remaining differences between the two datasets were considered significant enough to be further investigated. Considering the resulting standard deviations of the difference maps and the resolution of the dataset (120m), a threshold of 4 x standard deviations of the histogram from difference map was chosen. This value was selected in order to guarantee that the area of change would always be superior to the data resolution. All values that fell within +/- 4 standard deviations were excluded from the display (Figure 4.9 Difference map without excluding values within the threshold and the corresponding histogram (top). Difference map with +/- 4 standard deviation values excluded from the display and corresponding histogram (bottom).

To help identifying new potential features, a contour operation was applied to the difference maps. A change was considered to be significant when the total area was superior of 10x the resolution (or 1200 m^2) and it produced contour lines that build up to a plausible topographic feature (Figure 4.8). The total area of change was calculated by digitizing a polygon around it.

After identifying potential changes, the images were visually inspected with help of the bathymetric contours and the difference maps in ArcMap. Simultaneously, the 3D models overlays were visually analyzed in ArcScene in order to confirm or discard the supposed change. To evaluate the change, the earthquake record for the area and the time spam covered was combined with the bathymetric display.

Figure 4.8 Example of change building up to plausible isobath contours (left) and change that did not produced realistic contours(right).

Figure 4.9 Difference map without excluding values within the threshold and the corresponding histogram (top). Difference map with +/- 4 standard deviation values excluded from the display and corresponding histogram (bottom).

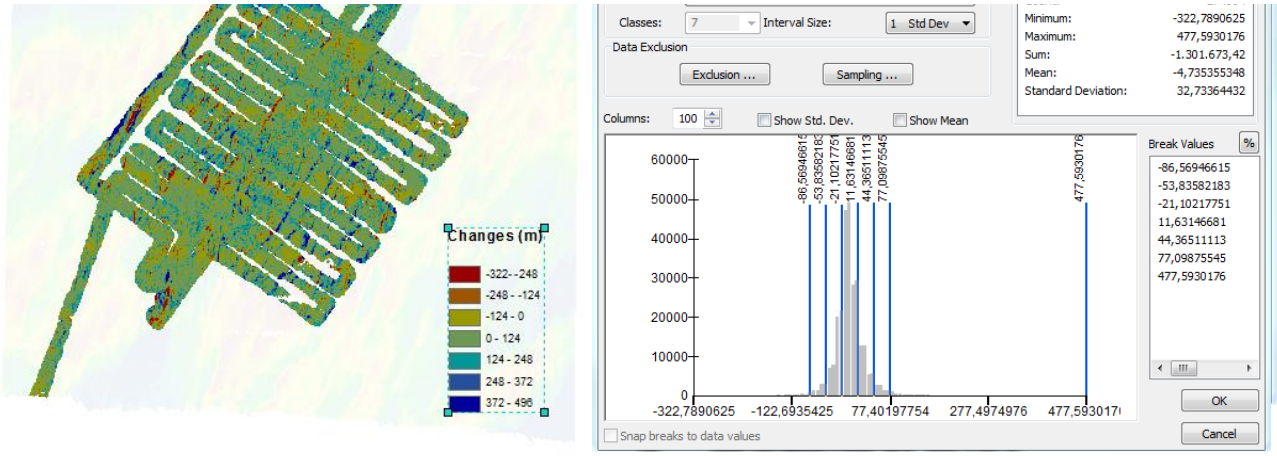

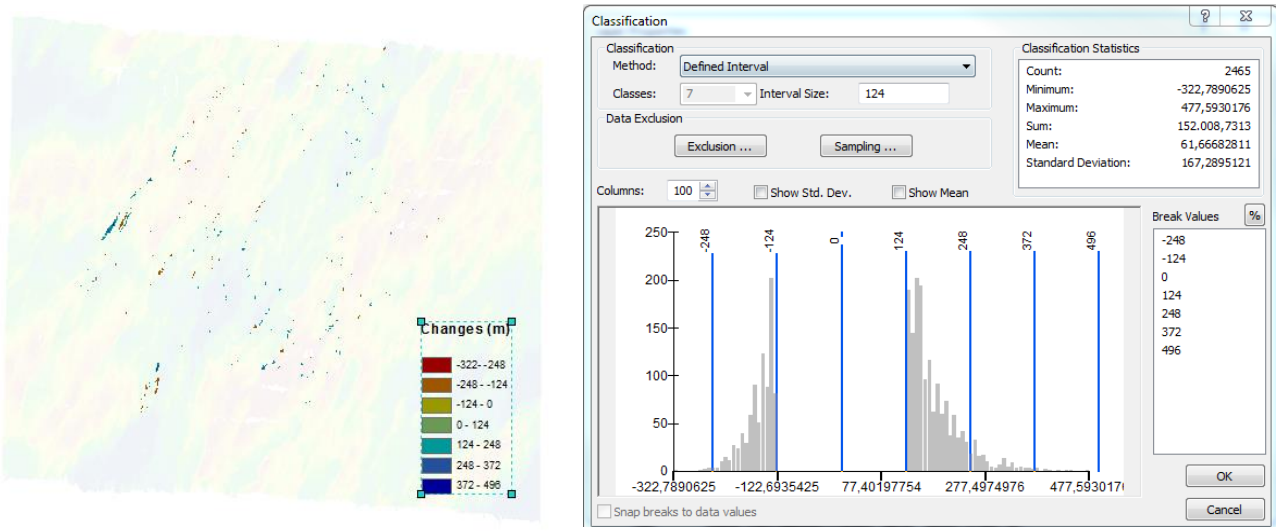

5 Results

This chapter presents the results of this research. The tables of data used for statistical analysis, the rose diagram for geological orientation analysis and additional maps are available on the appendixes, as follows:

- Appendix B – Contains bathymetric maps of all surveys used in this thesis;
- Appendix C - Contains tables of descriptive statistics for the normal faults;
- Appendix D – Contain tables of descriptive statistics for the central valley;
- Appendix E – Is a map with the plot of Earthquakes data used for interpretation of the change detection results;
- Appendix F - Contains topographic cross Sections along one of the profiles analyzed on the study area (Only 12 of the 240 profiles that were analyzed are shown here, for illustrative purpose);
- Appendix G – Contains rose diagrams for geological orientation of the 22,000 random points, for each of the buffer zones in both West and East provinces

5.1 General Bathymetry

Figure 5.1 General bathymetry with colour shaded relief, generated with 135^{o} azimuth.

Figure 5.2 Classified general bathymetry. This map was classified in 10 depth intervals and the contour lines were plotted for 320m isobaths.

Figure 5.3 3D model of the DEM with vertical exaggeration 10:1, on different perspective views.

5.1.1 Central Valley

Figure 5.4 Central valley bathymetry with 3D model of the DEM. with 135^{o} azimuth, and its respective 3D model.

Figure 5.5 Classified bathymetry of the Central Valley. This map was classified in 5 depth intervals and the contour lines were plotted for 200m isobaths.

Figure 5.6 Central valley topography with digitized seamounts (volcanoes).

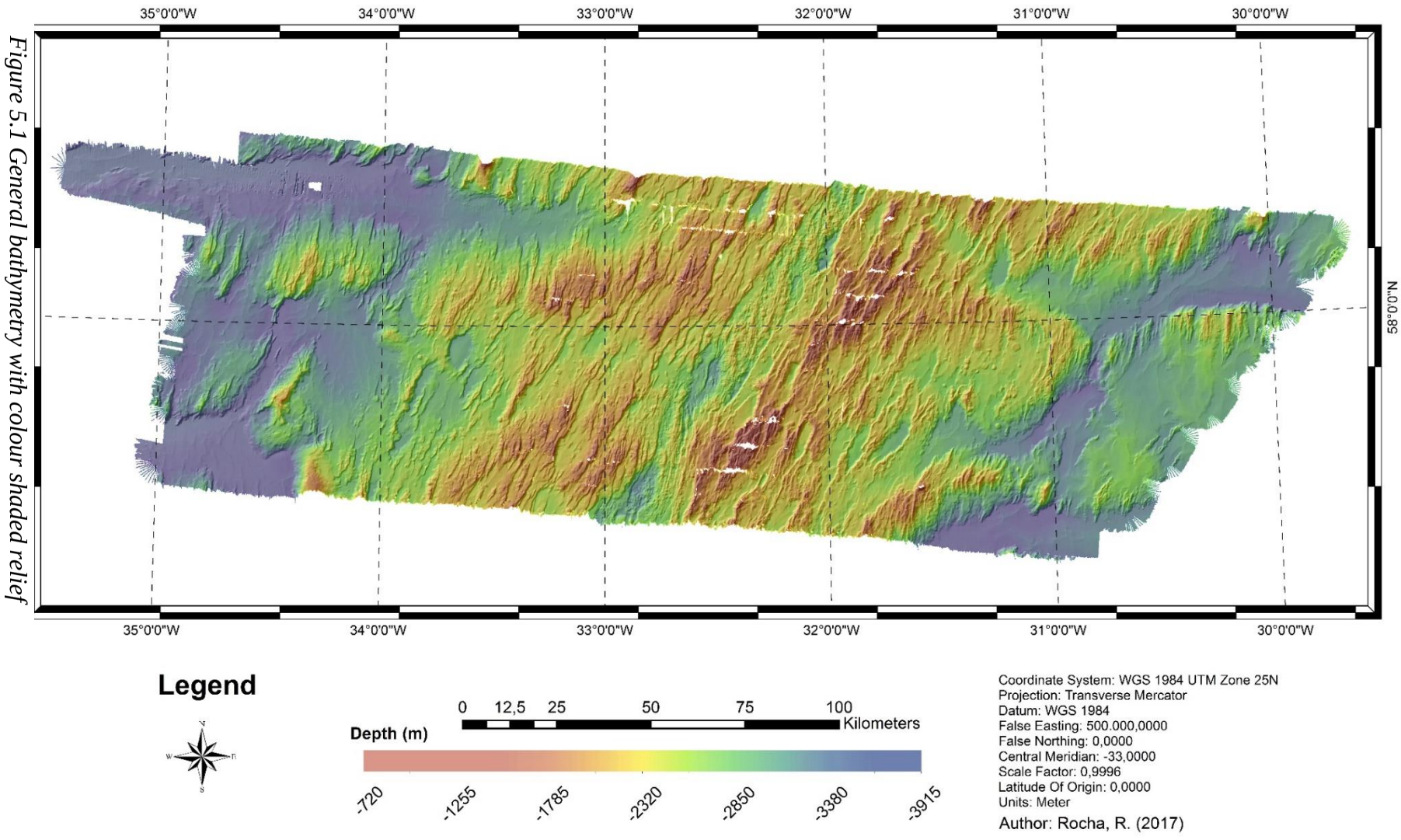

Figure 5.1 General bathymetry with colour shaded relief

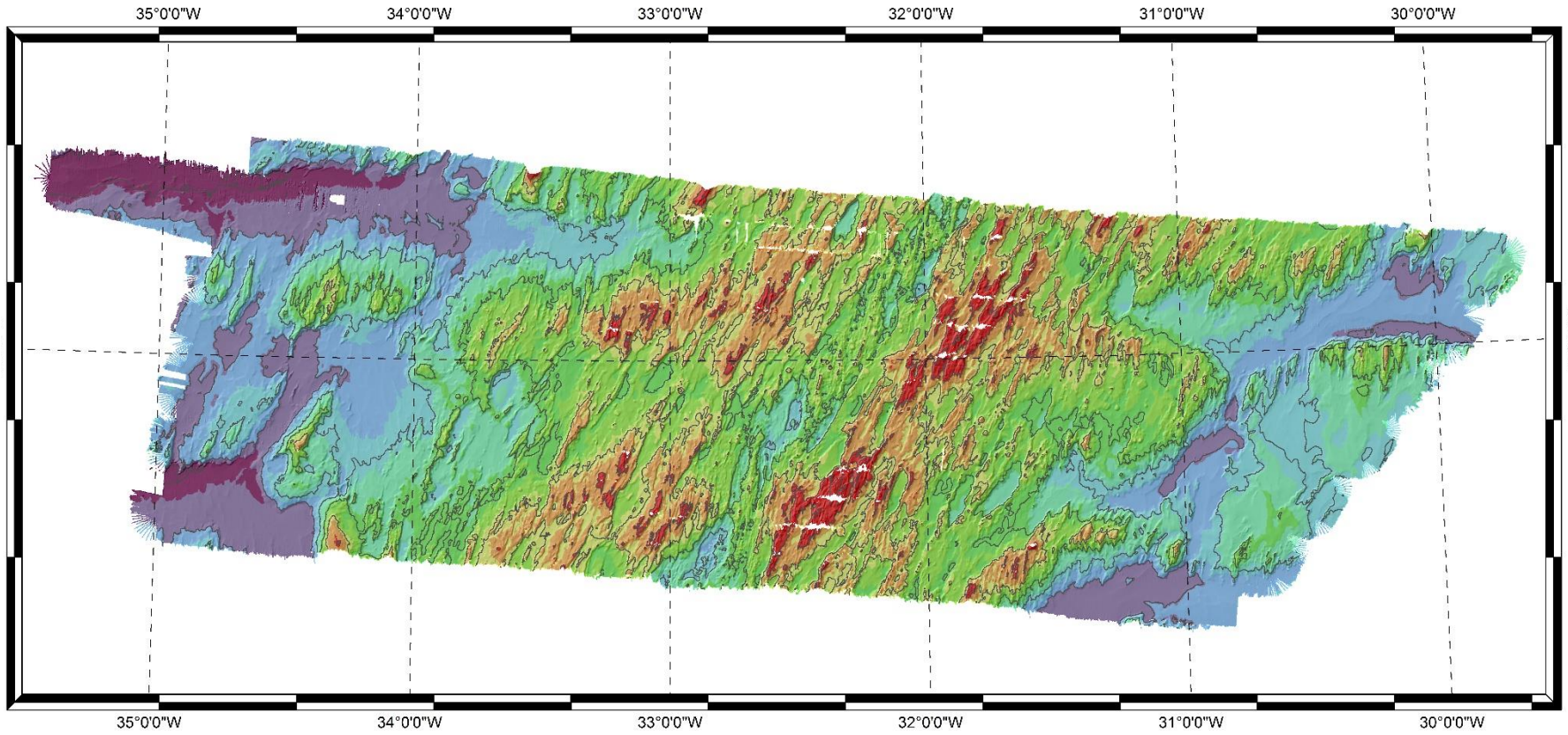

Figure 5.2 Classified general bathymetry

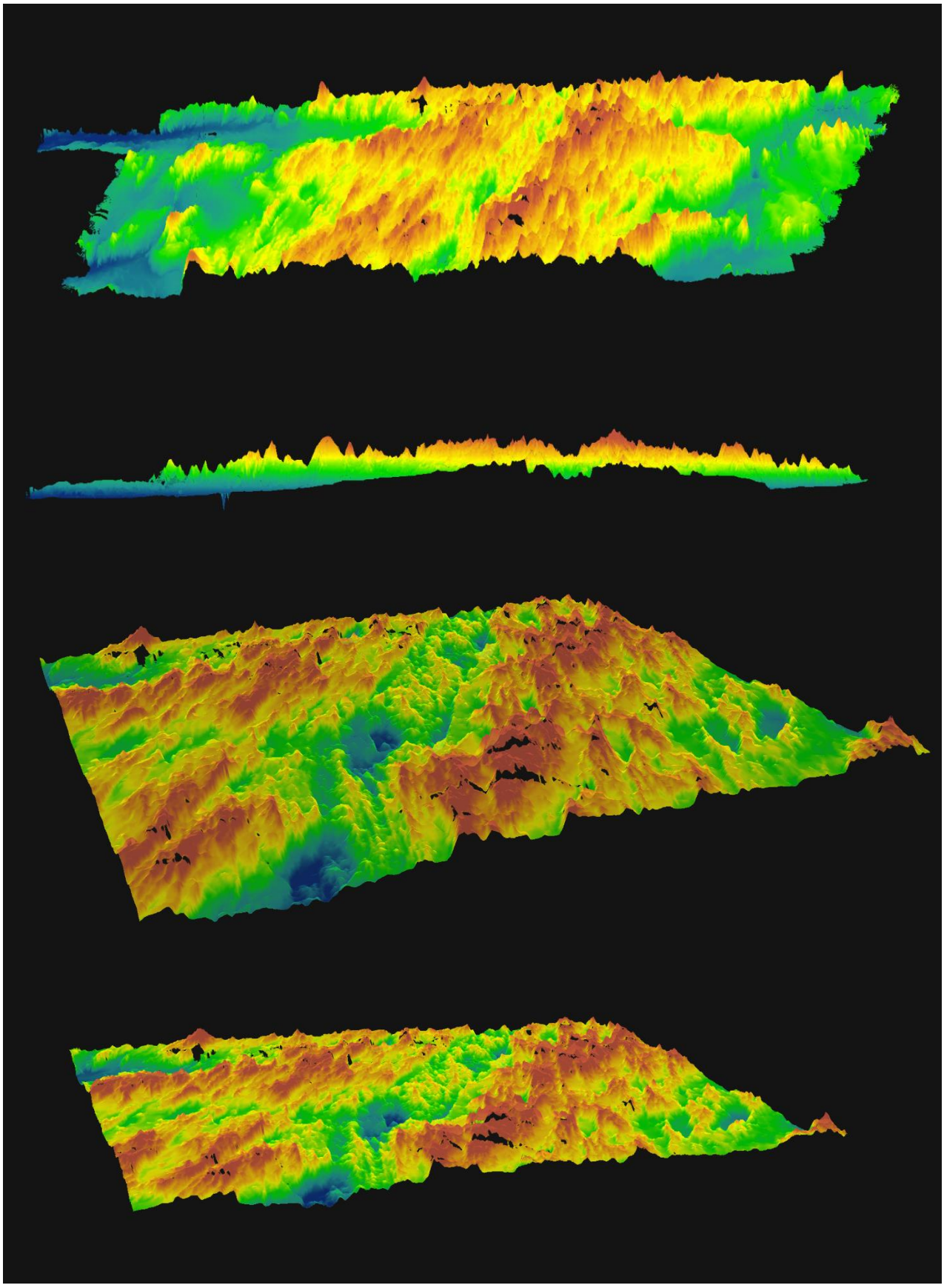

Figure 5.3 3D model of the DEM

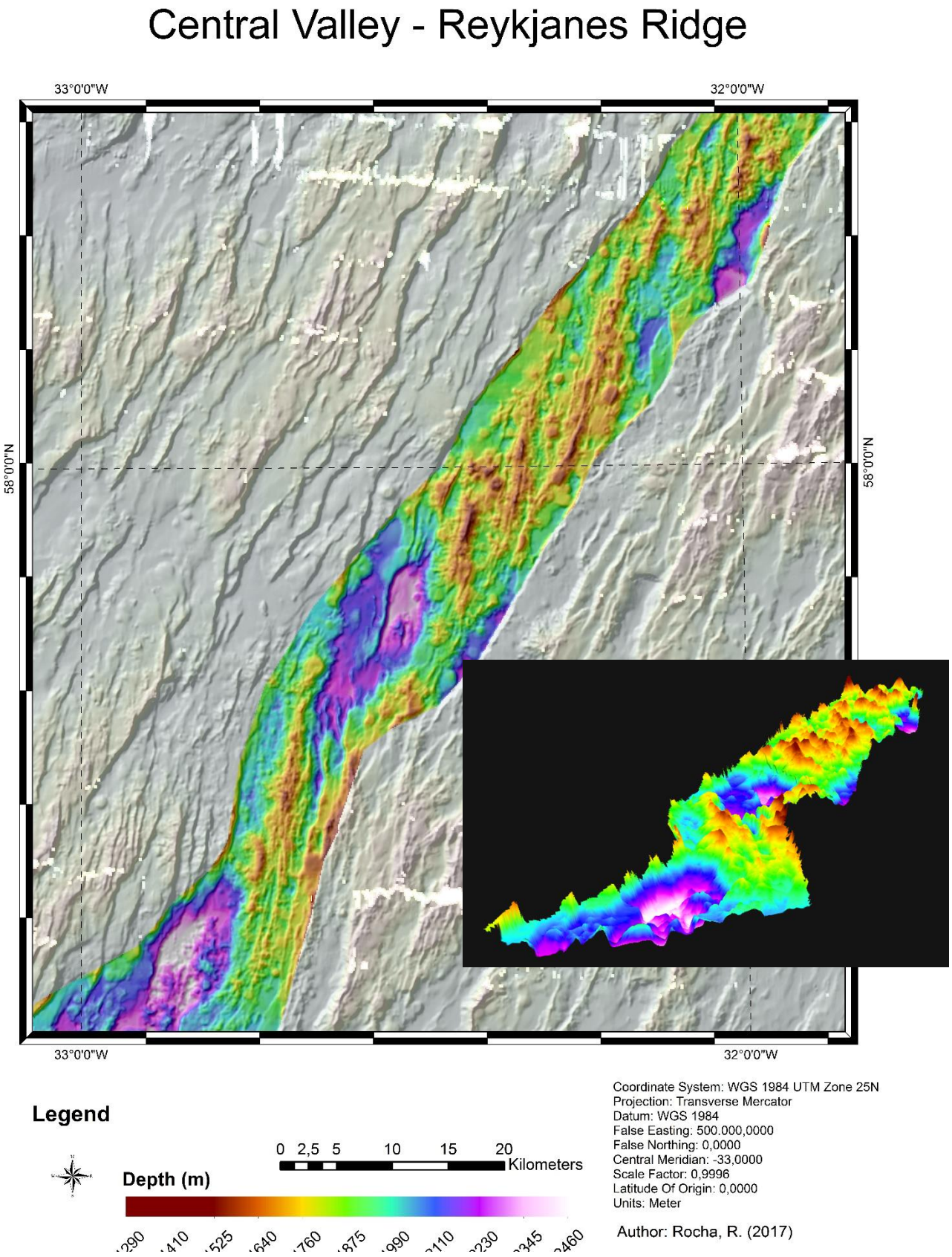

Figure 5.4 Central valley bathymetry with 3D model of the DEM.

.

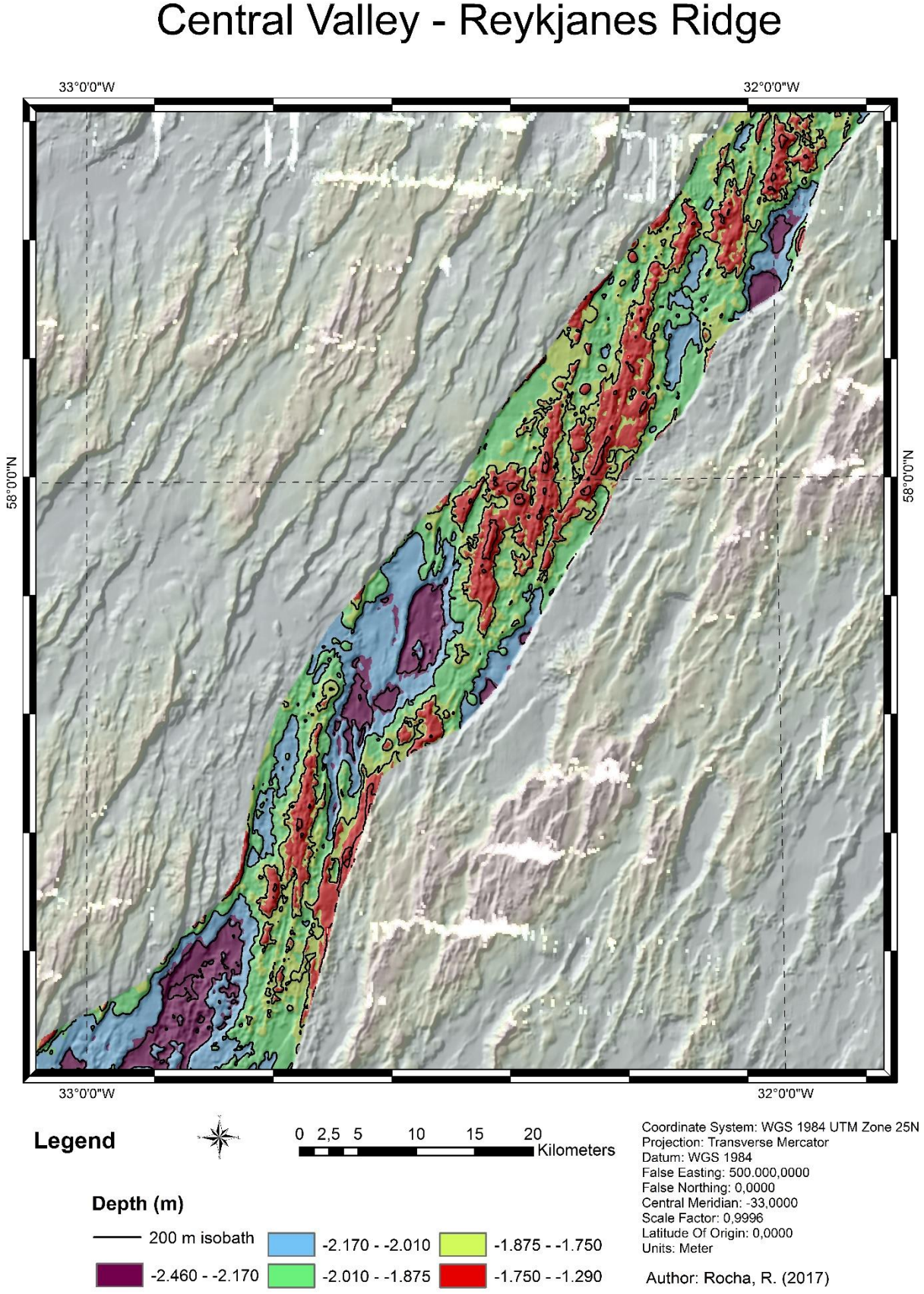

Figure 5.5 Classified bathymetry of the Central Valley.

Volcanic Activity

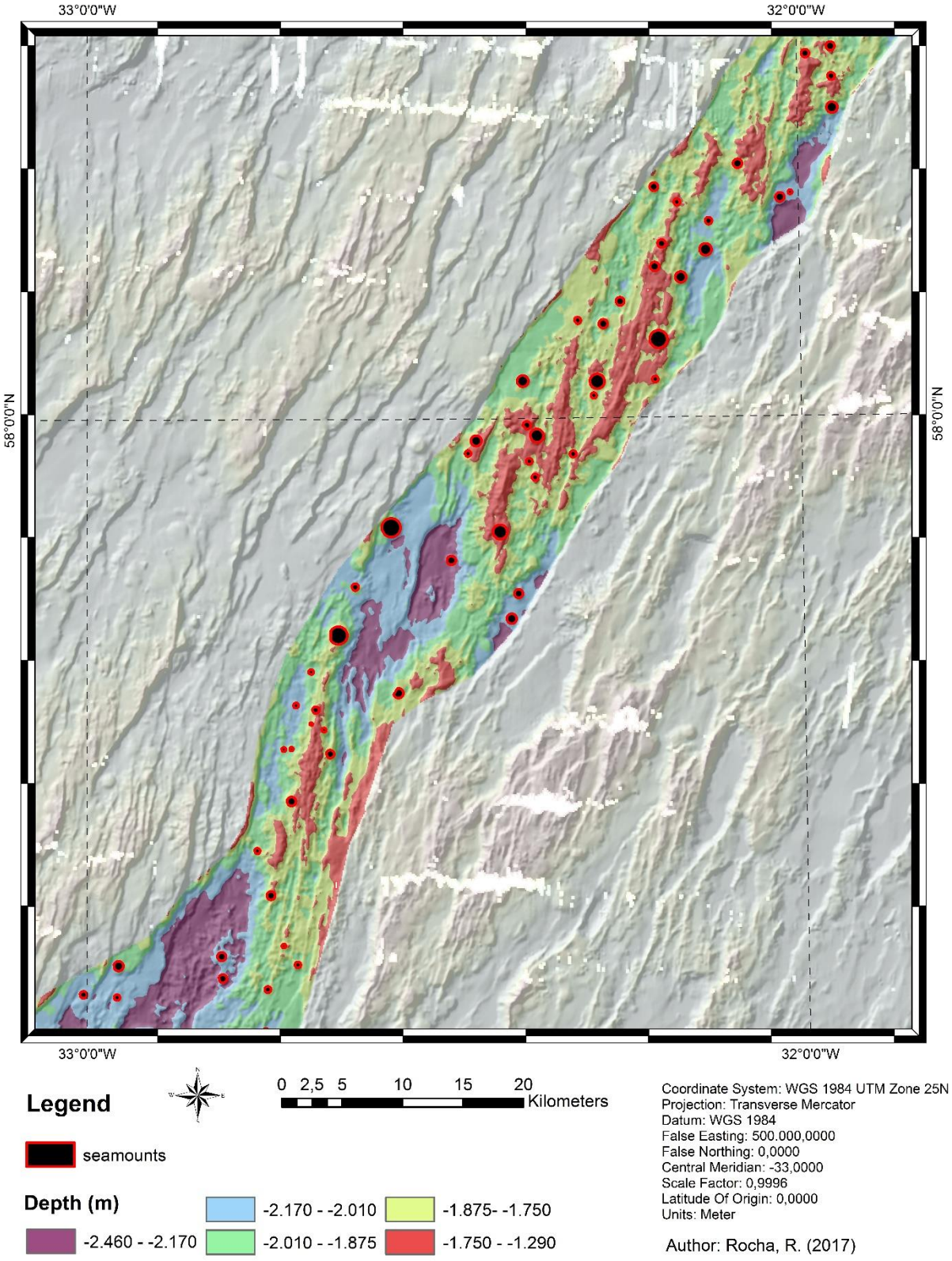

5.2 Normal Faults

Figure 5.7 is a map showing the normal faults in both East and West provinces and in the central valley.

Figure 5.8 is a map showing the results of the line density analysis for the normal faults.

Figure 5.9 is a map showing the locations of the topographic profiles, for which the normal faults heights were analyzed and the 10 km buffer zones around the central valley and topographic profiles.

Figure 5.10 is a graph showing the total number of normal faults counted in each buffer zone for both East and West provinces.

Figure 5.11 is a graph showing the maximum and minimum number of faults counted per profile in the East province.

Figure 5.12 is a graph showing the maximum and minimum number of faults counted per profile in the West province.

Figure 5.13 is a graph showing the maximum and minimum fault heights measured in the East province.

Figure 5.14 is a graph showing the maximum and minimum fault heights measured in the West province.

Figure 5.15 is a graph showing the average fault height for each buffer zone and each province. Blue bars represent West and red bars East.

Figure 5.16 is a graph showing the maximum fault height per buffer zone. Blue bars represent West and red bars East.

Normal Faults

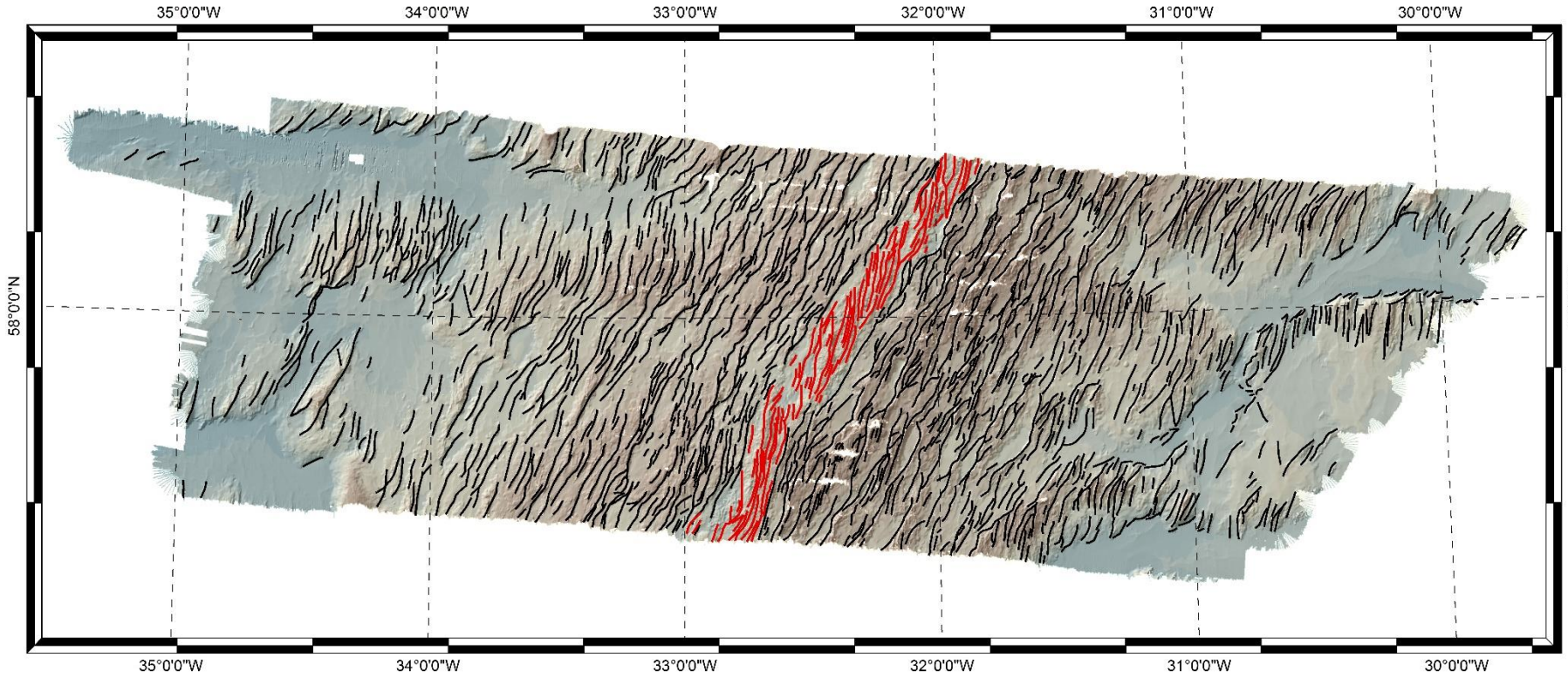

Legend

Faults in the Graben

Normal Faults

Depth (m)

-3.300 - -2.750
-2.750 - -2.550
-2.550 - -2.374
-2.374 - -2.187
-2.187 - -2.011
-2.011 - -1.836
-1.836 - -1.673
-1.673 - -1.510
-1.510 - -1.310
-1.310 - -721

0 12,5 25 50 75 100 Kilometers

Coordinate System: WGS 1984 UTM Zone 25N
Projection: Transverse Mercator
Datum: WGS 1984
False Easting: 500.000,0000
False Northing: 0,0000
Central Meridian: -33,0000
Scale Factor: 0,9996
Latitude Of Origin: 0,0000
Units: Meter

Author: Rocha, R. (2017)

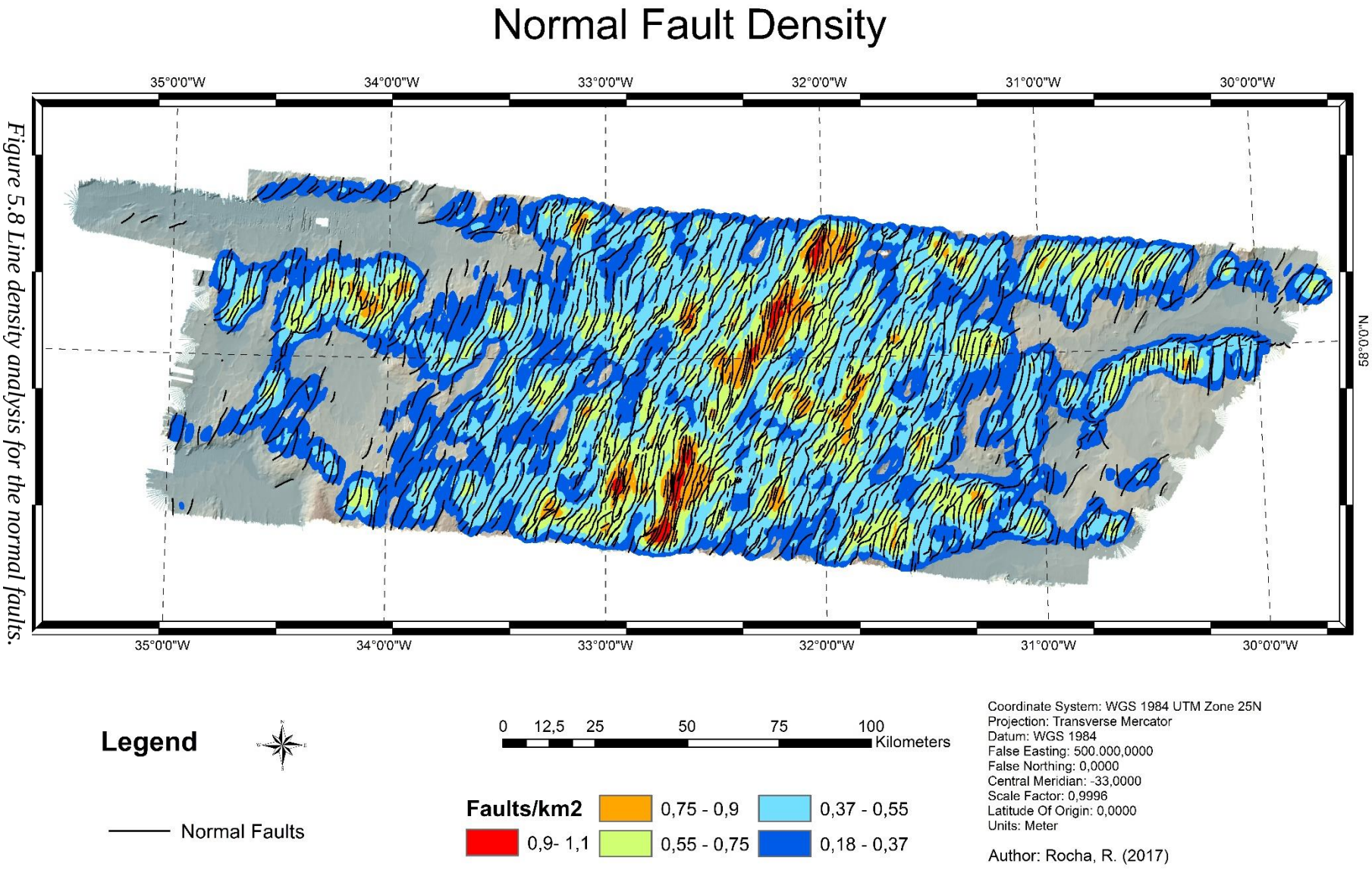

Figure 5.8 Line density analysis for the normal faults.

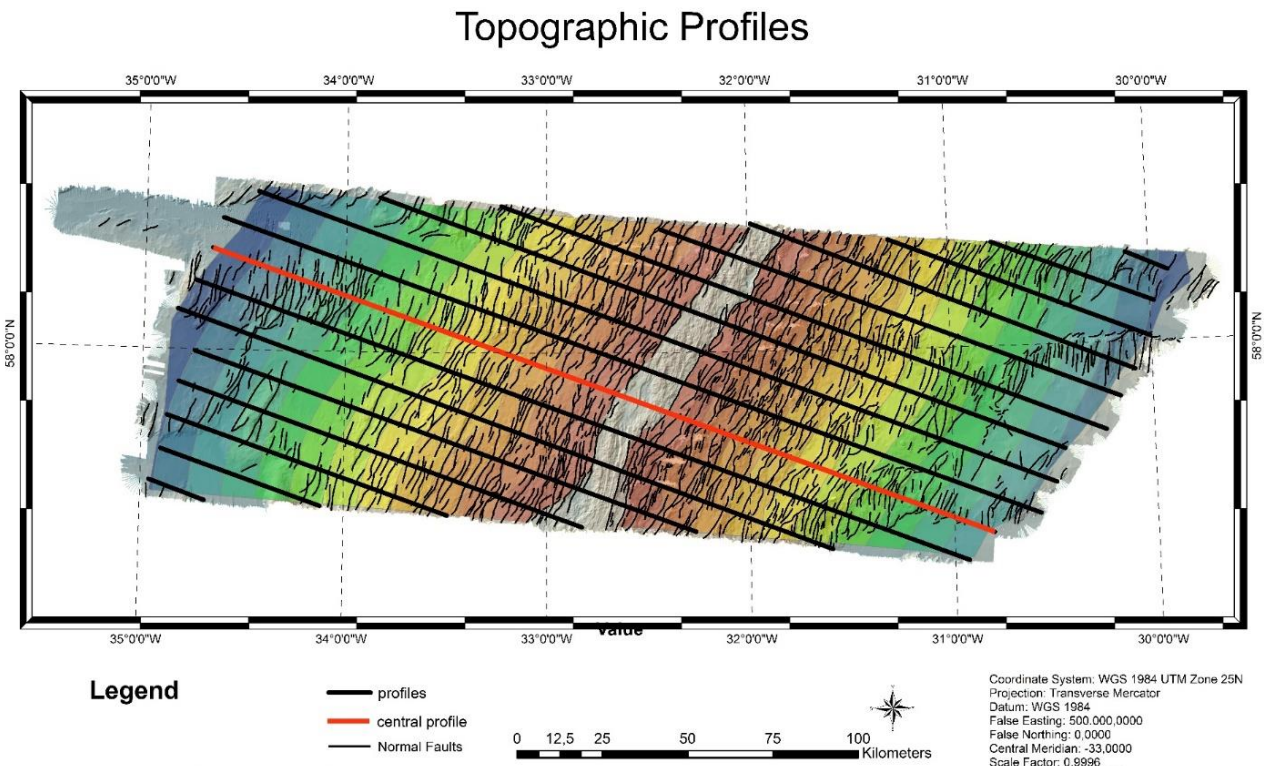

Figure 5.9 10 km buffer zones around the central valley (in gradual colours: red to blue), and topographic profiles (solid orthogonal black lines). The red line is the profile which examples are shown on the appendix.

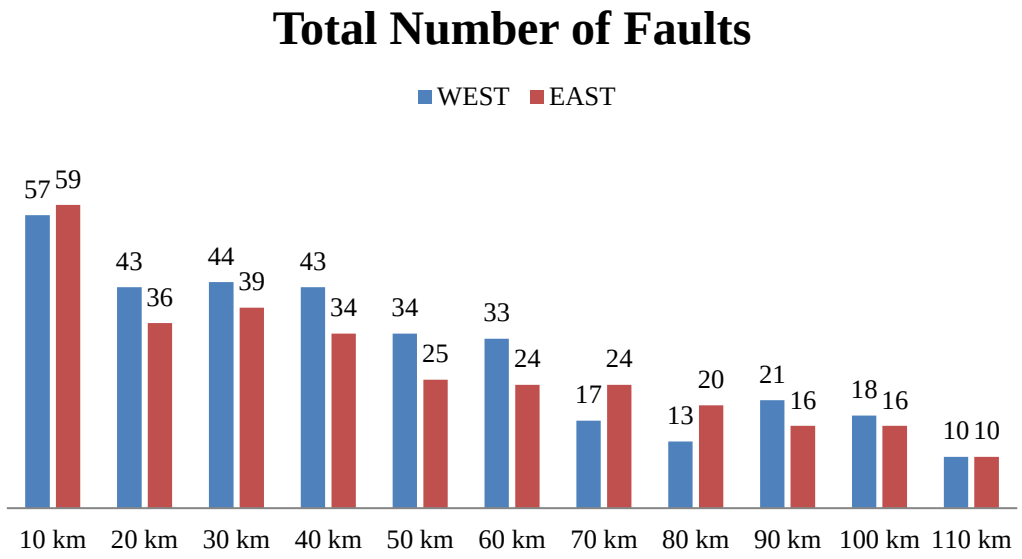

Figure 5.10 Total number of normal faults counted in each buffer zone. Blue bars represent the west province and red, the east.

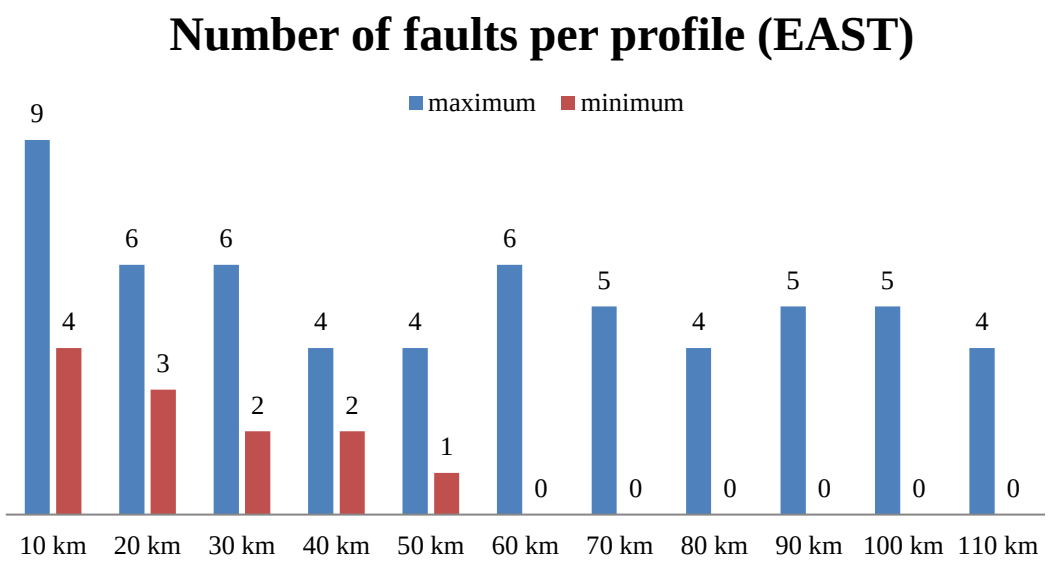

Figure 5.11 Number of faults per profile in the East province. Blue bars represent the maximum count and red bars are the minimum.

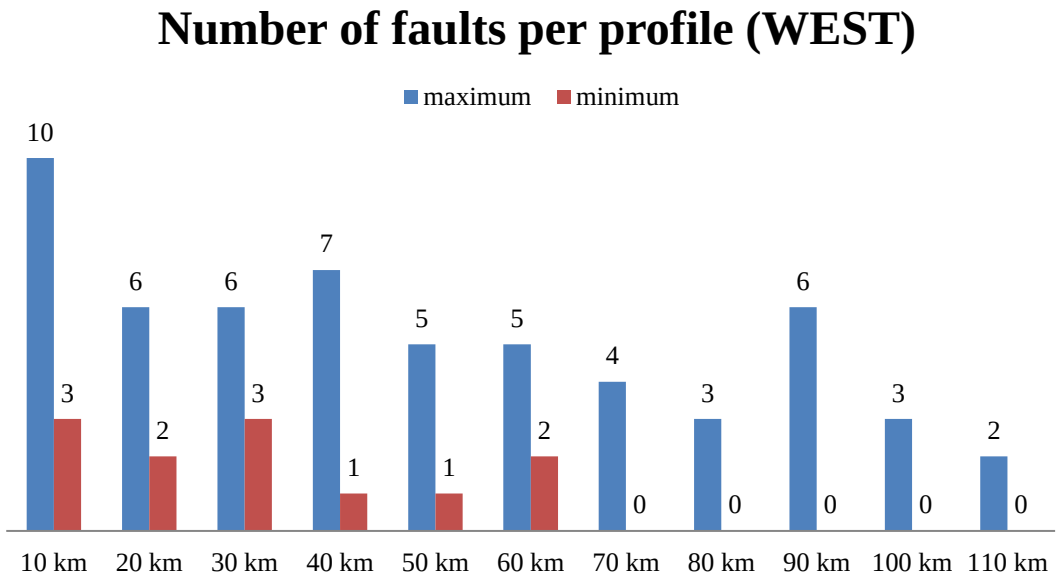

Figure 5.12 Number of faults per profile in the West province. Blue bars represent the maximum count and red bars are the minimum.

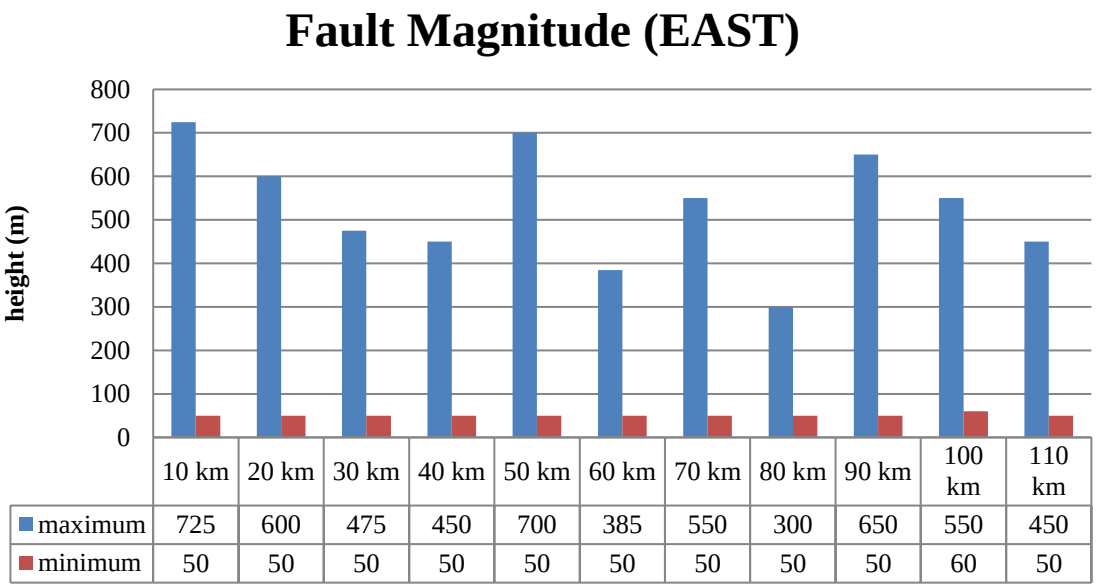

Figure 5.13 Fault height in the East province. Blue bars are the maximum height accounted and red bars are the minimum.

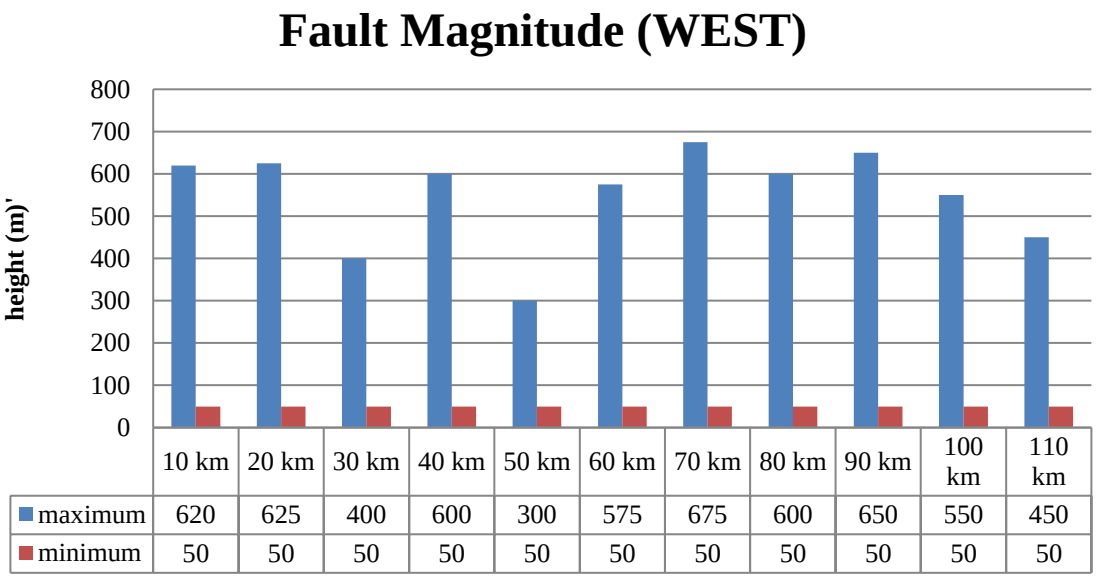

Figure 5.14 Fault heights in the West province. The blue bars are the maximum height accounted and red bars are the minimum.

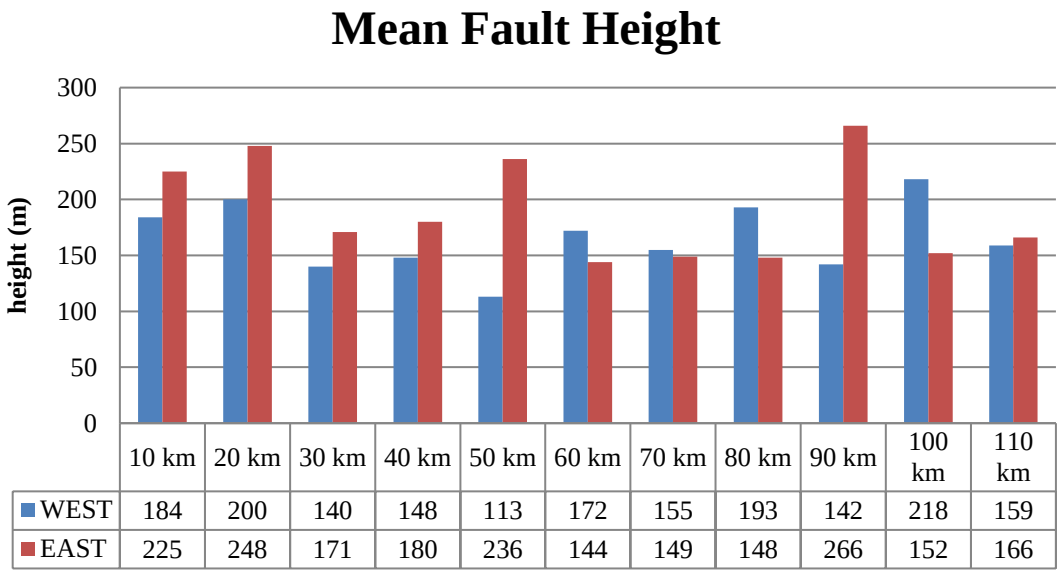

	10 km	20 km	30 km	40 km	50 km	60 km	70 km	80 km	90 km	100 km	110 km
WEST	184	200	140	148	113	172	155	193	142	218	159
EAST	225	248	171	180	236	144	149	148	266	152	166

Figure 5.15 Mean fault height per buffer zone. Blue bars represent west and red bars east.

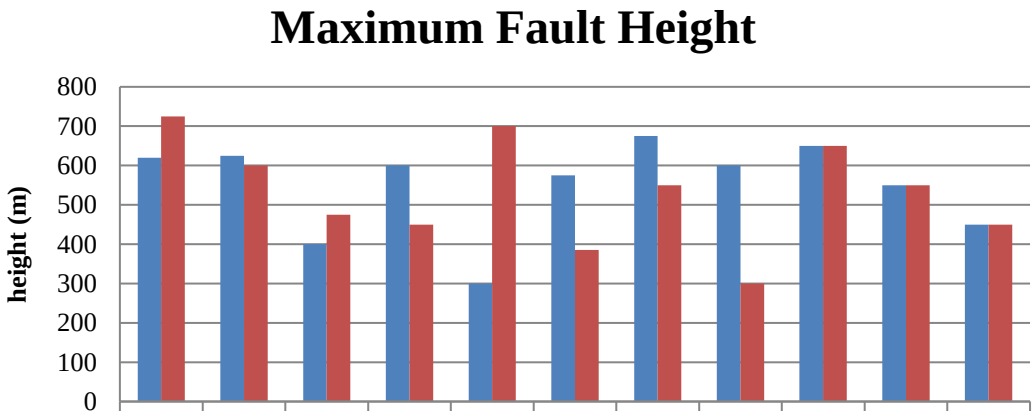

	10 km	20 km	30 km	40 km	50 km	60 km	70 km	80 km	90 km	100 km	110 km
WEST	620	625	400	600	300	575	675	600	650	550	450
EAST	725	600	475	450	700	385	550	300	650	550	450

5.3 Geological Orientation

Figure 5.16 Maximum fault height per buffer zone. Blue bars represent west and red bars east.

Figure 5.17 Fault strikes for the West province with summary statistics.

Figure 5.19 Faults strikes for the central valley with summary statistics.

Figure 5.20 Aspect map.

Figure 5.21 Slope map.

Figure 5.22 Dip/Strike map plotted over the estimated age of seafloor.

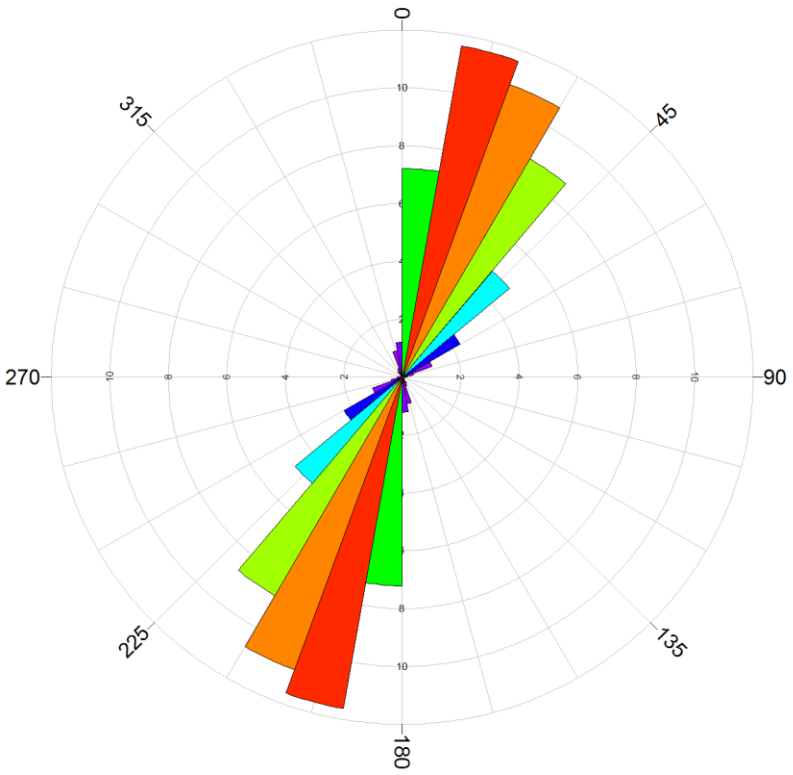

Rose Diagram

Statistical Summary

Calculation Method:	Length
Class Interval:	10.0 Degrees
Min.Length Filtering:	Deactivated
Max.Length Filtering:	Deactivated
Azimuth Filtering:	Deactivated
Data Type:	Bidirectional
Population:	6,403
Total Length of All Lineations:	8,839,142.38
Maximum Bin Population:	1,439.0
Mean Bin Population:	355.72
Standard Deviation of Bin Population:	502.02
Maximum Bin Population (%):	11.24
Mean Bin Population (%):	2.78
Standard Deviation of Bin Population (%):	3.92
Maximum Bin Length:	1,027,444.54
Mean Bin Length:	245,531.73
Standard Deviation of Bin Lengths:	348,408.88
Maximum Bin Length (%):	11.62
Mean Bin Length (%):	2.78
Standard Deviation of Bin Lengths (%):	3.94
Vector Mean:	23.8 Degrees
	203.84 Degrees
Confidence Interval:	0.6 Degrees
	(80 Percent)
R-mag:	0.81

Figure 5.17 Fault strikes for the West province with summary statistics.

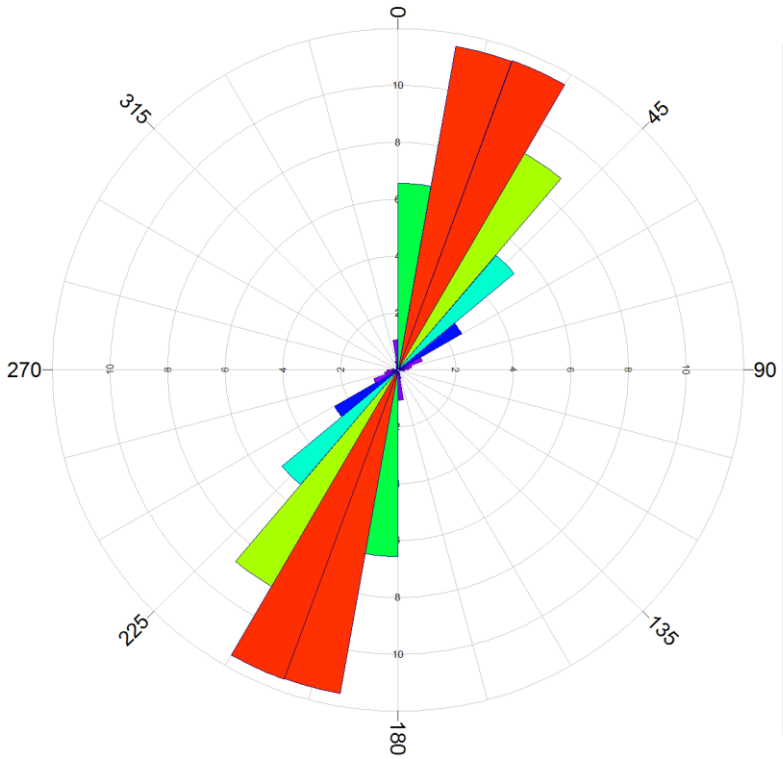

Rose Diagram

Statistical Summary

Calculation Method:	Length
Class Interval:	10.0 Degrees
Min.Length Filtering:	Deactivated
Max.Length Filtering:	Deactivated
Azimuth Filtering:	Deactivated
Data Type:	Bidirectional
Population:	5,392
Total Length of All Lineations:	8,809,147.19
Maximum Bin Population:	1,219.0
Mean Bin Population:	299.56
Standard Deviation of Bin Population:	425.49
Maximum Bin Population (%):	11.3
Mean Bin Population (%):	2.78
Standard Deviation of Bin Population (%):	3.95
Maximum Bin Length:	1,019,706.02
Mean Bin Length:	244,698.53
Standard Deviation of Bin Lengths:	355,813.15
Maximum Bin Length (%):	11.58
Mean Bin Length (%):	2.78
Standard Deviation of Bin Lengths (%):	4.04
Vector Mean:	25.5 Degrees
	205.52 Degrees
Confidence Interval:	0.6 Degrees
	(80 Percent)
R-mag:	0.82

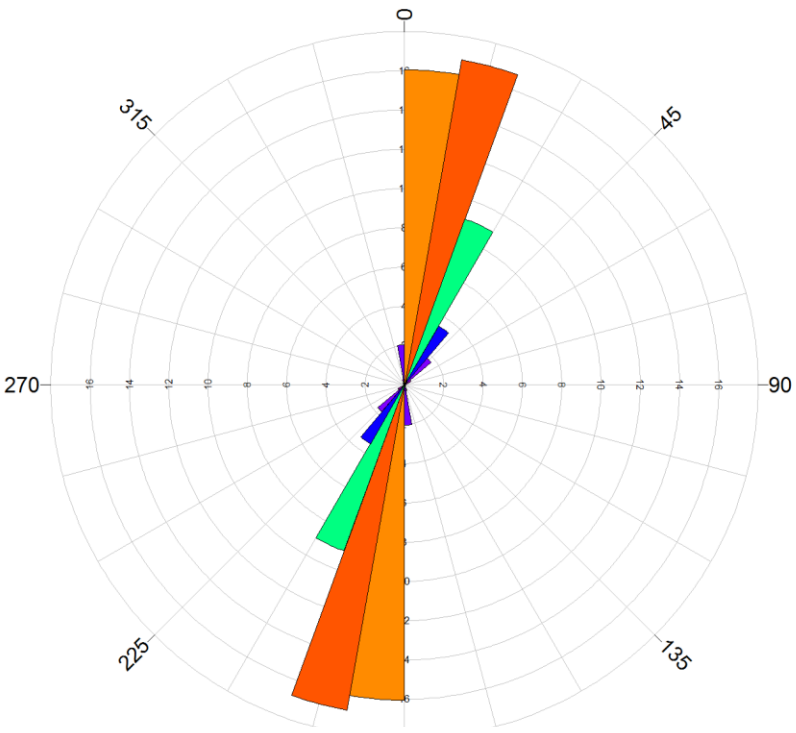

Rose Diagram

Statistical Summary	
Calculation Method:	Length
Class Interval:	10.0 Degrees
Min.Length Filtering:	Deactivated
Max.Length Filtering:	Deactivated
Azimuth Filtering:	Deactivated
Data Type:	Bidirectional
Population:	630
Total Length of All Lineations:	1,573,168.21
Maximum Bin Population:	212.0
Mean Bin Population:	63.0
Standard Deviation of Bin Population:	79.25
Maximum Bin Population (%):	16.83
Mean Bin Population (%):	5.0
Standard Deviation of Bin Population (%):	6.29
Maximum Bin Length:	264,373.12
Mean Bin Length:	78,658.41
Standard Deviation of Bin Lengths:	100,884.6
Maximum Bin Length (%):	16.81
Mean Bin Length (%):	5.0
Standard Deviation of Bin Lengths (%):	6.41
Vector Mean:	14.4 Degrees
	194.45 Degrees
Confidence Interval:	1.3 Degrees
	(80 Percent)

Figure 5.18 Fault strikes for the East province with summary statistics.

Figure 5.19 Faults strikes for the central valley with summary statistics.

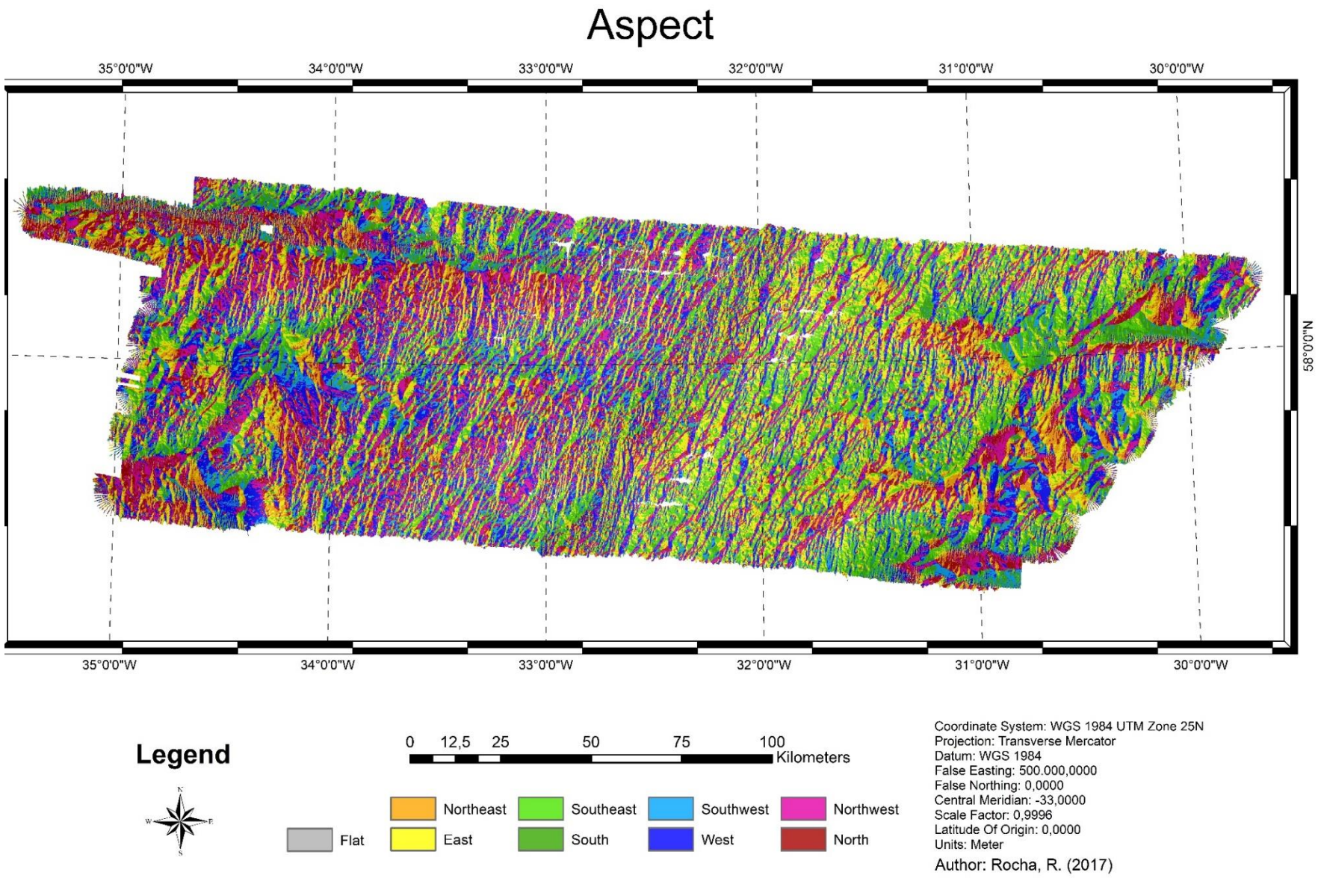

Figure 5.20 Aspect map

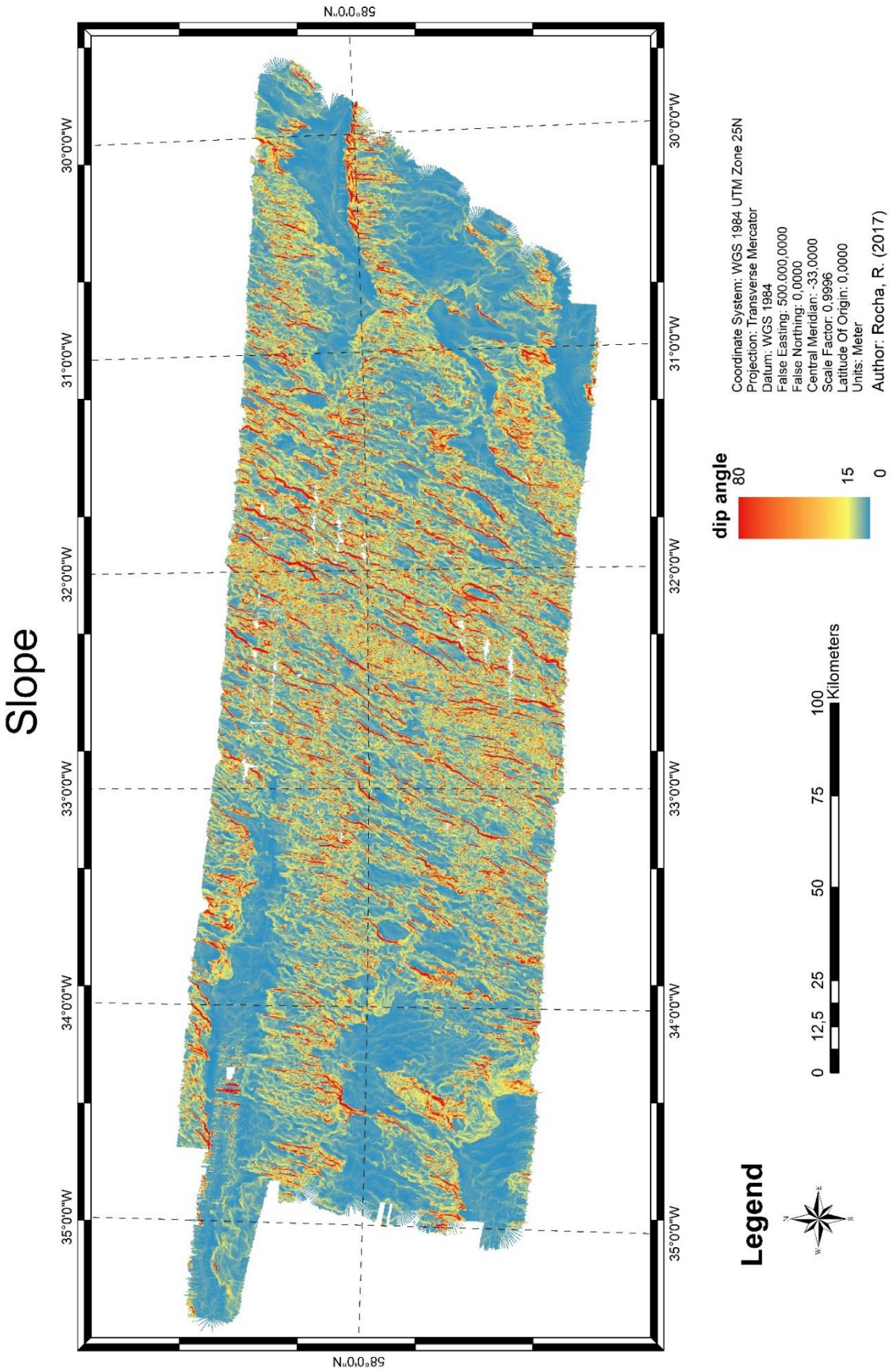

Figure 5.21 Slope map

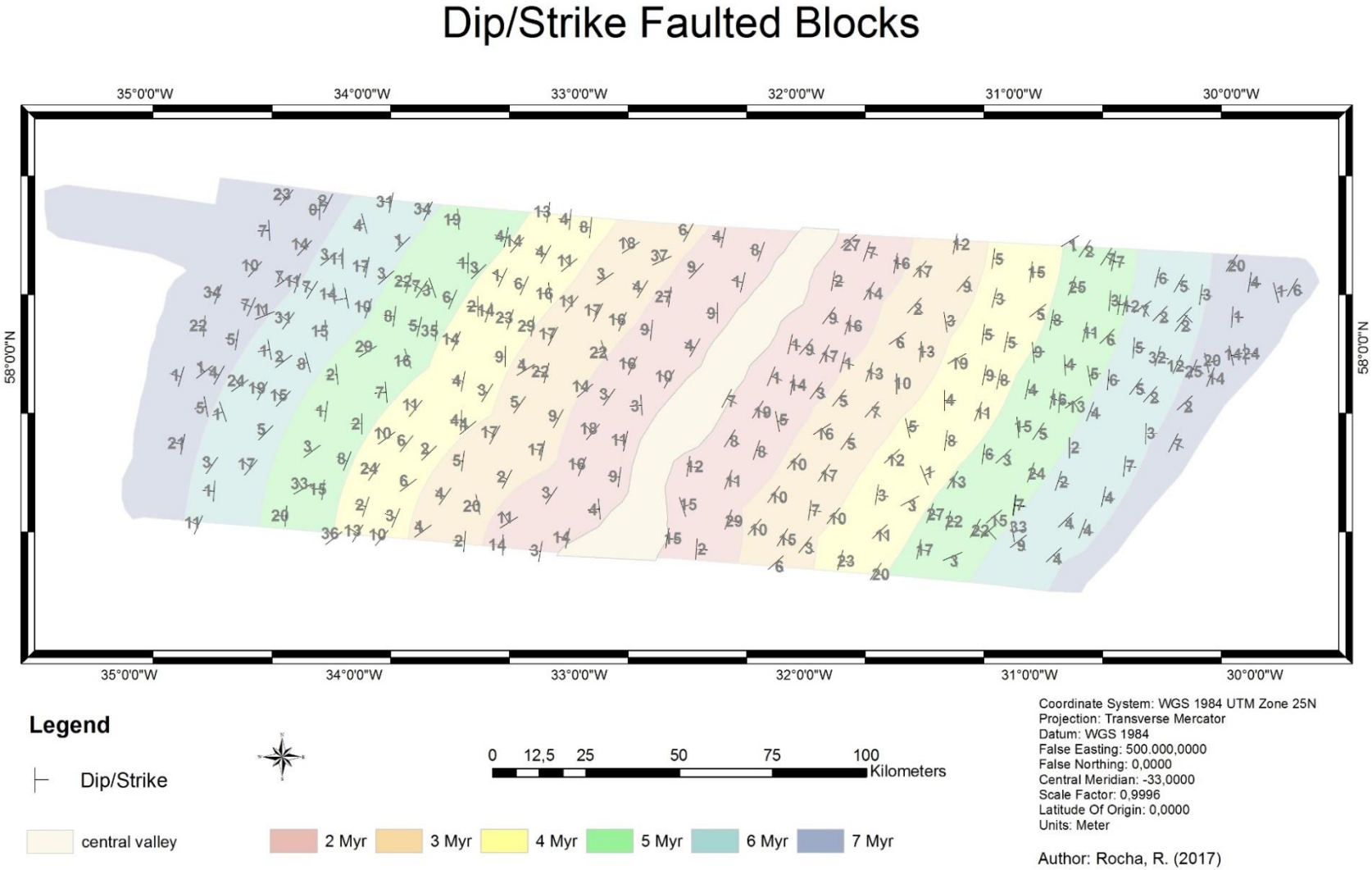

Figure 5.22 Dip/Strike map plotted over the estimated age of seafloor.

5.4 Changes on Seafloor Topography

Figure 5.23 is the resulting difference map between BRIDGE and EW9008/9004.

Figure 5.24 is the resulting difference map between MGL1309 and BRIDGE.

Figure 5.25 is the resulting difference map between MGL1309 and EW9008/9004.

With help of the contours on the change maps, it was possible to identify two areas of potential changes. The contour lines generated by them build up to a plausible geomorphologic shape and they are located in regions of possible volcanic activity or tectonism.

These features persist in both difference maps, although with some differences in area. These areas will be from now on referred to as AOI_1 and AOI_2 as a short for "area of interest".

Figure 5.26 Areas of potential change on seafloor topography (AOIs), with color shaded relief and contour lines plotted for 2 standard deviations.

Figure 5.27 AOIs, with contour lines on isobaths from the compared DEMs.

Figure 5.28 3D models of the AOI_1 in both BRIDGE and M. Ewing bathymetry (colors) overlaid on the MGL1309 bathymetry (grey). The AOI shape in each DEM and respective calculated area is also shown.

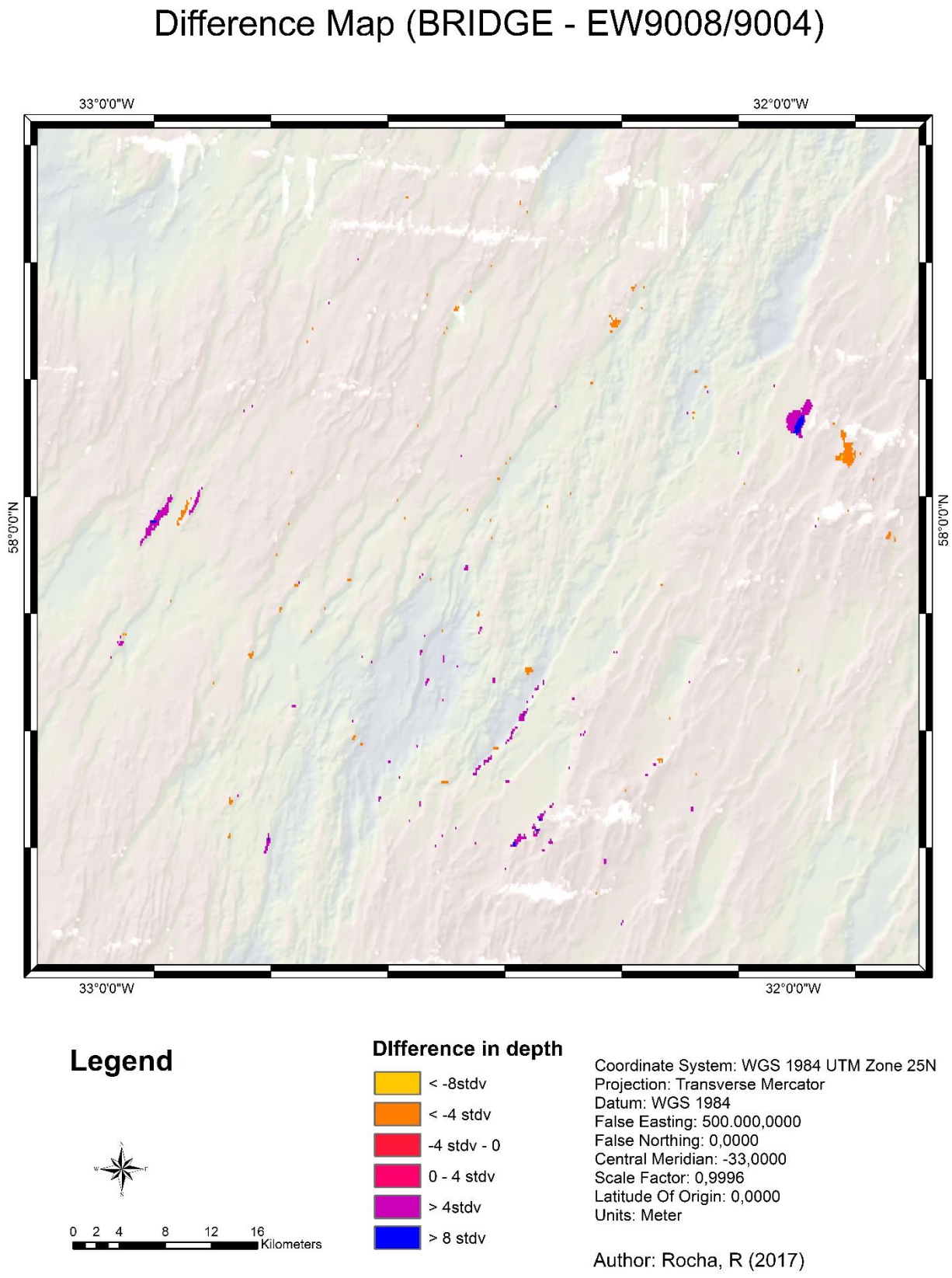

Figure 5.23 Difference map between BRIDGE and EW9008/9004

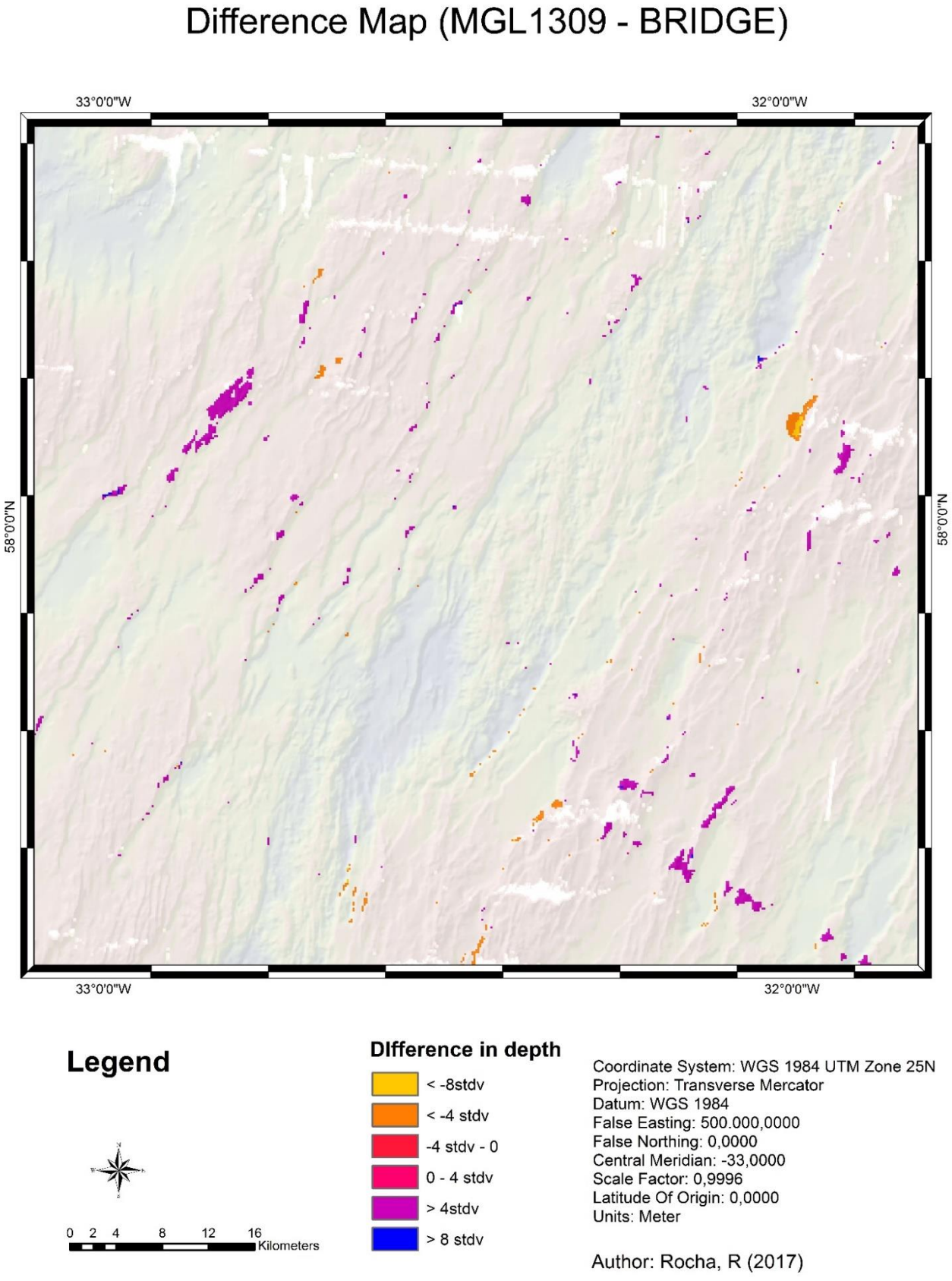

Figure 5.24 Difference map between MGL1309 and BRIDGE

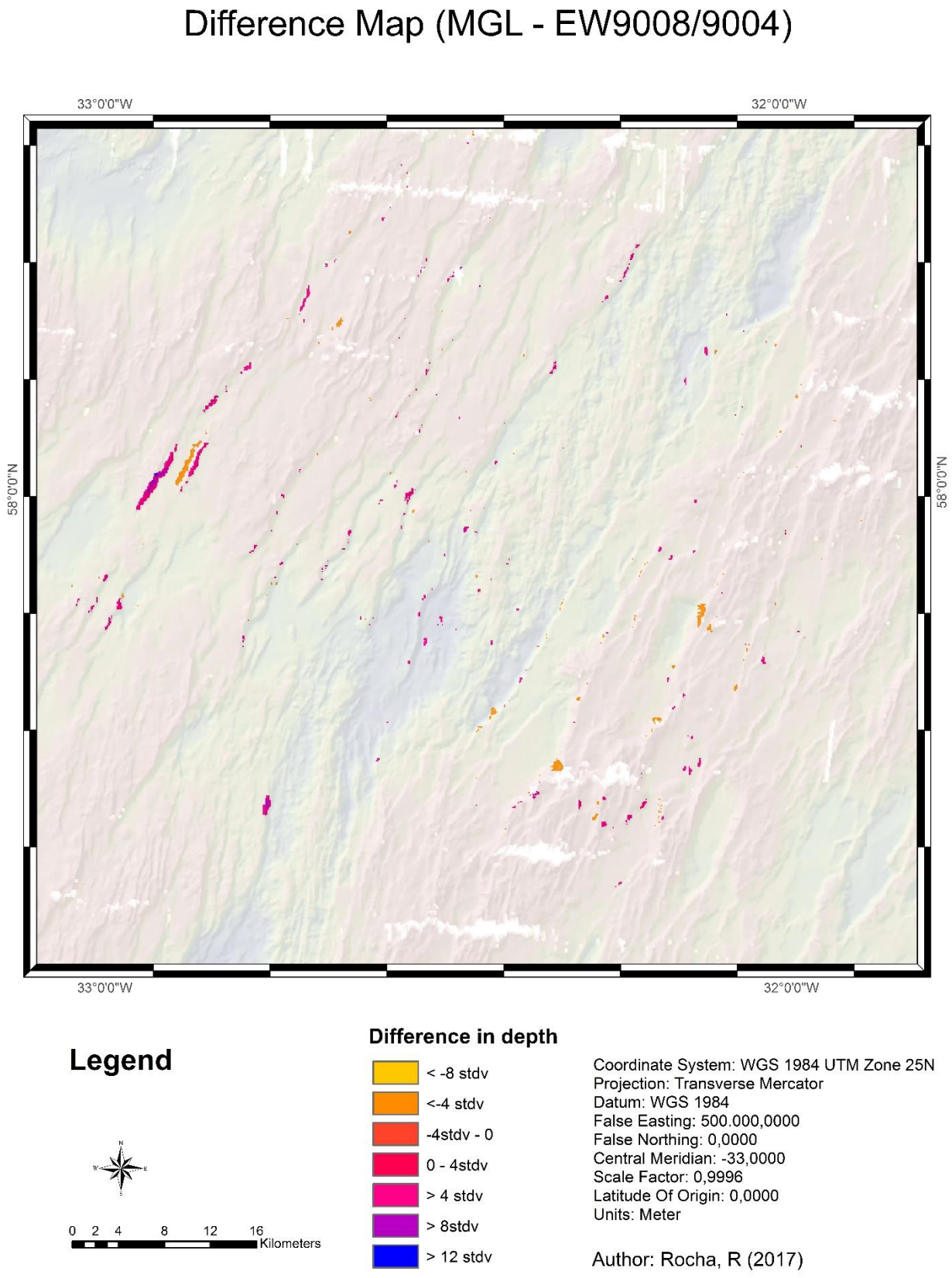

Figure 5.25 Difference map between MGL1309 and EW9008/9004

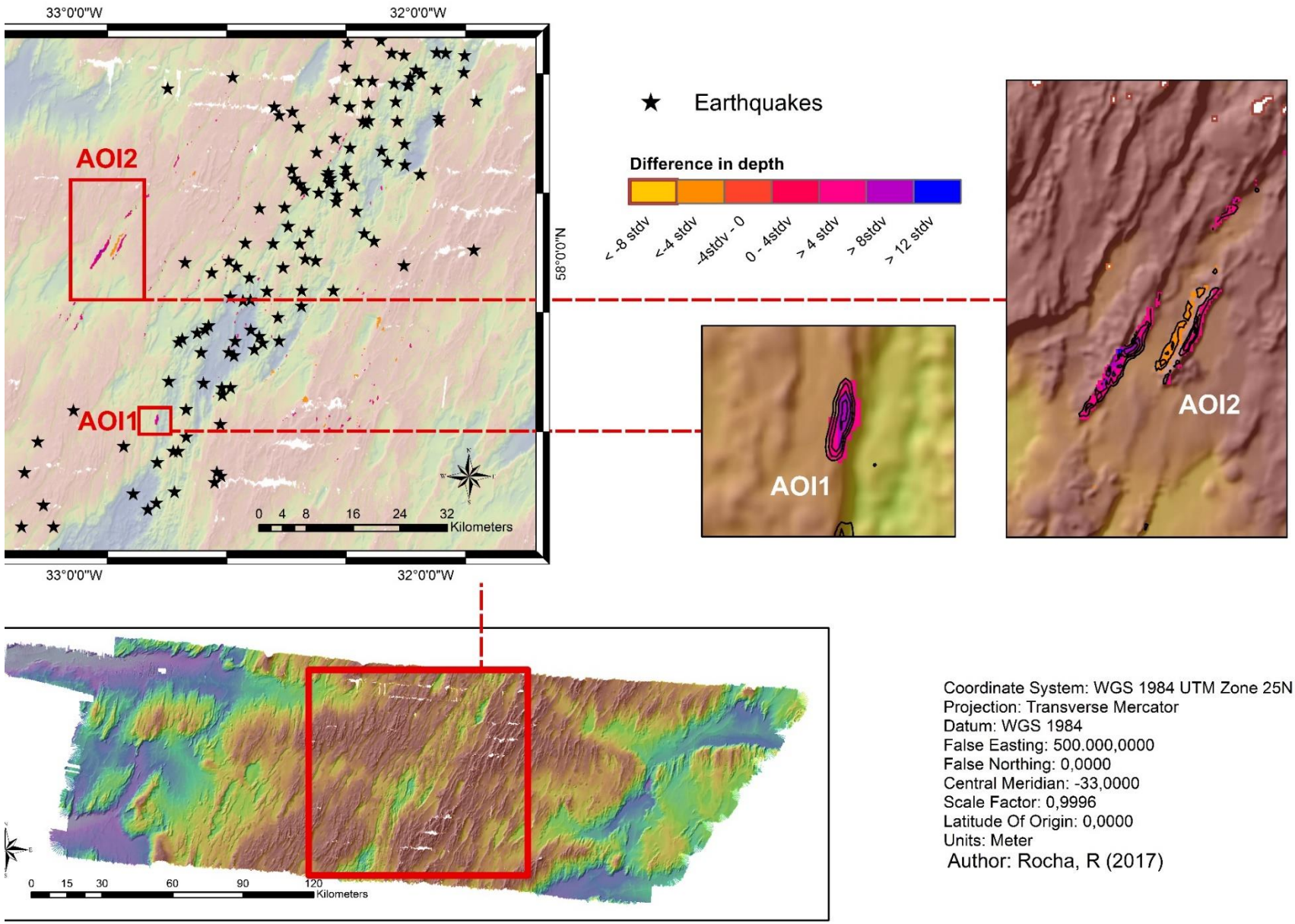

Figure 5.26 Areas of potential change on seafloor topography. Stars represent earthquake locations.

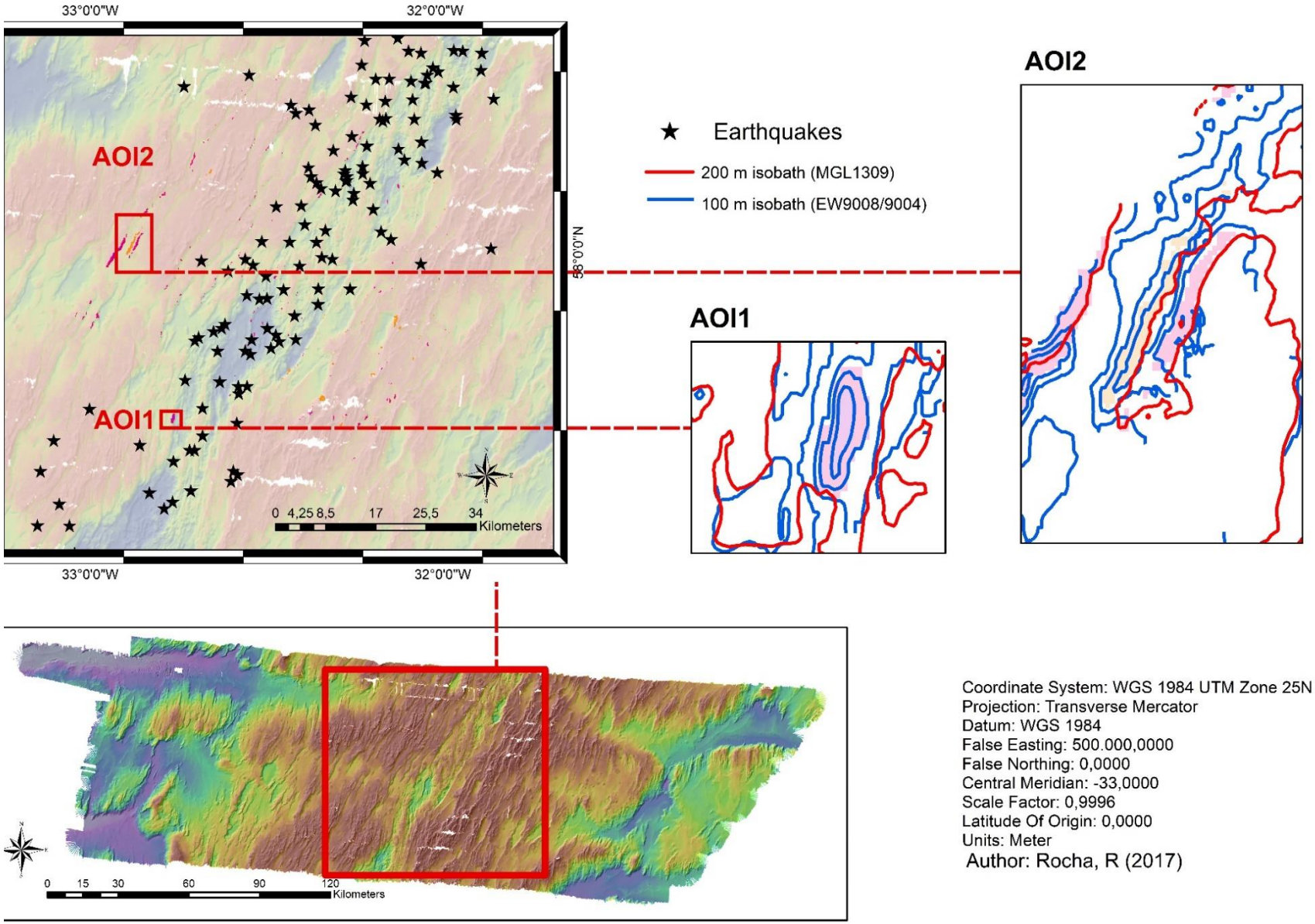

Figure 5.27 Areas of potential change on seafloor topography. Stars represent earthquake locations.

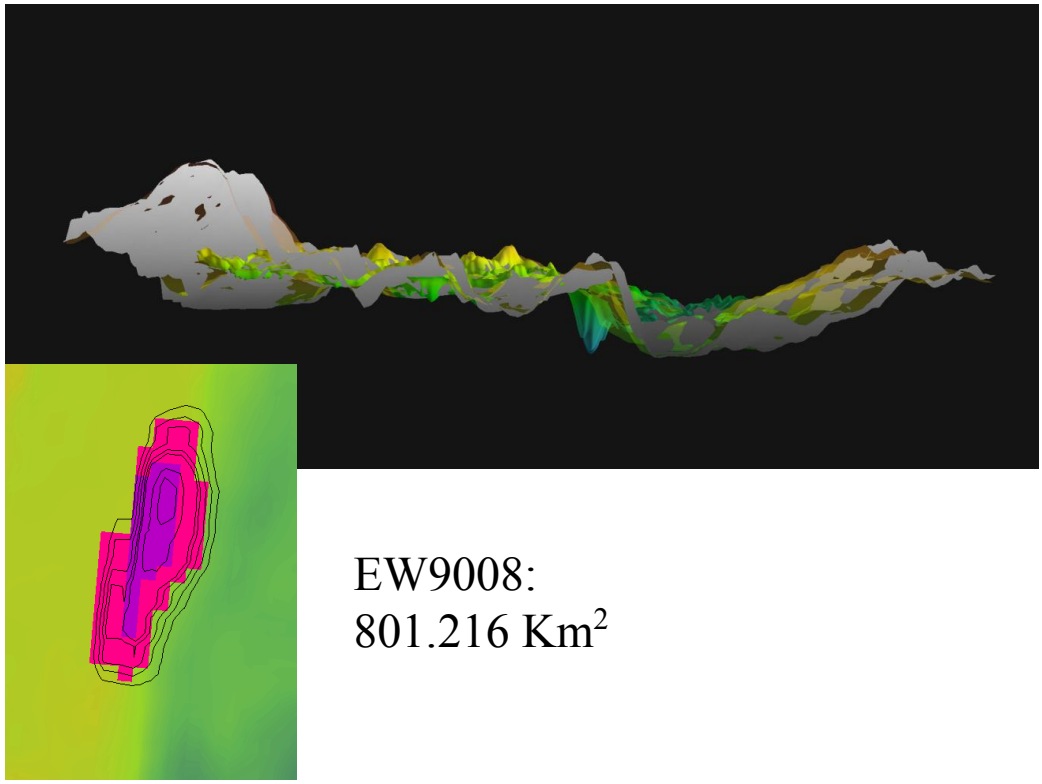

EW9008:
801.216 Km^2

BRIDGE:
102.514 Km^2

Figure 5.28 AOI$_1$ in EW9008/9004 (top) and in BRIDGE (bottom) with the respective 3D models of the compared DEMs: MGL1309 in grey and EW9008/9004 (top) and BRIDGE (bottom) in colors.

6 Discussion

6.1 Bathymetry

The study area is located near the southern end of the Reykjanes Ridge, where the ridge axial low transits to an axial high (Figures 5.1 & 5.2). It presents a few transform faults that were decoupled by the southward propagation of the v-shaped RR (Benediktsdóttir, Hey, Martinez & Wessel, 2011; Benediktsdóttir et al., 2016; Martinez, Hey, & Hoskuldsson, 2014). These faults are the deepest portions of the dataset, and present a generally flat appearance, interrupted by the eventual presence of what could be interpreted as sand dunes.

This ridge/transform staircase geometry was inherited from the second phase of evolution of the RR, between ~37 and ~34Ma (White, 1997). There are three decoupled transform faults crossing the study area, two of which were named by Vogt & Avery (1974) as *Morganore* and *Merlin* (Figure 2.12 Magnetic anomaly map with interpretation from Hey 2015. Solid horizontal lines are transform faults with names of from (Vogt & Avery, 1974). Dashed black lines with numbers (5,6,13) are the V-shaped diachrones of spreading. Numbers 15,18,21 and 24 represent the first evolutionary phase of orthogonal spreading. The white dashed line represents the tectonic boundary.). The unnamed transform fault, undetected by previous surveys, is located in between these two.

According to Hey et al., (2015) the third phase of the RR evolution, from ~34Ma to present, happened in pulses that caused the southward propagation to temporarily pause at ~22, ~18 and ~13Ma. This pauses happened over some transform faults, the last of which lasted for ~3 Ma at Morganore. As the ridge restarted propagating South at a speed of ~110 Km/Myr (Benediktsdóttir et al., 2012), Morganore got eliminated at ~10 Ma and Merlin at ~9 Ma.

Since the unnamed transform fault is in between those two, it can also be concluded that this was eliminated at ~9.5Ma. Currently, the southward propagation of the RR is eliminating the *Moodred* transform fault. Moodred is located to the South of the study area, and it had evolved to a non-transform offset (Hey et al., 2015).

The Abyssal Hills covering the West and East provinces are formed by back tilted faulted blocks, with the great majority of normal faults facing inwards to the tectonic boundary. The blocks of seafloor that intercalate the faults are the highest portions of the datasets, reaching a maximum depth of -720m in the East side. The analysis of normal faults magnitude and orientation will be presented in subchapter 6.2.

The East side is generally shallower than the West, or in other words, is where the abyssal hills are higher. Whole volcanoes can be found in the abyssal hills, even at long distances from the tectonic boundary. A few core complex massifs can also be observed, especially close to the transform faults.

The transition between axial valley and axial high at the RR happens just North of the study area, around ~58 N (Laughton et al., 1979). It is thus possible to notice that the Northern portion of the central graben on the study area is slightly higher than the Southern part (Figures 5.3 & 5.4). Further characteristics of the central valley will be discussion in the subchapter 6.1.1.

6.1.1 Central Valley

The central valley (Figures 5.4, & 5.5) is located over the tectonic boundary, and therefore it is represents the area of active volcanism. The depths of the central valley range from -1290m at spreading segment middles, to -2460m at segment ends. The main graben is in average 10-15km wide. Considering a spreading rate of 20km/Myr (DeMets et al., 2010), the age of this province if of ~500 to 750,000 years.

This central region presents a series of highly faulted en-echelon axial volcanic ridges (red in Figure 5.5), which strikes are orthogonal to the spreading direction (Parson et al., 1993). These AVRs are located at segment middles and represent areas where seafloor is created, thus presenting thicker crust than its surroundings. At least three AVRs can be found in the study area, being in average 20km long.

The formation of the AVRs is dominated by pillow lavas in fissure eruptions. In places where the magma supply is higher and the spreading speed is locally faster, the crust is stable enough to support volcanic seamounts (Macdonald, 2001). A total of 56 seamounts were mapped (Figure 5.6), with areas ranging from 47 to 1885km^2 (Appendix D)..

The lowest depths are reached by the volcanic seamounts that populate the AVRs. The deepest portions, on the other hand, are flatter areas with very little faulting, caused by magma starvation at segment ends (Macdonald, 2001; Macdonald & Atwater, 1978). These are areas present thinner crust and correspond to the latitude of the decoupled transform faults (blue in Figure 5.5).

6.2 Normal Faults

A total of 1440 normal faults were mapped in the area, being 100 in the central valley, 643 in the West and 697 in the East (Figure 5.7). From this total, 636 inward facing faults were sampled and analyzed, for measuring fault heights over 220 topographic profiles (Figure 5.9). Appendix F contains a sub-sample of 12 cross-sections over a central topographic profile sampled in the study area. Most of the faults face inwards; however, in the East it is possible to observe a few outward facing faults.

It is already possible to visualize on the line density map (Figure 5.8) that the central valley presents the highest concentration of normal faults, and that this concentration decreases with the distance to this central region. There are a few areas where the densities are locally higher (red in Figure 5.8). In the central valley, these areas correspond to the middle of spreading segments, where the AVRs are present. There are no normal faults on the transform faults, and the corresponding latitudes present lower fault densities throughout the whole study area.

In the West and East provinces, it is also possible to observe some higher density areas. Considering that, in the central valley, the areas of higher density occur over spreading segments, it can be suggested that, in the abyssal hills, they indicate ancient spreading segment middles.

The tables of Appendix C show the summary statistics for the count of faults per profile, buffer zone and provinces (East and West). The average, maximum and minimum number of faults found per profile and the total number of faults per buffer zone have a strong negative correlation with the distance from the tectonic boundary (Figures 5.10, 5.11 & 5.12)

The calculated correlation coefficient for the mean was of -0.94 (West) and -0.92 (East); for the maximum of -0.82 (West) and -0.63 (East) and of -0.94 (West) and -0.92(East) for the minimum count. These numbers prove that the number of faults decreases as the distance to the tectonic boundary increases.

The maximum measured fault height was of 725m, in a profile from the East side. The maximum height measured in the West was of 675m. From figures 5.13, 5.14, 5.15 and 5.16 it is possible to notice that the faults' magnitude does not seem to correlate very well with distance to the tectonic boundary. Very high faults can be found either closer or further away from the central valley, and the minimum sample height of 50m is consistent throughout the dataset. The correlation coefficients for mean was of -0.083 (West) and -0.36 (East) and for the maximum high of -0.0065(West) and -0.34 (East). These numbers show a very weak negative correlation, that is however stronger in the East side.

6.3 Geological Orientation

Figures 5.20, 5.21 & 5.22 show the results of the geological orientation analysis on maps. The statistical geological orientation of different features in the study area can be observed in the rose diagrams of Appendix G and Figures 5.17, 5.19 & 5.19.

The rose diagrams for normal faults in the abyssal hills (Figures 5.17 & 5.18) shows that normal fault strikes vary between 0° and 45°. The mean strike in the West is of 23.8° and in the East of 25.8°. The faults strikes over the AVRs in the central valley is clearly distinct, presenting a mean value of 14.4°.This distinction is resultant of the different tectonic origin of these provinces. The abyssal hills were formed on the second evolution phase of the RR, of orthogonal spreading. The central valley, on the other hand, is resultant from the third evolution phase, of southward propagation (Hey et al., 2015).

The Aspect map (Figure 5.20) shows that the dip directions are opposite for the East and West abyssal hills. The preferential dip direction in the West is N/NW and S/SE in the East, reflecting the back tilted faulted blocks that form these mountain ranges.

Close to the decoupled transform faults, in the West and East extremities and generally across the same latitudes throughout the study area, the terrain aspect is more variable. The rose diagrams of Appendix G reflect this variability. The aspect in the central valley is also very variable, as this region is of recent formation and not yet subjected to uplifting and rifting organization.

The Slope map (Figure 5.21) shows that the dip angles vary from a minimum of 0° at the transform faults and 80° at the normal faults. The faulted blocks in the Abyssal hills correspond to the intermediate dipping angles, oscillating around 15°. The rose diagrams of Appendix G show these results numerically. The dip/strike map from Figure 5.22 shows the dip angle values for points selected over the faulted blocks of the abyssal hills. It is possible to see that the dip angles vary between 5° and 35°.

6.4 Differences on Seafloor Topography

The comparison between the raster image from the Bridge project (Keeton et al., 1996) and the M. Ewing data (Figure 5.23) resulted in a couple of small differences. Considering that the M. Ewing data were part of the Bridge map, this differences can only have been originated by different processing methodology applied on these datasets.

The interpolation method is the most likely source of these differences. For the Bridge bathymetry map, data were processed and analyzed with the open software MB-system®, while this work used ArcGIS®. The interpolation algorithm used by these softwares might be slightly different. Distinct interpolation algorithms give different results (Arun, 2013; Chaplot et al., 2006; Šiljeg A., Lozic, S., 2015; Zhang et al., 2015) and therefore, when comparing maps that were processed differently, small differences are always expected.

As described by Keeton et al. (1996), the raw data had to be split in many smaller areas for processing. The individual files were then reintegrated after processing in order to create a continuous map. As much as this analysis was carried out with care for data quality, the computer power from the time was limited and error can be generated by splitting the data and later reintegrating it. The difference map between MGL3109 and Bridge shows clearly the locations where the data were split and re-integrated, as they form horizontal linear differences.

Furthermore, after downloading the raw data from the M. Ewing survey, it was acknowledged that the survey lines from the MBES did not overlap each other. In this work, differently than for the bridge bathymetry, the spaces in between, caused by this lack of overlap, were not interpolated. This interpolation is another potential source of inaccuracies on change detection analysis.

From the visual analysis of the potential sites of change (Figures 5.26 & 5.27), two areas of interest (AOIs) were detected to be more closely investigated. These areas are large and consistent in both difference maps, forming plausible bathymetric contours. Figure 5.26 shows the AOIs and its respective bathymetric contours and Figure 5.27 shows the AOIs with the isobaths of the compared DEMs. AOI_1 is located in the central valley, and if confirmed, would potentially represent a magmatic change. AOI_2 is located in the West Abyssal Hills, and if confirmed, would represent land uplift.

When investigating the three-dimensional model of AOI_2 in combination with the DEMs isobaths (Figure 5.27), it was easily noticed that this difference resulted from misplacement of bathymetric data. This displacement was most likely caused by differences on the navigation systems used by the RV M. Ewing and the RV M. G. Langseth. The navigation system used in 1990 was not integrated with the MBES acquisition, leading to some error in positioning. Therefore, this AOI was discarded and not considered on further analysis.

The three-dimensional model for AOI_2 (Figure 5.28) showed that this difference resulted from the presence of a deeper area in the M. Ewing data. This area was somehow covered in the newer survey. In the BRIDGE bathymetry, this area is also not so apparent, but nevertheless it is still present. The calculated area of change was of ~100km^2 in the BIRDGE bathymetry and of ~800km^2 in the M. Ewing bathymetry. This once more indicates that the algorithms used for interpolation of the bridge map, might have over-smoothed the data.

Considering that sedimentation in the area is very little, this is a highly unlikely cause of change. Another explanation would be a volcanic eruption or lava flow into the whole, filling it up in an abrupt event. However, the earthquake plot for this time interval do not show an earthquakes cluster around the area, therefore not proving the occurrence of a volcanic eruption. It is therefore difficult to tell if this change was indeed real, or a simple artifact from computational mistakes.

The analysis showed that with one exception, there were no significant changes on seafloor topography during the period between 1990 and 2013. The site of change does not appear as strong in the previously processed dataset by Keeton et al., (1996). Nevertheless, it has an arguably significant area to be completely discarded. It is however important to acknowledge that the use of previously processed data might have compromised this investigation.

7 Conclusions

Multibeam surveys allow bathymetric mapping and topographic analysis of the ocean floor. In this study, a selected area of the Southern Reykjanes Ridges was mapped and its main volcano tectonic characteristics were described. The general bathymetry consists of decoupled transform faults interrupted by a southward propagating central valley filled with en-echelon axial volcanic ridges. This central valley contains several volcanic seamounts and it is slightly higher in its northern region, as it starts to transition into the RR axial high.

The abyssal hills are formed by back tilted faulted blocks, which are slightly higher in the East side of the rift. The normal fault density decreases with increasing distance to the tectonic boundary. The normal faults' amplitude varies greatly throughout the dataset, without much apparent relation to its locations. The fault strikes in the abyssal hills (~20°) differ from the strikes in the central valley (~15°), as a result of the different tectonic origin of these provinces.

The preferential dip direction is of N/NW on the West and S/SW. This preference is weaker as the transform faults are approached. The dip angles vary between 80° in the normal faults and 0° in the transform faults, while the abyssal hills have dip angles varying around ~15°.

Older datasets were investigated for change detection analysis. Only one area showed consistent potential change during this investigation. However, due to the great differences in the datasets, it seems difficult to confirm the reliability of this result. Considering that volcanic eruptions at slow spreading ridges are not very often, it is sensible to conclude that there hadn't been any, in the area and time spam covered by this research.

References

Anderson, D. L. (1989). *Theory of the Earth*. Blackwell Scientific Publicationa.

Anderson, D. L. (2007). *New Theory of The Earth*. Cambridge University Press. Retrieved from http://old.geology.lnu.edu.ua/phis_geo/fourman/library-Earth/Cambridge University Press - New Theory Of The Earth - 2007.pdf

Appelgate, B., & Shor, A. N. (1994). The northern Mid-Atlantic and Reykjanes Ridges: Spreading center morphology between 55°50′N and 63°00′N. *Journal of Geophysical Research: Solid Earth*, *99*(B9), 17935–17956. http://doi.org/10.1029/93JB03459

Arun, P. V. (2013). A comparative analysis of different DEM interpolation methods. *The Egyptian Journal of Remote Sensing and Space Science*, *16*(2), 133–139. http://doi.org/10.1016/j.ejrs.2013.09.001

Ásdís Benediktsdóttir, B., Hey, R., & Fernando Martinez Paul Wessel, C. (2011). DETAILED TECTONIC EVOLUTION OF THE REYKJANES RIDGE DURING THE PAST 15 MA USING MAGELLAN, A NEW TOOL FOR MODELING MAGNETIC ANOMALIES. Retrieved from https://www.soest.hawaii.edu/GG/resources/theses/MS_2011_Benediktsdottir.pdf

Banul, K. (2014). Bathymetry of Reykjanes Ridge : A methodological approach, (June), 95. Retrieved from http://hdl.handle.net/1946/18739

Bartholomew, J. G. (1922). http://www.davidrumsey.com. Retrieved May 5, 2017, from http://www.davidrumsey.com/luna/servlet/detail/RUMSEY~8~1~3059~430018:World---bathy-orographical-?qvq=q:author%3D%22Bartholomew%2C%2BJ.%2BG.%2B(John%2BGeorge)%2C%2B1860-1920%22;lc:RUMSEY~8~1&mi=6&trs=137#

Beaulieu, S. E., Baker, E. T., & German, C. R. (2015). Where are the undiscovered hydrothermal vents on oceanic spreading ridges? http://doi.org/10.1016/j.dsr2.2015.05.001

Behn, M. D., & Ito, G. (2008). Magmatic and tectonic extension at mid-ocean ridges: 1. Controls on fault characteristics. *Geochem. Geophys. Geosyst*, *9*(8), 8–10. http://doi.org/10.1029/2008GC001965

Behn, M. D., Lin, J., & Zuber, M. T. (2002). Mechanisms of normal fault development at mid-ocean ridges. *JOURNAL OF GEOPHYSICAL RESEARCH*, *107*(B4). http://doi.org/10.1029/2001JB000503

Benediktsdóttir, Á., Hey, R., Martinez, F., & Hskuldsson, Á. (2012). Detailed tectonic evolution of the Reykjanes Ridge during the past 15 Ma. *Geochemistry, Geophysics, Geosystems*, *13*(2). http://doi.org/10.1029/2011GC003948

Benediktsdóttir, Hey, R., Martinez, F., & Hoskuldsson, A. (2016). A new kinematic model of the Mid-Atlantic Ridge between 55??55'N and the Bight Transform Fault for the past 6 Ma. *Journal of Geophysical Research B: Solid Earth*, *121*(2), 455–468. http://doi.org/10.1002/2015JB012504

Bjørnø, L. (2017a). Chapter 10 – Sonar Systems. In *Applied Underwater Acoustics* (pp. 587–742). http://doi.org/10.1016/B978-0-12-811240-3.00010-2

Bjørnø, L. (2017b). Chapter 10 – Sonar Systems. http://doi.org/10.1016/B978-0-12-811240-3.00010-2

Buchanan, J. L., Gilbert, R. P., Wirgin, A., & Xu, Y. S. (2004). *Marine Acoustics - Direct and Inverse Problems*.

Buck, W. R. (1998). *Faulting and magmatism at mid-ocean ridges*. American Geophysical Union.

Buck, W. R., Lavier, L. L., & Poliakov, A. N. B. (2005). Modes of faulting at mid-ocean ridges. *Nature*, *434*(7034), 719–723. http://doi.org/10.1038/nature03358

Calmant, S., Berge-Nguyen, M., & Cazenave, A. (2002). Global seafloor topography from a least-squares inversion of altimetry-based high-resolution mean sea surface and shipboard soundings. *Geophysical Journal International*, *151*(3), 795–808. http://doi.org/10.1046/j.1365-246X.2002.01802.x

Cann, J. (n.d.). BRIDGE: full text only version. Retrieved May 7, 2017, from http://www.southampton.ac.uk/~jtc/fierydeep.html

Cann, J., & Smith, D. (1994). Volcanoes of the mid-ocean ridges and the building of new oceanic crust. *Endeavour*, *18*(2), 61–66. http://doi.org/10.1016/0160-9327(94)90064-7

Carbotte, S., Welch, S. M., & Macdonald, K. C. (1991). Spreading Rates, Rift Propagation, and Fracture Zone Offset Histories during the Past 5 my on the Mid-Atlantic Ridge; 25-27.3S and 31-34.3S. *Marine Geophysical Researches*, *13*, 51–80.

Chaplot, V., Darboux, F., Bourennane, H., Leguédois, S., Silvera, N., & Phachomphon, K. (2006). Accuracy of interpolation techniques for the derivation of digital elevation models in relation to landform types and data density. *Geomorphology*, *77*(1), 126–141. http://doi.org/10.1016/j.geomorph.2005.12.010

Coffin, M. F., & Whittaker, J. M. (2016). Intraplate Magmatism. *Encyclopedia of Marine Geosciences*, 1–961. http://doi.org/10.1007/978-94-007-6644-0

Condie, K. C. (1976). *Palte Tectonics and Crustal Evolution* (4th ed.). Butterwoth-Heinemann. Retrieved from http://onlinelibrary.wiley.com/doi/10.1002/cbdv.200490137/abstract

Cowie, P. A. (1998). Normal fault growth in three-dimensions in continental and oceanic crust (pp. 325–348). http://doi.org/10.1029/GM106p0325

Dekov, V. M., Petersen, S., Garbe-Schönberg, C.-D., Kamenov, G. D., Perner, M., Kuzmann,

E., & Schmidt, M. (2010). Fe–Si-oxyhydroxide deposits at a slow-spreading centre with thickened oceanic crust: The Lilliput hydrothermal field (9°33′S, Mid-Atlantic Ridge). http://doi.org/10.1016/j.chemgeo.2010.09.012

DeMets, C., Gordon, R. G., & Argus, D. F. (2010). Geologically current plate motions. *Geophysical Journal International*, *181*(1), 1–80. http://doi.org/10.1111/j.1365-246X.2009.04491.x

Dierssen, H. M., & Theberge, A. E. (2014). Bathymetry: History of Seafloor Mapping. *Encyclopedia of Natural Resources*. http://doi.org/10.1081/E-ENRW-120047531

ESRI. (2017). Documentation | ArcGIS Desktop. Retrieved May 6, 2017, from http://desktop.arcgis.com/en/documentation/

Ganju, N. K., Suttles, S. E., Beudin, A., Nowacki, D. J., Miselis, J. L., & Andrews, B. D. (2017). Quantification of Storm-Induced Bathymetric Change in a Back-Barrier Estuary. *Estuaries and Coasts*, *40*(1), 22–36. http://doi.org/10.1007/s12237-016-0138-5

Garcia, R. A., Fearns, P. R. C. S., & McKinna, L. I. W. (2014). Detecting trend and seasonal changes in bathymetry derived from HICO imagery: A case study of Shark Bay, Western Australia. *Remote Sensing of Environment*, *147*, 186–205. http://doi.org/10.1016/j.rse.2014.03.010

German, C. R., Briem, J., Chin, C., Danielsen, M., Holland, S., James, R., … Rudnicki, M. D. (1994). Hydrothermal activity on the Reykjanes Ridge: the Steinahóll vent-field at 63°06′N. *Earth and Planetary Science Letters*, *121*(3–4), 647–654. http://doi.org/10.1016/0012-821X(94)90098-1

German, C. R., & Parson, L. M. (1998). Distributions of hydrothermal activity along the Mid-Atlantic Ridge: interplay of magmatic and tectonic controls. *Earth and Planetary Science Letters*, *160*, 327–341.

German, C. R., Parson, L. M., Murton, B. J., & Needham, H. D. (n.d.). Hydrothermal activity and ridge segmentation on the Mid-Atlantic Ridge: a tale of two hot-spots? Retrieved from http://citeseerx.ist.psu.edu/viewdoc/download?doi=10.1.1.1030.8694&rep=rep1&type=pdf

German, C. R., Parson, L. M., Murton, B. J., & Needham, H. D. (1996). Hydrothermal activity and ridge segmentation on the Mid-Atlantic Ridge: a tale of two hot-spots? Retrieved from http://citeseerx.ist.psu.edu/viewdoc/download?doi=10.1.1.1030.8694&rep=rep1&type=pdf

German, C. R., Petersen, S., & Hannington, M. D. (2016). Hydrothermal exploration of mid-ocean ridges: Where might the largest sulfide deposits be forming? *Chemical Geology*, *420*, 114–126. http://doi.org/10.1016/j.chemgeo.2015.11.006

Gille, S. T., Metzger, J. E., & Tokmakian, R. (2004). Seafloor Topography and Ocean Circulation. *Oceanography*, *17*(Special Issue—Bathymetry from Space), 47–54.

Goud, M. R., & Karson, J. A. (1985). Tectonics of short-offset, slow-slipping transform zones in the FAMOUS area, Mid-Atlantic Ridge. *Marine Geophysical Researches*, *7*(4), 489–514. http://doi.org/10.1007/BF00368952

Hekinian, R. (2014). *Sea Floor Exploration*. Springer Oceanography. http://doi.org/10.1007/978-3-319-03203-0_5

Hey, R., Martinez, F., Höskuldsson, Á., & Benediktsdóttir, Á. (2010). Propagating rift model for the V-shaped ridges south of Iceland. *Geochem. Geophys. Geosyst*, *11*. http://doi.org/10.1029/2009GC002865

Hey, R., Martinez, F., Höskuldsson, Á., Eason, D. E., Sleeper, J., Thordarson, S., … Merkuryev, S. (2015). Multibeam investigation of the active North Atlantic plate boundary reorganization tip. *Earth and Planetary Science Letters*, *435*, 115–123. http://doi.org/10.1016/j.epsl.2015.12.019

Höskuldsson, Á., Hey, R., Kjartansson, E., & Guðmundsson, G. B. (2007). The Reykjanes Ridge between 63°10′N and Iceland. *Journal of Geodynamics*, *43*(1), 73–86. http://doi.org/10.1016/j.jog.2006.09.003

ITC. (2012). *The core of GIScience: a systems-based approach*. The International Institute for Geo-Information Science and Earth Observation (ITC).

Jain, S. (2014). *Fundamentals of Physical Geology*. Springer. http://doi.org/10.1007/978-81-322-1539-4

Jones, S. M. (2003). Test of a ridge–plume interaction model using oceanic crustal structure around Iceland. *Earth and Planetary Science Letters*, *208*(3–4), 205–218. http://doi.org/10.1016/S0012-821X(03)00050-5

Jones, S. M., White, N., Maclennan, J., Jones, S., White, N., & Maclennan, J. (2002). V-shaped ridges around Iceland: Implications for spatial and temporal patterns of mantle convection. *Geochem. Geophys. Geosyst*, *3*(10). http://doi.org/10.1029/2002GC000361

Keeton, J. A., Searle, R. C., Peirce, C., Parsons, B., White, R. S., Sinha, M. C., … Parson, L. M. (1996a). Bathymetry of the Reykjanes Ridge. *Marine Geophysical Researches*, *15*, 55–64.

Keeton, J. A., Searle, R. C., Peirce, C., Parsons, B., White, R. S., Sinha, M. C., … Parson, L. M. (1996b). Bathymetry of the Reykjanes Ridge. *Marine Geophysical Researches*, *19*(1), 55–64. http://doi.org/10.1023/A:1004266721393

Langmuir, C. H., & Forsyth, Do. W. (2007). Mantle Melting Beneath Mid-Ocean Ridges. *Oceanography*, *20*(1), 78–89.

Laughton, A. S., Searle, R. C., & Roberts, D. G. (1979). The Reykjanes Ridge Crest and the Transition between its rifted and non-rifted regions. *Tectonophysics*, *55*, 173–177.

Lawrence, D. M. (2009). Oceanographic Mapping. *International Encyclopedia of Human Geography*, *1*, 14–20. Retrieved from

http://www.elsevier.com/locate/permissionusematerial

Lizarralde, D., Gaherty, J. B., Collins, J. A., Hirth, G., & Kim, S. D. (2004). Spreading-rate dependence of melt extraction at mid-ocean ridges from mantle seismic refraction data. *Nature*, *432*. Retrieved from http://www.ipgp.jussieu.fr/~singh/download/Ocean_litho/papers/Lisarralde_etal_Nature_2004.pdf

Lu, D., Mausel, P., Brondínios, E., & Moran, E. (2003). Change detection techniques. *International Journal of Remote Sensing*, *25*(12), 2365–2407. http://doi.org/10.1080/0143116031000139863

Macdonald, K. C. (1998). Linkages between faulting, volcanism, hydrothermal activity and segmentation on fast spreading centers (pp. 27–58). http://doi.org/10.1029/GM106p0027

Macdonald, K. C. (2001). MID-OCEAN RIDGE TECTONICS, VOLCANISM, AND GEOMORPHOLOGY. *Encyclopedia of Marine Geosciences*, *3*, 1798–1813.

Macdonald, K. C., & Atwater, T. M. (1978). EVOLUTION OF RIFTED OCEAN RIDGES. *Earth and Planetary Science Letters*, *39*, 319–327.

Macleod, C. J., Searle, R. C., Murton, B. J., Casey, J. F., Mallows, C., Unsworth, S. C., … Harris, M. (2009). Life cycle of oceanic core complexes. *Earth and Planetary Science Letters*, *287*, 333–344. http://doi.org/10.1016/j.epsl.2009.08.016

Martinez, F., & Hey, R. (2017). Propagating buoyant mantle upwelling on the Reykjanes Ridge. *Earth and Planetary Science Letters*, *457*, 10–22. http://doi.org/10.1016/j.epsl.2016.09.057

Martinez, F., Hey, R., & Hoskuldsson, A. (2014). Reykjanes Ridge evolution and the elimination of transform faults in the North Atlantic. *Geophysical Research Abstracts EGU General Assembly*, *16*, 2014–9939. Retrieved from http://meetingorganizer.copernicus.org/EGU2014/EGU2014-9939.pdf

McAllister, E., Cann, J., & Spencer, S. (1995). The evolution of crustal deformation in an oceanic extensional environment. *Journal of Structural Geology*, *17*(2), 183–199. http://doi.org/10.1016/0191-8141(94)E0043-X

Medwin, H., & Clay, C. S. (1998). *Fundamentals of Acoustical Oceanography*. Academic Press.

Miller, P. I., Read, J. F., & Dale, A. C. (2013). Thermal front variability along the North Atlantic Current observed using microwave and infrared satellite data. *Deep Sea Research Part II: Topical Studies in Oceanography*, *98*, 244–256. http://doi.org/10.1016/j.dsr2.2013.08.014

Muller, R. D., Roest, W. R., Royer, J.-Y., Gahagan, L. M., & Sclater, J. G. (1997). Digital ishochrons of the world's ocean floor. *Journal of Geophysical Research*, *102*, 3211–3214.

Müller, R. D., Sdrolias, M., Gaina, C., & Roest, W. R. (2008). Age, spreading rates, and spreading asymmetry of the world's ocean crust. *Geochemistry, Geophysics, Geosystems*. http://doi.org/10.1029/2007GC001743

Multibeam Sonar Theory of Operation. (n.d.). Retrieved from https://www.ldeo.columbia.edu/res/pi/MB-System/sonarfunction/SeaBeamMultibeamTheoryOperation.pdf

Murton, B. J., & Parson, L. M. (1993). Segmentation, volcanism and deformation of oblique spreading centres: A quantitative study of the Reykjanes Ridge. *Tectonophysics*, *222*(2), 237–257. http://doi.org/10.1016/0040-1951(93)90051-K

Murton, B. J., & Rona, P. A. (2015). Carlsberg Ridge and Mid-Atlantic Ridge: Comparison of slow spreading centre analogues. *Deep Sea Research Part II: Topical Studies in Oceanography*, *121*, 71–84. http://doi.org/10.1016/j.dsr2.2015.04.021

Navin, D. A., Peirce, C., & Sinha, M. C. (1998). The RAMESSES experiment-II. Evidence for accumulated melt beneath a slow spreading ridge from wide-angle refraction and multichannel reflection seismic profiles. *Geophysical Journal International*, *135*(3), 746–772. http://doi.org/10.1046/j.1365-246X.1998.00709.x

Niedzielski, T., Høines, Å., Shields, M. A., Linley, T. D., & Priede, I. G. (2013). A multi-scale investigation into seafloor topography of the northern Mid-Atlantic Ridge based on geographic information system analysis. *Deep Sea Research Part II: Topical Studies in Oceanography*, *98*, 231–243. http://doi.org/10.1016/j.dsr2.2013.10.006

NOAA. (2004, January 1). Multibeam Bathymetry Database (MBBDB). http://doi.org/10.7289/V56T0JNC

North, G. W. (2010). Marie Tharp: The lady who showed us the ocean floors. *Physics and Chemistry of the Earth, Parts A/B/C*, *35*(15), 881–886. http://doi.org/10.1016/j.pce.2010.05.007

Odom, R. I. (2003). An Introduction to Underwater Acoustics: Principles and Applications. *Eos, Transactions American Geophysical Union*, *84*(28), 265. http://doi.org/10.1007/978-3-642-13835-5_2

Parnell-Turner, R., White, N., Henstock, T., Murton, B., Maclennan, J., Jones, S. M., … Jones Stephen M. (2014). A continuous 55-million-year record of transient mantle plume activity beneath Iceland. *Nat. Geosci.*, *7*(12), 914–919. http://doi.org/http://dx.doi.org/10.1038/ngeo2281 10.1038/ngeo2281

Parson, L. M. (1993). RV Maurice Ewing Cruise EW9008, 29 Sep-26 Oct 1990. Sidescan sonar and swath bathymetry investigations of the Reykjanes Ridge, southwest of Iceland. *Cruise Report - UK Natural Environment Research Council, Institute of Oceanographic Sciences*, *237*. Retrieved from https://www.engineeringvillage.com/share/document.url?mid=geo_1630ab910af228d3cfM2b4120613774210&database=geo

Parson, L. M., Murton, B. J., Searle, R. C., Booth, D., Evans, J., Field, P., … Walker, C. (1993). En echelon axial volcanic ridges at the Reykjanes Ridge: a life cycle of volcanism and tectonics. *Earth and Planetary Science Letters*, *117*(1–2), 73–87.

http://doi.org/10.1016/0012-821X(93)90118-S

Richardson, M. D., & Jackson, D. R. (2017). Chapter 8 – The Seafloor. In *Applied Underwater Acoustics* (pp. 469–552). http://doi.org/10.1016/B978-0-12-811240-3.00008-4

Searle, R. ., Keeton, J. ., Owens, R. ., White, R. ., Mecklenburgh, R., Parsons, B., & Lee, S. . (1998). The Reykjanes Ridge: structure and tectonics of a hot-spot-influenced, slow-spreading ridge, from multibeam bathymetry, gravity and magnetic investigations. *Earth and Planetary Science Letters*, *160*(3–4), 463–478. http://doi.org/10.1016/S0012-821X(98)00104-6

Searle, R. C., Field, P. R., & Owens, R. B. (1994). Segmentation and a nontransform ridge offset on the Reykjanes Ridge near 58°N. *Journal of Geophysical Research: Solid Earth*, *99*(B12), 24159–24172. http://doi.org/10.1029/94JB01549

Searle, R. C., Murton, B. J., Achenbach, K., LeBas, T., Tivey, M., Yeo, I., … Waters, C. (2010). Structure and development of an axial volcanic ridge: Mid-Atlantic Ridge, 45°N. *Earth and Planetary Science Letters*, *299*(1–2), 228–241. http://doi.org/10.1016/j.epsl.2010.09.003

Šiljeg A., Lozic, S., Š. S. (2015). A comparison A comparison of interpolation methods on the basis of data obtained from a bathymetric survey of Lake Vrana, Croatia. *Hydrology and Earth System Sciences*, *19*, 3653–3666. http://doi.org/10.5194/hess-19-3653-2015

Smith, D. K., Escartín, H. S., & Cann, J. R. (2012). Active long-lived faults emerging along slow-spreading mid-ocean ridges. *Oceanography*, *25*(1), 94–99. http://doi.org/http://dx.doi.org/10.5670/ oceanog.2012.07

Smith, W. H. F., & Sandwell, David, T. (1977). Global Sea Floor Topography from Satellite Altimetry and Ship Depth Soundings. *Science*, *277*, 1956–1962.

USGS. (n.d.). Earthquake Catalog. Retrieved May 7, 2017, from https://earthquake.usgs.gov/earthquakes/search/

Vogt, P. R., & Avery, O. E. (1974). Detailed magnetic surveys in the Northeast Atlantic and Labrador Sea. *Journal of Geophysical Research*, *79*(2), 363–389. http://doi.org/10.1029/JB079i002p00363

White, R. S. (1997). Rift–plume interaction in the North Atlantic. *Philosophical Transactions of the Royal Society of London A: Mathematical, Physical and Engineering Sciences*, *355*(1723). Retrieved from http://rsta.royalsocietypublishing.org/content/355/1723/319

Wille, P. C. (2005). *Sound images of the ocean in research and monitoring*. *Sound Images of the Ocean in Research and Monitoring*. Springer. http://doi.org/10.1007/3-540-27910-5

Wilson, J. T. (1965). A New Class of Faults and their Bearing on Continental Drift. *Nature*, *207*(4995), 343–347. http://doi.org/10.1038/207343a0

WILSON, J. T. (1954). The Development and Structure of the Crust. In *The Earth as a Planet* (pp. 138–214). Retrieved from http://articles.adsabs.harvard.edu/full/1954eap..book..138W

Zhang, T., Xu, X., & Xu, S. (2015). Method of establishing an underwater digital elevation terrain based on kriging interpolation. *Measurement*, *63*, 287–298. http://doi.org/10.1016/j.measurement.2014.12.025

Zirek, E., & Sunar, F. (2014). Change detection of seafloor topography by modeling multitemporal multibeam echosounder measurements. In *International Archives of the Photogrammetry, Remote Sensing and Spatial Information Sciences - ISPRS Archives*. http://doi.org/10.5194/isprsarchives-XL-7-221-2014

Appendix A - Data

Multibeam Bathymetric Survey: **EW9008**

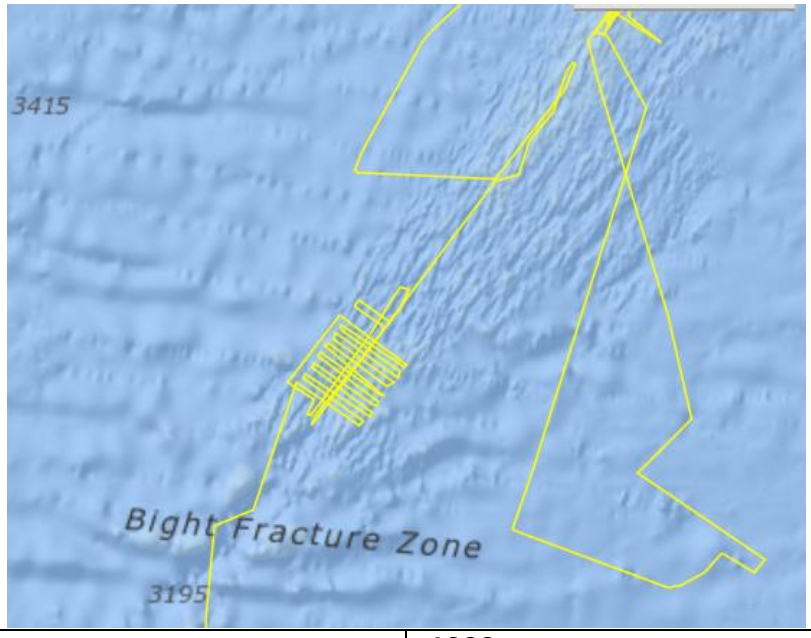

Survey Year	**1990**
Platform Name	Maurice Ewing
Survey Year	1990
Source Organization	Marine Geoscience Data System (MGDS)
Chief Scientist	Parson, L.
Instrument	Atlas Hydrosweep DS
File Count	30
Track Length	9993.8258 km
Total Time	614.1729 hours
Bathymetry Beams	20.304142 million

Multibeam Bathymetric Survey: **EW9004**

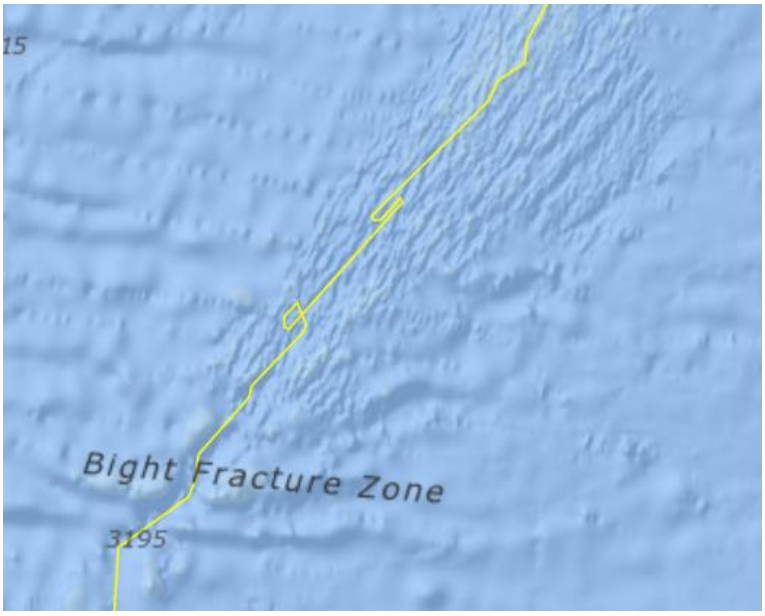

Survey Year	**1990**
Platform Name	Maurice Ewing
Survey Year	1990
Source Organization	Marine Geoscience Data System (MGDS)
Chief Scientist	Shor, A., Applegate, B., and Nishmura, C.
Instrument	Atlas Hydrosweep DS
File Count	6
Track Length	2389 km
Total Time	126 hours
Bathymetry Beams	3.270311 million

Multibeam Bathymetric Survey: **MGL13909**

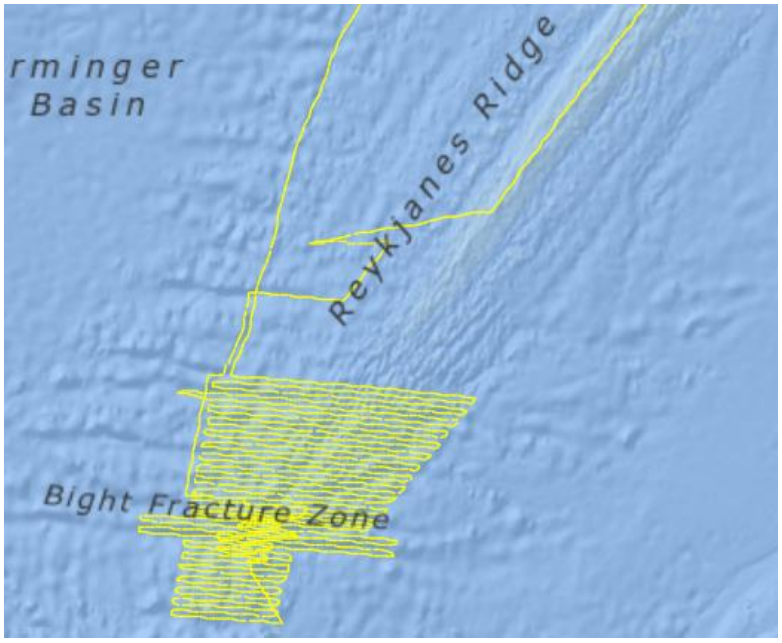

Survey Year	**2013**
Platform Name	Marcus G. Langseth
Survey Year	2013
Source Organization	UNOLS R2R
Chief Scientist	Hey, Richard
Instrument	Kongsberg EM122
File Count	1698
Track Length	12995 km
Total Time	774 hours
Bathymetry Beams	335.038464 million
Amplitude Beams	335.038464 million
Sidescan	794.165248 million pixels

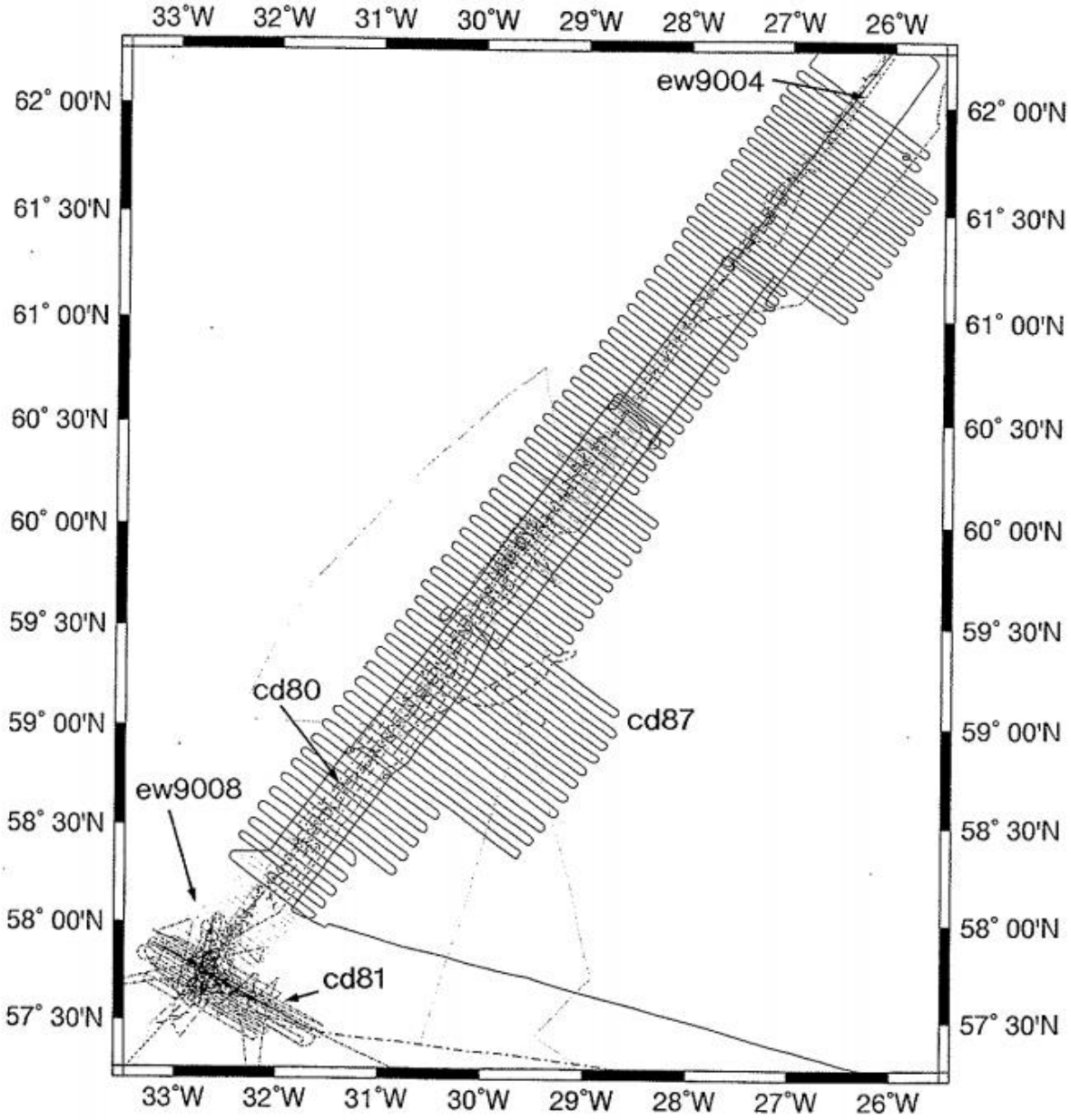
33°W
32°W
31°W
30°W
29°W
28°W
27°W
26°W
62° 00'N
61° 30'N
61° 00'N
60° 30'N
60° 00'N
59° 30'N
59° 00'N
58° 30'N
58° 00'N
57° 30'N
ew9004
cd80
cd87
ew9008
cd81

Appendix B – Bathymetric Maps

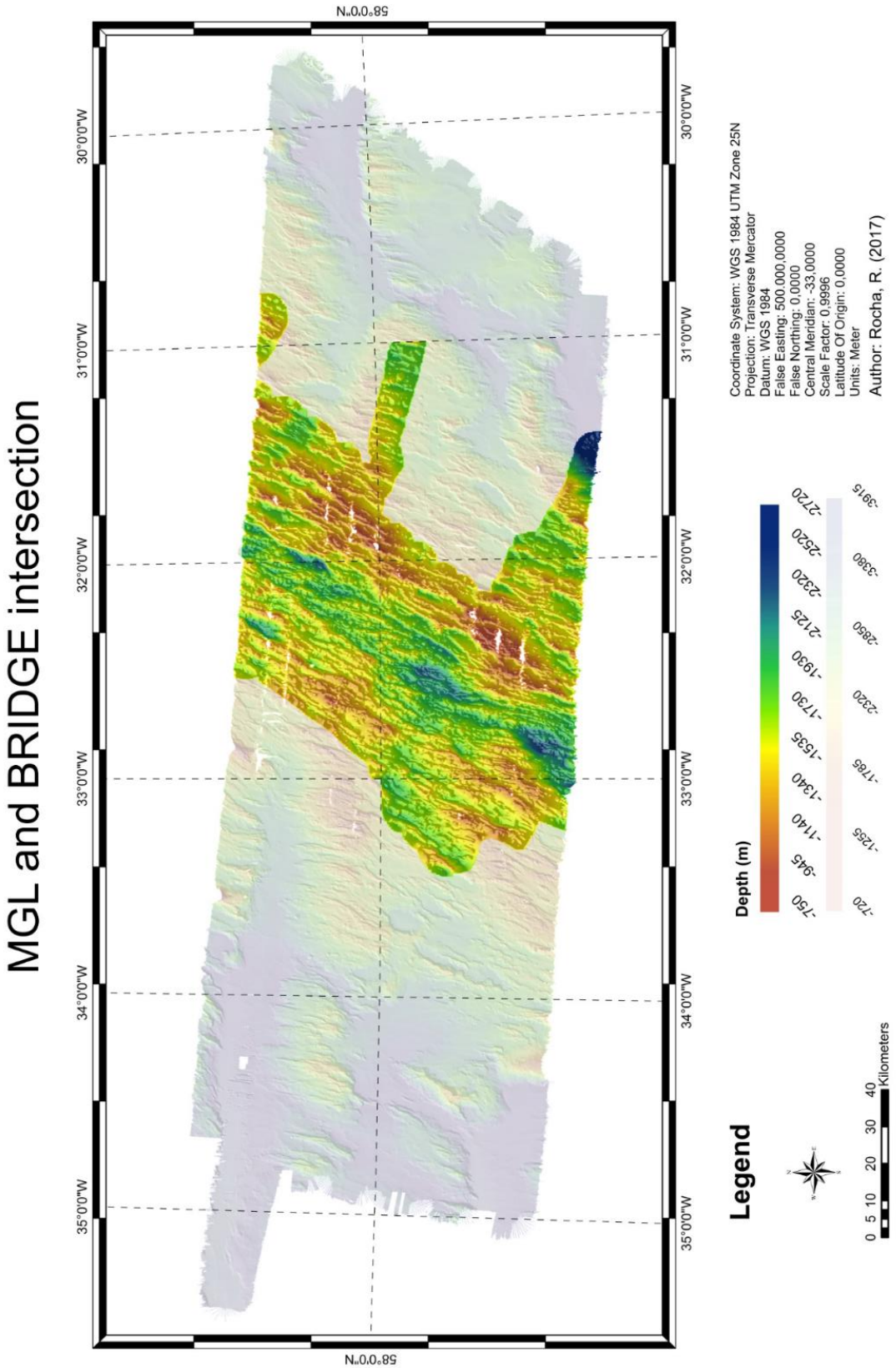

BRIDGE Bathymetry

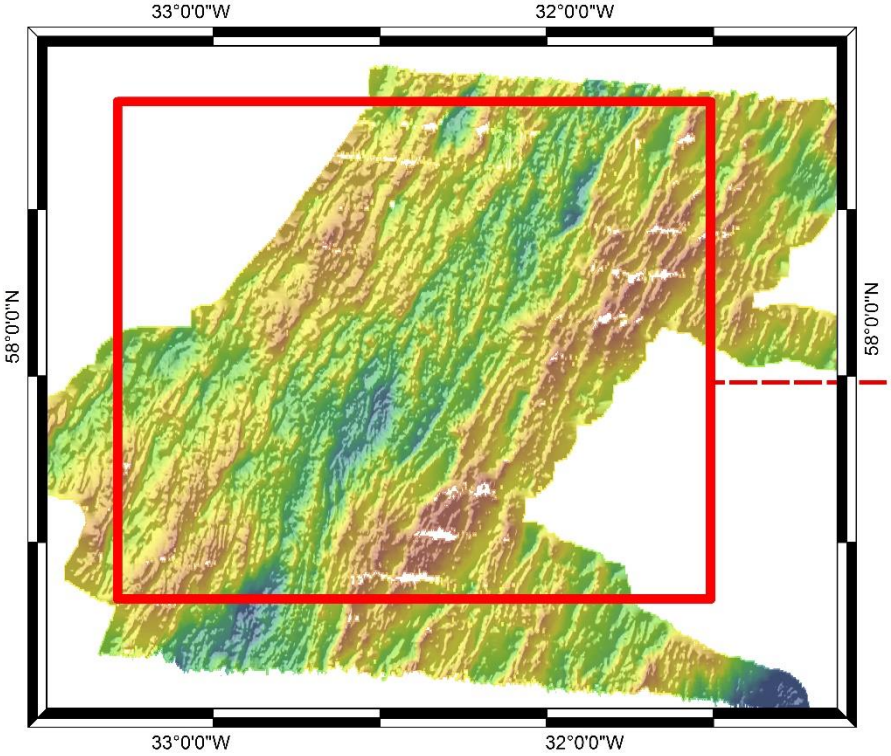

M. Ewing Bathymetry

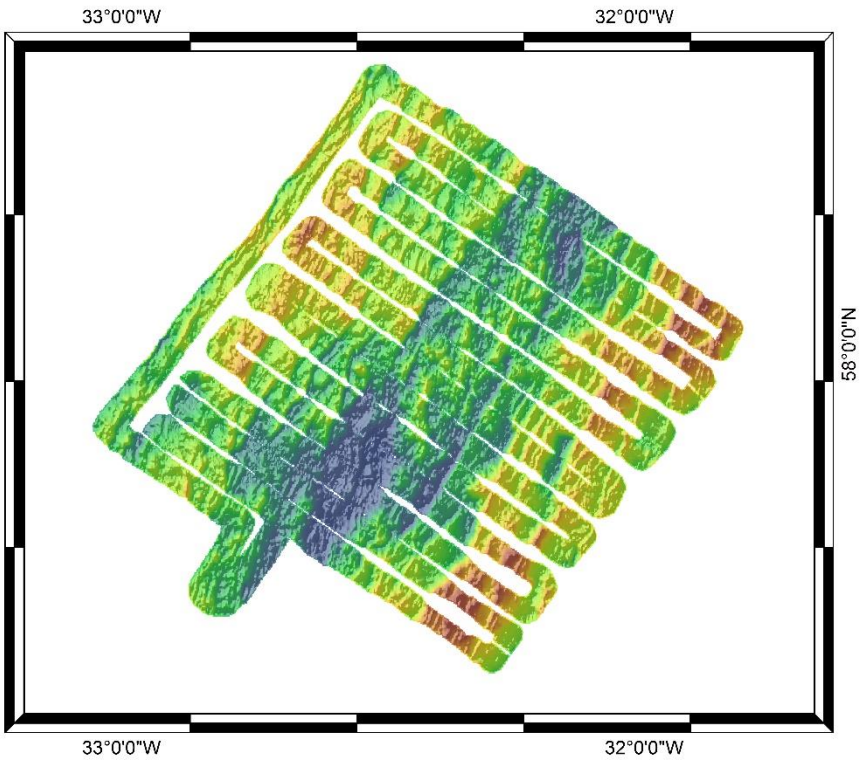

Legend

Depth (m)

-740 -930 -1115 -1300 -1490 -1675 -1860 -2050 -2235 -2420 -2610

Coordinate System: WGS 1984 UTM Zone 25N
Projection: Transverse Mercator
Datum: WGS 1984
False Easting: 500.000,0000
False Northing: 0,0000
Central Meridian: -33,0000
Scale Factor: 0,9996
Latitude Of Origin: 0,0000
Units: Meter

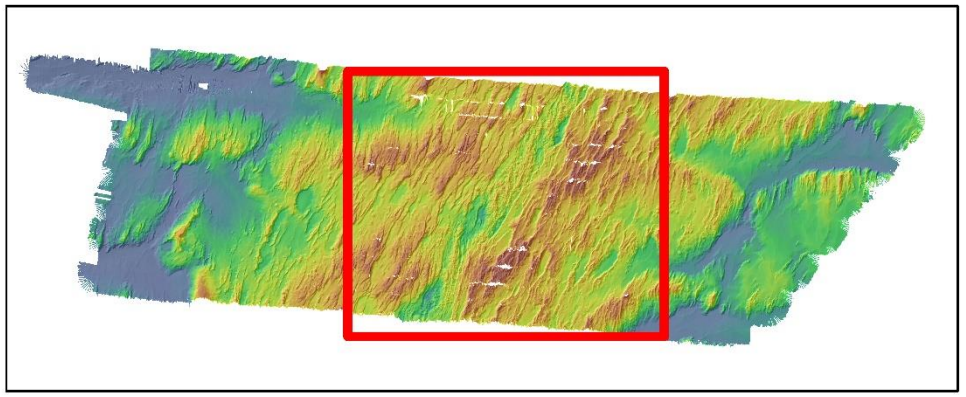

Author: Rocha, R. (2017)

Appendix C – Descriptive Statistics

WEST

0-10km W		
statistics	N faults	height
mean	5,7	184,2105
median	5	140
mode	5	50

10-20km W		
statistics	N faults	height
mean	4,3	199,6341
median	4,5	150
mode	5	50

20-30km W		
statistics	N faults	height
mean	4,4	139,7727
median	4,5	100
mode	4	50

30-40km W		
statistics	N faults	height
mean	4,3	147,7907
median	4,5	100
mode	5	50

40-50km W		
statistics	N faults	height
mean	3,4	112,6471
median	3	100
mode	3	50

50-60km W		
statistics	N faults	height
mean	3,3	171,6667
median	3	150
mode	3	200

60-70km W		
statistics	N faults	height
mean	1,7	154,7059
median	1,5	100
mode	1	100

70-80km W		
statistics	N faults	height
mean	1,3	193,4615
median	1	150
mode	0	275

80-90km W		
statistics	N faults	height
mean	2,1	141,5789
median	2	132,5
mode	0	150

90-100km W		
statistics	N faults	height
mean	1,8	218,0556
median	2	162,5
mode	2	100

100-110km W		
statistics	N faults	height
mean	1	158,75
median	1	112,5
mode	1	100

NUMBER OF FAULTS PER PROFILE			
buffer	mean	median	mode
10	5,7	5	5
20	4,3	4,5	5
30	4,4	4,5	4
40	4,3	4,5	5
50	3,4	3	3
60	3,3	3	3
70	1,7	1,5	1
80	1,3	1	0
90	2,1	2	0
100	1,8	2	2
110	1	1	1
CORREL	-0,94202	-0,91634	-0,86001

HEIGHT			
buffer	mean	median	mode
10	184	140	50
20	200	150	50
30	140	100	50
40	148	100	50
50	113	100	50
60	172	150	200
70	155	100	100
80	193	150	275
90	142	132,5	150
100	218	162,5	100
110	159	112,5	100
CORREL	0,083134	0,133493	0,507673

NUMBER OF FAULTS PER PROFILE			
buffer	max	min	TOTAL
10	10	3	57
20	6	2	43
30	6	3	44
40	7	1	43
50	5	1	34
60	5	2	33
70	4	0	17
80	3	0	13
90	6	0	21
100	3	0	18
110	2	0	10
CORREL	-0,82553	-0,86426	-0,94202

HEIGHT		
buffer	max	min
10	620	50
20	625	50
30	400	50
40	600	50
50	300	50
60	575	50
70	675	50
80	600	50
90	650	50
100	550	50
110	450	50
CORREL	-0,00645	-

(Normal Faults)

EAST

0-10km E		
statistics	N faults	height
mean	5,9	225,339
median	5,5	160
mode	5	75

10-20km E		
statistics	N faults	height
mean	3,6	248
median	3	200
mode	3	125

20-30km E		
statistics	N faults	height
mean	3,9	171,5385
median	4	150
mode	4	60

30-40km E		
statistics	N faults	height
mean	3,4	179,7059
median	4	127,5
mode	4	100

40-50km E		
statistics	N faults	height
mean	2,5	236
median	2,5	203
mode	4	50

50-60km E		
statistics	N faults	height
mean	2,4	143,75
median	2	137,5
mode	2	175

60-70km E		
statistics	N faults	height
mean	2,4	148,625
median	2,5	125
mode	3	150

70-80km E		
statistics	N faults	height
mean	2	148
median	2	138
mode	2	200

80-90km E		
statistics	N faults	height
mean	1,777778	266,7647
median	1	300
mode	1	300

90-100km E		
statistics	N faults	height
mean	1,6	151,7857
median	1	95
mode	0	60

100-110km E		
statistics	N faults	height
mean	1	166
median	0	140
mode	0	100

NUMBER OF FAULTS PER PROFILE			
buffer	mean	median	mode
10	5,9	5,5	5
20	3,6	3	3
30	3,9	4	4
40	3,4	4	4
50	2,5	2,5	4
60	2,4	2	2
70	2,4	2,5	3
80	2	2	2
90	1,8	1	1
100	1,6	1	0
110	1	0	0
CORREL	-0,92334	-0,92486	-0,90725

HEIGHT			
buffer	mean	median	mode
10	225	160	75
20	248	200	125
30	171	150	60
40	180	127,5	100
50	236	202,5	50
60	144	137,5	175
70	149	125	150
80	148	137,5	200
90	266	300	300
100	152	95	60
110	166	140	100
CORREL	-0,36275	-0,06904	0,352929

NUMBER OF FAULTS PER PROFILE			
buffer	max	min	TOTAL
10	9	4	59
20	6	3	36
30	6	2	39
40	4	2	34
50	4	1	25
60	6	0	24
70	5	0	24
80	4	0	20
90	5	0	16
100	5	0	16
110	4	0	10
CORREL	-0,62758	-0,89661	-0,92607

HEIGHT		
buffer	max	min
10	725	50
20	600	50
30	475	50
40	450	50
50	700	50
60	385	50
70	550	50
80	300	50
90	650	50
100	550	60
110	450	50
CORREL	-0,34016	-

Appendix D - Descriptive Statistics (Central Valley)

Seamount	Area (Km2)
1	932,85
2	299,91
3	592,60
4	736,08
5	653,93
6	285,24
7	343,90
8	404,08
9	757,09
10	376,54
11	264,20
12	423,11
13	371,53
14	429,89
15	408,40
16	1643,05
17	217,03
18	1151,32
19	174,72

Seamount	Area (Km2)
20	194,41
21	686,36
22	202,62
23	457,29
24	1639,31
25	413,84
26	396,37
27	531,75
28	1885,58
29	338,44
30	194,41
31	350,14
32	214,65
33	503,10
34	270,38
35	185,07
36	258,84
37	335,47
38	215,47

Seamount	Area (Km2)
39	1084,21
40	190,11
41	227,98
42	227,82
43	237,80
44	102,33
45	47,48
46	149,25
47	137,90
48	436,54
49	76,69
50	97,22
51	372,54
52	87,36
53	392,95
54	167,35
55	93,11
56	93,11

statistics	
MIN	47,48
MAX	1885,58
AVERAGE	433,96
MEDIAN	338,44

Appendix F – Topographic Cross Sections

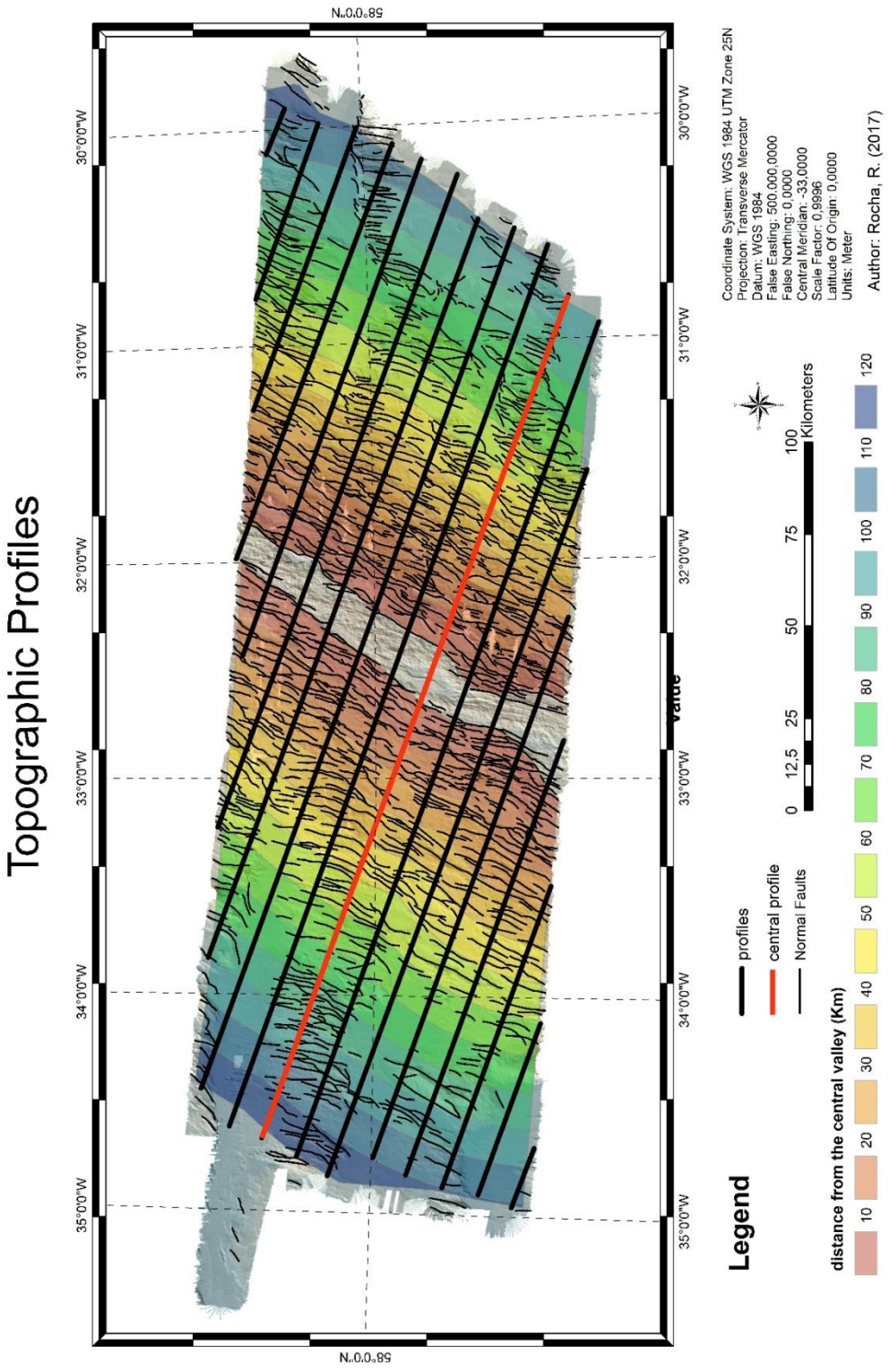

West Topography

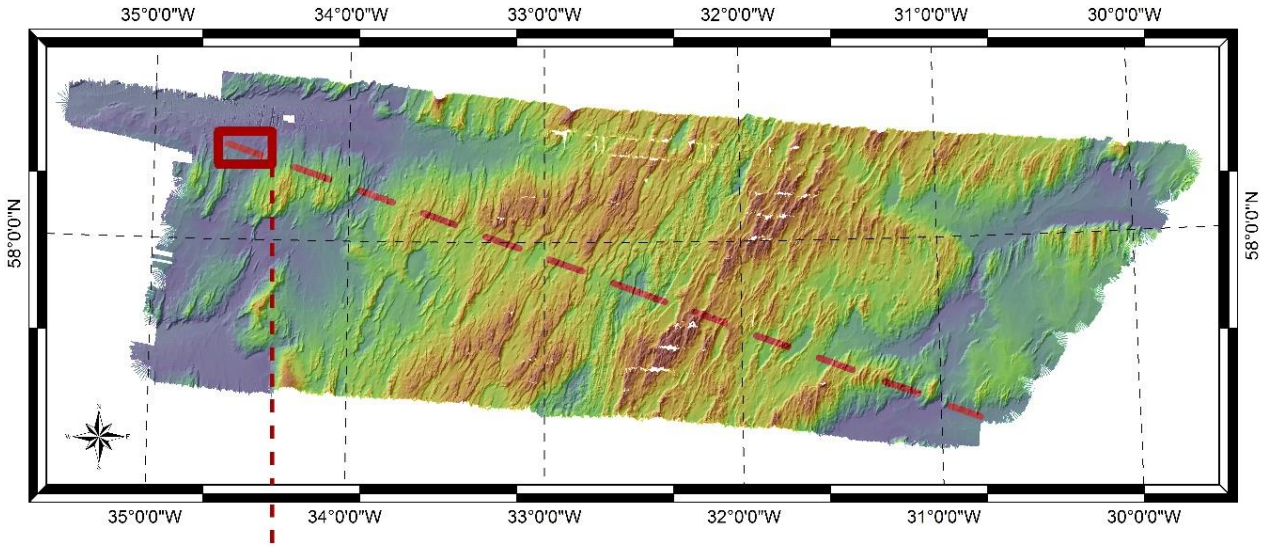

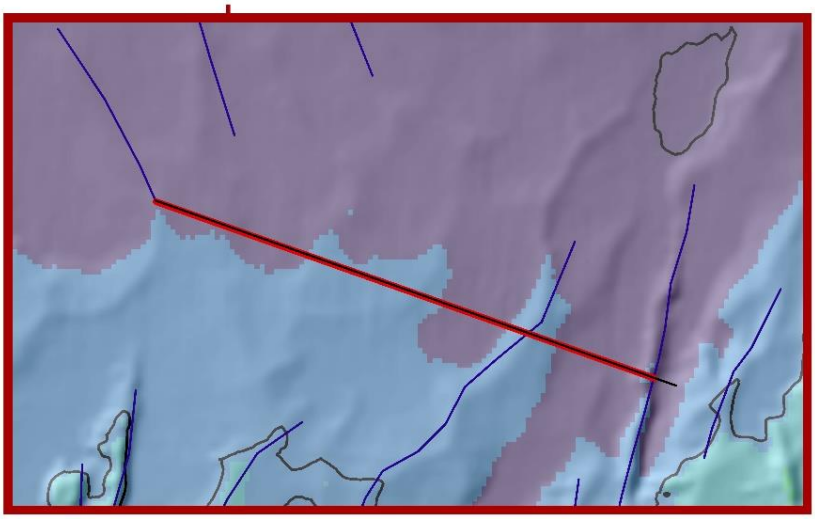

Legend

Depth (m)

- -3.300 - -2.750
- -2.750 - -2.550
- -2.550 - -2.374
- -2.374 - -2.187
- -2.187 - -2.011
- -2.011 - -1.836
- -1.836 - -1.673
- -1.673 - -1.510
- -1.510 - -1.310
- -1.310 - -721

- 300 m isobath
- Topographic Profile
- Normal Faults

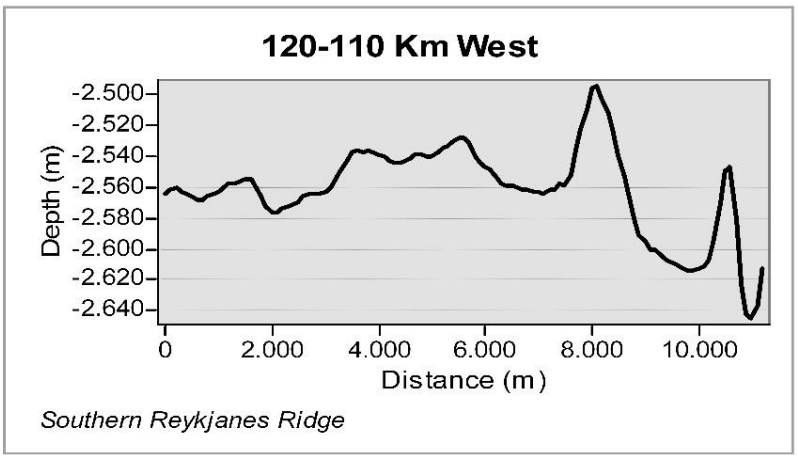

Coordinate System: WGS 1984 UTM Zone 25N
Projection: Transverse Mercator
Datum: WGS 1984
False Easting: 500.000,0000
False Northing: 0,0000
Central Meridian: -33,0000
Scale Factor: 0,9996
Latitude Of Origin: 0,0000
Units: Meter

Author: Rocha, R. (2017)

West Topography

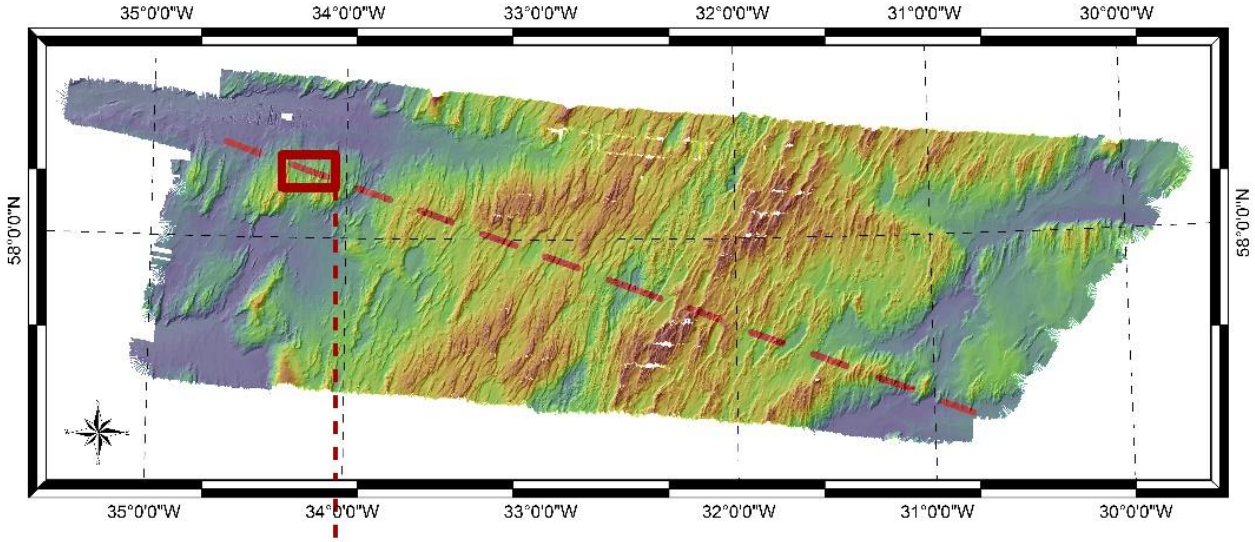

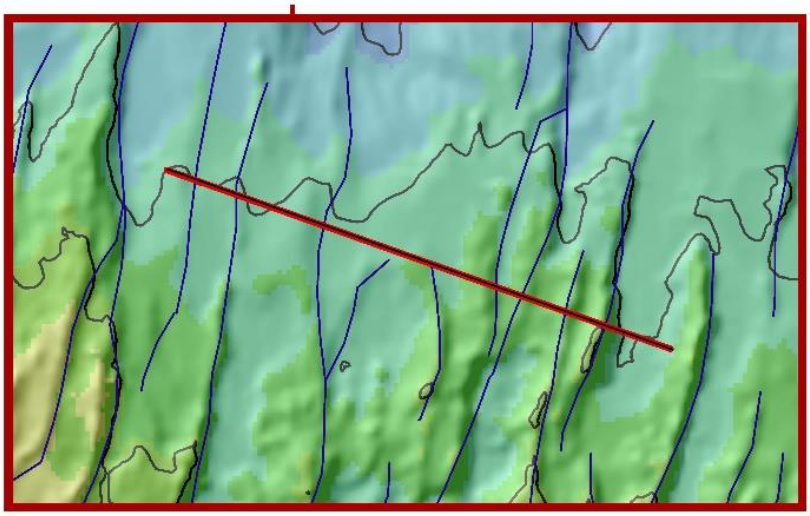

Legend

Depth (m)

- -3.300 - -2.750
- -2.750 - -2.550
- -2.550 - -2.374
- -2.374 - -2.187
- -2.187 - -2.011
- -2.011 - -1.836
- -1.836 - -1.673
- -1.673 - -1.510
- -1.510 - -1.310
- -1.310 - -721

- 300 m isobath
- Topographic Profile
- Normal Faults

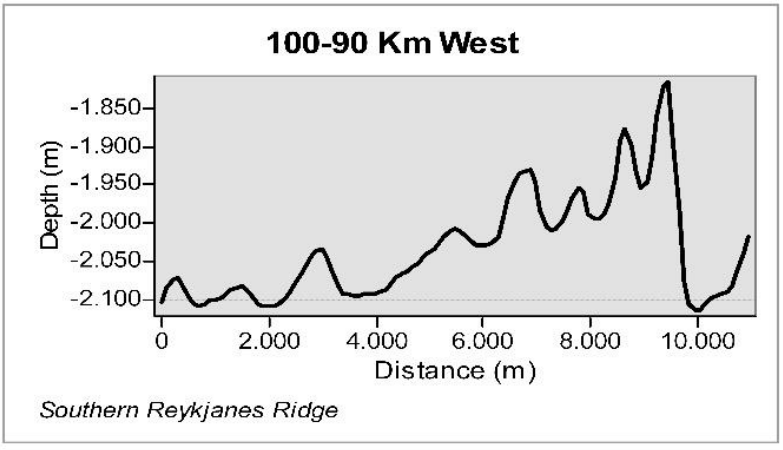

Coordinate System: WGS 1984 UTM Zone 25N
Projection: Transverse Mercator
Datum: WGS 1984
False Easting: 500.000,0000
False Northing: 0,0000
Central Meridian: -33,0000
Scale Factor: 0,9996
Latitude Of Origin: 0,0000
Units: Meter

Author: Rocha, R. (2017)

West Topography

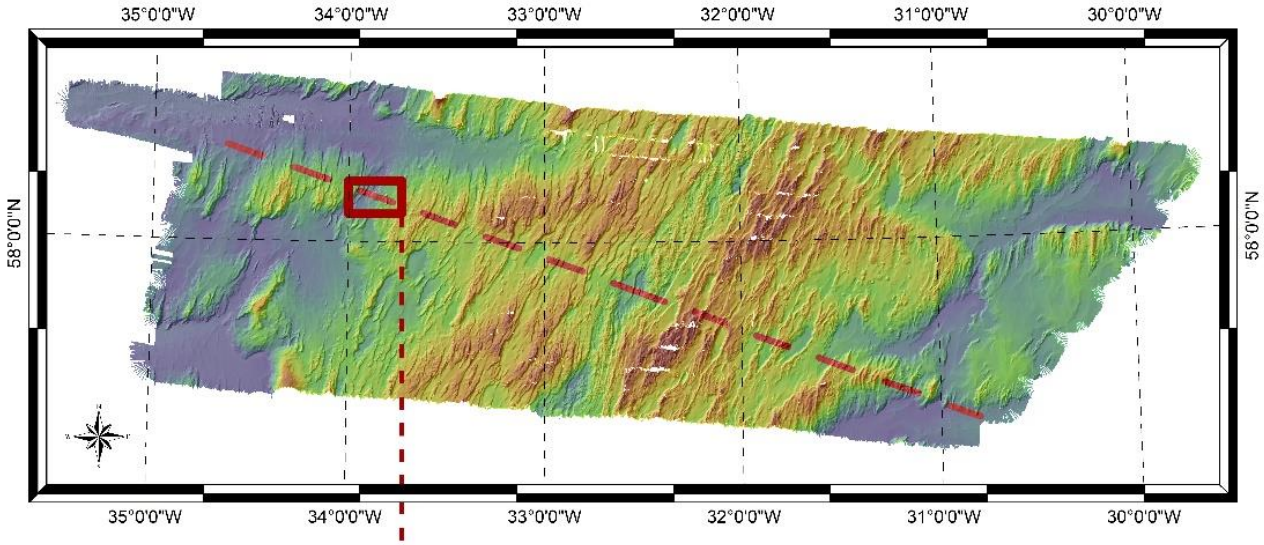

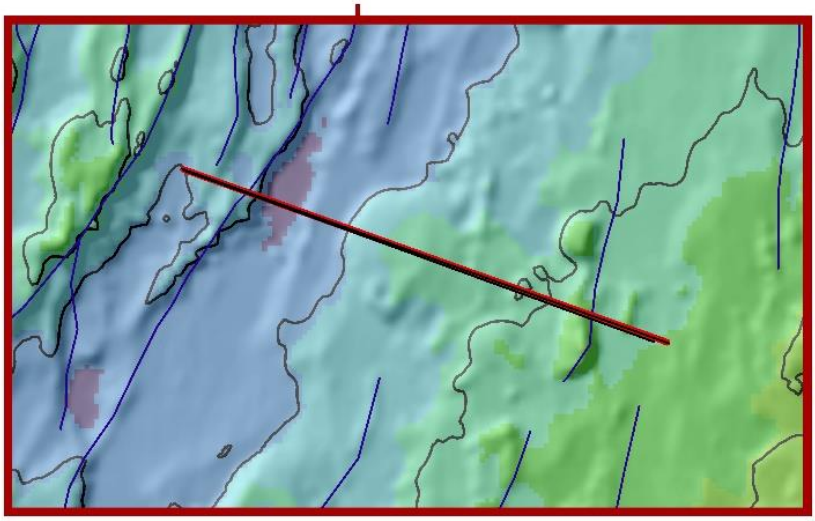

Legend

Depth (m)

- -3.300 - -2.750
- -2.750 - -2.550
- -2.550 - -2.374
- -2.374 - -2.187
- -2.187 - -2.011
- -2.011 - -1.836
- -1.836 - -1.673
- -1.673 - -1.510
- -1.510 - -1.310
- -1.310 - -721

- 300 m isobath
- Topographic Profile
- Normal Faults

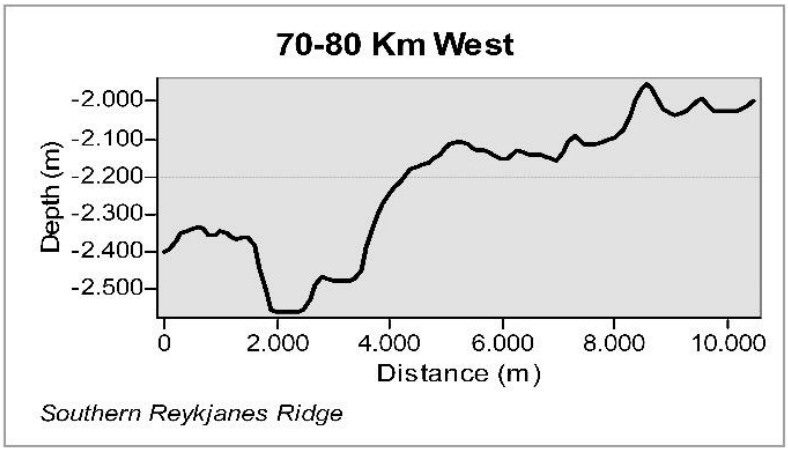

Coordinate System: WGS 1984 UTM Zone 25N
Projection: Transverse Mercator
Datum: WGS 1984
False Easting: 500.000,0000
False Northing: 0,0000
Central Meridian: -33,0000
Scale Factor: 0,9996
Latitude Of Origin: 0,0000
Units: Meter

Author: Rocha, R. (2017)

West Topography

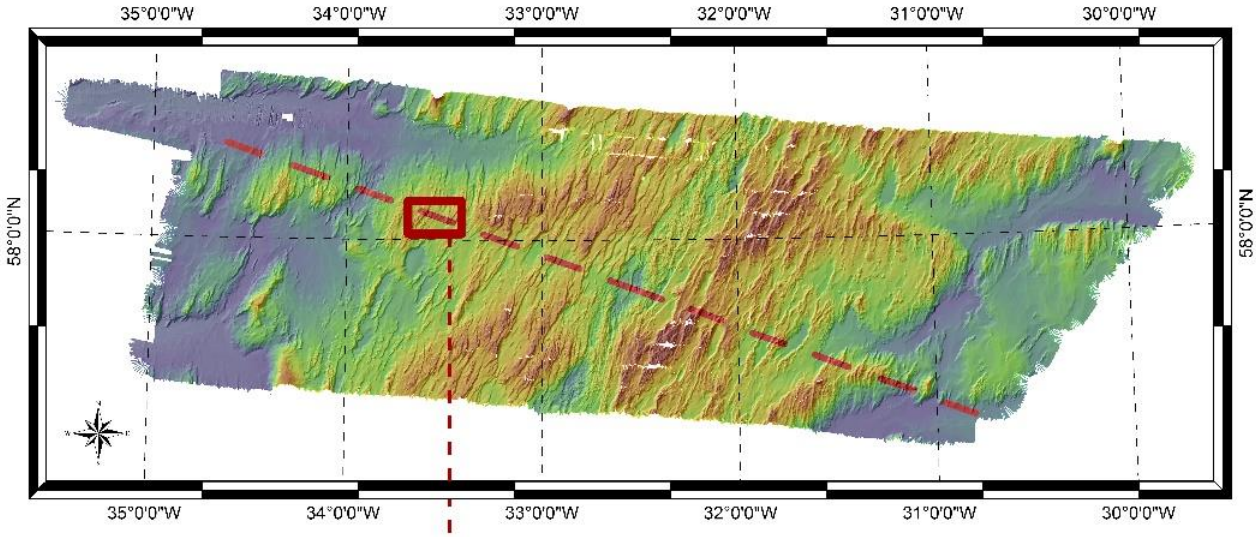

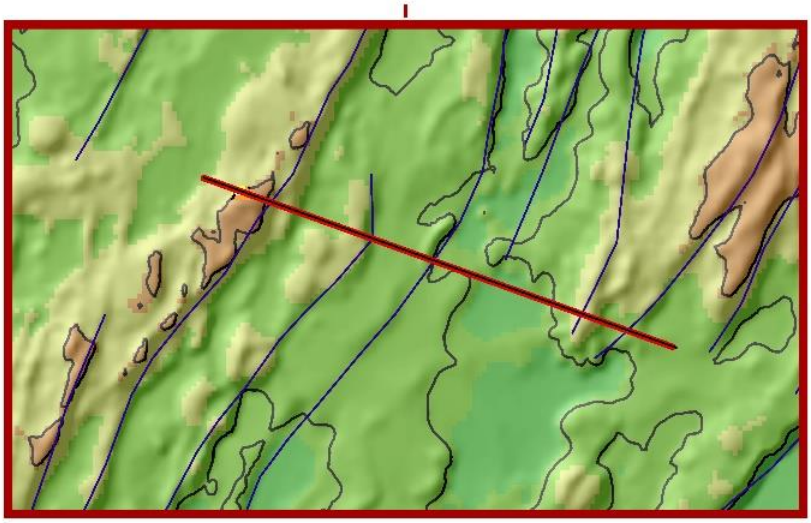

Legend

Depth (m)

- -3.300 - -2.750
- -2.750 - -2.550
- -2.550 - -2.374
- -2.374 - -2.187
- -2.187 - -2.011
- -2.011 - -1.836
- -1.836 - -1.673
- -1.673 - -1.510
- -1.510 - -1.310
- -1.310 - -721

- 300 m isobath
- Topographic Profile
- Normal Faults

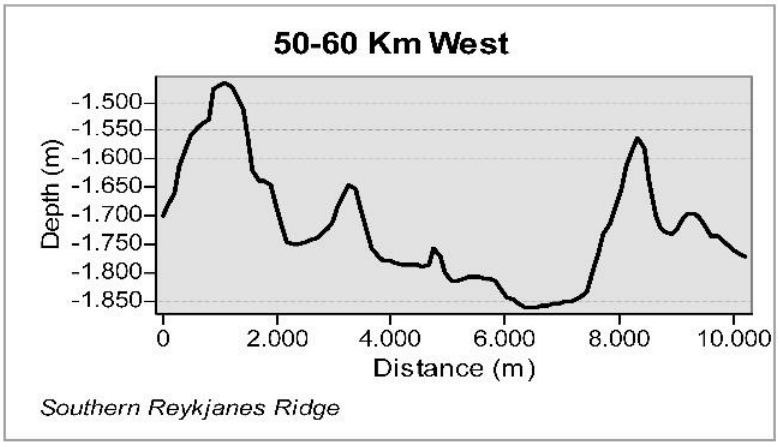

Coordinate System: WGS 1984 UTM Zone 25N
Projection: Transverse Mercator
Datum: WGS 1984
False Easting: 500.000,0000
False Northing: 0,0000
Central Meridian: -33,0000
Scale Factor: 0,9996
Latitude Of Origin: 0,0000
Units: Meter

Author: Rocha, R. (2017)

West Topography

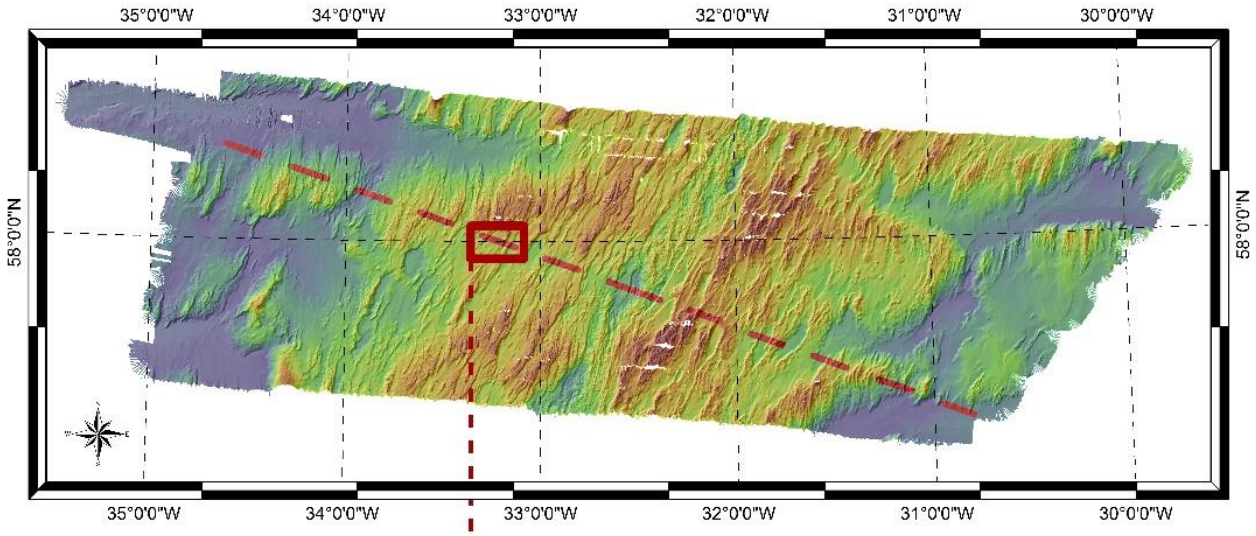

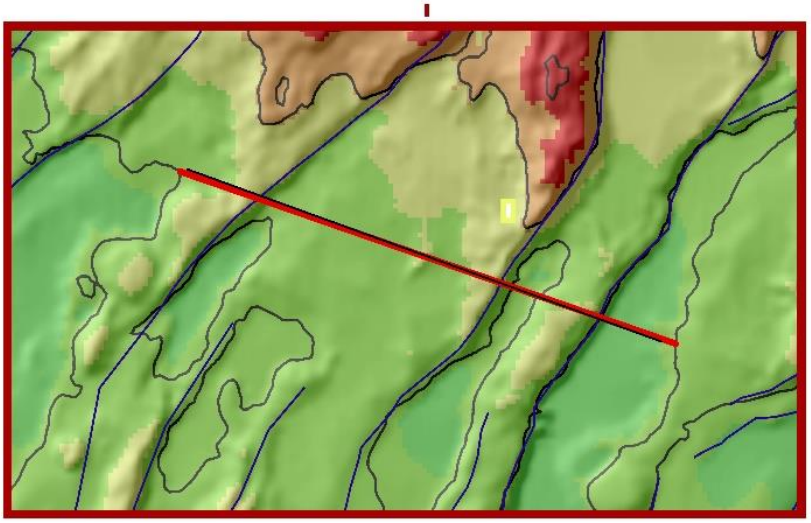

Legend

Depth (m)

- -3.300 - -2.750
- -2.750 - -2.550
- -2.550 - -2.374
- -2.374 - -2.187
- -2.187 - -2.011
- -2.011 - -1.836
- -1.836 - -1.673
- -1.673 - -1.510
- -1.510 - -1.310
- -1.310 - -721

- 300 m isobath
- Topographic Profile
- Normal Faults

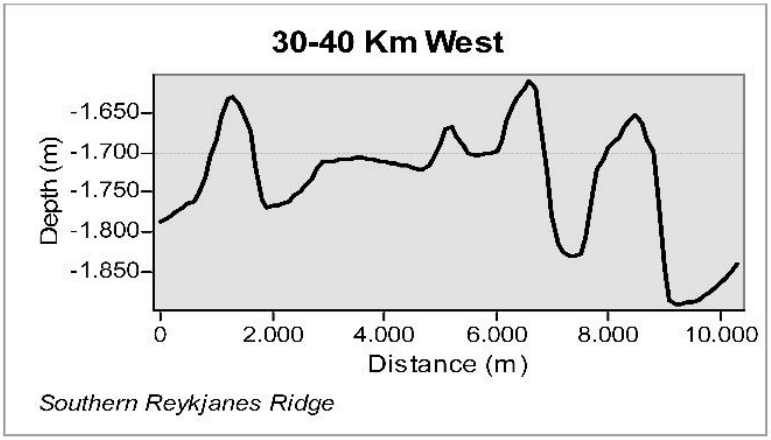

Coordinate System: WGS 1984 UTM Zone 25N
Projection: Transverse Mercator
Datum: WGS 1984
False Easting: 500.000,0000
False Northing: 0,0000
Central Meridian: -33,0000
Scale Factor: 0,9996
Latitude Of Origin: 0,0000
Units: Meter

Author: Rocha, R. (2017)

West Topography

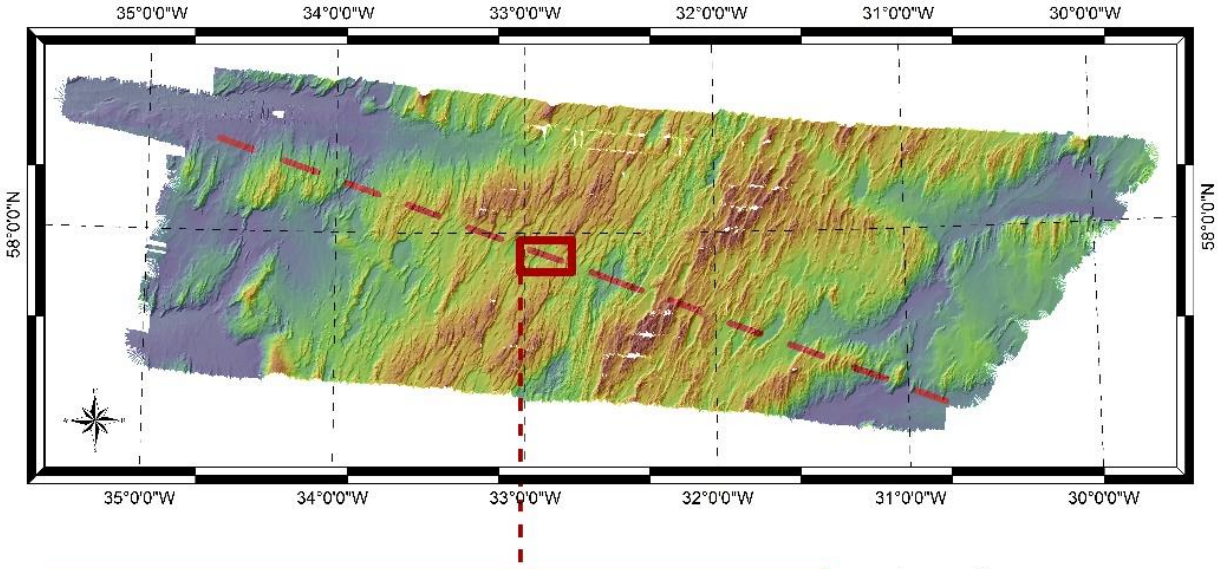

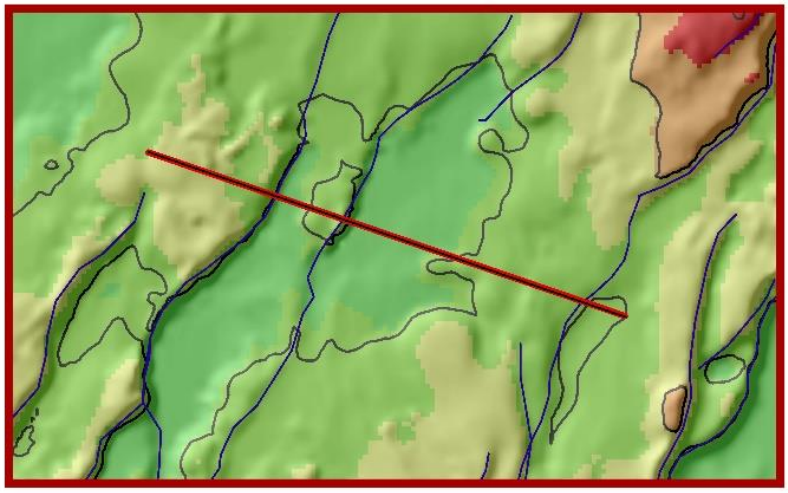

Legend

Depth (m)

- -3.300 - -2.750
- -2.750 - -2.550
- -2.550 - -2.374
- -2.374 - -2.187
- -2.187 - -2.011
- -2.011 - -1.836
- -1.836 - -1.673
- -1.673 - -1.510
- -1.510 - -1.310
- -1.310 - -721

- 300 m isobath
- Topographic Profile
- Normal Faults

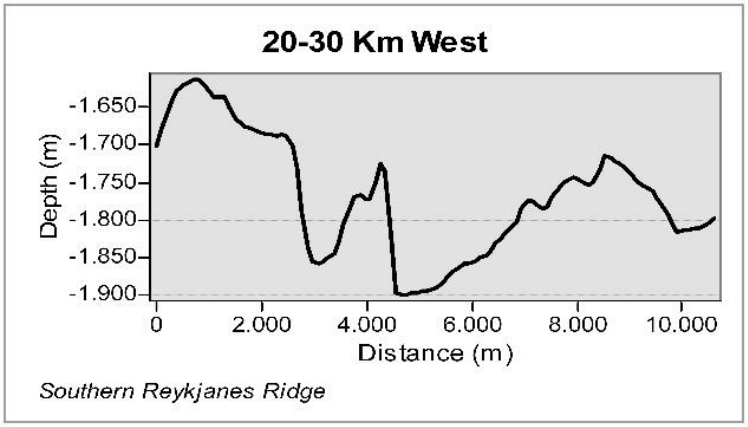

Coordinate System: WGS 1984 UTM Zone 25N
Projection: Transverse Mercator
Datum: WGS 1984
False Easting: 500.000,0000
False Northing: 0,0000
Central Meridian: -33,0000
Scale Factor: 0,9996
Latitude Of Origin: 0,0000
Units: Meter

Author: Rocha, R. (2017)

Central Valley Topography

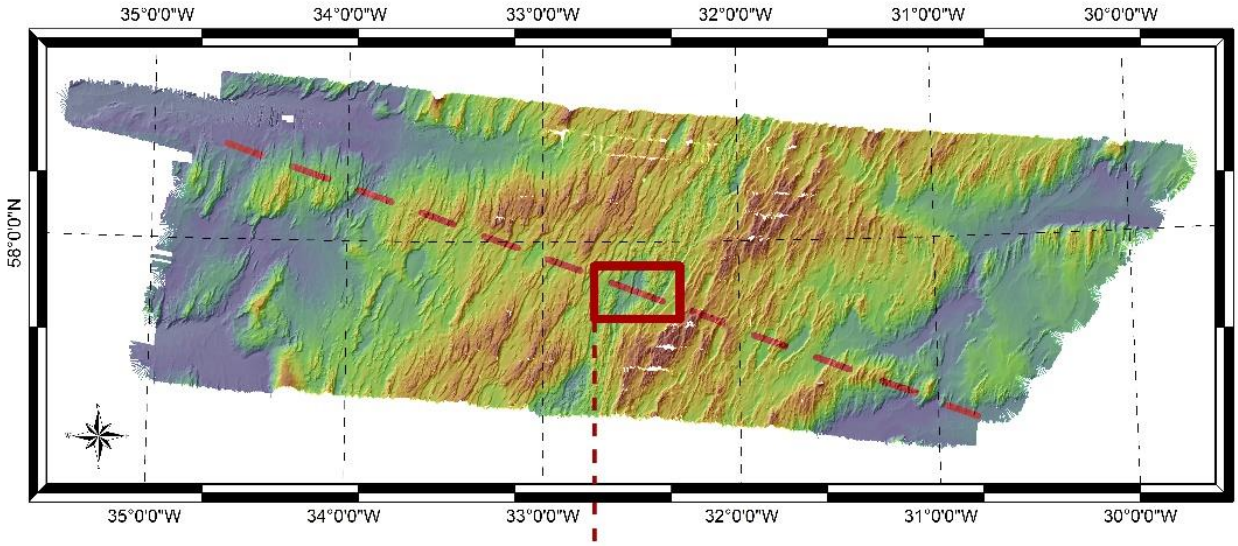

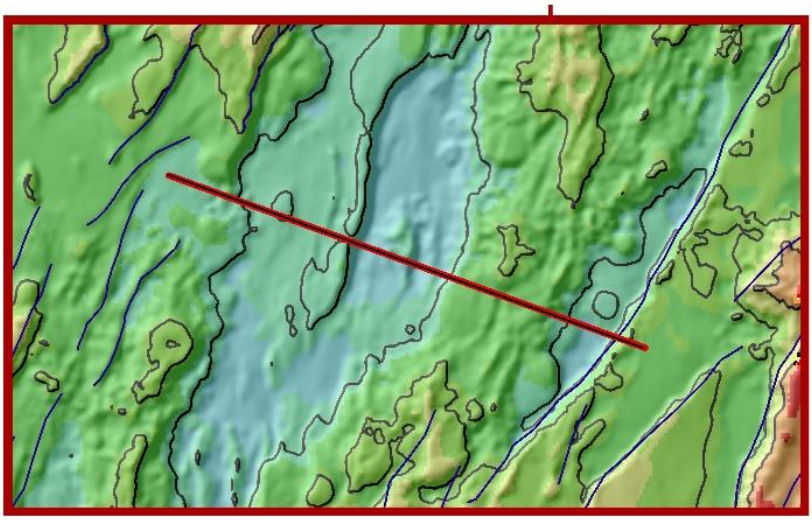

Legend

Depth (m)

- -3.300 - -2.750
- -2.750 - -2.550
- -2.550 - -2.374
- -2.374 - -2.187
- -2.187 - -2.011
- -2.011 - -1.836
- -1.836 - -1.673
- -1.673 - -1.510
- -1.510 - -1.310
- -1.310 - -721

- 300 m isobath
- Topographic Profile
- Normal Faults

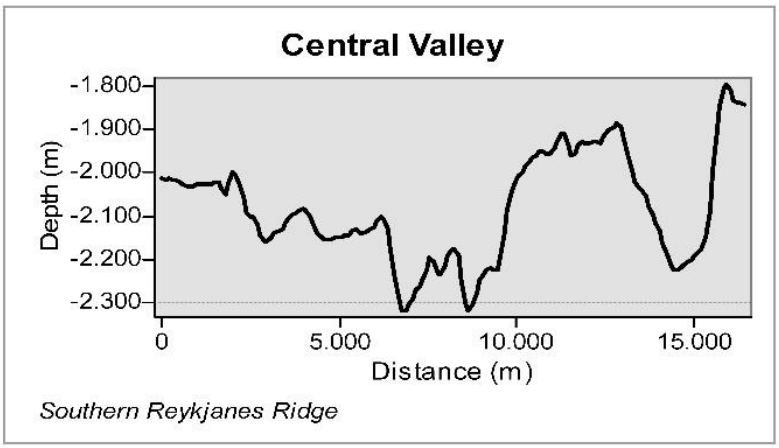

Coordinate System: WGS 1984 UTM Zone 25N
Projection: Transverse Mercator
Datum: WGS 1984
False Easting: 500.000,0000
False Northing: 0,0000
Central Meridian: -33,0000
Scale Factor: 0,9996
Latitude Of Origin: 0,0000
Units: Meter

Author: Rocha, R. (2017)

East Topography

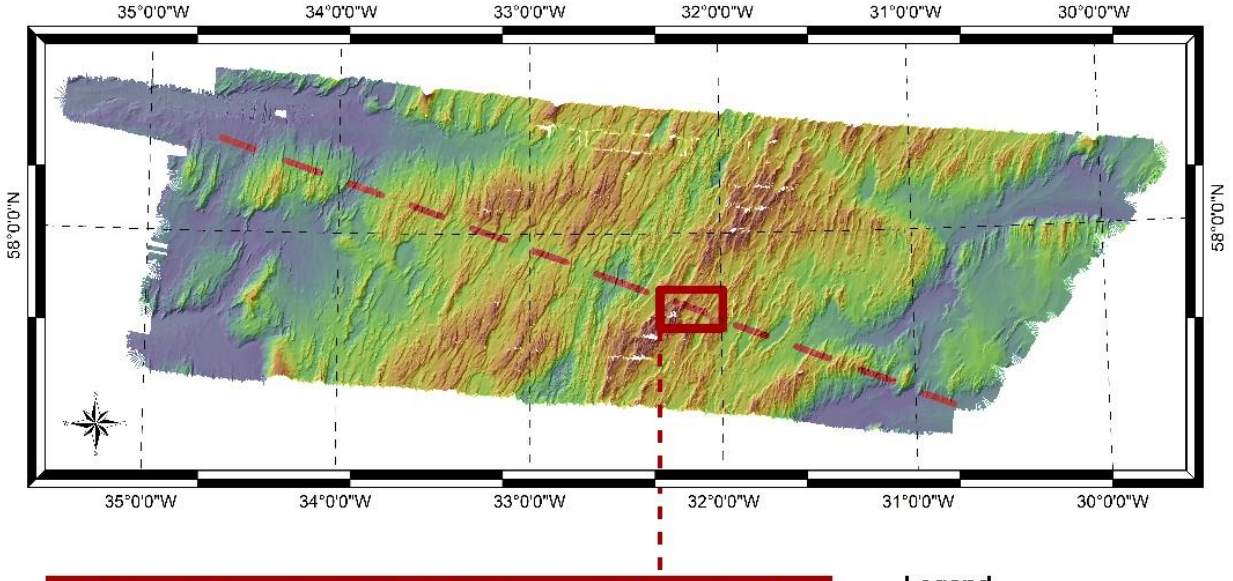

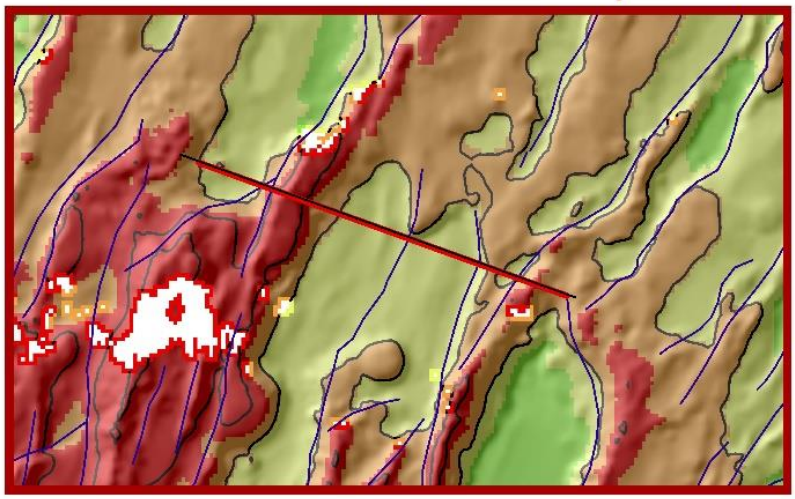

Legend

Depth (m)

- -3.300 - -2.750
- -2.750 - -2.550
- -2.550 - -2.374
- -2.374 - -2.187
- -2.187 - -2.011
- -2.011 - -1.836
- -1.836 - -1.673
- -1.673 - -1.510
- -1.510 - -1.310
- -1.310 - -721

- 300 m isobath
- Topographic Profile
- Normal Faults

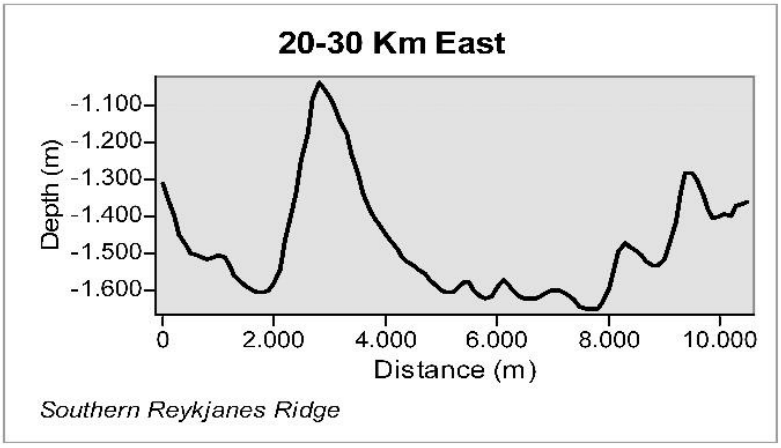

Coordinate System: WGS 1984 UTM Zone 25N
Projection: Transverse Mercator
Datum: WGS 1984
False Easting: 500.000,0000
False Northing: 0,0000
Central Meridian: -33,0000
Scale Factor: 0,9996
Latitude Of Origin: 0,0000
Units: Meter

Author: Rocha, R. (2017)

East Topography

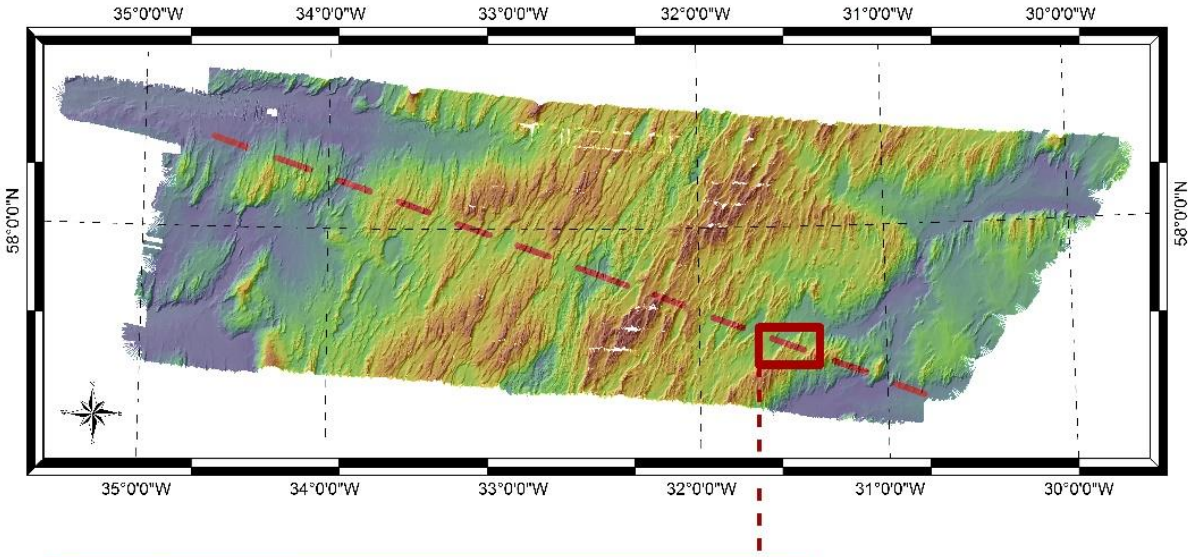

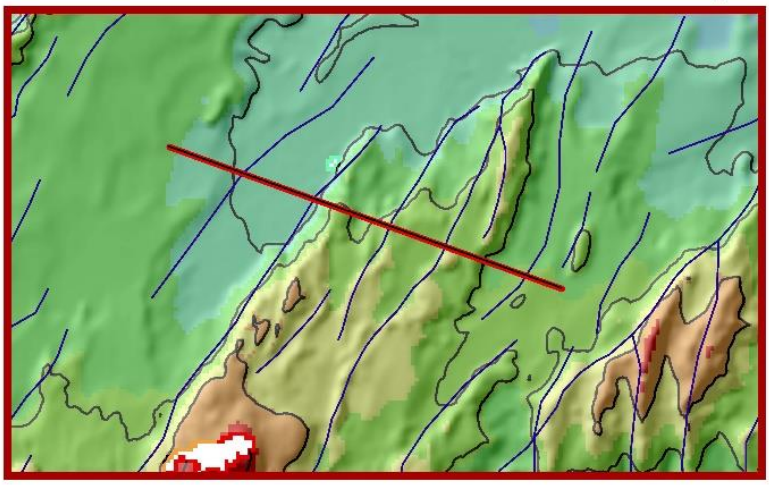

Legend

Depth (m)

- -3.300 - -2.750
- -2.750 - -2.550
- -2.550 - -2.374
- -2.374 - -2.187
- -2.187 - -2.011
- -2.011 - -1.836
- -1.836 - -1.673
- -1.673 - -1.510
- -1.510 - -1.310
- -1.310 - -721

- 300 m isobath
- Topographic Profile
- Normal Faults

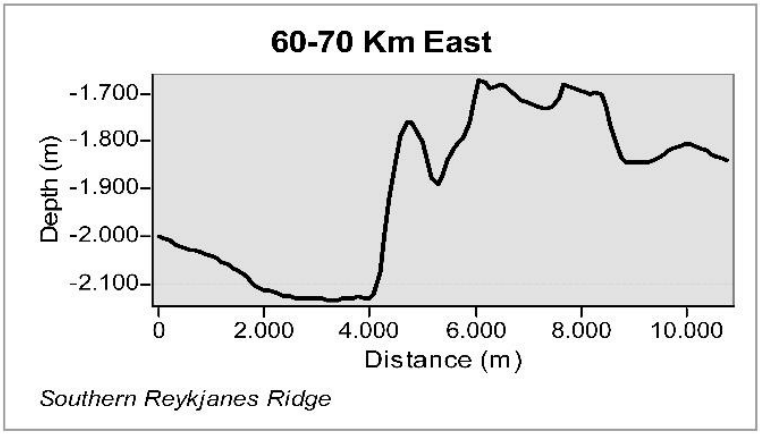

Coordinate System: WGS 1984 UTM Zone 25N
Projection: Transverse Mercator
Datum: WGS 1984
False Easting: 500.000,0000
False Northing: 0,0000
Central Meridian: -33,0000
Scale Factor: 0,9996
Latitude Of Origin: 0,0000
Units: Meter

Author: Rocha, R. (2017)

East Topography

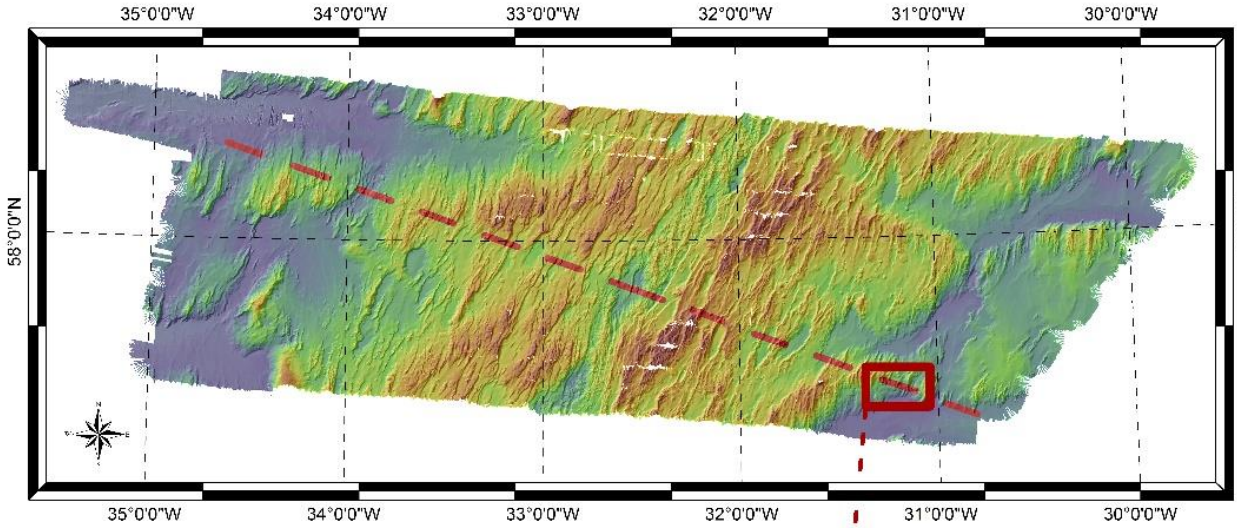

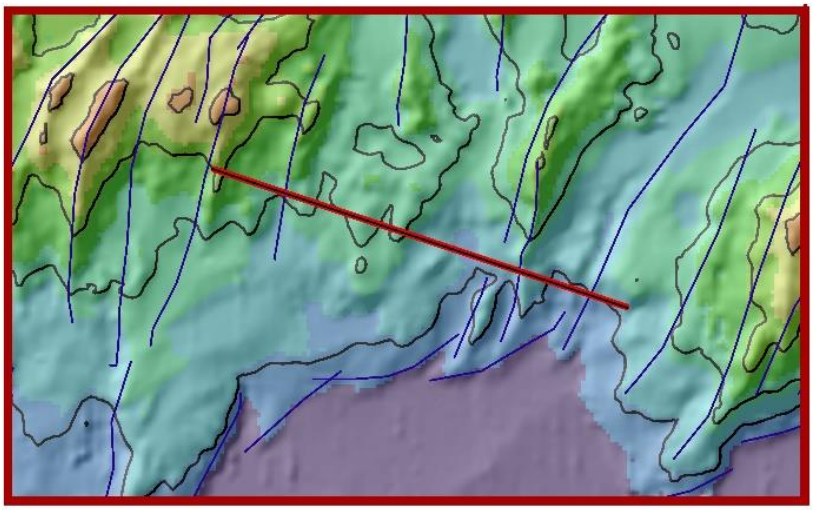

Legend

Depth (m)

- -3.300 - -2.750
- -2.750 - -2.550
- -2.550 - -2.374
- -2.374 - -2.187
- -2.187 - -2.011
- -2.011 - -1.836
- -1.836 - -1.673
- -1.673 - -1.510
- -1.510 - -1.310
- -1.310 - -721

- 300 m isobath
- Topographic Profile
- Normal Faults

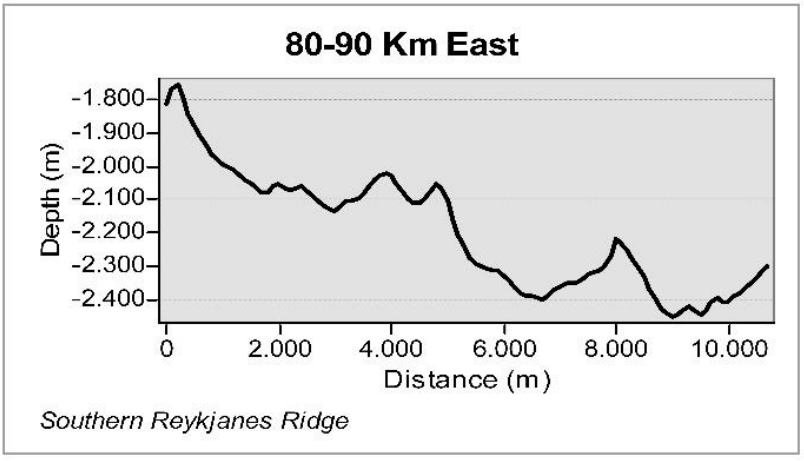

Coordinate System: WGS 1984 UTM Zone 25N
Projection: Transverse Mercator
Datum: WGS 1984
False Easting: 500.000,0000
False Northing: 0,0000
Central Meridian: -33,0000
Scale Factor: 0,9996
Latitude Of Origin: 0,0000
Units: Meter

Author: Rocha, R. (2017)

East Topography

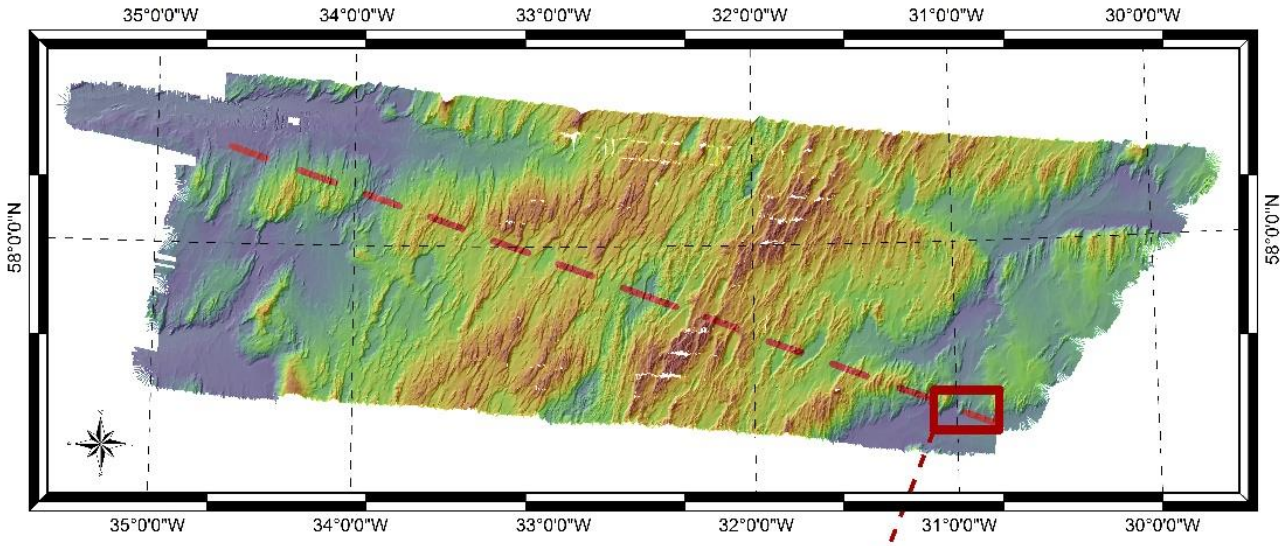

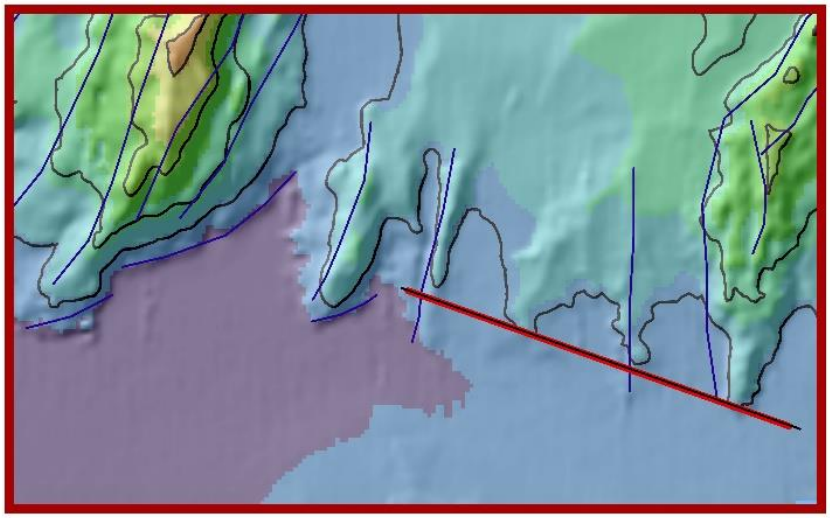

Legend

Depth (m)

- -3.300 - -2.750
- -2.750 - -2.550
- -2.550 - -2.374
- -2.374 - -2.187
- -2.187 - -2.011
- -2.011 - -1.836
- -1.836 - -1.673
- -1.673 - -1.510
- -1.510 - -1.310
- -1.310 - -721

- 300 m isobath
- Topographic Profile
- Normal Faults

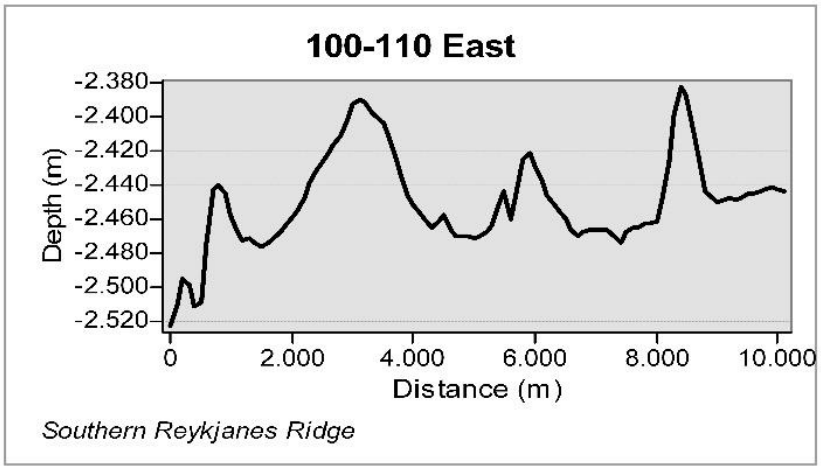

Coordinate System: WGS 1984 UTM Zone 25N
Projection: Transverse Mercator
Datum: WGS 1984
False Easting: 500.000,0000
False Northing: 0,0000
Central Meridian: -33,0000
Scale Factor: 0,9996
Latitude Of Origin: 0,0000
Units: Meter

Author: Rocha, R. (2017)

Appendix E - Earthquakes

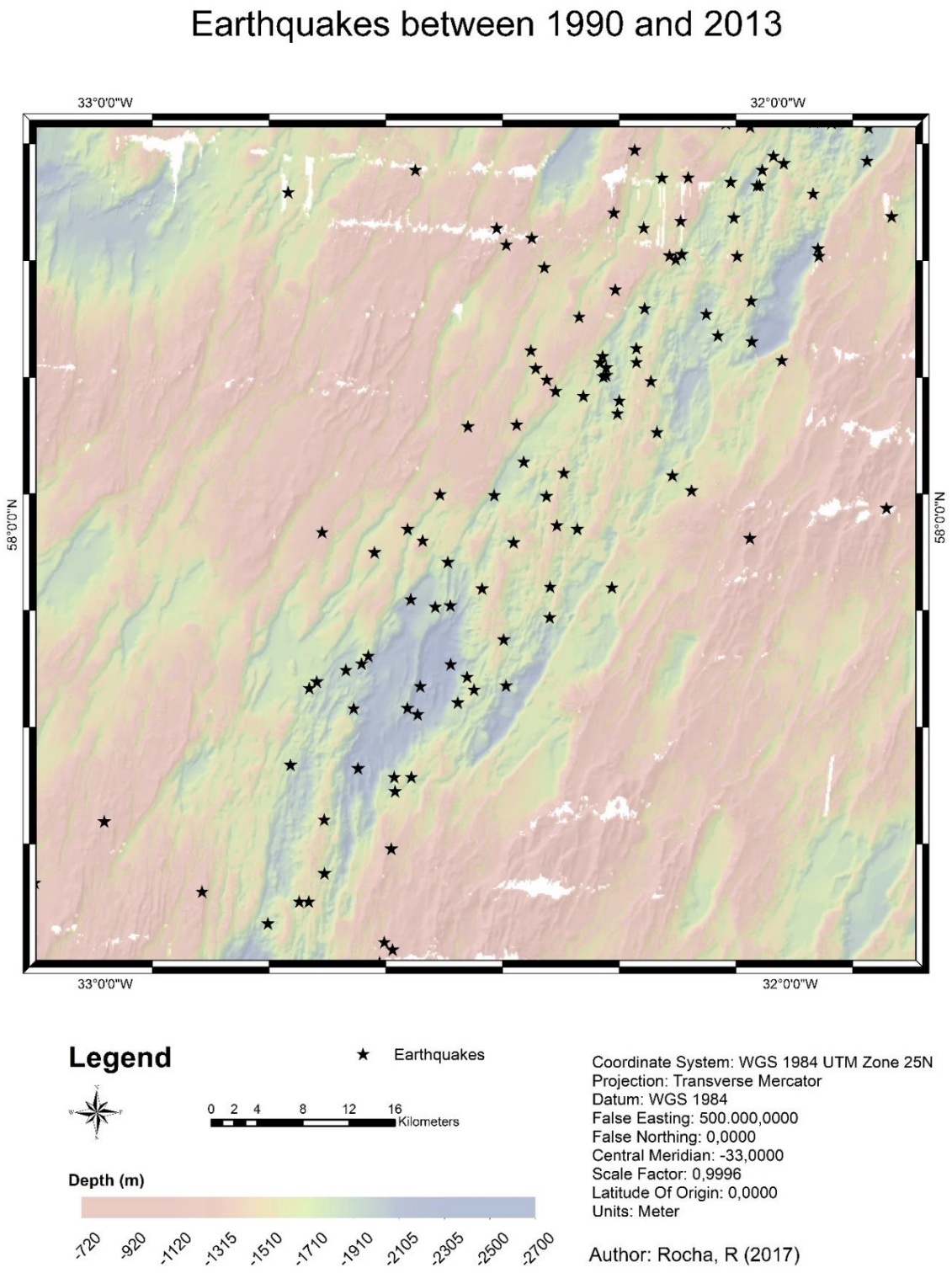

Appendix G – Rose Diagrams

DIP DIRECTION		
Distance from the Graben (Km)	**WEST**	**EAST**
0-10	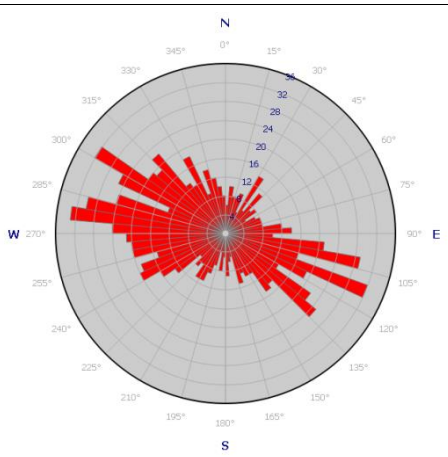	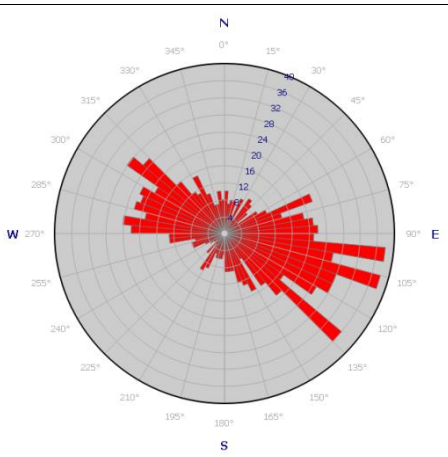
10-20	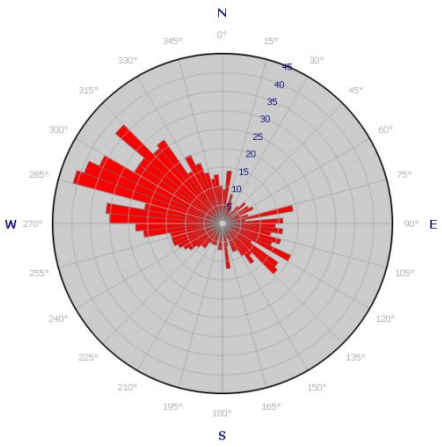	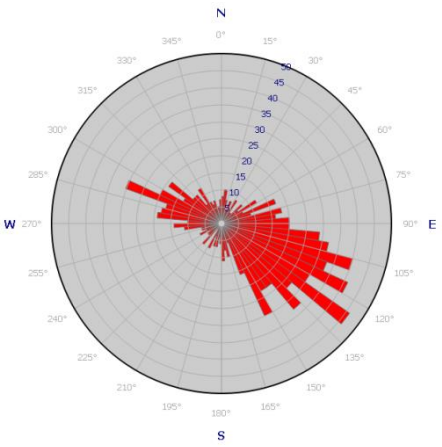
20-30	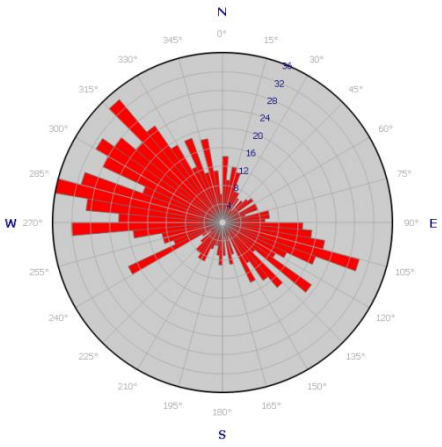	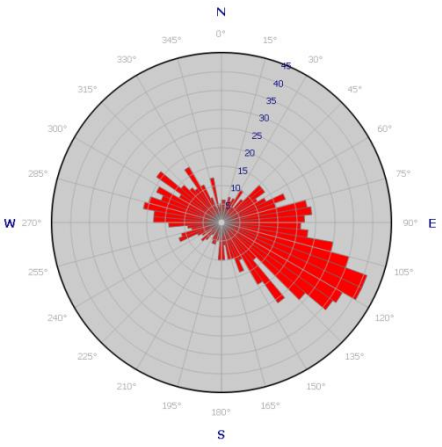

30-40	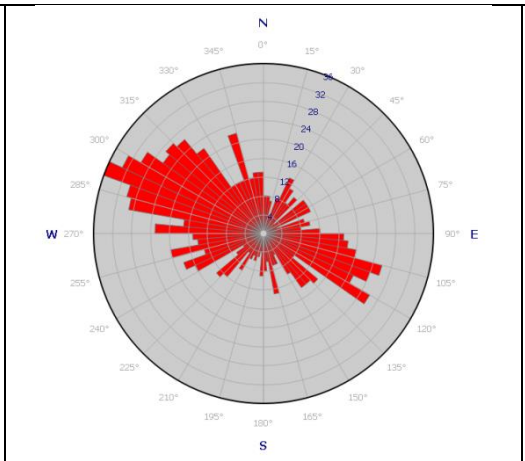	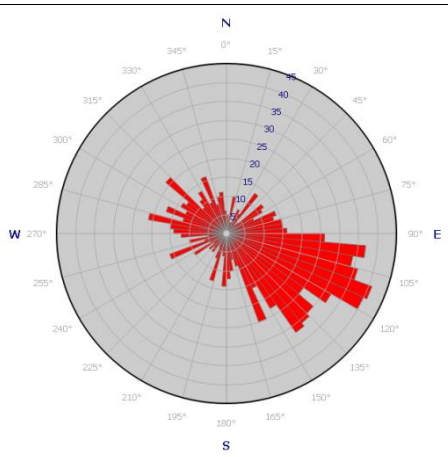
40-50	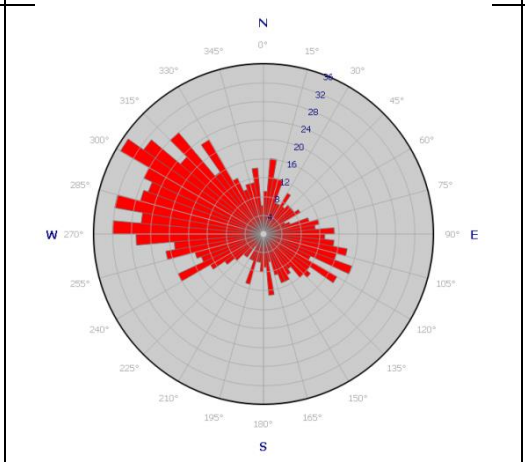	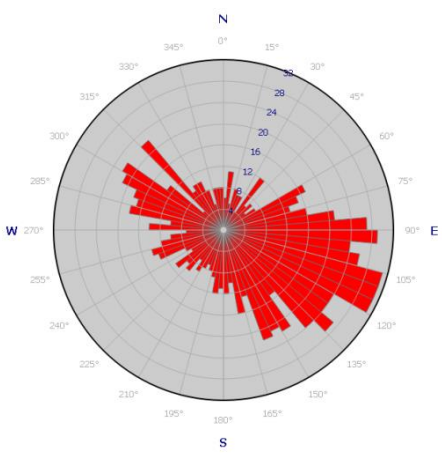
50-60	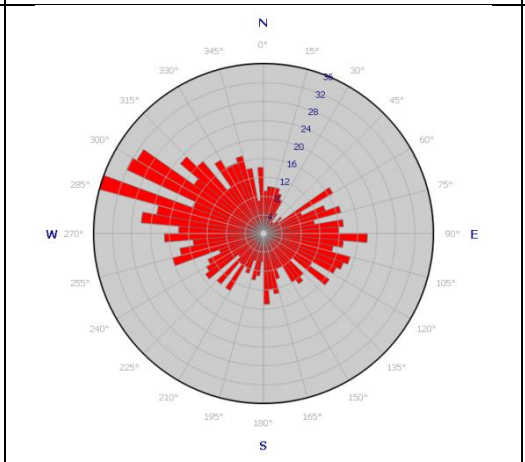	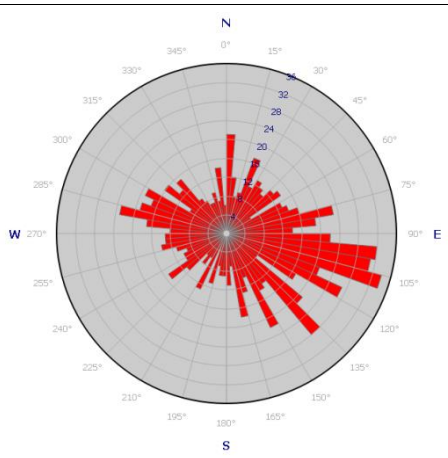
60-70	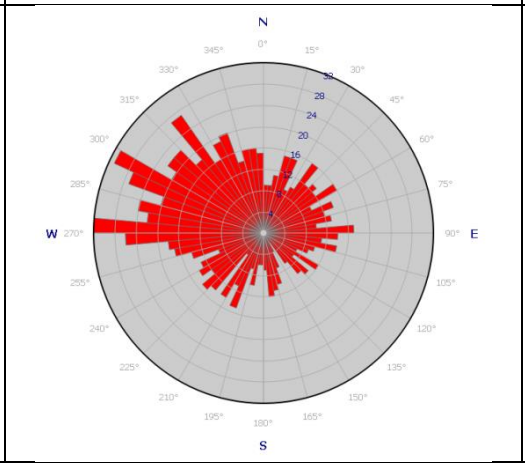	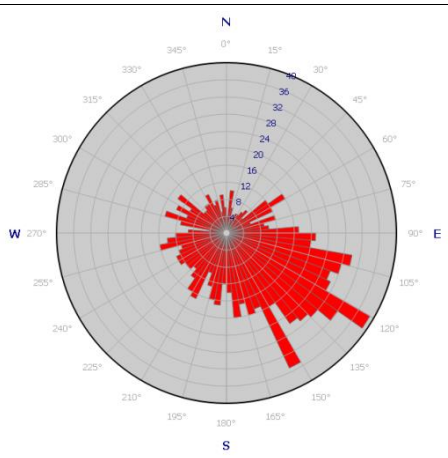

70-80	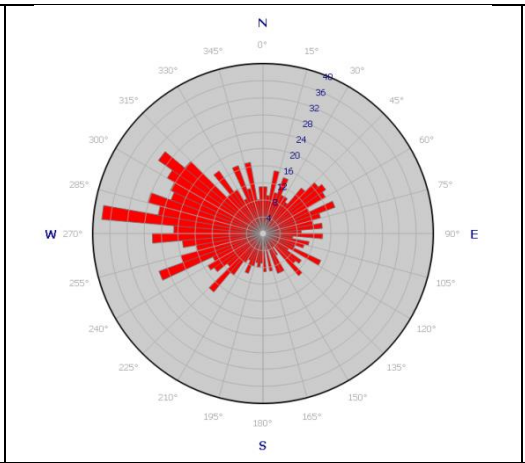	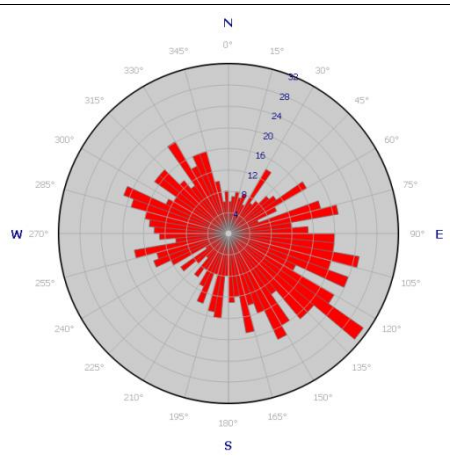
80-90	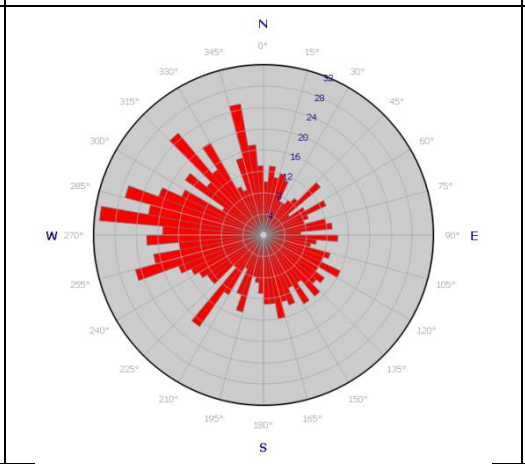	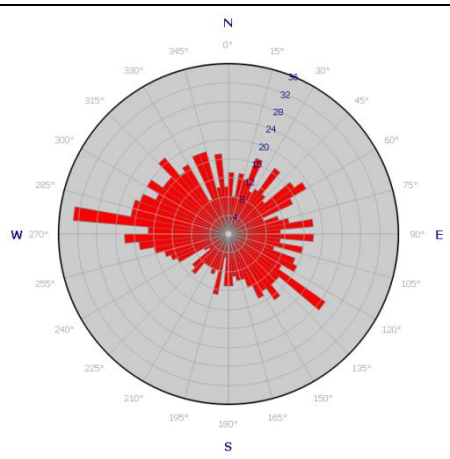
90-100	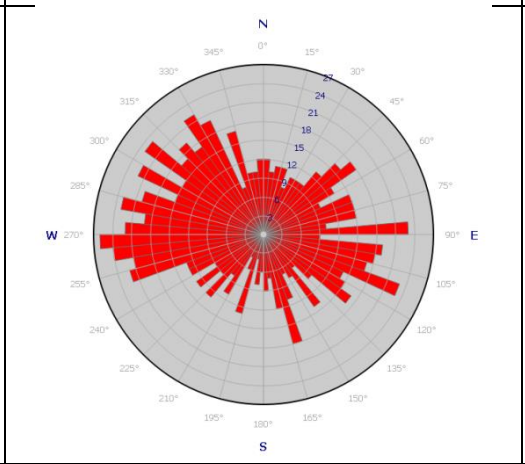	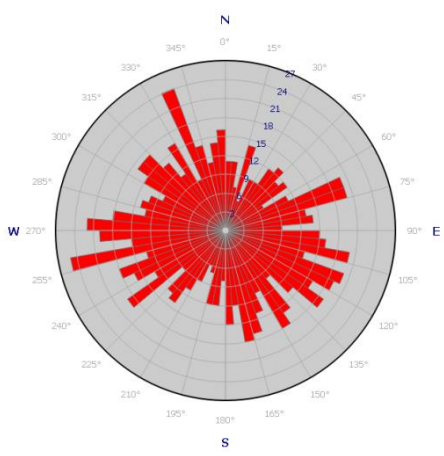
100-110	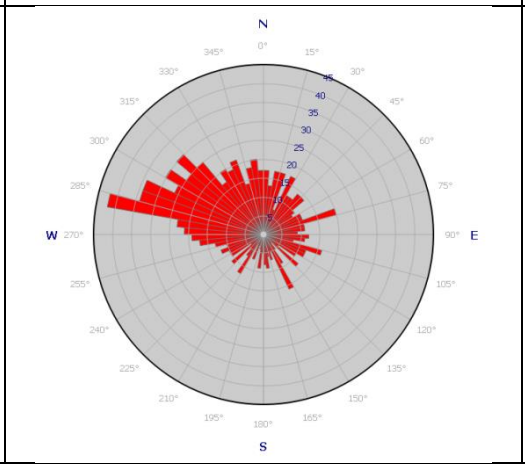	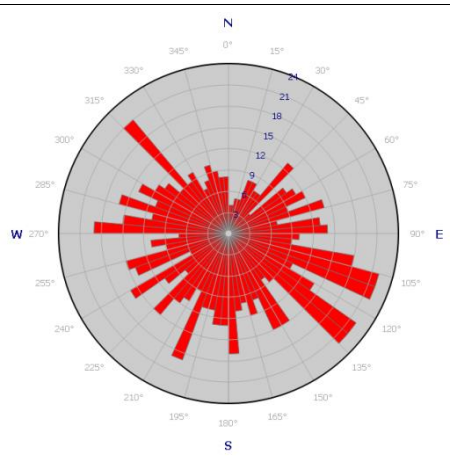

STRIKE		
Distance from the Graben (Km)	**WEST**	**EAST**
0-10	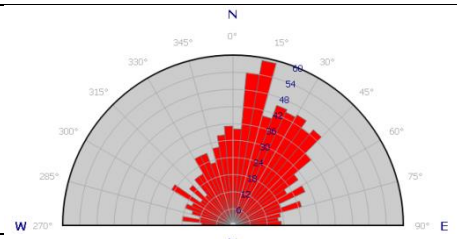	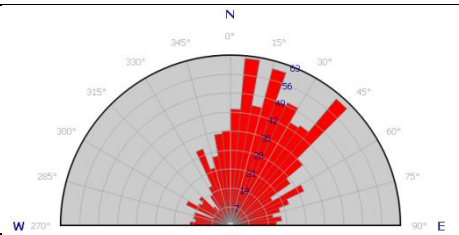
10-20	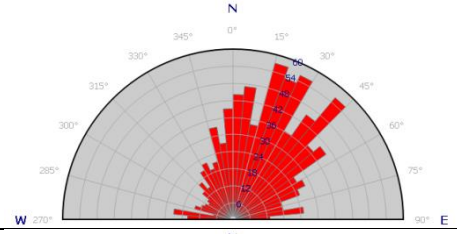	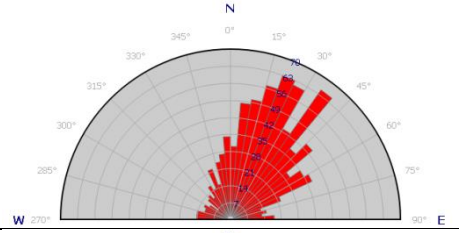
20-30	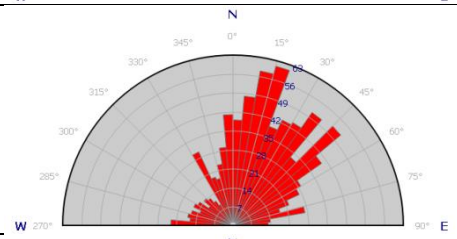	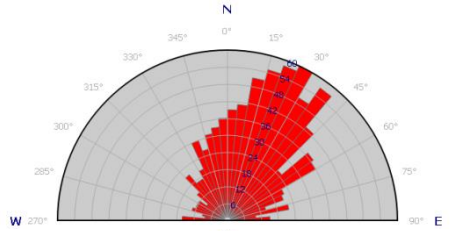
30-40	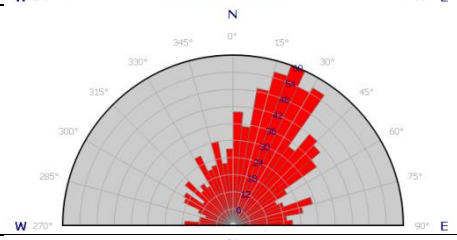	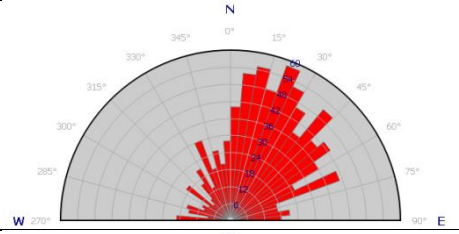
40-50	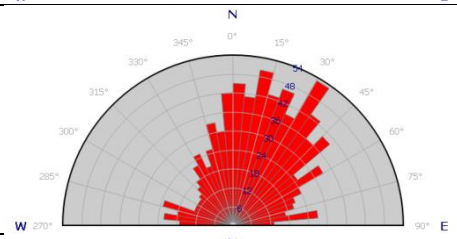	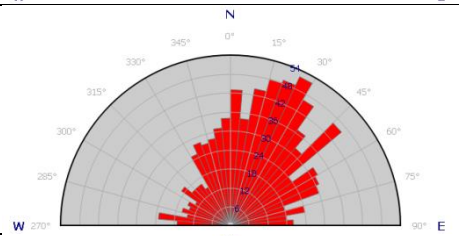
50-60	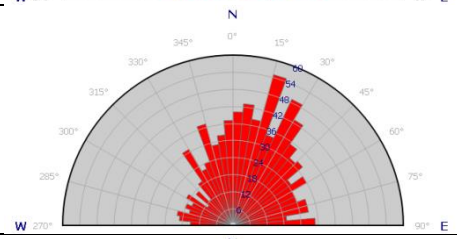	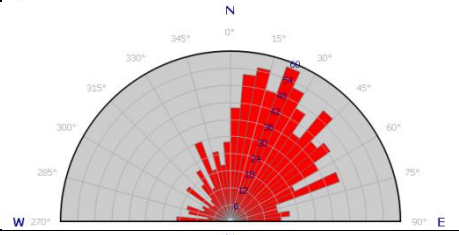
60-70	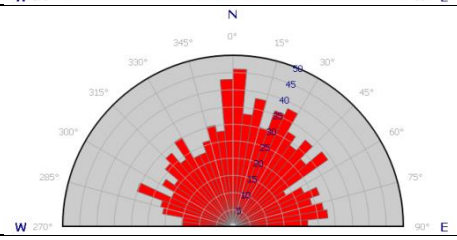	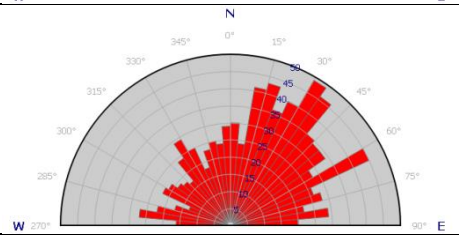

70-80	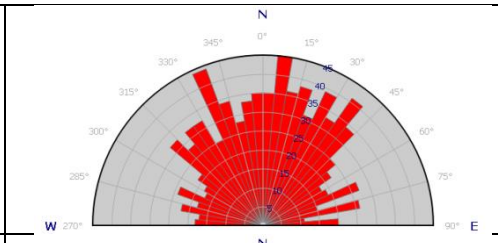	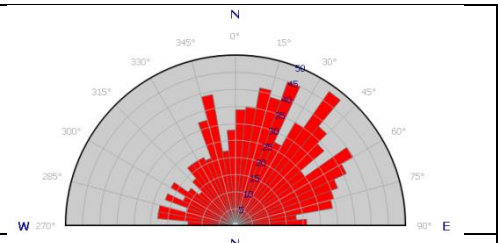
80-90	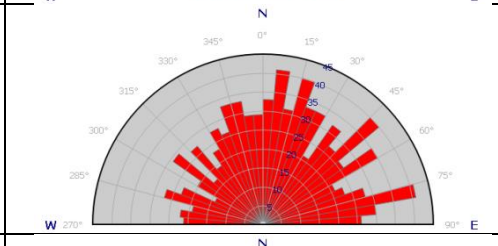	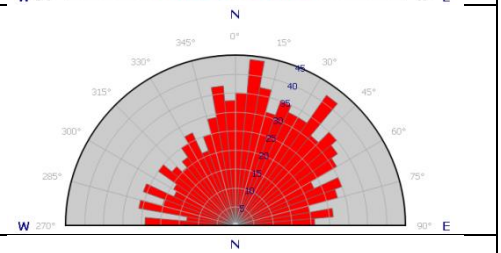
90-100	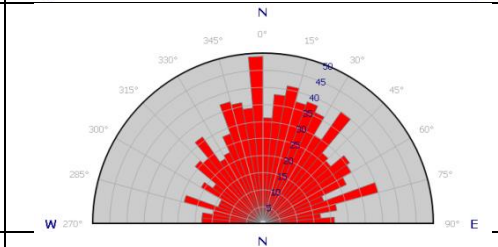	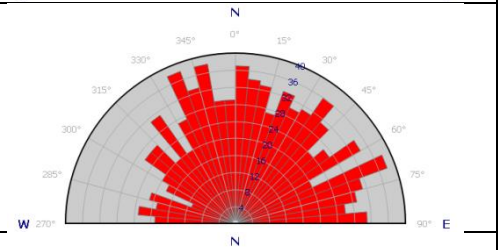
100-110	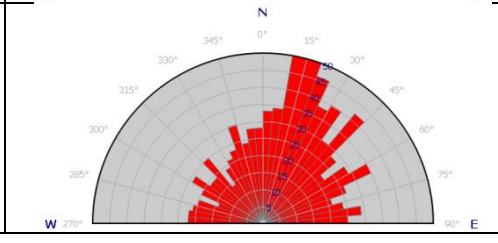	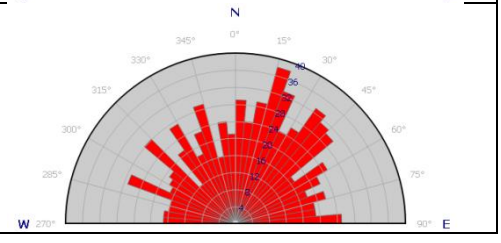

DIP ANGLE		
Distance from the Graben (Km)	**WEST**	**EAST**
0-10	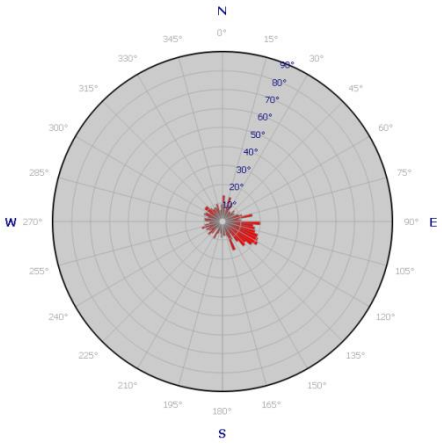	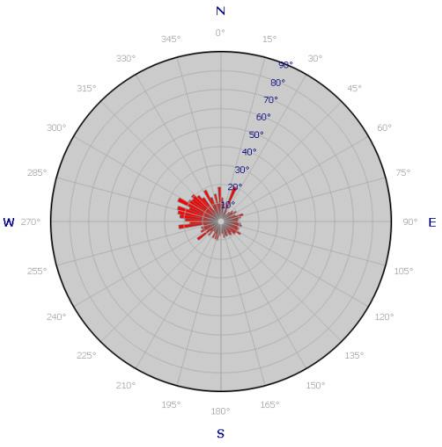 e
10-20	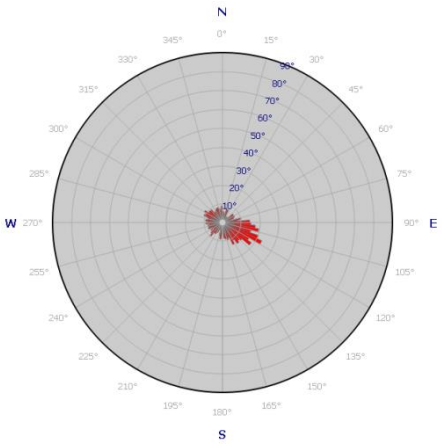	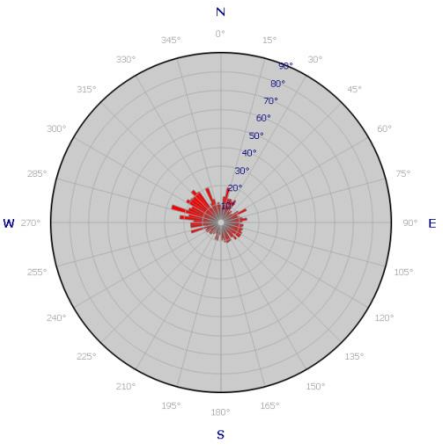
20-30	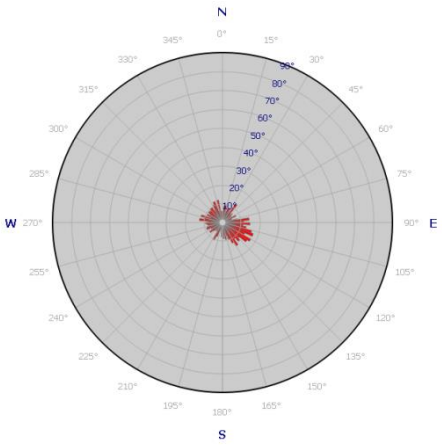	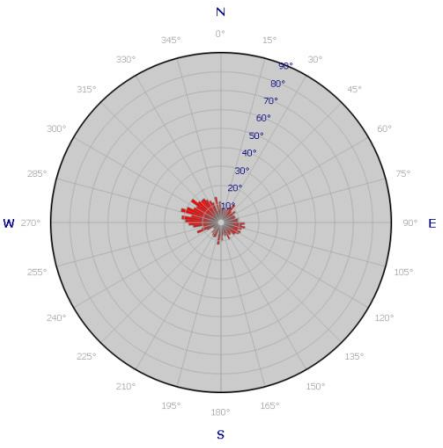

30-40	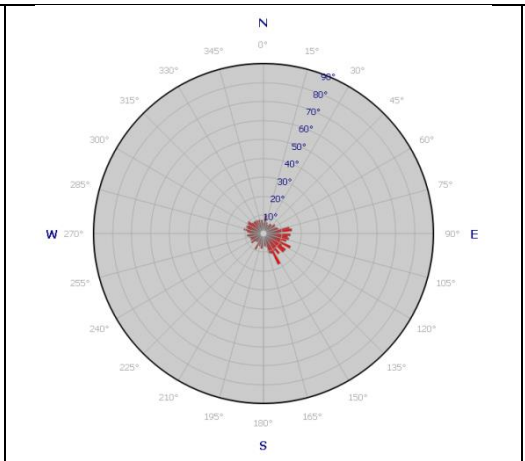	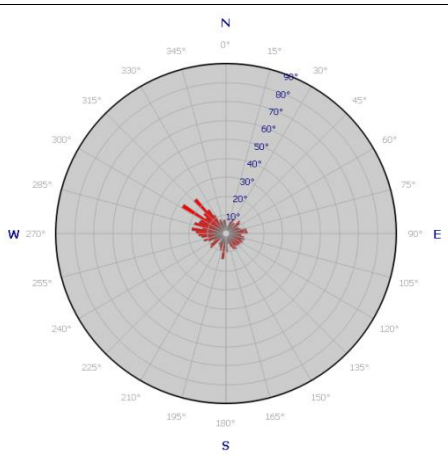
40-50	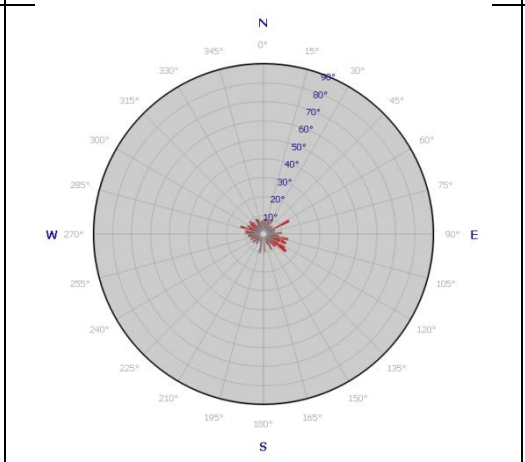	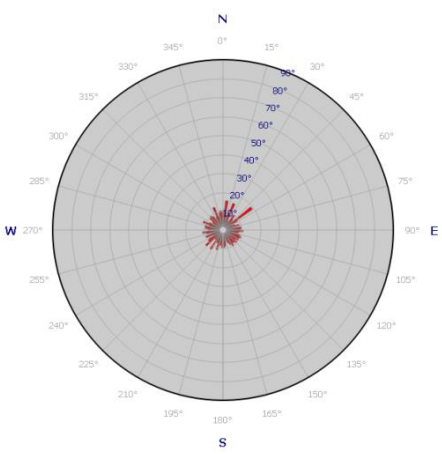
50-60	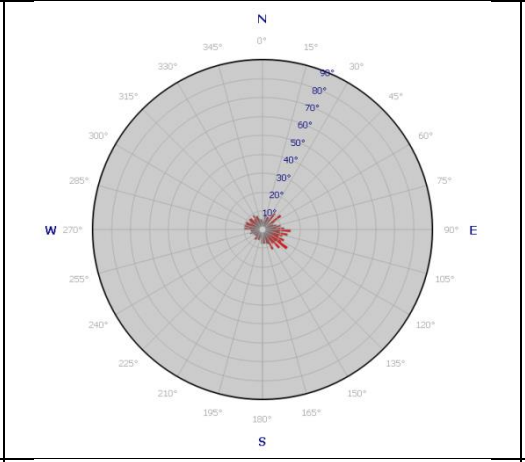	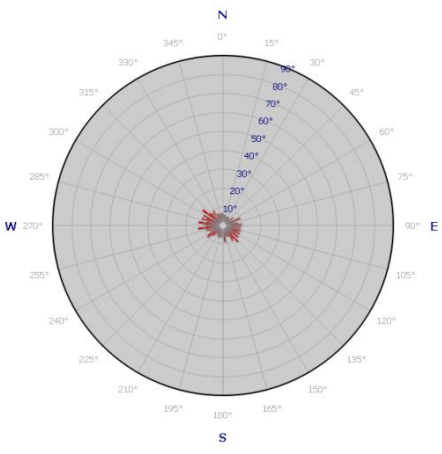
60-70	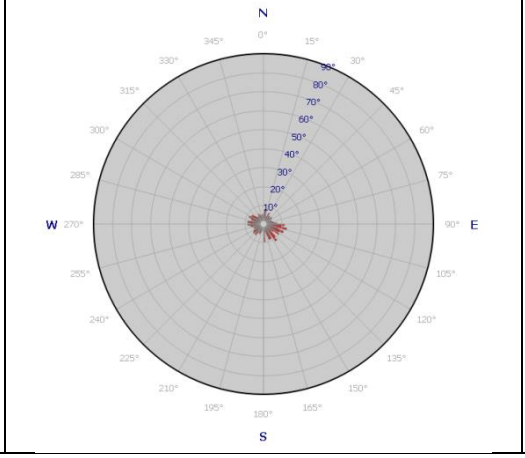	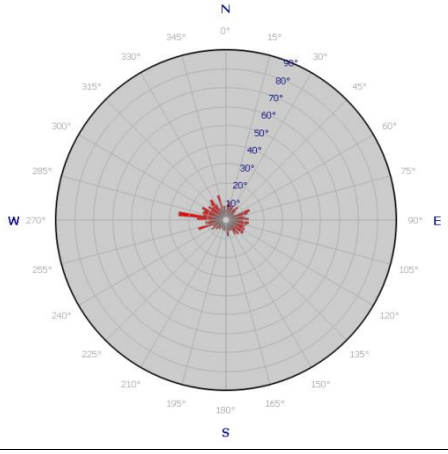

70-80	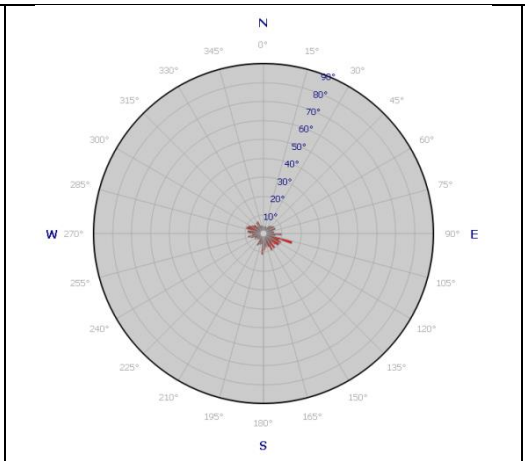	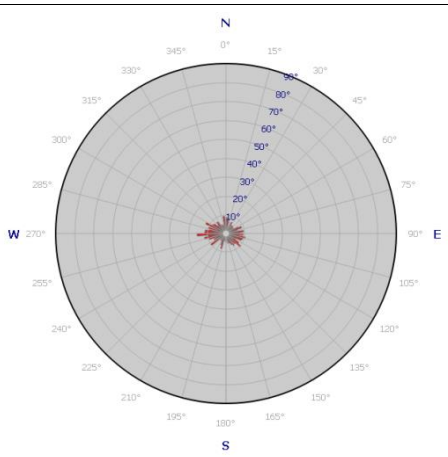
80-90	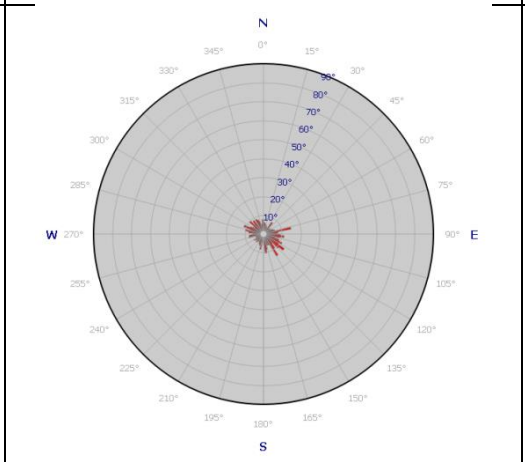	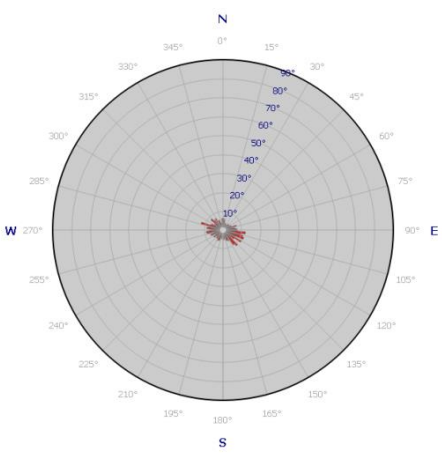
90-100	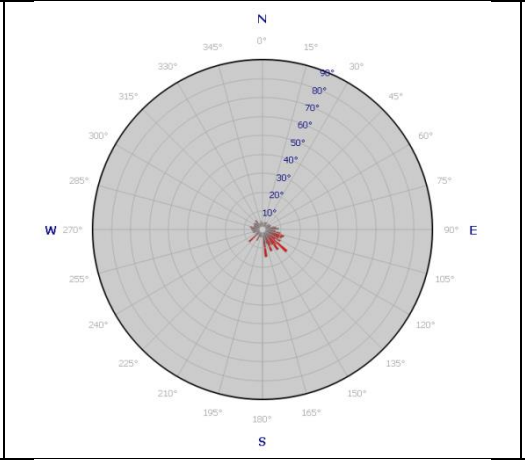	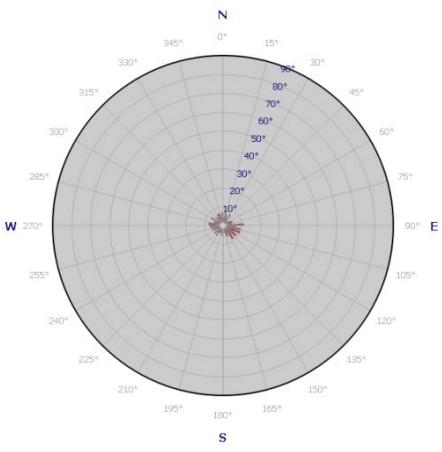
100-110